Universidad de Concepción
Dirección de Postgrado
Facultad de Ciencias Químicas
Programa Doctorado en Ciencias Geológicas

Comprendiendo el ciclo sísmico en la costa de Chile central y su complejo registro geológico

Understanding the seismic cycle on the central Chilean coast and its complex geological record

Tesis para optar al grado de Doctor en Ciencias Geológicas

BLADIMIR EGARDO SALDAÑA VALDÉS
CONCEPCIÓN-CHILE
2025

Profesor Guía: Dr. Marco Cisternas Vega
Instituto de Geografía
Pontificia Universidad Católica de Valparaíso

Profesor Co-Guía: Dr. Joaquín Cortés Aranda
Dpto. de Ciencias de la Tierra, Facultad de Ciencias Químicas
Universidad de Concepción

A mi madre, a quien le debo todo.

Agradecimientos

Esta tesis refleja años de arduo trabajo y sacrificio, así como frustraciones y alegrías que quizás solo un estudiante de postgrado puede entender, pero por sobre todo representa mi aprendizaje personal como futuro científico y amante de la geología.

En este apartado quisiera agradecer a todas aquellas personas que me brindaron su apoyo incondicional y que hicieron posible esta investigación. En primer lugar, mis agradecimientos van dedicados a mi familia, en especial mi mamá y mi hermano, quienes son los pilares fundamentales en mi vida.

Quisiera también expresar mis más sinceros agradecimientos al Laboratorio GeoTsunami de la Pontificia Universidad Católica de Valparaíso y a las maravillosas personas que lo integran, a quienes desde hace ya varios años considero como mi segunda familia.

Agradezco al programa de Doctorado en Ciencias Geológicas de la Universidad de Concepción, especialmente a Joaquín Cortés y María Esperanza, quienes tuvieron una infinita paciencia con mis constantes atrasos en el término de este manuscrito.

Para mis amigos y compañeros, mi más sincera admiración y cariño.

Gracias a cada uno de los que hicieron esto posible. Me llevo conmigo todas las experiencias aprendidas en esta enriquecedora etapa.

Resumen

Las costas adyacentes a zonas de subducción son continuamente amenazadas por grandes terremotos y tsunamis, cuyos efectos generan significativos impactos ambientales y sociales. En este contexto, los registros geológicos completos de eventos pasados constituyen una herramienta clave para evaluar apropiadamente la amenaza futura. Sin embargo, en Chile central, donde reside la mayor población costera del país, estos registros son fragmentarios y discontinuos, producto de la interacción entre factores tectónicos, climáticos y antrópicos que dificultan tanto su formación como su preservación a lo largo del tiempo.

Esta tesis doctoral tuvo como objetivo general evaluar cómo dichos factores condicionan el registro geológico de terremotos y tsunamis, y determinar en qué medida un enfoque multidisciplinario, basado en la integración de evidencias satelitales, estratigráficas, paleoecológicas, históricas e instrumentales, puede mejorar la reconstrucción de la deformación costera y la distribución espacial de los depósitos de tsunami. Las principales preguntas de investigación se centraron en identificar qué factores explican el escaso registro paleosismológico en Chile central, cómo ha variado la deformación vertical costera durante el último siglo, y cuál es el potencial de la percepción remota en la detección de modernos depósitos de tsunami. Estas interrogantes fueron abordadas en dos áreas clave: la costa del Maule, entre Lipimávida y la desembocadura del Río Mataquito, y el humedal de Campiche en la Bahía de Quintero.

Los resultados identificaron tres factores principales que limitan el registro paleosismológico en Chile central: (i) el alzamiento tectónico sostenido, que reduce el espacio de acomodación y favorece la erosión; (ii) el clima mediterráneo semiárido, que restringe la preservación del registro geológico y limita la formación de ambientes de baja energía y (iii) la intervención antrópica, que ha modificado o destruido numerosos sitios con potencial paleosismológico.

A pesar de estas limitaciones, la aplicación de percepción remota permitió identificar y mapear el depósito de tsunami del 2010, demostrando el potencial de técnicas satelitales en la asistencia de trabajos de campo. Asimismo, el análisis de diatomeas, apoyado por mediciones mareográficas y geodésicas, permitió reconstruir la deformación vertical de la costa de Chile central durante todo el siglo XX, sugiriendo que terremotos con fuente profunda en la zona de subducción podrían estar contribuyendo a la construcción de topografía a largo plazo.

En conjunto, se concluye que la integración de enfoques metodológicos multidisciplinarios resulta esencial para asistir en la reconstrucción de patrones de deformación vertical costera y áreas de inundación de tsunamis en este segmento altamente vulnerable del margen chileno. Los hallazgos y enfoques desarrollados en este estudio pueden servir como referencia para otros segmentos del margen de subducción chileno, donde el registro geológico también presenta desafíos significativos para su identificación y comprensión.

Abstract

Coasts adjacent to subduction zones are continuously threatened by large earthquakes and tsunamis, whose effects cause significant environmental and social impacts. In this context, complete geological records of past events represent a key tool to properly assess future hazards. However, in central Chile, where most of the country's coastal population resides, these records are fragmentary and discontinuous, as a result of the interplay between tectonic, climatic, and anthropogenic factors that hinder both their formation and long-term preservation.

This doctoral thesis aimed to evaluate how these factors condition the geological record of earthquakes and tsunamis, and to determine to what extent a multidisciplinary approach, based on the integration of satellite, stratigraphic, paleoecological, historical, and instrumental evidence, can improve the reconstruction of coastal deformation and the spatial distribution of tsunami deposits. The main research questions focused on identifying the factors that explain the scarce paleoseismological record in central Chile, assessing how coastal vertical deformation has varied over the last century, and evaluating the potential of remote sensing in detecting modern tsunami deposits. These questions were addressed in two key areas: the Maule coast, between Lipimávida and the mouth of the Mataquito River, and the Campiche wetland in Quintero Bay.

The results identified three main factors that limit the paleoseismological record in central Chile: (i) sustained tectonic uplift, which reduces accommodation space and enhances erosion; (ii) the semi-arid Mediterranean climate, which restricts geological preservation and limits the development of low-energy depositional environments; and (iii) anthropogenic disturbance, which has modified or destroyed numerous sites with paleoseismological potential.

Despite these limitations, the application of remote sensing techniques allowed the identification and mapping of the 2010 tsunami deposit, demonstrating the potential of satellite-based methods to support fieldwork. Likewise, diatom analysis, supported by

tide-gauge and geodetic measurements, enabled the reconstruction of vertical coastal deformation throughout the 20th century, suggesting that deep-source earthquakes along the subduction interface may contribute to long-term coastal uplift and landscape building.

Overall, this study concludes that the integration of multidisciplinary methodological approaches is essential to assist in the reconstruction of coastal vertical deformation patterns and tsunami inundation areas in this highly vulnerable segment of the Chilean margin. The findings and approaches developed here may serve as a reference for other sectors of the Chilean subduction margin, where geological records also pose significant challenges for their identification and interpretation.

Índice de contenidos

Índice de figuras

Índice de tablas

Capítulo 1. Introducción

1.1 Planteamiento del problema y motivación

Las costas adyacentes a zonas de subducción son frecuentemente amenazadas por grandes terremotos, cuyos efectos generan graves consecuencias para la sociedad (e.g., Wirth et al., 2022). Tan solo durante el presente siglo, grandes terremotos como el de Sumatra-Andaman en 2004 (Mw 9.2), Chile en 2010 (Mw 8.8), Japón en 2011 (Mw 9.0) y Rusia en 2025 (Mw 8.8) han causado impactos notables en la costa, incluyendo pérdidas de vidas, daños a infraestructura y modificaciones en el paisaje (e.g., Lay et al., 2005; Norio et al., 2011; Vargas et al., 2011). Particularmente, dos de los principales efectos causados por estos recientes terremotos fueron el repentino cambio del nivel de la costa y un masivo tsunami como consecuencia de la deformación cortical (e.g., Titov et al., 2005; Meltzner et al., 2006; Farías et al., 2010; Fritz et al., 2011; Mori et al., 2011; Ozawa et al., 2011). Por ejemplo, gran parte de la costa noreste de Japón fue hundida cosísmicamente cerca de 1 m durante el terremoto del 2011 y afectada por un posterior tsunami que inundó hasta 5 km tierra adentro (e.g., Goto et al., 2011; Nishimura, 2014). Eventos destructivos como este ocurren en un contexto de ciclo sísmico (e.g., Reid, 1910; Wirth et al., 2022), retornando después de décadas a siglos de acumulación de energía en el contacto interplaca (Figura 1.1). Por lo tanto, comprender estos fenómenos y sus consecuencias resulta fundamental para la evaluación del riesgo y la planificación costera.

Estudios paleosismológicos han desempeñado un papel crucial en la reconstrucción de la historia sísmica de zonas de subducción, permitiendo identificar patrones de recurrencia, estimar la magnitud y delimitar la extensión espacial de grandes terremotos y tsunamis (e.g., Atwater y Hemphill-Haley, 1997; Nanayama et al., 2003; Jankaew et al., 2008; Monecke et al., 2008; Sawai et al., 2012). A partir de la información geológica preservada en secuencias de sedimentos costeros, como capas de arena depositadas por tsunamis o evidencia de cambios del nivel costero asociado a terremotos (ver sección 1.2), es posible extender el registro de estos

eventos más allá del periodo instrumental e histórico (e.g., Atwater, 1987; Nelson et al., 1996). Tal aproximación proporciona un marco temporal más extenso y robusto para evaluar el peligro sísmico y tsunamigénico asociado al ciclo de los terremotos de subducción.

Diversos estudios paleosismológicos han sido conducidos en la costa chilena con el objetivo de reconstruir la historia de terremotos y tsunamis pasados. Estos trabajos han permitido cuantificar la deformación vertical costera durante ciclos de terremotos, inferir la magnitud e intervalos de recurrencia de grandes eventos sísmicos, y estimar el área de inundación de tsunamis históricos y prehistóricos (e.g., Cisternas et al., 2005; 2017; Moernaut et al., 2014; Garret et al., 2015; Hocking et al., 2021). No obstante, la mayoría de estas investigaciones se han concentrado principalmente en el sur de Chile (Figura 1.2), particularmente dentro del área de ruptura del terremoto de 1960 (Mw 9.5), el evento sísmico más grande registrado instrumentalmente a nivel mundial. Esta limitación espacial ha dejado considerablemente relegados otros segmentos del margen de subducción chileno que también poseen un alto potencial sísmico, como es el caso de Chile central. Esta región, que abarca sectores densamente poblados y con una importante infraestructura, ha sido pobremente caracterizada en términos de su comportamiento sísmico-tsunamigénico a largo plazo (León et al., 2023). En consecuencia, existe una brecha significativa en el conocimiento paleosismológico de esta zona, lo que limita la capacidad de evaluar adecuadamente la amenaza y la preparación frente a futuros terremotos de subducción. Esta situación resulta especialmente preocupante considerando que Chile central alberga la mayor población costera del país, con cerca de 3.000.000 de habitantes (Figura 1.2), lo que incrementa su vulnerabilidad ante la ocurrencia de grandes terremotos y tsunamis.

La escasez de estudios paleosismológicos en Chile central probablemente está condicionada por múltiples factores, los cuales aún no han sido abordados conceptualmente. Motivado por esta problemática, la presente investigación doctoral pretende explorar los principales factores que limitan el estudio del registro

paleosismológico en Chile central, incluyendo complejidades tectónicas, climáticas y antrópicas. Adicionalmente, se propone la integración de múltiples enfoques, tales como satelitales, estratigráficos, sedimentológicos, paleoecológicos, históricos, mareográficos y geodésicos, para asistir en la reconstrucción de tanto las áreas de inundación de tsunamis recientes como los patrones de deformación vertical costera inducidos por terremotos de subducción en este segmento del margen chileno.

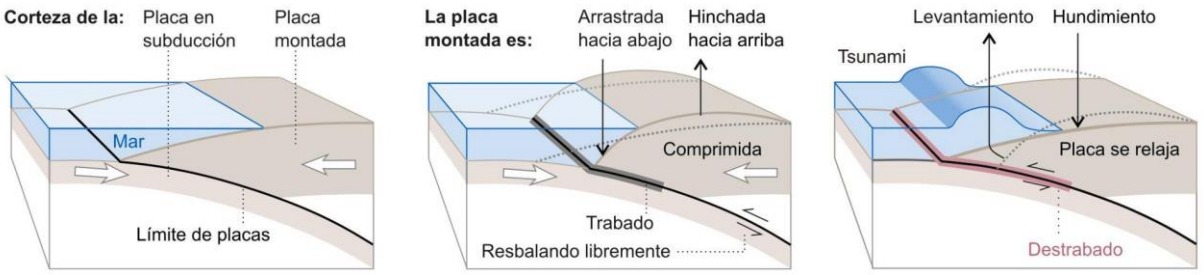

Figura 1.1. Representación esquemática de una zona de subducción. Flechas blancas indican la convergencia entre ambas placas tectónicas, donde una de ellas desciende respecto a la otra. En el caso del margen chileno la placa oceánica (Placa de Nazca) desciende bajo la placa continental (Placa Sudamericana). En el contacto interplaca ambas placas se encuentran fuertemente acopladas, acumulando energía durante décadas a siglos. Durante un terremoto ambas placas ceden y la energía es bruscamente liberada. Tsunamis y repentinos cambios del nivel de la costa son una consecuencia directa de los terremotos interplaca. Tomado de Atwater et al. (2015).

1.2 Depósitos de tsunami y cambios verticales costeros

Los depósitos de tsunami corresponden a capas de sedimento, generalmente arena, que pueden extenderse por varios kilómetros tierra adentro a medida que las olas de un tsunami ingresan desde la línea de costa. Estos depósitos proporcionan información crítica sobre las características propias del tsunami, tales como condiciones de flujo, número de olas y la fuente (e.g, Spiske, 2020). Particularmente, la distribución espacial de un depósito de tsunami es clave para delimitar la extensión real de la inundación (e.g., Abe et al., 2020; MacInnes et al., 2010). Recientes estudios desde tsunamis modernos han mostrado que el área cubierta por un depósito de tsunami puede ser una confiable aproximación del área mínima de inundación (Gelfenbaum and Jaffe, 2003; Jaffe et al., 2003, 2006; MacInnes et al.,

2009a; MacInnes et al., 2010; Moore et al., 2006, 2011; Srinivasalu et al., 2007; Szczuciński et al., 2012). Sin embargo, otros estudios cuestionan su real utilidad como *proxy,* permaneciendo aún el debate (Abe et al., 2012; Chagué-Goff et al., 2015; Cheng and Weiss, 2013; Goto et al., 2011; Morton et al., 2011).

Una de las principales dificultades al estudiar la completa distribución espacial de un depósito de tsunami es que requiere de extenso trabajo de campo, consistiendo en una tarea altamente demandante de tiempo. Adicionalmente, para depósitos modernos, tales levantamientos de campo deben ser hechos prontamente después de la ocurrencia del evento para minimizar el enmascaramiento o destrucción del depósito por causas humanas o naturales (Bahlburg and Spiske, 2015; Nichol and Kench, 2008; Spiske et al., 2020; Szczuciński, 2012; Szczuciński et al., 2006). Estos desafíos incentivan a que otros enfoques alternativos sean explorados, tales como la percepción remota, la cual permite mapear extensas áreas en un corto periodo. Datos satelitales han sido particularmente útiles en el mapeo de áreas de inundación, daño a infraestructura y cambios costeros (e.g., Koshimura et al., 2020; Ramírez-Herrera and Navarrete-Pacheco, 2013; Richmond et al., 2012; Sublime and Kalinicheva, 2019; Tappin et al., 2012). Sin embargo, técnicas de teledetección y aprendizaje automático no han sido aplicadas específicamente a la detección de depósitos de tsunami.

Mayores desafíos surgen al estudiar depósitos de tsunami desde secuencias de sedimentos costeros. Durante las últimas décadas, estudios paleosismológicos han utilizado depósitos de tsunami preservados en marismas, humedales y otros ambientes costeros para reconstruir la historia de tsunamis pasados (e.g., Cisternas et al., 2005; Jankwaew et al., 2008; Costa y Andrade, 2020). Sin embargo, la identificación y correcta interpretación de los depósitos en el registro geológico puede ser desafiante. Los depósitos arenosos dejados por tsunamis pueden ser sorprendentemente similares a aquellos originados por otros eventos de alta energía, tales como tormentas e inundaciones de ríos (Kortekaas y Dawson, 2007; Morton et al., 2007; Engel y Brückner, 2011; Goff et al., 2012; Phantuwongraj y Choowong,

2012; Ramírez-Herrera et al., 2012; Shanmugam, 2012; Delile y Salomon, 2020; Kongsen et al., 2022). Esto último es especialmente problemático, ya que numerosos estudios sobre depósitos de tsunami en Chile han sido conducidos en las inmediaciones de desembocaduras de ríos andinos (Ely et al., 2014; Hong et al., 2016; Aedo et al., 2021; Hocking et al., 2021; Easton et al., 2022; Araya et al., 2022; 2024), donde la superposición de aportes continentales y marinos pueden generar un mezclado registro.

Más allá del análisis de los depósitos de tsunami, el registro geológico costero constituye una fuente de información esencial para la reconstrucción de cambios verticales asociados a ciclos de terremotos (e.g., Shennan et al., 2014; Dura et al., 2015). Estos cambios, expresados como alzamiento o subsidencia, reflejan la dinámica del ciclo sísmico en la interfaz de subducción y pueden presentar patrones espaciales altamente heterogéneos. Aunque los registros geodésicos modernos han permitido medir estos desplazamientos con gran precisión, su cobertura temporal se limita a las últimas décadas, por lo que no capturan la deformación costera a largo plazo.

En este sentido, los indicadores paleoecológicos, especialmente las diatomeas (microalgas silíceas), se han consolidado como herramientas fundamentales para extender las observaciones geodésicas hacia el pasado (e.g., Dura et al., 2016; DePaolis et al., 2024). Gracias a su marcada sensibilidad a gradientes de salinidad y a la posición vertical respecto al nivel del mar, las diatomeas permiten reconstruir desplazamientos verticales de pocos decímetros mediante la identificación de transiciones entre comunidades marinas, salobres y dulces en perfiles sedimentarios (Hemphill-Haley, 1995; Atwater and Hemphill-Haley, 1997; Dura et al., 2015, 2016; Garrett et al., 2015). Esta aproximación ha demostrado ser eficaz en distintos márgenes de subducción (Shennan et al., 1999; Sawai et al., 2004; Hamilton and Shennan, 2005b; Dura et al., 2015), donde los cambios en las asociaciones de diatomeas han permitido cuantificar la magnitud y sentido de la deformación.

De esta forma, la integración de registros sedimentarios, indicadores paleoecológicos y observaciones geodésicas contemporáneas amplía la ventana temporal y espacial de observación de la deformación costera, proporcionando una base sólida para interpretar la evolución del relieve y su relación con el ciclo sísmico. Los resultados de esta tesis se inscriben dentro de este marco conceptual, buscando no solo mejorar el estudio de los depósitos de tsunami, sino también evaluar la magnitud, persistencia y distribución espacial de los cambios verticales costeros asociados a los grandes terremotos históricos en Chile central.

1.3 Chile central

1.3.1 Generalidades

La zona centro de Chile, comprendida entre los 30° y 38°S, se caracteriza por una compleja interacción entre factores tectónicos, climáticos y demográficos, que condicionan su evolución geográfica y su vulnerabilidad ante fenómenos naturales.

Desde el punto de vista tectónico, esta región se encuentra emplazada sobre el margen activo de subducción entre las placas de Nazca y Sudamericana, las cuales convergen a una tasa de ~65 mm/año (Angermann et al., 1999; Norabuena et al., 1999; Jarrin et al., 2023). Esta dinámica ha dado origen a una intensa actividad sísmica, frecuente ocurrencia de megaterremotos y tsunamis, así como al levantamiento de terrazas marinas y procesos de deformación costera. Ejemplos recientes incluyen los terremotos tsunamigénicos del 2010 (Mw 8.8) y 2015 (Mw 8.3), los cuales rompieron la porción sur y norte de Chile central, respectivamente (Figura 1.3; Moreno et al., 2012; Tilmann et al., 2016). Entre ambas rupturas, un segmento de costa localizado entre ~32° y 34°S ha permanecido sin romper en un gran terremoto desde 1730 (Carvajal et al., 2017a; Carvajal et al., 2019), probablemente acumulando suficiente energía para ser liberada en un futuro evento tsunamigénico (Métois et al., 2016; Melnick et al., 2017; Sippl et al., 2021). Esta brecha sísmica y de tsunami incrementa el nivel de amenaza para zonas costeras industrializadas y densamente pobladas tales como San Antonio, Valparaíso y Viña del mar,

evidenciando la necesidad urgente de considerar el riesgo de terremotos y tsunamis en la planificación costera.

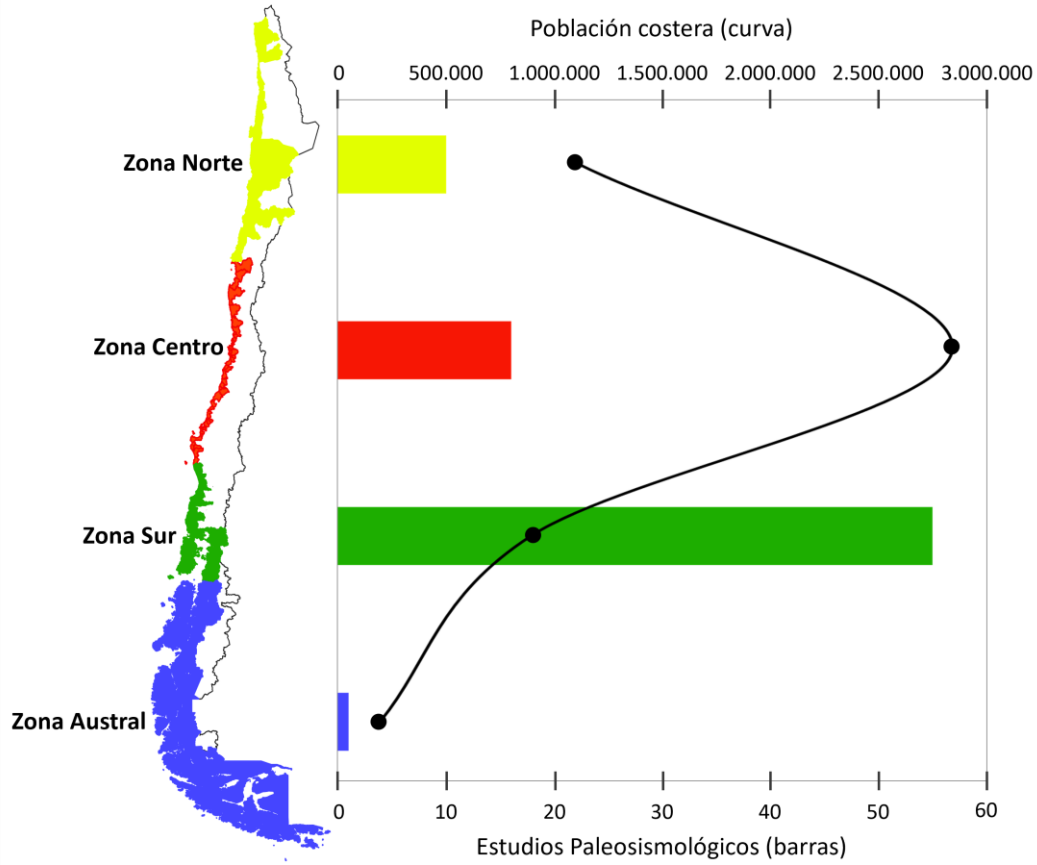

Figura 1.2. Relación entre la población costera (N° de habitantes) y la cantidad de estudios paleosismológicos realizados (N° de estudios) en cada zona de Chile. Notar que en la zona centro de Chile, donde la mayor población costera del país reside, pocos trabajos paleosismológicos han sido llevados a cabo. Población costera por comuna desde datos del censo del 2024 (www.ine.gob.cl).

En cuanto al clima, Chile central presenta un régimen mediterráneo semiárido, caracterizado por un prolongado déficit hídrico durante los meses de verano y precipitaciones moderadas concentradas entre mayo y agosto (~943 mm/año; Toledo y Zapater, 1989; Peel et al., 2007). Este patrón climático genera una fuerte estacionalidad en la disponibilidad de agua, condicionando tanto los ecosistemas como las actividades económicas. Las escasas precipitaciones anuales limitan el desarrollo de ambientes sedimentarios de baja energía, tales como humedales y marismas, los cuales son lugares propicios para generar y registrar evidencia

paleosismológica (León et al., 2023). A su vez, el escaso desarrollo de suelo orgánico y bajas tasas de sedimentación impiden la rápida protección del registro sedimentario de terremotos y tsunamis una vez que ocurren, condicionando así su preservación.

De acuerdo con datos del último censo poblacional del 2024 (www.ine.gob.cl), Chile central alberga la mayor población costera del país, con 2.839.953 habitantes. Esta se ha incrementado de forma sostenida en las últimas décadas, impulsada por la urbanización, el desarrollo portuario y el turismo. Ciudades como Valparaíso, Viña del Mar, San Antonio, Constitución y Concepción concentran una parte importante de la población regional, la infraestructura crítica y las actividades productivas. Esta expansión urbana ha generado una creciente presión sobre los sistemas litorales, con procesos de erosión costera, ocupación de zonas de riesgo, pérdida de humedales y deterioro ambiental (Moris et al., 2021; Hidalgo-Corrotea et al., 2023; Martínez et al., 2023). A su vez, la concentración poblacional en áreas expuestas a terremotos y tsunamis, sumada a los efectos del cambio climático, como el ascenso progresivo del nivel del mar, plantea desafíos urgentes para la planificación territorial y la resiliencia de las comunidades costeras.

En conjunto, la zona costera de Chile central constituye un espacio dinámico, en el que confluyen procesos geológicos activos, condiciones climáticas cambiantes y una alta densidad poblacional, lo que exige enfoques integrados de gestión del riesgo y ordenamiento del territorio.

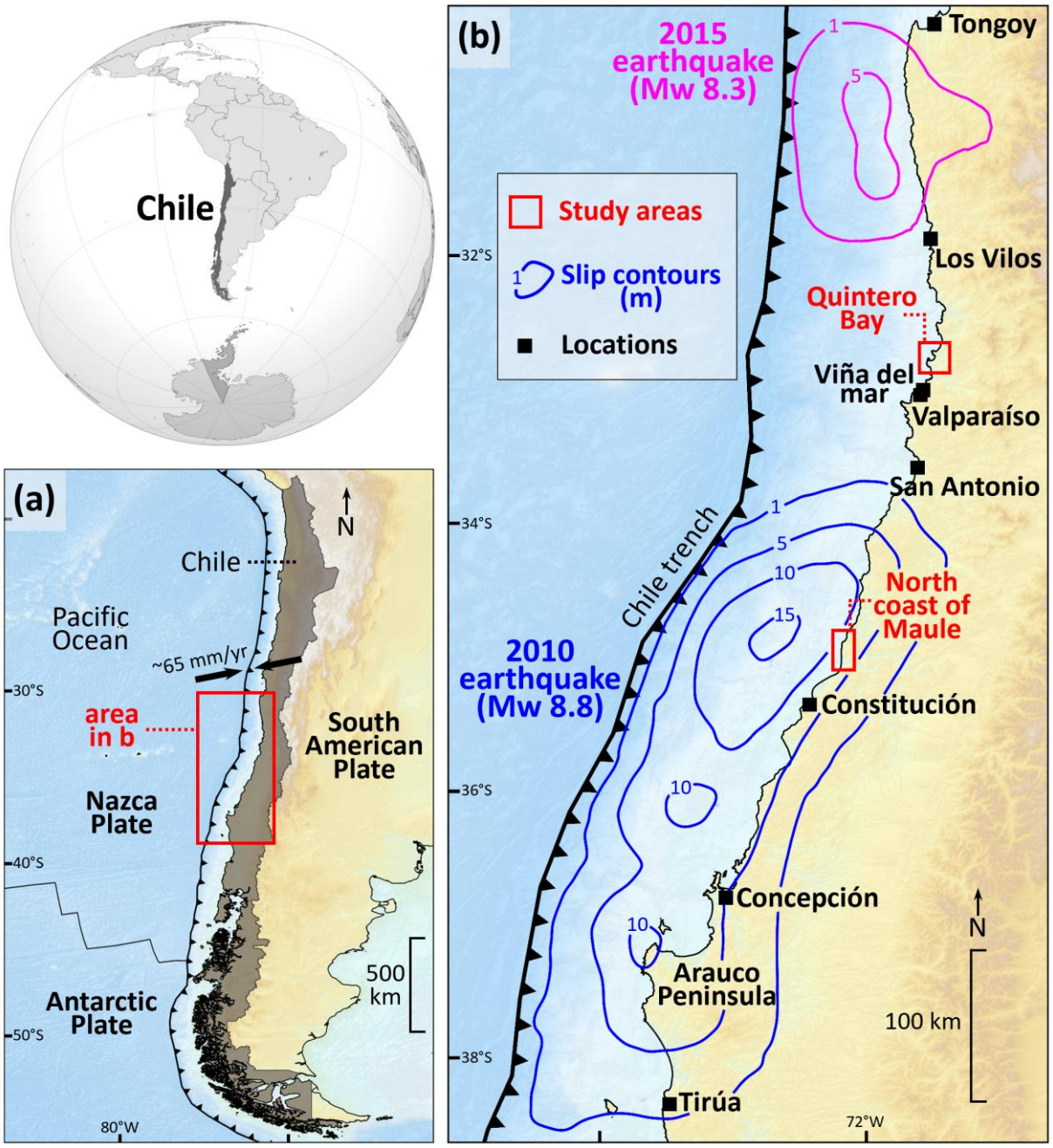

Figura 1.3. Mapas índices. (a) Configuración tectónica de placas en el margen suroeste de Sudamérica. Línea negra con púas indica el borde hacia el mar de la zona de subducción entre las placas de Nazca y Sudamericana. Flechas pareadas indican la velocidad de convergencia entre ambas placas (Jarrin et al., 2023). (b) Recientes terremotos en Chile central. Contornos de slip (m) para el terremoto del 2010 y 2015 desde Moreno et al., 2012 y Tilmann et al., 2016. Las dos áreas que fueron estudiadas en esta investigación son indicadas en rojo.

1.3.2 Áreas de estudio

Para efectos de esta investigación se ha trabajado en dos áreas de estudio en Chile central (Figura 1.3). La primera corresponde a la costa norte de la región del Maule, entre las localidades de Lipimávida y La Pesca, incluyendo la desembocadura del Río Mataquito. Esta área, localizada en frente de la zona donde ocurrió el máximo slip del terremoto del 2010 (Moreno et al., 2012; Saldaña et al., 2025a), resulta clave para evaluar el área de inundación del tsunami resultante, así como para identificar evidencias sedimentarias de tsunamis previos basados en este análogo moderno. Esta investigación doctoral demostrará que el estudio de depósitos de tsunami en el área es complejo, debido principalmente a procesos erosivos, tanto naturales como antrópicos, y múltiples fuentes de sedimentos que dificultan las interpretaciones.

La segunda área de estudio se localiza aproximadamente 250 km al norte, en la densamente industrializada Bahía de Quintero (Figura 1.3), la cual se encuentra justo entre las rupturas de los recientes grandes terremotos de 2010 (Mw 8.8) y 2015 (Mw 8.3). Adyacente al Estero Puchuncaví se ubica el terreno bajo de Campiche, comúnmente conocido como el humedal de Campiche. Este sitio constituye un área de especial interés debido a su potencial para preservar un completo registro estratigráfico de cambios en el nivel del terreno.

1.4 Preguntas de investigación, hipótesis y objetivos principales

Del anterior planteamiento y marco conceptual surgen las siguientes preguntas de investigación que guían esta tesis:

PI1. ¿El estudio de depósitos de tsunami puede ser asistido por técnicas de percepción remota?

PI2. ¿Las desembocaduras de ríos andinos son útiles registradores de tsunamis pasados?

PI3. ¿Cómo ha variado la deformación vertical de la costa de Chile central durante el último siglo?

PI4. ¿Qué factores limitan nuestro conocimiento paleosismológico en Chile central? ¿Estos corresponden a factores naturales o metodológicos?

La siguiente hipótesis de trabajo ha sido propuesta:

La combinación de factores tectónicos, climáticos y antrópicos condiciona la generación, preservación e interpretación del registro geológico de terremotos y tsunamis en Chile central. Sin embargo, aproximaciones multidisciplinarias que integren diferentes metodologías y enfoques podrían reducir estas limitaciones y contribuir a una mejor comprensión del ciclo sísmico y tsunamigénico de la región.

De lo anterior se proponen los siguientes objetivos:

Objetivos generales:

OG1. Comprender los efectos del ciclo sísmico en la costa de Chile central y evaluar los factores que limitan el estudio del registro paleosismológico en la región.

OG2. Validar novedosos enfoques multidisciplinarios que puedan asistir en el estudio de depósitos de tsunami y deformación costera.

Objetivos específicos:

OE1. Determinar la distribución espacial del depósito de tsunami del 2010 mediante la aplicación y validación de un mapeo satelital automatizado.

OE2. Analizar las complejidades involucradas en la interpretación del registro geológico de tsunamis preservado en sitios altamente dinámicos.

OE3. Reconstruir la deformación vertical costera durante el último siglo en Chile central y comprender su implicancia en el registro paleosismológico.

1.5 Estructura de la tesis

Esta tesis ha sido desarrollada en 6 capítulos, en los cuales se presentan los principales hallazgos e implicancias paleosismológicas para la costa de Chile central. En el Capítulo 1 se introduce el problema de investigación, se presentan las áreas de estudio en un contexto general, se plantea la hipótesis de trabajo junto con los objetivos principales y se describen brevemente las principales metodologías y aproximaciones utilizadas. En los Capítulos 2 al 4 se presentan los tres artículos científicos derivados de la investigación, en los cuales el autor de esta tesis es el autor principal. Estos artículos muestran distintos estados de avance (publicado y en preparación); los artículos de los Capítulos 2 y 4 fueron sometidos a revistas internacionales de alto impacto e indexadas en Web of Science (WoS).

El artículo del Capítulo 2, recientemente publicado en *Earth Surface Processes and Landforms*, presenta una novedosa técnica capaz de mapear depósitos de tsunami integrando percepción remota y *machine learning*. Esta técnica fue probada en una franja costera de la Región del Maule, una década después del tsunami del 2010, alcanzando altas precisiones y logrando optimizar el tiempo que requieren mapeos tradicionales de campo. El artículo del Capítulo 3 se encuentra en un estado avanzado de preparación. Este artículo describe las complejidades de estudiar depósitos de tsunami en las desembocaduras de ríos andinos, ya que inundaciones fluviales pueden dejar un registro sedimentario similar al originado por tsunamis. Tales complejidades pueden conducir a una malinterpretación de la evidencia estratigráfica y, por tanto, de la amenaza. El artículo del Capítulo 4, que aborda los cambios del nivel de la costa de Chile central asociados a terremotos y periodos intersísmicos, ha sido recientemente publicado en *Quaternary Science Advances*. En este artículo se presenta una reconstrucción de la deformación vertical costera durante el siglo XX, abarcando los grandes terremotos de 1906 (M>8) y 1985 (M8) y el periodo intersísmico. Para los artículos de los Capítulos 2 y 4 se ha preferido

mantener en esta tesis su idioma original (inglés), mientras que el Capítulo 3, al encontrarse aún en estado de preparación, se ha incluido en idioma español, así como también el resto del escrito.

En el Capítulo 5 se discuten conjuntamente los resultados de estos tres artículos y se evalúan sus principales implicancias para Chile central. Finalmente, en el Capítulo 6 se mencionan las conclusiones más relevantes de la investigación.

1.6 Metodología

La presente investigación combina diversas metodologías de análisis espacial, sedimentológico y paleoambiental con el fin de comprender los procesos de deformación vertical y sedimentación asociados a eventos recientes y pasados en la costa de Chile central. El enfoque adoptado integra herramientas de teledetección, trabajo de campo y análisis de laboratorio, permitiendo abordar la dinámica costera desde una perspectiva amplia y multidisciplinaria.

En primer lugar, se aplicaron técnicas de procesamiento y clasificación de imágenes satelitales de alta resolución para mapear la distribución espacial del depósito de tsunami del 2010 y cuantificar su extensión tierra adentro. Estos resultados fueron contrastados con observaciones de campo y datos topográficos obtenidos mediante modelos digitales del terreno, lo que permitió evaluar con mayor precisión el control ejercido por la morfología costera sobre la inundación (ver sección 1.6.1 a 1.6.3).

Posteriormente, se llevaron a cabo campañas de terreno en la desembocadura del Río Mataquito, orientadas al estudio de depósitos de arena originados por tsunamis e inundaciones fluviales. Las observaciones de campo se complementaron con análisis granulométricos, mineralógicos y de susceptibilidad magnética, buscando identificar criterios claves que pudieran asistir en la diferenciación de ambos tipos de depósitos (ver sección 1.6.4 a 1.6.6).

Asimismo, se incorporó el estudio de microfósiles, principalmente diatomeas, junto con el análisis de semillas y materia orgánica, con el propósito de reconstruir los cambios relativos del nivel del mar y los ambientes de depositación durante el último siglo en el humedal de Campiche. Estos resultados fueron reforzados mediante datos cronológicos, cartográficos, mareográficos y geodésicos, lo que permitió integrar líneas de evidencia independientes para la interpretación de los procesos costeros (ver sección 1.6.7 a 1.6.12).

En conjunto, las metodologías descritas a continuación reflejan un enfoque sistemático y complementario, en el que cada etapa aporta una pieza esencial para reconstruir la evolución ambiental y tectónica de la costa de Chile central. Detalles específicos de cada procedimiento se presentan en los capítulos correspondientes. Un resumen gráfico de los diferentes pasos metodológicos conducidos en esta investigación y su relación con cada objetivo específico (OE) es proporcionado en la Figura 1.4.

1.6.1 Análisis de imágenes satelitales y modelo de clasificación

Para el mapeo satelital del depósito de tsunami del 2010 (Capítulo 2) se emplearon imágenes multiespectrales de alta resolución obtenidas desde los satélites QuickBird (años 2004 y 2005) y WorldView-2 (años 2010 y 2021). Estas imágenes fueron ortorrectificadas, corregidas atmosféricamente y mejoradas mediante pansharpening para alcanzar una resolución espacial de 0.5 metros. Para detectar áreas cubiertas por la arena del tsunami se diseñó un modelo de clasificación supervisada utilizando el algoritmo Random Forest (Breiman, 2001), el cual fue ajustado con 500 árboles de decisión y cuatro variables predictoras (bandas azul, verde, rojo e infrarrojo cercano). Para cada localidad estudiada (Lipimávida, Duao e Iloca) 900 puntos fueron seleccionados, de los cuales un 80% fue utilizado para entrenar el modelo y el 20% restante fue separado al azar para realizar una rutina de validación independiente. Mapas con 9 clases resultantes fueron obtenidos tanto para las imágenes satelitales pre y post-tsunami. Estas clases fueron luego combinadas para una mejor visualización del depósito de tsunami. Finalmente, cambios de cobertura del terreno

entre los mapas pre y post-tsunami fueron conducidos mediante un algoritmo de detección de cambios.

1.6.2 Distribución espacial del depósito de tsunami del 2010

Para cuantificar la extensión del depósito de tsunami del 2010 y evaluar su variabilidad espacial, se utilizaron 162 transectas perpendiculares a la línea de costa y espaciadas cada 100 m. La extensión máxima tierra adentro del depósito fue medida sobre cada transecta y comparada con la inundación real del tsunami determinada por levantamientos previos (Fernández et al., 2010; Fernández y Venegas, 2010). Mediante un Modelo Digital de Terreno (DTM) generado a partir de datos LiDAR fue posible obtener mediciones de runups y evaluar el control de la topografía sobre la inundación.

1.6.3 Evaluación del mapeo satelital

Los resultados del mapeo satelital del depósito de tsunami del 2010 fueron contrastados con datos de campo recolectados entre el 2010 y 2023. En total, 97 entrevistas a testigos sobrevivientes y 73 excavaciones fueron realizadas para recopilar información sobre la extensión del depósito de tsunami del 2010. Esta información de campo fue cruzada con las predicciones del modelo de clasificación para evaluar su precisión.

1.6.4 Trabajo de campo en la desembocadura del Río Mataquito

El trabajo de campo en la desembocadura del Río Mataquito (Capítulo 3) consistió en dos campañas: una previa (7 de mayo) y otra posterior (14 de julio) al catastrófico evento hidrometeorológico ocurrido en junio de 2023. Inicialmente, el objetivo fue el estudio del depósito de tsunami del 2010 y el de sus posibles predecesores. Sin embargo, tras la gran inundación fluvial del 2023, el foco se reorientó hacia el análisis del nuevo depósito de arena generado por este evento. Se estudió su distribución superficial, se excavaron cuatro fosas a lo largo de un perfil transversal a la marisma para registrar su espesor y se recolectaron ocho muestras discretas de sedimento para análisis posteriores. La elevación del perfil fue referida al nivel medio del mar mediante un dGPS y un punto de referencia local.

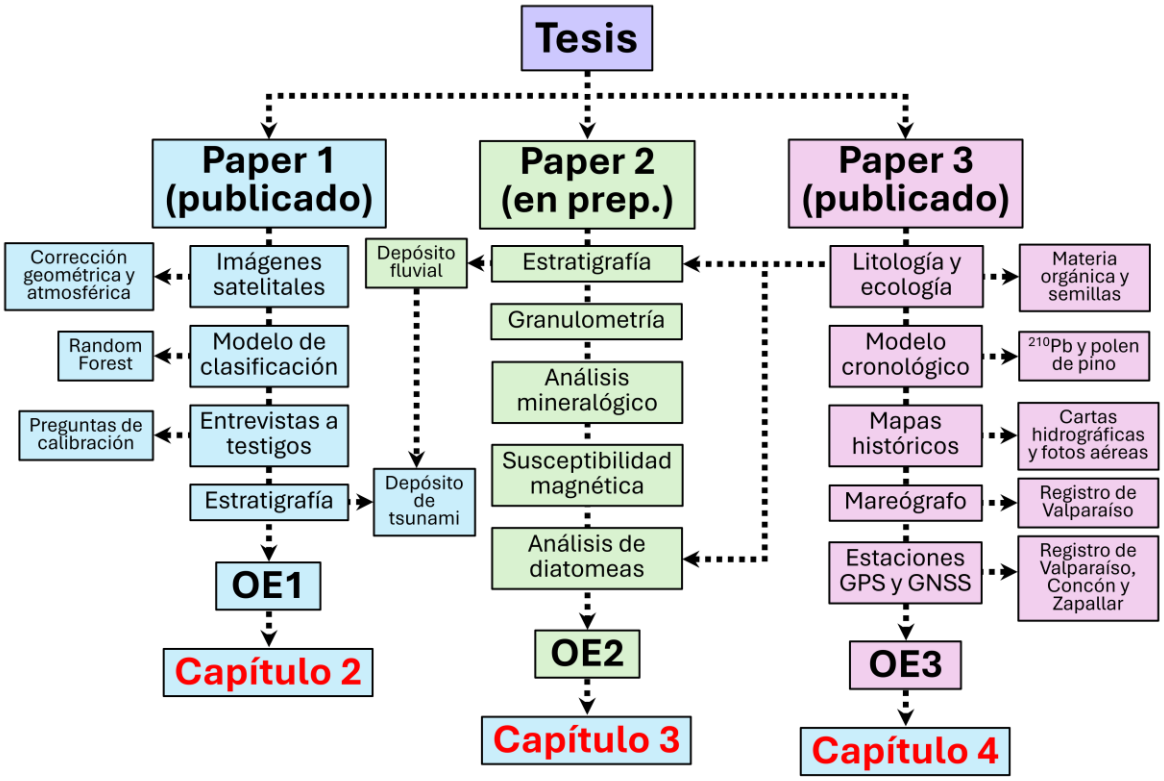

Figura 1.4. Mapa conceptual resumiendo los principales pasos metodológicos conducidos por cada publicación científica. Notar como estos se relacionan con cada objetivo específico (OE) y capítulo de esta tesis.

1.6.5 Granulometría y análisis mineralógico

Para caracterizar el depósito fluvial del 2023 en la desembocadura del Río Mataquito, se realizó un análisis granulométrico y mineralógico detallado, cuyos resultados fueron comparados con los del depósito de tsunami de 2010. Cada muestra fue secada y separada mecánicamente mediante una tamizadora, con tamaños de partícula entre -1 y 4 φ a intervalos de 0.5 φ. Parámetros estadísticos fueron estimados mediante el software GRADISTAT v. 9.1 (Blott y Pye, 2001). Descripciones mineralógicas de cada muestra fueron hechas bajo un microscopio estereoscopio binocular, expresando como porcentajes la abundancia relativa de cada mineral.

1.6.6 Susceptibilidad magnética

La susceptibilidad magnética de las muestras fue medida utilizando un sensor Bartington MS2E. Cada muestra fue analizada al menos tres veces y los valores promedios fueron reportados. Para asegurar la consistencia de los datos, todas las mediciones se realizaron bajo condiciones controladas de laboratorio: mismo volumen de sedimento y misma hora del día, minimizando así posibles alteraciones por variaciones térmicas ambientales.

1.6.7 Trabajo de campo en Campiche

La estratigrafía de Campiche (Capítulo 4) fue estudiada a través de 30 testigos manuales y 7 secciones con vibracorer recuperados entre octubre del 2023 y diciembre del 2024. Las elevaciones de cada testigo y sección fueron referenciadas al nivel medio del mar usando un dGPS y un datum mareal del Servicio Hidrográfico y Oceanográfico de la Armada de Chile (SHOA). El análisis se enfocó en la estratigrafía superficial, incluyendo un contacto litológico abrupto de turba sobre fango inorgánico. Descripciones de campo fueron complementadas con análisis de laboratorio.

1.6.8 Análisis de diatomeas

La reconstrucción de los cambios relativos del nivel del mar (RSL) se basó en el análisis de diatomeas fósiles preservadas en los sedimentos de Campiche. Siguiendo a Dura y Hemphill-Haley (2020), dos testigos y cuatro secciones de sedimento fueron muestreados a intervalos verticales de 2 a 3 cm. Para cada muestra se contaron más de 300 valvas de diatomeas, las cuales fueron identificadas al nivel de especie bajo un microscopio con magnificación de 1000x. Las especies fueron clasificadas según su preferencia a la salinidad (dulces, salobres y marinas) y su forma de vida (bentónicas, epifíticas y planctónicas). Cambios en el RSL fueron inferidos cualitativamente a partir de una razón entre diatomeas salobres más marinas versus dulces. Se optó por esta aproximación debido a la ausencia de análogos modernos en Chile central para realizar reconstrucciones cuantitativas mediante funciones de transferencia.

Para identificar agrupaciones significativas de especies de diatomeas en la columna estratigráfica se aplicó un análisis de conglomerados CONISS (Grimm, 1986), que permite agrupar muestras adyacentes con asociaciones ecológicas similares. Este análisis se realizó considerando solo especies con más del 5% de abundancia relativa en al menos una muestra. Esto para evitar el sesgo de taxones poco representativos. La aplicación de esta herramienta permitió identificar estadísticamente cambios en los ensambles de diatomeas.

1.6.9 Estimación de materia orgánica y análisis de semillas

El contenido de materia orgánica se determinó mediante el método de pérdida por ignición, incinerando cada muestra a 550 °C según la técnica de Dean (1974). Paralelamente, se realizó un reconocimiento y conteo de semillas de *Schoenoplectus californicus*, especie de planta emergente indicadora de ambientes tolerantes a la sal. Para ello, se tamizaron 10 cm^3 de sedimento por muestra, y se contaron todas las semillas bajo un microscopio estereoscópico binocular. Este análisis permitió complementar las inferencias ecológicas realizadas a partir de las diatomeas.

1.6.10 Cronología basada en ^{210}Pb y polen de pino introducido

La cronología para los sedimentos de Campiche se obtuvo mediante un modelo de edad basado en ^{210}Pb previamente reportado por Gayo et al. (2022) en el humedal. Adicionalmente, polen de pino fue utilizado como un marcador cronoestratigráfico ya que los pinos fueron introducidos en Chile a finales del siglo XIX y comienzos del siglo XX. La primera aparición de polen de pino en profundidad permite estimar una edad de depositación en torno a la década de 1900. Adicionalmente, un aumento marcado en niveles más superficiales permite estimar su edad hacia la década de 1970, correspondiendo con la expansión de las plantaciones de pinos debido a los incentivos estatales. Los granos de polen fueron extraídos siguiendo los procedimientos de Faegri y Iversen (1989).

1.6.11 Mapas históricos

Con el objetivo de apoyar las interpretaciones ecológicas procedentes del análisis de diatomeas y semillas, se analizaron siete mapas hidrográficos de la Bahía de

Quintero entre 1803 y 1930, así como una fotografía aérea de 1954. Esta información cartográfica fue complementada con reportes de naturalistas contemporáneos (Pissis, 1854; Vicuña Mackenna, 1874; Pomar, 1876; Vidal Gormaz, 1880).

1.6.12 Datos mareográficos y geodésicos

Para evaluar los cambios verticales de la costa durante el último siglo, se analizó la serie del mareógrafo de Valparaíso (1944 a 2025; SHOA). Se identificaron tendencias lineales en el nivel relativo del mar, las que se compararon con la señal inferida desde los ensamblajes diatomeas. Además, se incorporaron datos de estaciones GNSS continuas y un GPS de campaña para estimar la tasa de subsidencia actual. Estos datos mareográficos y geodésicos proporcionaron apoyo a las interpretaciones derivadas del análisis del registro estratigráfico.

Capítulo 2. Mapping tsunami deposits through a classification model based on satellite images

Saldaña, B., Cisternas, M., Chávez, R.O., Aedo, D., Guerra, M. & Carreño, A. (2025a). Mapping tsunami deposits through a classification model based on satellite images. Earth Surface Processes and Landforms, 50(1), e6055. Available from: https://doi.org/10.1002/esp.6055

Abstract

Assessing tsunami risk requires knowledge of the potential inundation area, which can be inferred from the spatial distribution of tsunami deposits. However, field surveys of tsunami deposits are time-consuming and occasionally pose challenges, such as disturbance of sedimentary evidence by human and natural causes. Here, we propose a novel technique capable of mapping tsunami deposits using remote sensing, which was tested along a coastal stretch of central Chile following the tsunami of 27 February 2010. We trained a classification model using high-resolution satellite images from before (September 2004 and January 2005) and after (April 2010) the 2010 tsunami to map the sand deposit, yielding an overall accuracy of about 86%. Our satellite mapping of the deposit was validated with field observations in pits and eyewitness interviews conducted about a decade after the tsunami. The field data matched the model predictions by 88%. Likewise, our satellite mapping was also contrasted with the inundation area reported by previous post-tsunami surveys. The spatial distribution of the tsunami sand deposit inferred from our model reproduces a minimum inundation area, which was almost as extensive as the actual inundation area. Sand inundation ranged from 50 to 600 m inland, matching about 90% of water inundation. Both sand and water inundation were controlled by the land slope. Application of our technique to a satellite image from 11 years after the tsunami (May 2021) shows that the detection ability of the sand deposit was lost by about 86%, which is attributed to human intervention and masking by new soil development. Our results suggest that extensive tsunami deposits can be accurately

mapped by a supervised classification model in a lesser time than that employed in field surveys.

Keywords

2010 Chile tsunami, automated mapping, eyewitness interviews, sand deposit, satellite images, stratigraphic observations

2.1 Introduction

Tsunamis are a recurrent threat to coastal communities. Therefore, estimates of inundation area and recurrence of these events are of utmost relevance for risk assessment (e.g., Jaffe and Gelfenbaum, 2002; Satake, 2014). Reconstructions of inundation area and associated recurrence intervals can be made using sedimentary evidence (e.g., Cisternas et al., 2005; Matos-Llavona et al., 2022; Pinegina et al., 2018). For example, Pinegina et al. (2018) quantified the inundation and recurrence intervals of 33 tsunamis recorded over the past ~4200 years in Avachinsky Bay using tsunami deposits and correlation of dated tephra layers.

Tsunami deposits, from either recent or ancient tsunamis, provide critical information about the inherent characteristics of the tsunami itself, such as flow conditions, number of waves and source (e.g., Spiske, 2020). Particularly, the spatial distribution of a tsunami deposit is key to delineating the actual extent of inundation (e.g., Abe et al., 2020; MacInnes et al., 2010). Recent studies of modern tsunamis have shown that the area covered by their sediments usually closely corresponds with the tsunami inundation, being a reliable proxy for estimating the minimum inundation area (Gelfenbaum and Jaffe, 2003; Jaffe et al., 2003, 2006; MacInnes et al., 2009a; MacInnes et al., 2010; Moore et al., 2006, 2011; Srinivasalu et al., 2007; Szczuciński et al., 2012). At least, two aspects should be considered for mapping tsunami deposits to determine inundation area. First, continuous sampling instead of discrete profilebased sampling can ensure that the full variability of the deposit is captured; this approach, however, is highly time-consuming and, in practice, is not possible with traditional field methods. Second, for modern tsunamis, the survey has to be done

soon after the event occurrence, to minimize destruction or masking of the deposit by human or natural causes (Bahlburg and Spiske, 2015; Nichol and Kench, 2008; Spiske et al., 2020; Szczuciński, 2012; Szczuciński et al., 2006). These considerations highlight the challenges involved in field surveys, and therefore alternative approaches could be explored.

Remote sensing emerges as a valuable tool for rapid and reliable assessment of large areas affected by tsunamis. Satellite data proved to be an effective complement to field surveys providing critical information from areas that were severely damaged by the 2004 Indian Ocean tsunami (e.g., Borrero, 2005; McAdoo et al., 2007; Ramakrishnan et al., 2005). Consequently, inundation areas, infrastructure damage and coastal changes have been successfully identified using satellite images in subsequent studies (e.g., Ramírez-Herrera and Navarrete-Pacheco, 2013; Richmond et al., 2012; Tappin et al., 2012). Ramírez-Herrera and Navarrete-Pacheco (2013) assessed the inundation area of the 2011 Tohoku-oki tsunami in some locations of Japan using markers from high-resolution satellite images, such as moistened soils, dead vegetation, scattered debris and deposited sediments. However, occasionally, such visual inspections can lead to subjective interpretations depending on the observer. Instead, automated approaches could be used to minimize bias in the results as much as possible. Although novel automated mapping techniques have been implemented to identify the extent of inundation, assess damage to buildings and monitor shoreline changes (e.g., Ishihara and Tadono, 2017; Koshimura et al., 2020; Minghelli et al., 2020; Sublime and Kalinicheva, 2019), these have not been yet used to specifically detect tsunami deposits.

In this study, using a supervised classification model based on high-resolution satellite images, we present an automated technique capable of mapping extensive tsunami deposits in a short time. We tested the accuracy of our technique by mapping the 2010 tsunami sand deposit on a 15-km stretch of coastline with run-ups typically ranging from 4 to 8 m and inundation distances from 50 to 600 m. We show that the sand deposit inferred from our model closely reproduces the actual tsunami

inundation area measured by previous surveys (Fernández et al., 2010; Fernández and Venegas, 2010). We propose that this mapping technique has the potential to assist or eventually replace field surveys where they cannot be carried out.

2.2 Background

2.2.1 The 2010 earthquake and tsunami

On 27 February 2010, a Mw 8.8 earthquake hit central Chile, the country's most populated region (Madariaga et al., 2010). This massive earthquake, more commonly known as the Maule earthquake, was triggered in the subduction interface between the Nazca and South American plates (Figure 2.1a,b) and ruptured an area previously identified as a mature seismic gap (Campos et al., 2002; Melnick et al., 2012b; Ruegg et al., 2009). The rupture, ~500 km long with an average slip of 6–8 m, extended from San Antonio in the north to Arauco Peninsula in the south (Figure 2.1b; Farías et al., 2010; Moreno et al., 2012). Peak slip of 12–20 m focused offshore in the northern third of the rupture, facing the coast including the study area between Lipimávida and Iloca (see a collection of 19 slip distribution models in Cienfuegos et al., 2018). Vertical coseismic deformation resulted in evident land level changes along the coast, ranging from -0.5 to +2.5 m (Farías et al., 2010; Kelson et al., 2012; Melnick et al., 2012a; Vargas et al., 2011; Vigny et al., 2011).

Concurrent coseismic displacement of the seafloor generated a destructive tsunami along 800 km of the central Chile coast (Fritz et al., 2011). Post-tsunami surveys reported run-ups typically ranging between 5 and 10 m and localized maximum run-ups of ~30 m at Constitución and 20 m at Tirúa (Figure 2.1b; Fritz et al., 2011). Extensive sand sheets were deposited by the tsunami on many low-lying coastal localities as reported by Bahlburg and Spiske, 2012; Chagué-Goff et al., 2015; Ely et al., 2014; Garrett et al., 2013; Horton et al., 2011; Lario et al., 2016; Morton et al., 2011.

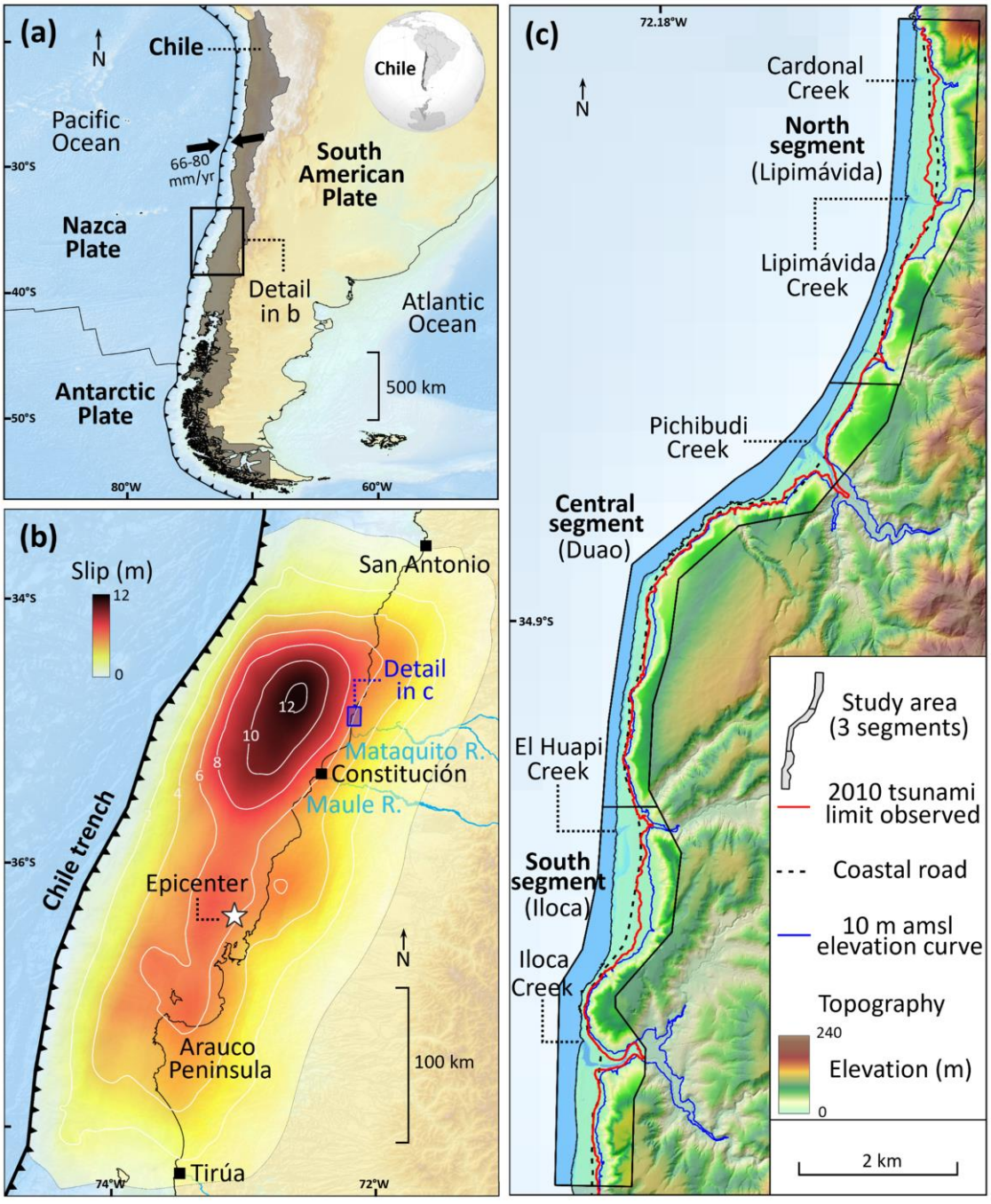

Figure 2.1. Index maps. (a) Plate-tectonic setting of Chile in southwestern South America. Black barbed line marks the seaward edge of the subduction zone between the Nazca and South American plates. Paired arrows indicate the rate of convergence between both plates. (b) Slip distribution of the 2010 rupture area, averaged from a collection of 19 slip distribution models compiled by Cienfuegos et al. (2018). (c) Shaded relief map of the Lipimávida-Iloca coast from LiDAR data showing the three studied segments and the localities they represent in parenthesis. Red line denotes the landward limit of the 2010 tsunami by Fernández et al. (2010) and Fernández and Venegas (2010).

2.2.2 Study area

We studied the 2010 tsunami deposit on a 15-km-long and about 500-m-wide coastal stretch in the northern third of the 2010 earthquake rupture, part of the area facing the largest coseismic slip (Figure 2.1b,c). The stretch extends from Lipimávida to Iloca (hereinafter the Lipimávida-Iloca coast or simply LIC) and is located 50 km north of Constitución (Figure 2.1b), a large city of 40 000 inhabitants, and where the maximum 2010 tsunami run-up, of ~30 m, was reported (Fritz et al., 2011).

The LIC is a ~500-m-wide gently westward sloping plain composed of Holocene dark sands that extends to the toe of an inactive sea cliff (Figure S6). This cliff, exposing Pleistocene marine sedimentary rocks, is an uplifted marine terrace about 30 m high (Acuña, 2012; Fernández and Venegas, 2010). The plain is dissected by short, seasonal east–west streams that drain minor catchments incised into the top of the uplifted platform. During the rainy season (June to November), these streams transport fine-grained and light-coloured sediments to the coast. In the dry season (December to May), when the outlets are closed because of low water flow and sand accumulation at their mouths, small coastal lagoons are temporally established. An active, discontinuous dune about 5 m high, composed of fine dark sand, runs parallel to the shoreline. Two large rivers, Mataquito and Maule, located 2 and 50 km south of the study area, respectively, are sourced in the Andes and supply most of the sand composing the plain (Figure 2.1b; Saldías, 2011). The sand has an evident dark colour due to its high content of heavy minerals, up to 35% of magnetite, among other volcanic minerals (Figure S8).

On the LIC, damage from the 2010 tsunami surpassed that from earthquake shaking (Contreras and Winckler, 2013). Although most of the houses withstood the shaking, over 75% of the buildings were flooded by the tsunami, washing out hundreds of houses (Fernández and Venegas, 2010). Eyewitnesses reported three main waves, which reached up to 8 m high (Fernández and Venegas, 2010). At Duao and Iloca, tsunami run-up ranged between 5 and 8 m, and inundation distances attained 300 m inland (Fritz et al., 2011; Lario et al., 2016). To the north of the area, at Lipimávida,

both the run-up and inundation distance were smaller, reaching 4 and 200 m, respectively (Fritz et al., 2011; Lario et al., 2016). Longer inundation distances, of at least 1 km, were locally observed in the channels of the main creeks (Lario et al., 2016). Severe geomorphological effects, observed along the LIC and a few kilometres further south, were produced by both the tsunami and coseismic subsidence, including strong coastal retreat, local lowering of the coastal dune and full erosion of the Mataquito River's bar at its mouth (Araya-Cornejo and Carvajal, 2016; Catalán et al., 2014; Villagran et al., 2013). Signs of strong localized tsunami erosion, such as scours and channels were also reported (Morton et al., 2011). A distinguishable tsunami deposit up to 12 cm thick and extending more than 200 m inland was observed in low-lying areas around Lipimávida, Duao and Iloca (Fritz et al., 2011; Lario et al., 2016).

2.3 Material and methods

2.3.1 Satellite mapping

To map the sand deposit left by the 27 February 2010 tsunami and its subsequent loss of satellite detection along the Lipimávida-Iloca coast (LIC), we used high-spatial-resolution satellite images from before (24 September 2004, 10 January 2005) and after (14 April 2010, 26 May 2021) the tsunami (Table 2.1). They allowed us to produce land use and land cover (LULC) maps at sub-metre resolution and to evaluate the changes generated. The process consisted of four steps, outlined as follows.

a) Sub-metric images processing

Two images from about 5 years before and one image from 6 weeks after the 2010 tsunami were used to map tsunami deposits along a 15-km-long segment of the Chilean coast (Table 2.1). Two multispectral QuickBird images from 24 September 2004 and 10 January 2005 capture pre-tsunami features. One WorldView-2 image from 14 April 2010 shows the resulting effects. These images, albeit 5 years apart, were chosen for being the closest in time to the event, cloud-free and having visible and near-infrared spectral bands. Such a time gap of 5 years is likely not significant

since the study area did not undergo major changes between late 2004 and early 2010, as seen in lower resolution open source satellite images. One additional WorldView-2 image from 26 May 2021 shows the current setting of the LIC and was used to map the loss of satellite detection of the tsunami deposit in the decade following the 2010 tsunami (Table 2.1). Images were georeferenced, orthorectified and atmospherically corrected. We then combined the multispectral bands of each image with its respective panchromatic band using a pansharpening technique and then resampled all the resulting images to 0.5 m using the nearest neighbour method (Parker et al., 1983). The resulting 0.5 m 4-band multispectral images were divided into three segments according to the areas of the LIC they cover: North, Central and South segments. Each segment corresponds, respectively, to each locality studied: Lipimávida, Duao and Iloca (Figure 2.1c; Table 2.1).

Table 2.1. Used satellite images and estimated uncertainties. Segments of the LIC covered by each image are also indicated.

Source of image	Date (UTC time)	Segments covered	Tide (m)	Spatial resolution (m)	Geoaccuracy (m)	Tidal correction (m)	RMSE (m)
QuickBird	24 September 2004 (15:01)	Central and South	-0.076	Pan: 0.6 MS: 2.4	1.17	1.24	1.81
QuickBird	10 January 2005 (15:08)	North	0.233	Pan: 0.6 MS: 2.4	1.22	3.81	4.05
WorldView-2	14 April 2010 (14:57)	North, Central and South	0.629	Pan: 0.5 MS: 2	0.88	10.28	10.33
WorldView-2	26 May 2021 (15:10)	North, Central and South	0.815	Pan: 0.5 MS: 2	1.02	13.33	13.37

Abbreviations: MS, Multispectral; Pan, Panchromatic; RMSE, Root-Mean-Square error.

b) Classification model

A supervised classification was used to produce LULC maps. The Random Forests classifier (Breiman, 2001) was selected because of its higher accuracy compared to other classifiers (Belgiu and Drăguţ, 2016). We implemented the classification model using the 'randomForest' R package by setting 500 decision trees and four predictor variables (Blue-Green-Red-NIR spectral bands). For each specific segment along the studied coast (North, Central and South segments), 900 calibration/validation points were selected, 720 of which (80%) were used as training sites, and the rest (20%) were randomly separated to perform an independent accuracy validation.

Images were classified into nine classes, including water, foam, wet sand, dry sand, urban, bare soil, crop, shadow and forest (Figure 2.2b,e). Local bedrock outcrops were classified as wet sand due to their spectral similarities. Because they have a small spatial extent, either on the beach or partially submerged, they were not significant to be classified as another class. The accuracy of the classification was evaluated using confusion matrices, leading to the overall accuracy, Kappa coefficients and producer's and user's accuracies. For a better visualization of the tsunami deposit, the resulting LULC map classes were combined in a post-classification process (Figure 2.2c,f). Water and foam were merged into one class called 'sea'. Wet sand and dry sand were grouped into 'sand'. The remaining classes were included into a larger class named 'soil'. Finally, the outlier 'sand' pixels located higher than 15 m high and on the 'sea' were manually removed as they showed a scattered distribution inconsistent with the tsunami deposit and beach sand.

c) Spatial distribution of the tsunami deposit

Land cover changes between pre- (2004 and 2005) and post- (April 2010) tsunami maps were identified using a change detection algorithm in QGIS software (Asokan and Anitha, 2019; Lu et al., 2004). For the map of detected changes (Figure 2.3), we added to the tsunami deposit the pre-existing surface sand of the beach and the dune in addition to the sand redistributed by the tsunami. This shows the deposit as a continuous sand sheet allowing for better measurements. A Digital Terrain Model

(DTM), from LiDAR data at a horizontal resolution of 1 m and vertical accuracy of 10 cm, was used for all measurements. The landward extent of the tsunami deposit (termed here as 'sand inundation') was obtained through 162 shore-normal transects spaced 100 m apart (Tables 2.2 and S4). The shoreline on each image was digitized using methods described in Monecke et al. (2015) and Aedo et al. (2023) and applying a tidal correction using the TPXO8-atlas global tidal model (Egbert and Erofeeva, 2002). For this, a beach slope of m = 0.06 (slope of about 3.5°) was estimated from the DTM and field measurements. Land slope values were obtained for each transect as an average from shoreline to the 10 m amsl curve. Following Monecke et al. (2015) and Aedo et al. (2023), an error analysis for our measurements along each transect is provided in Table 2.1. The estimated error (root-mean-square error, RMSE) is a function of the spatial resolution of the images, geoaccuracy and tidal correction. Since our measurements were made from the shoreline on the post-tsunami image of April 2010, the resulting error is less than 10.33 m. Horizontal change in the shoreline position was not considered in this study and is therefore not shown in Figure 2.3 as a result of the change detection algorithm.

d) Loss of satellite detection of the tsunami deposit

Like the previous step, land cover changes between 6 weeks (April 2010) and 11 years (May 2021) post-tsunami maps were identified using a change detection algorithm in QGIS software (Figure 2.6). We determined the satellite detection percentage of the deposit that was lost by the classification model about a decade after the tsunami by quantifying the sand pixels that were removed for each segment. For this, only the missing sand that was further inland was considered, since the beach and dune sand did not show significant changes, except for the evident retreat of the coast.

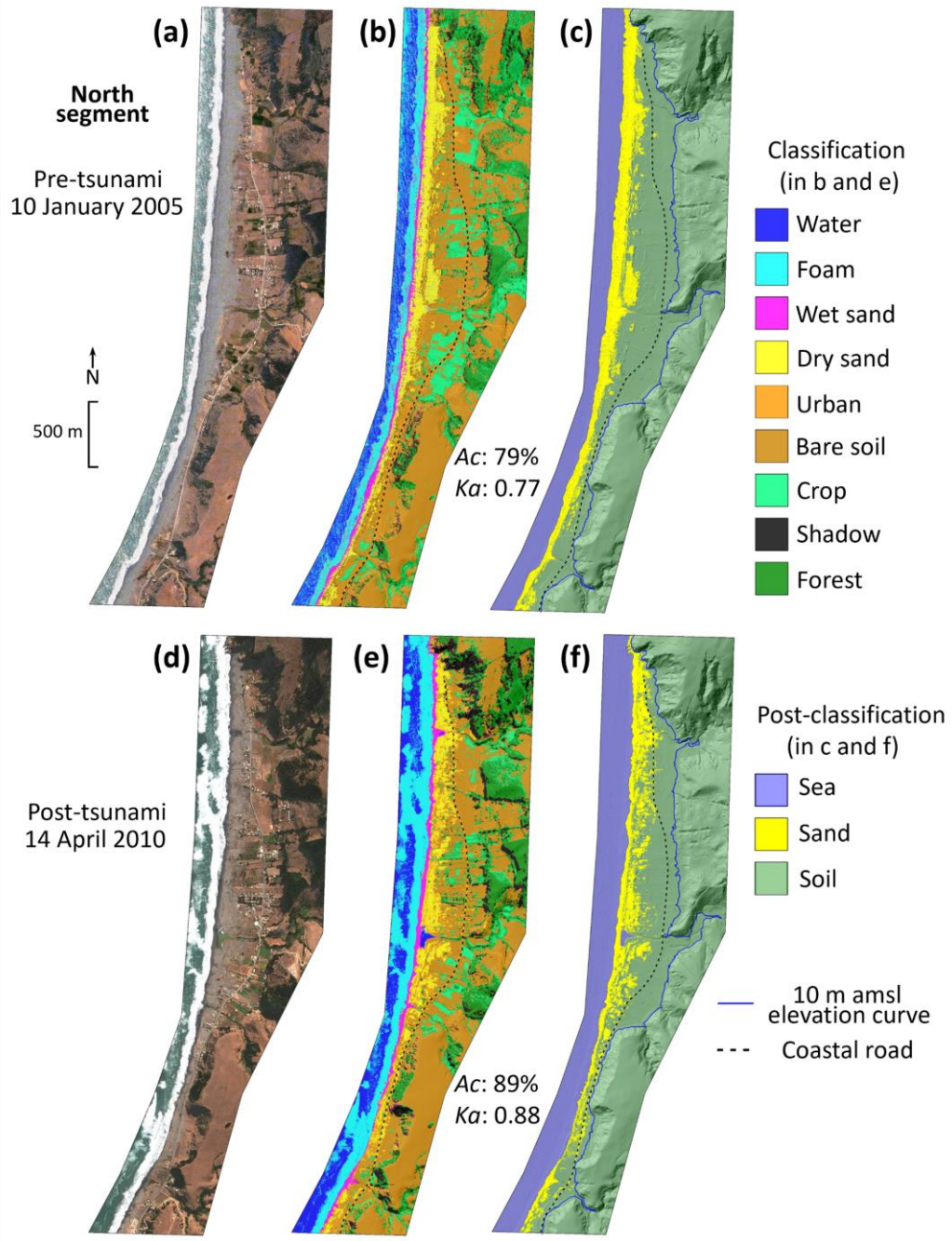

Figure 2.2. Pre- and post-tsunami satellite images and the resulting land use and land cover (LULC) maps from the classification model for the North segment (see Figure 2.1). (a) A true-colour composition of the pre-tsunami satellite image. (b) LULC map obtained from the supervised classification model applied to (a). Ac and Ka indicate the overall accuracy and Kappa coefficient resulting from the classification model, respectively. Confusion matrices and specific accuracies for sand classes are shown in the Supporting Information (Anexo 1). (c) LULC map with classes shown in (b) combined and outlier pixels removed. (d–f) As in (a–c) for the post-tsunami image. See Supporting Information for Central and South segments (Anexo 1).

2.3.2 Ground truth validation

To validate our satellite mapping, we obtained data provided by direct observation of the stratigraphy and eyewitnesses reports, which began to be collected in mid-2010, a few months after the tsunami, and were completed in subsequent years. Brief post-tsunami surveys were made in August 2010 and July 2015. One decade after, between 2021 and 2023, we made a systematic survey collecting the bulk of the data shown here.

a) Stratigraphy and eyewitness reports

The satellite mapping of the 2010 tsunami sand deposit was compared with ground truth observations from the stratigraphy in 73 pits (of which 63 are at one locality) (Figure 2.3; Table S2) and from 97 interviews with survivors of the 2010 tsunami (Figure 2.3; Table S1), totaling 170 studied sites. In the pits, we looked for evidence of the 2010 tsunami inundation as a preserved sand sheet (Figure 2.4). Pit locations were selected to sample only areas that had not been disturbed by sand removal, ploughing or other human activity. From the interviews, we collected information about the tsunami sand deposit and about water inundation. We considered only the data that fulfilled our criteria of reliability (see Supporting Information in Anexo 1). Both approaches were guided by a pre-2010 tsunami stratigraphic and interviewing reconnaissance made by one of us (MC) in March 2009. This previous work allowed us to identify the residents and owners of the places and to know that no superficial sand sheet existed prior to the event except in the areas covered by dunes.

The elevations corrected to mean sea level and coordinates of both pits and interviews were obtained by a dGPS. We then checked whether these points obtained from the field matched our model predictions by overlapping with pixels classified as sand (Tables S1 and S2; Figure S7). To assign a sand layer seen in a pit as deposited by the 2010 tsunami, we applied the following criteria: (i) absence in 2009 field observations, (ii) presence after the tsunami as reported by witnesses and (iii) further sedimentary analysis, including grain size, mineralogy and magnetic

susceptibility. Methodological details of sampling and laboratory analysis in the Supporting Information (Anexo 1).

Finally, sand inundation, inferred from our classification model, was compared to the observed inundation (termed here as 'water inundation'), obtained from (i) the inundation limits reported by eyewitness, (ii) debris lines marked in satellite images and aerial photos and (iii) inundation delimited by a post-tsunami survey made by the Chilean National Geology and Mining Service (Fernández et al., 2010; Fernández and Venegas, 2010). The terms 'sand inundation' and 'water inundation', sensu MacInnes et al. (2009a) and MacInnes et al. (2010), were preferred to simplify comparisons between the inland extent of the tsunami deposit and the observed (water) inundation, respectively. Run-ups shown in Tables 2.2 and S4 are derived from inundation delineated by previous post-tsunami surveys (Fernández et al., 2010; Fernández and Venegas, 2010).

2.4 Results

2.4.1 Accuracy of the classification model

Our model showed a good performance with a high overall accuracy (see Supporting Information in Anexo 1). The Kappa coefficients were higher than 0.75, the overall accuracy of about 86% and above 80% for wet and dry sand classes. Although the urban class showed lower accuracy, usually between 50% and 77% (see Supporting Information in Anexo 1), these values were not able to reduce the overall good average. An example of the high accuracy obtained from the classification model is shown in the pre- and post-tsunami LULC maps for the North segment (Figure 2.2b,e). The results for the Central and South segments can be found in the Supporting Information (Figures S1 and S2).

2.4.2 Changes detected along the coast 6 weeks after the tsunami

The LIC was covered by a sand sheet that extended hundreds of metres landward due to the 2010 tsunami. Figure 2.3 shows the detected changes between before (2004 and 2005) and 6 weeks after the 2010 event from our classification model and

change detection algorithm. The tsunami deposit, in red, is shown as a conspicuous change along the entire coast.

The inferred deposit is marked as an extensive but discontinuous cover of sand spanning about 90% of the area actually inundated by the tsunami (Tables 2.2 and S4). The deposit is relatively homogeneous close to the shoreline and patchier landward. Sand inundation varied between 50 and 600 m, showing a good correspondence with the water inundation (R2 = 0.92; Figure 2.5; Tables 2.2 and S4). Gaps between sand and water inundation were often less than 30 m, except in creeks and plains where these reached up to almost 200 m. Additionally, both sand (R2 = 0.72) and water (R2 = 0.82) inundation showed a negative exponential correlation with the land slope (Figure 2.5).

a) North segment

The North segment, with a low land slope of about 2.1°, exhibited an intermediate sand inundation between the Central and South segments. Sand reached an average inland extent of 170 m and peaks of about 300 m upstream in the creeks (Figure 2.5; Tables 2.2 and S4). More restricted sand inundations between 80 and 100 m were measured to the south, where there are dunes and/or rocky cliffs. Sand inundation resembled the water inundation in its spatial distribution, covering 88% of the area actually inundated, with an average horizontal gap of less than 30 m between the two. Run-ups typically ranged from 3 to 6 m, reaching peaks between 7 and 10 m to the south.

b) Central segment

The Central segment exhibited the most restricted sand inundation of the LIC, likely due to its steep average slope (3.4°). In average, sand extended inland 132 m, with a peak of 450 m in Pichibudi Creek and less than 100 m to the south (Figure 2.5; Tables 2.2 and S4). Sand inundation was 92% in agreement with the water inundation, with a horizontal gap of less than 15 m between them. Run-ups ranged between 5 and 8 m with local peaks up to 10 m.

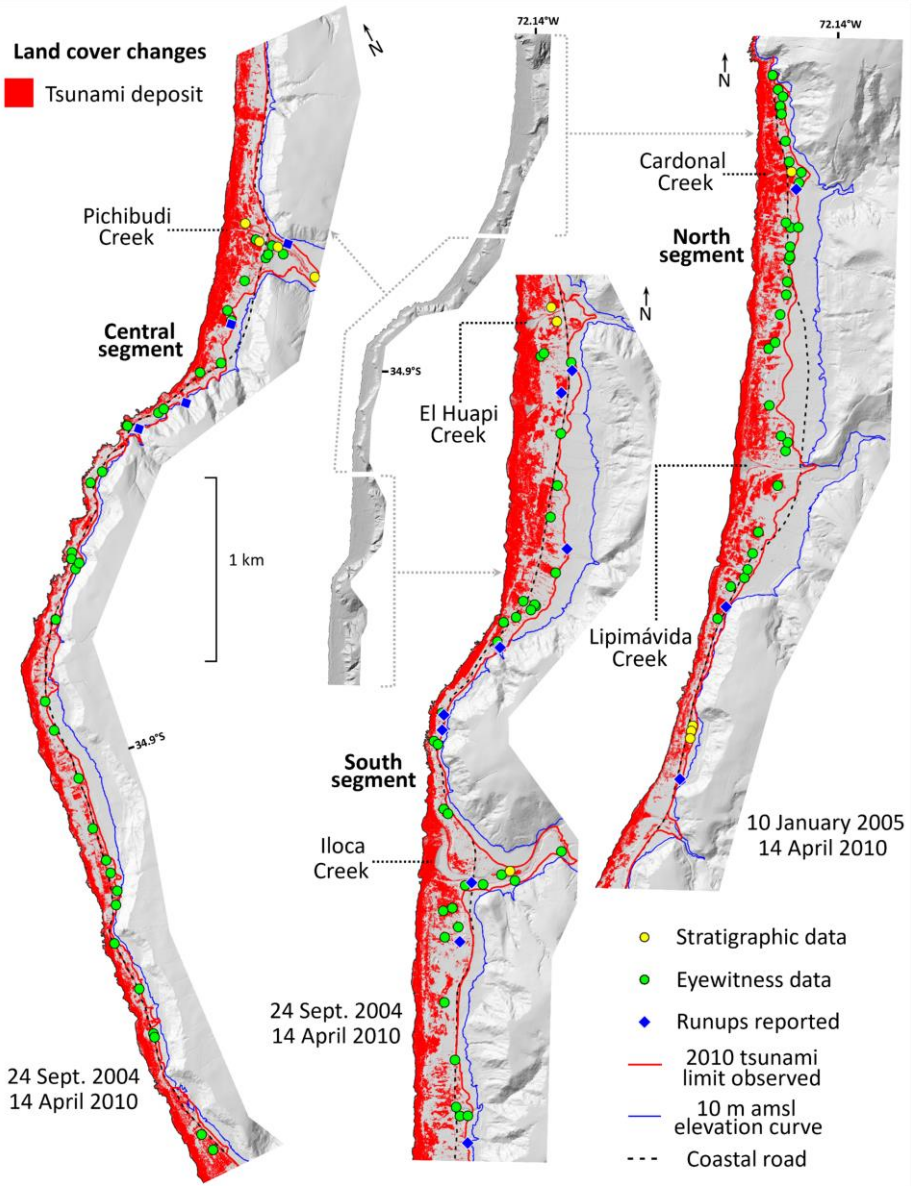

Figure 2.3. Changes detected between before (2004 and 2005) and after (14 April 2010) the 27 February 2010 tsunami along the LIC (see Figure 2.1). Dates of the images used for each segment are specified. Ground truth data from stratigraphic observations in 73 pits and 97 testimonies of 2010 tsunami survivors are marked by yellow and green dots, respectively. Both pits and interviews were conducted at sites where sand did not exist prior to the 2010 tsunami. In Iloca Creek, 63 pits were excavated and are symbolized by a single yellow dot. Blue diamonds show previously reported run-up measurements (Fritz et al., 2011; Lario et al., 2016). The landward limit reached by the 2010 tsunami is shown by a red line (Fernández et al., 2010; Fernández and Venegas, 2010), which is usually located between the coastal road (black dashed line) and the curve marking the elevation of 10 m amsl (blue line). Note the similarity between the observed tsunami inundation (red line) and the inland extent of tsunami sand inferred from our model (sand inundation, red shading).

c) South segment

The South segment, with a low average land slope of about 2.3°, showed the most extensive sand inundation of the LIC. Sand extended inland on average 223 m, consistently exceeding 200 m throughout the entire segment (excluding a rocky area directly north of Iloca Creek) with a peak in Iloca Creek, where reached about 600 m (Figure 2.5; Tables 2.2 and S4). Sand inundation covered 88% of the water inundation, with a horizontal gap of less than 30 m between both limits. Run-ups usually ranged from 4 to 8 m.

Table 2.2. Measurements averaged every 10 transects for water inundation, sand inundation, run-up and land slope. The difference between water and sand inundation is indicated as a gap. Measurements averaged with less than 10 transects are marked with an asterisk. Average for each segment and total average are indicated in bold. See Table S4 for extended data.

Segment	Transect	Water inundation (m)	Sand inundation (m)	Gap (m)	% Sand inundation	Runup (m)	Land slope (°)
North	1-10	187.13	170.58	16.55	91.16	5.48	2.44
	11-20	228.43	186.18	42.25	81.50	4.95	1.19
	21-30	278.67	241.58	37.09	86.69	4.28	1.25
	31-40	107.25	100.54	6.71	93.74	8.05	3.47
	41-47*	169.88	144.99	24.89	85.35	7.65	2.59
	Average	**195.83**	**170.29**	**25.54**	**87.90**	**5.98**	**2.16**
Central	48-57	180.05	164.79	15.26	91.52	6.95	2.43
	58-67	213.43	192.18	21.25	90.04	6.17	2.42
	68-77	85.44	75.74	9.70	88.65	7.91	5.99
	78-87	124.58	113.69	10.89	91.26	7.89	3.97
	88-97	156.00	146.56	9.44	93.95	6.17	2.52
	98-107	94.09	86.98	7.11	92.44	5.83	3.69
	108-112*	165.19	158.39	6.80	95.88	7.77	2.55
	Average	**144.03**	**132.17**	**11.86**	**91.76**	**6.89**	**3.39**
South	113-122	308.99	273.01	35.98	88.36	5.60	1.19
	123-132	271.69	250.67	21.02	92.26	5.63	1.39
	133-142	93.35	82.29	11.06	88.15	7.12	5.68
	143-152	322.41	282.65	39.76	87.67	6.46	1.53
	153-162	266.52	227.93	38.59	85.52	7.03	1.72
	Average	**252.59**	**223.31**	**29.28**	**88.31**	**6.37**	**2.30**
Total average		**192.56**	**171.36**	**21.21**	**89.57**	**6.47**	**2.70**

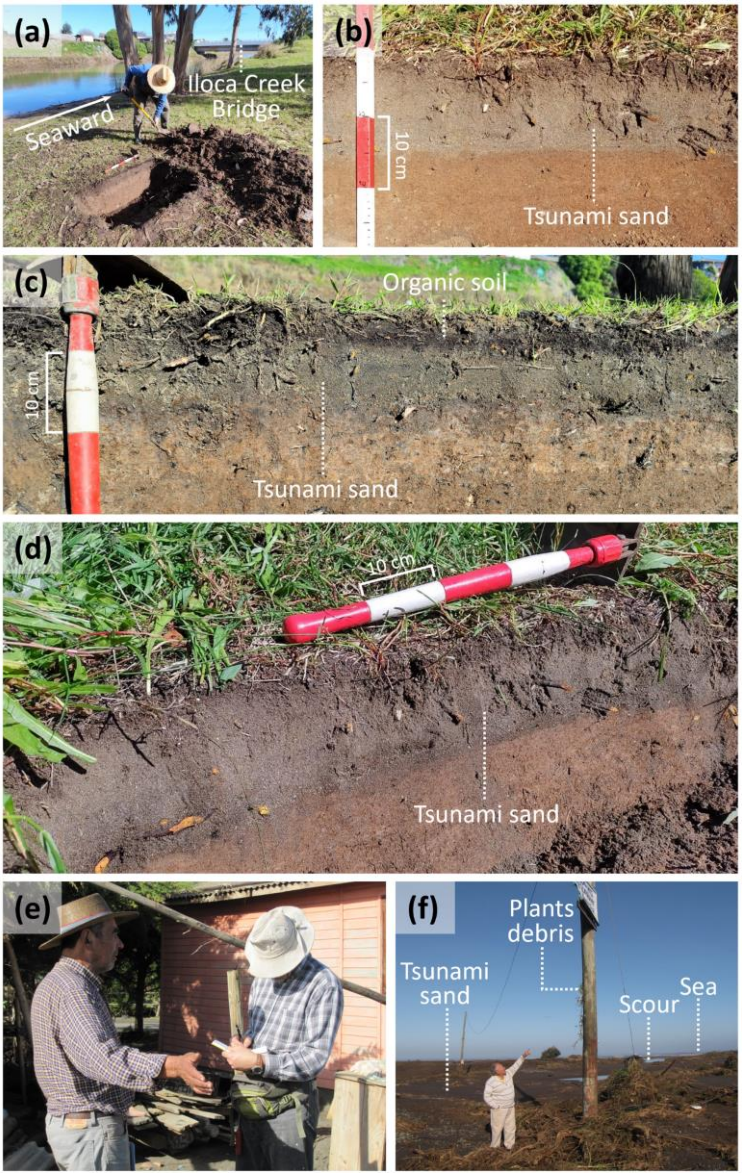

Figure 2.4. Examples of ground truth from stratigraphy and interviews. (a) Pit excavated to study stratigraphy. Iloca Creek can be seen in the background. (b–d) Pit walls showing the sand deposit of the 2010 tsunami. Photos of pit 12 (a) and (c) were taken in July 2023 (Table S2). Photos of pits 30 (b) and 36 (d) were taken in October 2021 (Table S2). Note that the tsunami deposit, a greyish tabular sand layer, contrasts with the underlying light-coloured finer grained sediment/soil and overlying organic-rich soil and vegetation. (e) Photo of Mr. José Luis Farías, a local farmer and eyewitness of the 2010 tsunami, being interviewed in August 2010. The day after the tsunami he found his crops extensively covered by a sand sheet (Figure S19; Table S1). (f) Photo of Mr. Claudio Ramírez taken a few hours after the 2010 tsunami when he was checking the damage on his land (provided by Mr. Ramírez; Table S1). In the photo, Mr. Ramirez points to plant debris left by the tsunami 5 m above sea level around a power pole. Note that the sign at the pole top was damaged by the waves. Debris and sand on the ground and a large seaward scour can also be observed.

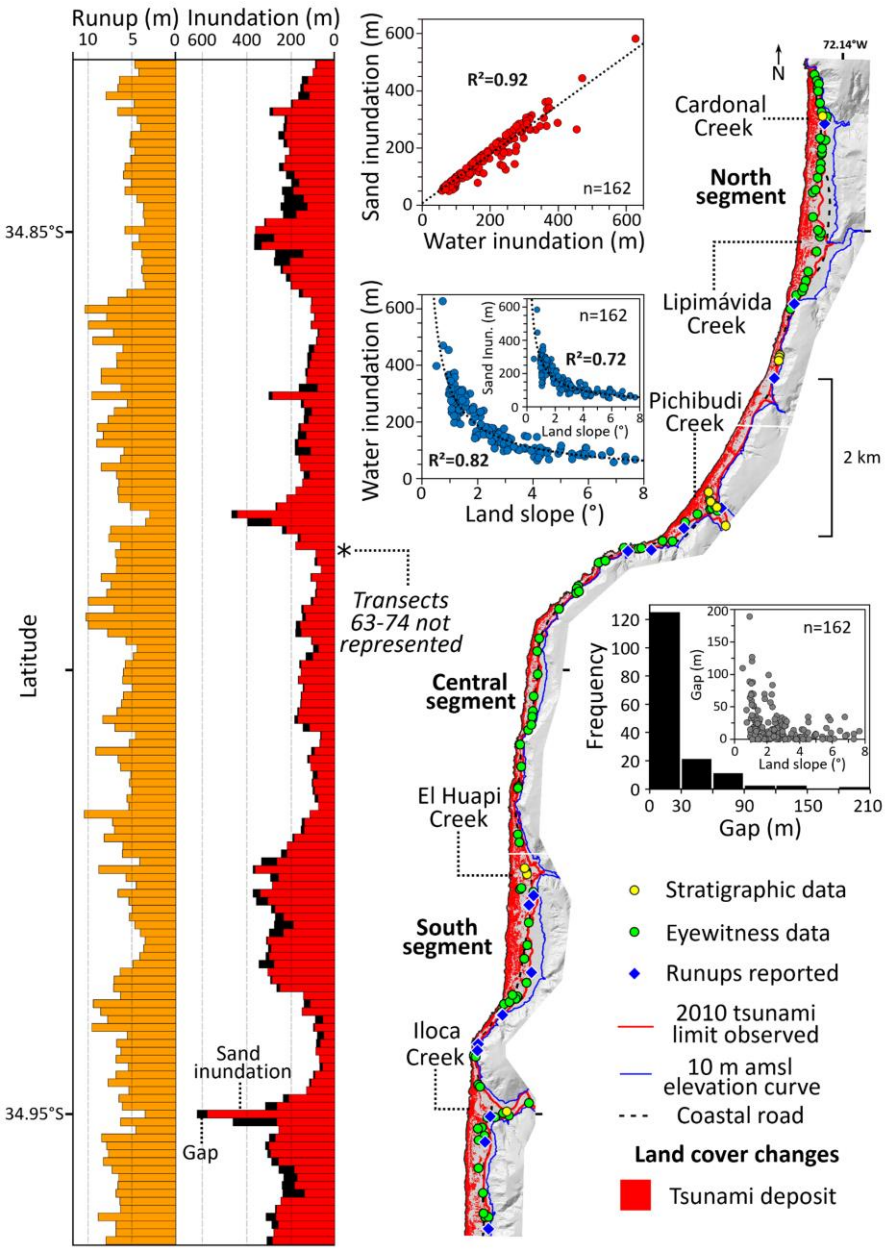

Figure 2.5. Bar plots indicating the amount of sand inundation and run-up along the LIC. Red bars indicate the amounts of sand inundation attained on each of the 162 shore-normal transects. Black bars beside the red bars indicate the gap between sand inundation and water inundation. Orange bars show the run-up on the same transects. Transects 63–74, marked by an asterisk in the Central segment, were not represented as they cover a stretch of mostly rocky coast. Graph with red dots shows the good match between sand inundation and water inundation. Note in the black bar histogram that the gaps between sand and water inundation are frequently less than 30 m. Graphs with blue dots show the negative exponential correlation between both sand and water inundation with the land slope. Note in the graph with grey dots that the gaps between sand and water inundation are also controlled by the land slope.

2.4.3 Validation through ground truth data

The spatial distribution of the 2010 tsunami deposit inferred from our model agrees well with the distribution from the stratigraphy and eyewitness reports (Figures 2.4 and 2.5). Out of the 73 points selected for validation through stratigraphy, where we in fact found the 2010 tsunami deposit (Table S2), in 53 of them (43 from Iloca Creek), our model predicted its occurrence (73%). However, for the remaining 20 points (27%), our model failed, as they did not coincide with sand pixels detected by satellite mapping (Table S2; Figure S7). Out of the 97 points selected for validation through witness interviews, where they assured the tsunami did leave sand (Table S1), the model predicted its occurrence in all of them (100%). Therefore, out of a total of 170 validation points, 88% coincided with the predictions of the model.

2.4.4 Loss of satellite detection of the tsunami deposit over time

Many sites that our model detected as covered by tsunami sand 6 weeks after the event (April 2010) showed an absent deposit when we applied the same model on a satellite image 11 years later (May 2021). Figure 2.6c shows a marked reduction in the inland extent of the sand deposit a decade after the tsunami along the South segment (see Supporting Information for North and Central segments). About 97% of the pixels that were initially classified as sand in the April 2010 satellite image (Figure 2.6b) were classified as soil in the May 2021 satellite image (Figure 2.6c), which is detected as an evident change (purple shading in Figure 2.6d). Consequently, the LULC map resulting from the 2021 image exhibits a similar classification to that prior to the 2010 event (Figure 2.6a), showing only sand restricted to beach and dune. North and Central segments also showed a significant reduction of pixels initially classified as sand, although less than the South segment, 84% and 78%, respectively. Considering the three segments studied, about 86% of the tsunami deposit vanished a decade after the 2010 tsunami.

Since we found the tsunami deposit still preserved at several sites along the LIC, its evident reduction from satellite data results of the loss of detection ability through the model rather than its actual loss. Based on our field observations, surface masking

caused by new soil development (Figure 2.4) and destruction of the deposit due to human activities (Table S1; Figure S19) contributed significantly to this loss of satellite detection.

2.5 Discussion

2.5.1 Performance and limitations of our classification model

Mapping tsunami deposits by remote sensing, integrating both supervised classification models and sub-metre spatial resolution satellite images, offers advantages over traditional field post-tsunami surveys. While field surveys are time-consuming and measure the inland extent of the deposit from few profiles (e.g., Jaffe et al., 2003, 2006; MacInnes et al., 2009a; Srinivasalu et al., 2007), our classification model based on satellite images is capable of mapping large areas in less time.

The automated mapping achieved both high overall accuracy and high class-specific accuracies. However, to reach such accuracy required that our satellite images had good visibility, had sub-metre resolution and were close in time to the event. Used images showed pre- and post-tsunami conditions completely cloud-free allowing optimal visibility. This could be a problem for areas with persistent cloudy weather. Considering that the spatial distribution of the 2010 tsunami deposit varied over short distances, it was critical that the images had a sub-metre resolution. Between the tsunami date (27 February 2010) and that of our post-tsunami satellite image (14 April 2010) about 6 weeks elapsed. In that time, the tsunami deposit may have been disturbed by human activity or weather conditions, as seen in other tsunami deposits (e.g., Szczuciński, 2012). However, the subsequent cleanup work and recovery from the tsunami aftermath were slow and delayed months due to the social impact generated by the catastrophe (Contreras and Winckler, 2013; Cowan et al., 2011; EERI, 2010), something also evident from the images. Likewise, considering that the 2010 tsunami occurred during dry season, rainfall did not modify the original distribution of the deposit. Therefore, we assumed minimal disturbance of the tsunami deposit captured by the April 2010 satellite image; although wind erosion, which was not assessed in this study, cannot be ruled out as an important factor of sediment

reworking (Goto et al., 2011; Higman and Bourgeois, 2008; Morton et al., 2011; Spiske et al., 2013).

The high degree of accuracy achieved for both wet and dry sand classes, above 80%, was also favoured because the deposit, including beach and coastal dune, exhibited a consistent and easily identifiable spectral signature in all images. This is because the sand class is homogeneous, not exhibiting large spectral variations between pixels as seen for other classes (e.g., urban class). Additionally, beach sand had a distinctive reflectance in the VNIR spectrum compared to bare soil or crop classes. This distinctive spectral signature makes it easily identifiable, something likely resulting from its mineralogy with high heavy minerals concentrations (e.g., Izawa et al., 2019; Schlegel et al., 1979). Since tsunami deposits can usually have high concentrations of heavy minerals from different coastal sources (e.g., Jaffe et al., 2003; Jagodziński et al., 2012), they could be easily detected using supervised classification techniques. However, future work should assess the performance of the classification model on beaches with low heavy mineral content or with different mineralogy than beaches in central Chile.

Despite the good performance of our model, some limitations in the spectral detection of the tsunami deposits were recognized. They include deposits hidden by canopy and shadows, and deposits barely detected because of their thinness and patchiness.

Canopies of leafy trees can hinder visibility in images, preventing detection of a tsunami sand deposit through the classification model. Likewise, shadows cast by tall trees, buildings, towers and pole posts partially obscure the ground (Figure S7). However, in the LIC these limitations did not affect the model performance, because of the dearth of thick vegetation and infrastructure. Similarly, the time and season at which the images were taken helped to diminish those undesired effects. The images used were obtained between early spring and early fall, so the sun did not cast an extended shadow, and were also taken at a similar time of day, around noon (Table 2.1). Both qualities, the lack of vegetation and infrastructure together with the timing

of the images, allowed us to group these shadows in a new class, instead of removing them, as shown by Dare (2005).

Perhaps a more significant limitation than shadowing was the thinness and patchiness of the tsunami deposit in some places making it barely detectable. When from field observations, the deposit was thinner than 1 cm or too patchy it was undetectable by the model, mixing the pixel spectral signature with the surrounding land cover classes. This limitation is important when considering the detection threshold of the deposit's landward limit.

2.5.2 Sand versus water inundation

The spatial distribution of the 2010 tsunami deposit matched well with the observed tsunami inundation on the LIC (Figures 2.3 and 2.5). The good fit between sand inundation, derived from our model, and water inundation, previously derived from post-tsunami surveys, is similar to that obtained in other studies (Abe et al., 2020; Gelfenbaum and Jaffe, 2003; Jaffe et al., 2003, 2006; MacInnes et al., 2009a; Moore et al., 2006, 2011; Srinivasalu et al., 2007; Szczuciński et al., 2012). However, those studies based their estimates on a limited number of transects. Because our work considered the areal distribution of sediments, performing quantifications through a greater number of transects, the good fit between sediments and water is likely more robust. Thus, our results reinforce the validity of using the sand deposit landward limit as a proxy for the tsunami inundation limit (MacInnes et al., 2010; MacInnes et al., 2009a; Martin et al., 2008).

On the other hand, discrepancies found between sand and water inundation have led other studies to question the use of tsunami deposits as a reliable proxy for inundation (Abe et al., 2012; Chagué-Goff et al., 2015; Cheng and Weiss, 2013; Goto et al., 2011; Morton et al., 2011). For instance, Goto et al. (2011) and Abe et al. (2012) found on the Sendai Plain that sand left by the 2011 Tohoku-oki tsunami indicated only 57%–76% of the actual water inundation, showing gaps of about 2 km between sandy sediment and water. However, Sugawara et al. (2014) explain such

gaps mainly by limited sediment supply and sediment blocking by artificial topography. Morton et al. (2011) reported gaps exceeding 150 m between the maximum inland extent of the sand deposit and the inundation limit for several sites in central Chile following the 2010 tsunami. About 12 km south of Constitución, Chagué-Goff et al. (2015) found that the 2010 tsunami deposit only reached 60% of the total inundation distance, suggesting that geochemical indicators and/or diatom assemblages are more reliable proxies for the tsunami intrusion. These large gaps between the deposit landward limit and the tsunami inundation limit are probably controlled by topographic factors, such as the land slope (Cheng and Weiss, 2013).

Since our work along the LIC covered both flat low-lying and steeper sites (Figure S6), we were able to assess the control of land slope over inundation. At least two important aspects emerge from our results. First, both sand and water inundation show a negative exponential correlation with land slope (Figure 2.5). While at lower slope sites sand and water inundation reached a longer distance inland, at steeper slope sites both were limited only to a few tens of metres from the shoreline. Despite the above, we did not identify a clear relationship of run-up with land slope. MacInnes et al. (2009b) determined that local topography strongly affected the 2006 middle Kurils tsunami inundation, but it slightly affected the run-up. Second, the size of the gaps between sand and water inundation is also influenced by the land slope. At steeper slope sites sand and water inundation reached similar inland extent, with gaps between the two less than 30 m. In contrast, at lower slope sites, such as plains and creeks, the gaps between sand and water inundation were much larger, reaching up to almost 200 m. Our findings suggest that the inland extent of tsunami sand deposits prove to be a better proxy for the actual inundation area on steep slopes rather than on low-lying plains, thus supporting the conclusions of Abe et al. (2020) for steep coastal valleys.

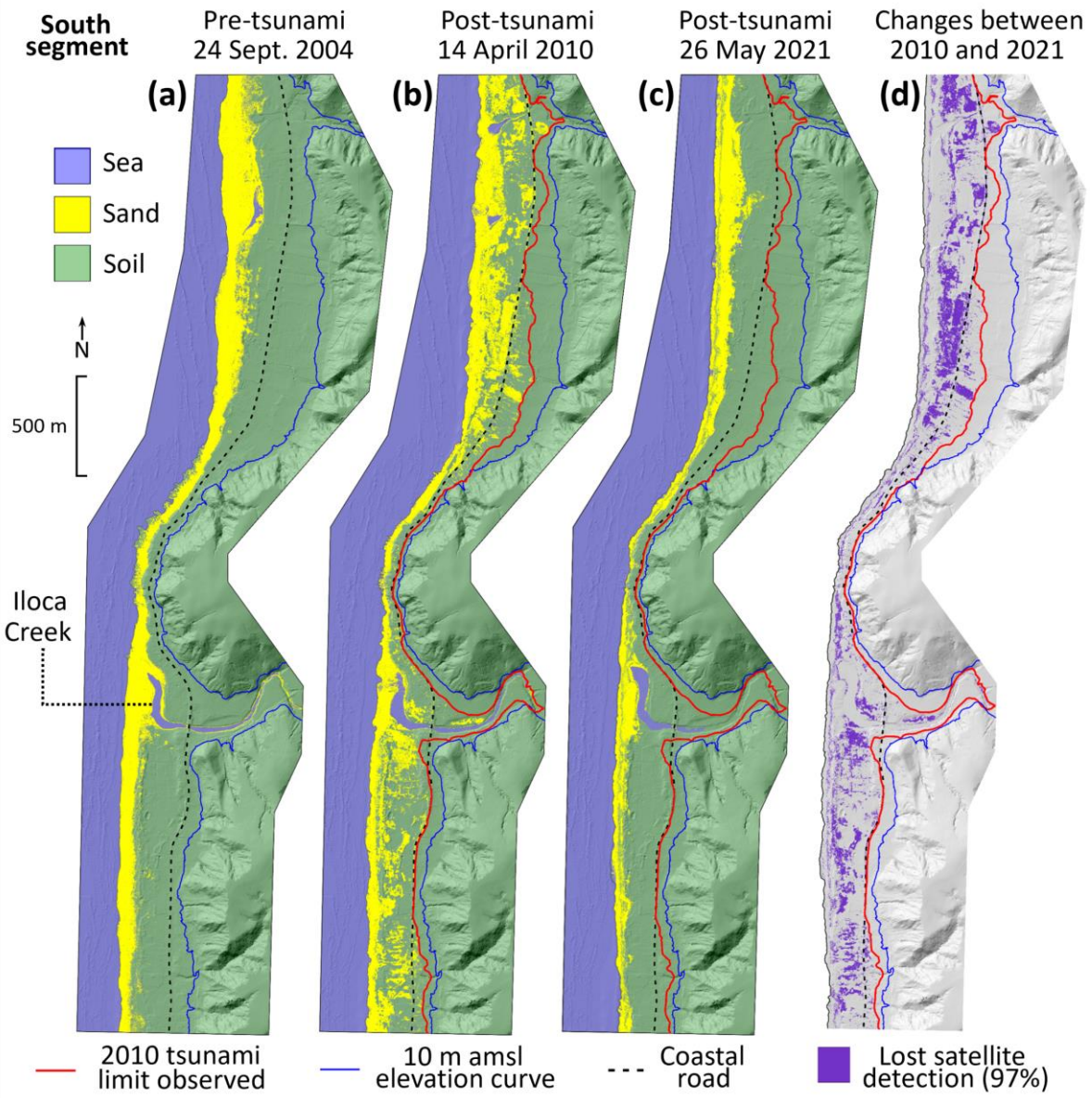

Figure 2.6. Satellite detection of the tsunami deposit that was lost by the classification model a decade after the 27 February 2010 event along the South segment (see Figure 2.1). (a) Sand detected before the 2010 tsunami, mainly restricted to beach and dune. (b) Sand detected weeks after the tsunami, including that from beach and dune but also that transported inland by the tsunami. (c) Sand detected a decade after the tsunami, resembling pre-tsunami condition. (d) Changes detected between the immediate post-tsunami condition and that of a decade later. The purple shading shows the area where the satellite detection of the tsunami deposit was lost (97%), either by masking due to new soil development or by destruction related to human activity. See Supporting Information for North and Central segments.

2.5.3 Masking and destruction of the 2010 tsunami deposit over time

Our work recognized two variables related to the time elapsed post event that should be considered for future work using the approach offered here. First, natural masking of the tsunami deposit due to new soil development and subsequent vegetation growth prevents complete detection of its spatial distribution. Our field observations in areas unaffected by human activities showed that over the deposit, a decade after the tsunami, a soil of a few centimetres had developed and was already capable of supporting abundant vegetation. Thus, classification models based on satellite images are unable to map deposits that have already been buried. Second, field observations additionally showed that the deposit was locally and progressively destroyed by human activities, mainly agricultural land use. In many sites, farmers reported that the sand deposit was removed, plowed or mixed with the underlying soil soon after the tsunami to resume planting potatoes, the main crop of the area (Table S1; Figure S19). Other sites were cleaned and filled in with debris to build new houses replacing the buildings lost to the tsunami. Similar activities have been also reported elsewhere, where tsunami deposits were lost soon after the inundation (Bahlburg and Spiske, 2015; Spiske et al., 2013, 2020; Szczuciński, 2012, 2020; Szczuciński et al., 2006). Along the Thai coast, Szczuciński (2012) estimated that about 50% of the landward extent of the 2004 tsunami deposit was reduced after 5 years due to intense human activity and new soil formation.

Considering both variables, surface masking by the development of a new soil and the destruction of the deposit by human activities, it is required that satellite images be acquired as close in time to the event as possible. These images should be no later than a few months after the event; otherwise, the detection ability of the deposit by supervised classification models will be lost.

2.6 Conclusions

We trained a classification model using high resolution pre- and post-tsunami satellite images to perform an automated mapping of the sand deposit left by the 2010 Chilean tsunami on the Lipimávida-Iloca coast. The classification model yielded an

overall accuracy of about 86% and specific accuracies for sand classes above 80%. Ground truth data from 170 sites, comprising 73 stratigraphic observations from pits and 97 testimonies from tsunami survivors, were used as an independent validation of the classification model, achieving 88% correspondence with the tsunami deposit inferred from the obtained model. The resulting spatial distribution of the tsunami deposit was found to be almost as extensive as the observed inundation area. Sand inundation and water inundation resulted comparable, both ranging between 50 and 600 m and being controlled by the land slope. In general, sand inundation covered about 90% of the inundated area. About 86% of the satellite detection ability of the sand deposit was lost 11 years after the tsunami. Human activities and the development of a new soil superficially masked the deposit making it undetectable by the model. Finally, our approach exhibits broad applicability to tsunami-prone sandy coasts. We propose that our novel, low-cost and time-saving method has the potential to assist or, eventually and under favourable conditions, replace the hard fieldwork involved in mapping tsunami deposits.

Capítulo 3. Complejidades de estudiar depósitos de tsunami en desembocaduras de ríos andinos

Saldaña, B., Cisternas, M., Carreño, A., Guerra, M. & Espinoza, A. (en prep.). Complejidades de estudiar depósitos de tsunami en desembocaduras de ríos andinos.

Resumen

El estudio de depósitos de tsunami ha sido ampliamente utilizado en la evaluación del riesgo de comunidades costeras, mediante la reconstrucción de áreas de inundación e intervalos de recurrencia. Sin embargo, una primera complejidad es discriminar entre depósitos realmente dejados por tsunamis y aquellos originados por otros fenómenos naturales. En este trabajo se muestra que inundaciones de ríos provenientes desde la alta cordillera son capaces de dejar un registro estratigráfico similar al de un tsunami. Para ilustrar esto, aquí se presenta un ejemplo en la desembocadura del río Mataquito, donde tanto el tsunami del 2010 como la reciente inundación fluvial del 2023 dejaron una capa de arena con similares características que las hacen indistinguibles. Ambos depósitos, aunque difieren en su origen, presentaron similar arquitectura, granulometría, mineralogía, susceptibilidad magnética y ensambles de diatomeas. Estas similitudes provenientes de análogos modernos bien estudiados destacan las complejidades de diferenciar entre ambos tipos de eventos a partir del registro estratigráfico, conduciendo probablemente a una malinterpretación de la amenaza. Se concluye que desembocaduras de ríos debiesen ser evitadas como blancos de exploración para la búsqueda de depósitos de tsunami. En su lugar, ambientes menos dinámicos como esteros o humedales, los cuales depositan sedimento fino y no experimentan grandes crecidas de su caudal, son mejores y más confiables registradores de tsunamis pasados.

Palabras claves

Río Mataquito, inundación fluvial del 2023, malinterpretación de depósitos de tsunami

3.1 Introducción

Los tsunamis representan una de las amenazas naturales más devastadoras para las comunidades costeras, causando significativas consecuencias humanas, económicas y ambientales. Recientes tsunamis como los del Océano Índico el 2004, Chile central el 2010, Tohoku el 2011 y Rusia el 2025 afectaron dramáticamente regiones densamente pobladas, conduciendo a pérdidas de vidas, daño a infraestructura y cambios costeros (e.g., Paris et al., 2009; Fritz et al., 2011; Morton et al., 2011; Goto et al., 2012; Richmond et al., 2012). Por lo tanto, comprender la recurrencia de estos eventos y sus probables áreas de inundación es esencial para la evaluación del riesgo y la planificación de estrategias de mitigación (Bernard et al., 2006; Kânoğlu et al., 2015).

Durante las últimas décadas, estudios paleosismológicos han utilizado depósitos de tsunami preservados en secuencias de sedimentos costeros para reconstruir la historia de tsunamis pasados (e.g., Cisternas et al., 2005; Jankwaew et al., 2008; Costa y Andrade, 2020). Depósitos de tsunami permiten inferir características como la extensión de la inundación, el dinamismo del flujo y la frecuencia con que ocurren estos eventos (Spiske, 2020), lo cual es especialmente valioso en zonas donde no existe un registro instrumental o histórico prolongado. Sin embargo, la identificación y correcta interpretación de los depósitos no está exenta de dificultades. A menudo la perturbación post-depositacional o pobre preservación, ya sea por causas humanas o naturales, complejiza la interpretación del registro geológico (Szczuciński, 2012, 2020; Spiske et al., 2020; Saldaña et al., 2025a). Sumado a esto, uno de los principales desafíos radica en la posibilidad de confundir depósitos dejados por tsunamis con aquellos originados por otros fenómenos naturales de alta energía, tales como tormentas (Kortekaas y Dawson, 2007; Morton et al., 2007; Engel y Brückner, 2011; Goff et al., 2012; Phantuwongraj y Choowong, 2012; Ramírez-Herrera et al., 2012; Shanmugam, 2012; Kongsen et al., 2022). Esta problemática se acentúa aún más en ambientes de alta dinámica sedimentaria, como las desembocaduras de ríos, donde la superposición de aportes continentales y marinos pueden generar un mezclado y similar registro (Delile y Salomon, 2020). Sitios con

estas características pueden inducir a interpretaciones erróneas sobre el origen de los sedimentos, afectando la reconstrucción de tsunamis pasados y, por tanto, la evaluación de la amenaza futura.

El presente estudio se enfoca en la desembocadura del Río Mataquito en Chile central (Figura 3.1), donde dos eventos de distinta naturaleza, el tsunami del 2010 y la inundación fluvial del 2023, dejaron depósitos de arena con características sorprendentemente similares. A partir del análisis comparativo de estos dos depósitos modernos utilizando diferentes enfoques, se evidencian los desafíos que implicaría discriminar entre ambos desde el registro estratigráfico. Debido al confuso registro presente en desembocaduras de ríos andinos, se cuestiona la utilidad de estos sitios como blancos de exploración para la búsqueda de depósitos de tsunami.

3.2 Contexto regional

3.2.1 El Río Mataquito

El Río Mataquito, localizado en la Región del Maule, es uno de los ríos andinos más importantes de Chile central. Este nace de la confluencia de los ríos Teno y Lontué, ambos provenientes de la Cordillera de los Andes, y corre por cerca de 95 km hasta desembocar en el Océano Pacífico, drenando una cuenca de 6190 Km^2 (Saldías et al., 2012). Su caudal medio ronda los 100 m^3/s, alcanzando sobre 1000 m^3/s durante los meses de invierno, entre mayo y septiembre (Saldías et al., 2012; Masotti et al., 2018). En las cercanías de su desembocadura, una barra de arena extendiéndose hacia el norte por cerca de 8 km de largo y alcanzando una altura de ~6 m separa el Río Mataquito del mar, configurando un protegido ambiente estuarino (Figura 3.1c). La extensa marisma es influenciada por un régimen micro mareal inferior a 1.5 m (Cienfuegos et al., 2014), generando condiciones de alta salinidad que favorecen el desarrollo de vegetación halófita (e.g., *Spartina sp*). El Río Mataquito es un importante suministro de arena proveniente desde los Andes, promoviendo la formación hacia el norte de extensas playas, las cuales son limitadas hacia el este por el acantilado costero (Saldaña et al., 2025a).

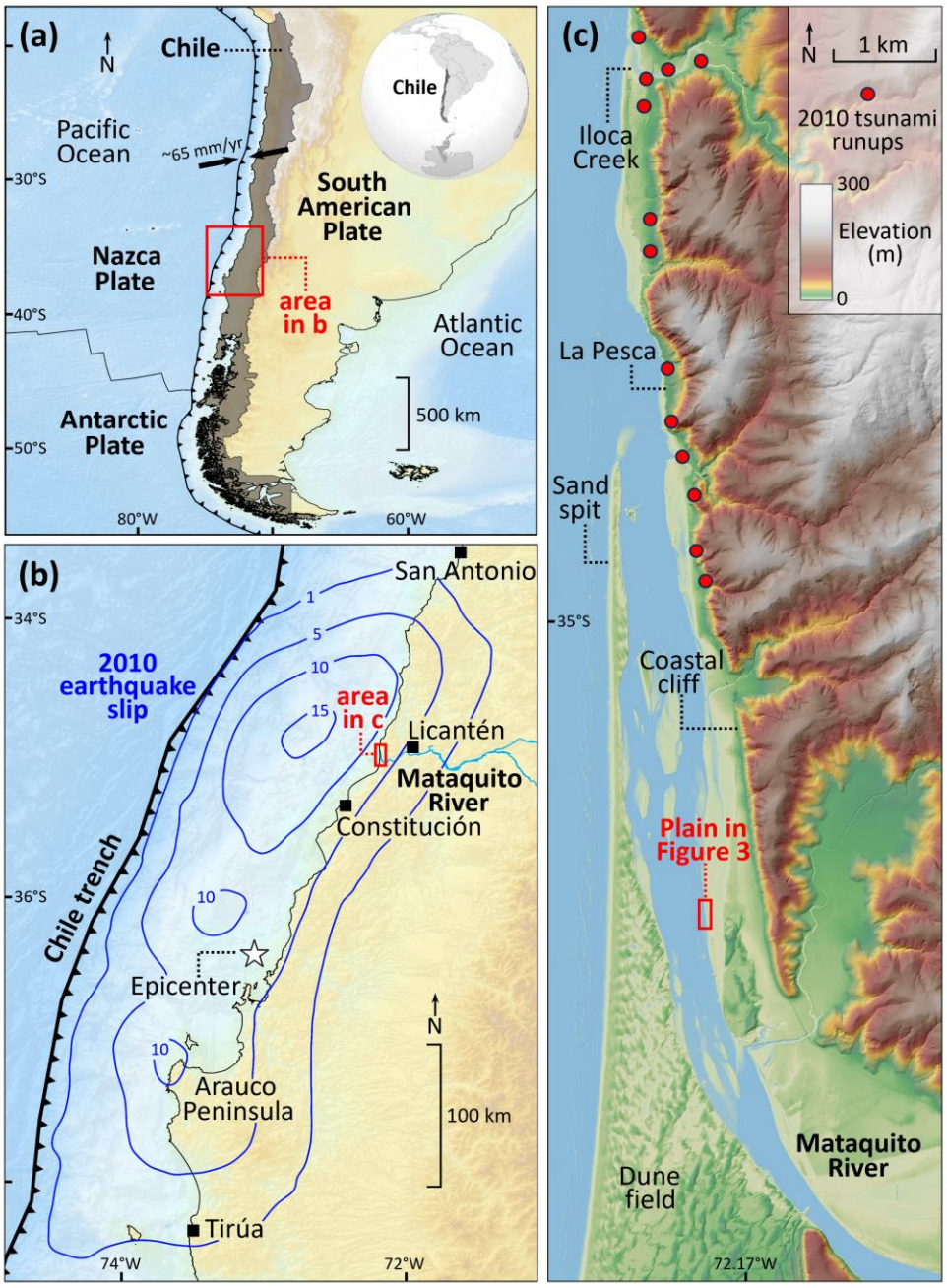

Figura 3.1. Mapas índices. (a) Configuración tectónica de placas en el margen suroeste de Sudamérica. Línea negra con púas marca el borde hacia el mar de la zona de subducción entre las placas de Nazca y Sudamericana. Flechas pareadas indican la velocidad de convergencia entre ambas placas (Jarrin et al., 2023). (b) Contornos de slip (m) del terremoto del 2010 en Chile central (Moreno et al., 2012). Notar la posición de la desembocadura del Río Mataquito justo frente al parche de máximo slip. (c) Desembocadura del Río Mataquito. Puntos rojos indican runups del tsunami del 2010 previamente reportados por Fritz et al. (2011), Vargas et al. (2011), Lario et al. (2016) y Saldaña et al. (2025a).

3.2.2 El tsunami del 2010

El 27 de febrero del 2010, un terremoto de subducción (Mw 8.8) con una ruptura de ~500 km de largo y un deslizamiento máximo de ~15 m frente a la Región del Maule (Moreno et al., 2012) gatilló un masivo tsunami que afectó gran parte de la costa de Chile central (Fritz et al., 2011). Los *runups* típicamente variaron entre 5 y 10 m, alcanzado máximos de ~30 m en Constitución y 20 m en Tirúa (Fritz et al., 2011). Los *runups* reportados en la desembocadura del Río Mataquito, cerca de La Pesca, excedieron los 9 m, alcanzando la base del acantilado costero (Fritz et al., 2011; Vargas et al., 2011; Lario et al., 2016). Al norte del Río Mataquito, en el Estero Iloca (Figura 3.1c), Saldaña et al. (2025a) reportó runups sobre 6 m y distancias de inundación cercanas a los 600 m. Severos efectos geomorfológicos tales como la completa erosión de la barra de arena en la desembocadura del Río Mataquito y retroceso costero debido a fuerte erosión local fueron observados en las cercanías del área de estudio (Araya-Cornejo y Carvajal, 2016; Catalán et al., 2014; Villagran et al., 2013). Extensos mantos de arena fueron dejados por el tsunami sobre muchas localidades bajas, incluyendo la desembocadura del Río Mataquito y el Estero Iloca (Horton et al., 2011; Morton et al., 2011; Bahlburg y Spiske, 2012; Garrett et al., 2013; Ely et al., 2014; Chagué-Goff et al., 2015; Lario et al., 2016; Saldaña et al., 2025a).

3.2.3 El evento hidrometeorológico del 2023

Entre el 21 y 26 de junio del 2023 un evento hidrometeorológico caracterizado por intensas y continuas precipitaciones afectó Chile central, provocando repentinas crecidas de ríos e inundaciones en numerosas localidades (CIGIDEN, 2023). Estaciones pluviométricas registraron precipitaciones acumuladas sobre los 300 mm en tan solo 85 horas, causando el aumento del caudal de los ríos principales, incluyendo el Río Mataquito (CIGIDEN, 2023). La estación fluviométrica en las inmediaciones de Licantén (Figura 3.1b) registró un aumento del caudal medio del Río Mataquito hasta en 50 veces, alcanzando un máximo cercano a los 5500 m^3/s antes de dejar de funcionar (Figura 3.2b). Este anómalo caudal ha sido el mayor registrado en los últimos 20 años, superando incluso al de finales de mayo del 2008,

cuando la estación fluviométrica también dejó de operar luego de que el caudal superara los 4000 m^3/s (Figura 3.2b). La imagen satelital Sentinel-2 mostrada en la Figura 3.2a evidencia los efectos geomorfológicos causados por la crecida del Río Mataquito en su desembocadura, incluyendo la erosión de la barra de arena y la pluma de sedimentos dirigida hacia el norte debido a la deriva litoral.

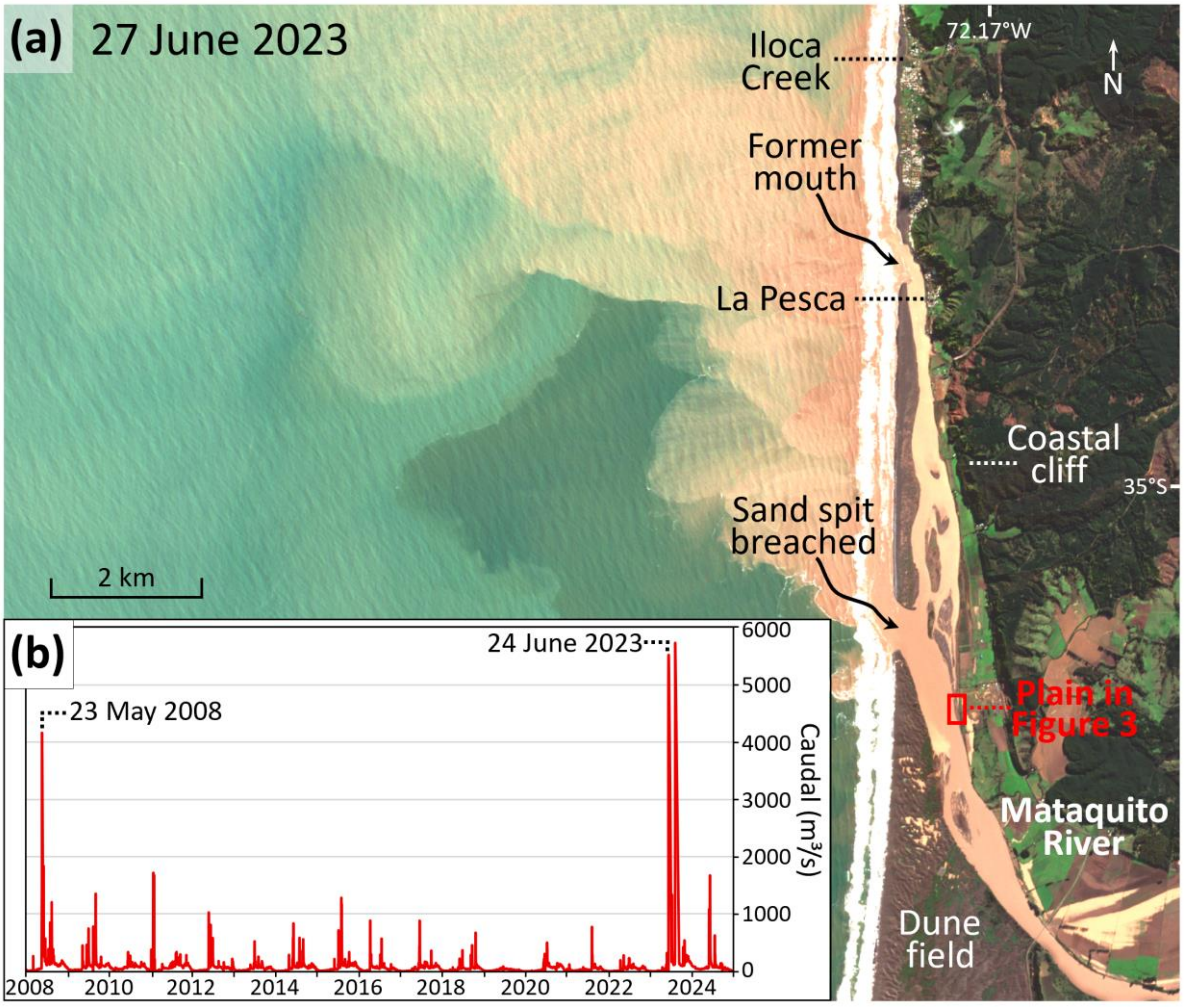

Figura 3.2. Efectos de la inundación fluvial del 2023 en la desembocadura del Río Mataquito y su caudal asociado. (a) Imagen satelital Sentinel-2 del 27 de junio del 2023 mostrando los efectos de la inundación, incluyendo la erosión de la barra de arena y el desplazamiento hacia el norte de la pluma de sedimentos. (b) Caudal del Río Mataquito registrado por la estación fluviométrica de Licantén entre 2008 y 2024 (Figura 3.1b; DGA). Notar que el caudal alcanzado durante la inundación del 2023 fue el más grande registrado en cerca de 20 años, superando hasta en 50 veces el caudal medio del río. Un caudal comparable, aunque inferior, fue registrado durante la inundación del 2008 (CIGIDEN, 2023).

3.3 Metodología

3.3.1 Trabajo de campo

Se visitó la desembocadura del Río Mataquito seis semanas antes (7 de mayo) y dos semanas después (14 de julio) del evento hidrometeorológico del 2023 (Figura 3.3). Durante el trabajo pre-evento, el interés fue centrado en el depósito de tsunami del 2010 y al menos tres capas de arena más antiguas preservadas en la planicie de inundación del río, que fueron interpretadas inicialmente como antiguos depósitos de tsunami dadas sus características estratigráficas. Sin embargo, la ocurrencia del evento hidrometeorológico de junio del 2023 reorientó el trabajo hacia la caracterización del depósito de arena dejado por la inundación del río y su similitud con el depósito de tsunami del 2010. Se estudió la distribución del depósito fluvial del 2023 en superficie y se excavaron cuatro fosas a lo largo de un perfil para medir su espesor y recolectar ocho muestras discretas de sedimento para análisis posteriores. La elevación del perfil fue relacionada al nivel medio del mar mediante un dGPS y un datum de referencia local.

3.3.2 Granulometría y mineralogía

El sedimento del depósito fluvial del 2023 fue caracterizado mediante un análisis granulométrico y mineralógico, cuyos resultados fueron comparados con los del depósito de tsunami del 2010. Para cada muestra 100 g de sedimento fueron secados y separados mecánicamente mediante una tamizadora, con tamaños de partícula desde -1 a 4 φ a intervalos de 0.5 φ. Parámetros estadísticos, incluyendo tamaño de grano medio y selección, fueron obtenidos mediante el software GRADISTAT v. 9.1 (Blott y Pye, 2001), usando el método de Folk y Ward (1957). Siguiendo los procedimientos de Saldaña et al. (2025a), un análisis mineralógico cuantitativo fue conducido mediante inspección visual en un microscopio estereoscópico binocular. El contenido de cada mineral identificado fue expresado como porcentaje de abundancia relativa.

3.3.3 Susceptibilidad magnética

Un sensor Bartington MS2E fue usado para medir la susceptibilidad magnética (Dearing, 1994). Cada muestra fue medida tres veces y sus resultados fueron expresados como valores promedio. Las mediciones fueron hechas sobre un volumen idéntico de sedimento preparado en el laboratorio y a una misma hora del día para evitar variabilidad debido a cambios de temperatura.

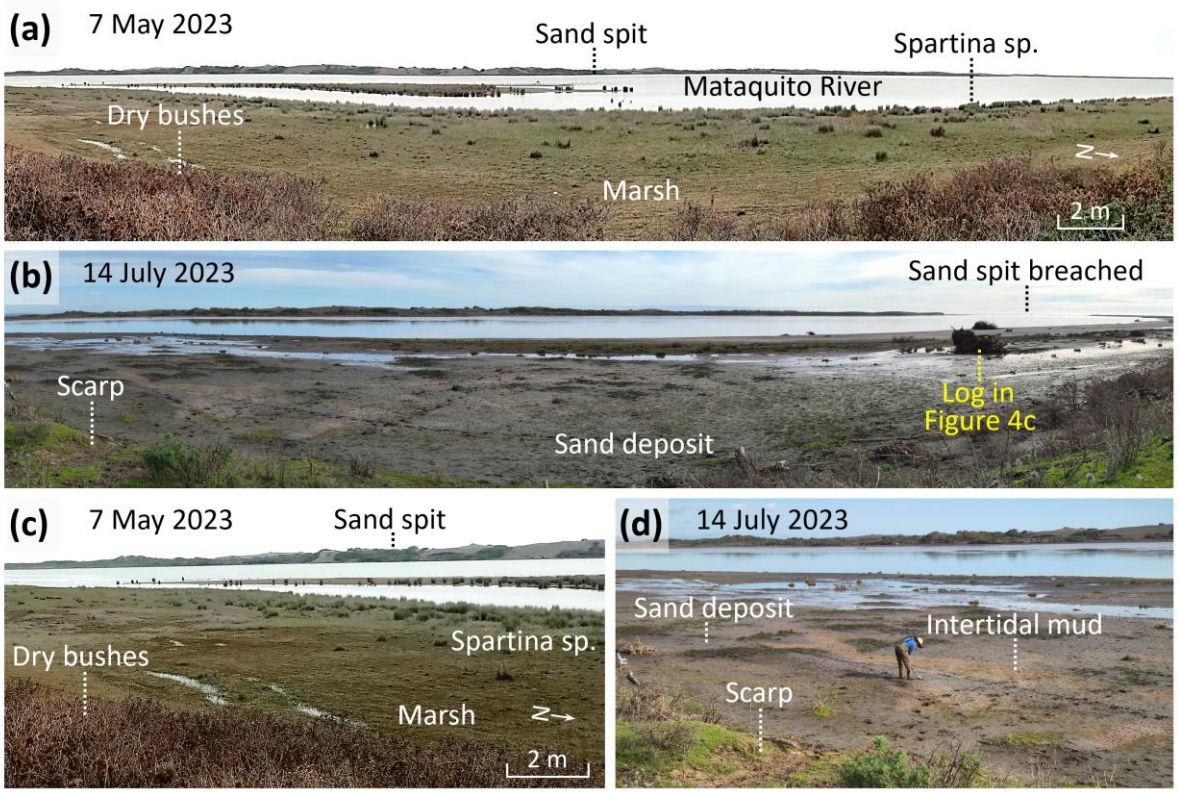

Figura 3.3. Fotografías mostrando la marisma en la desembocadura del Río Mataquito antes y después del evento hidrometeorológico del 2023. (a) y (c) muestran la marisma con abundante vegetación antes del evento del 2023. (b) y (d) muestran la marisma cubierta por el depósito de arena dejado por la inundación del río. Notar en (b) la barra de arena erosionada (Figura 3.2a). Notar en (d) cómo el fango intermareal comienza a cubrir el depósito de arena.

3.3.4 Análisis de diatomeas

Se estudiaron los ensambles de diatomeas en la capa de arena de la inundación del 2023 y fueron comparados con aquellos del depósito de tsunami del 2010. Siguiendo los procedimientos descritos por Dura y Hemphill-Haley (2020), secciones delgadas

de sedimento fueron preparadas para ser observadas al microscopio bajo un aumento de 1000x. Un mínimo de 300 valvas de diatomeas fue contado para cada muestra, las cuales fueron identificadas al nivel de especies y clasificadas por preferencias de salinidad (dulce, salobre, y marino). La identificación y clasificación fue hecha usando referencias locales (Garret et al., 2013), regionales (Horton et al., 2011; Chagué-Goff et al., 2015; Dura et al., 2017; Hocking et al., 2017; Sawai et al., 2017) y globales (Vos and de Wolf, 1988; 1993; Denys,1991; Hemphill-Haley, 1993; Van Dam et al., 1994; Sawai et al., 2004; Hassan et al., 2009; Zong and Sawai, 2015; Spaulding et al., 2021; DePaolis et al., 2024).

3.4 Resultados

3.4.1 El depósito de tsunami del 2010

El tsunami del 2010 inundó la mayoría de las áreas bajas adyacentes a la desembocadura del Río Mataquito, depositando una capa de arena con continuidad lateral por varios kilómetros. El depósito conforma una capa tabular de arena fina (2.5 φ), moderadamente bien seleccionada y de color gris oscuro a rojizo. Hoy, la capa se encuentra ~30 cm bajo la superficie de la marisma y se extiende por cerca de 500 m tierra adentro hasta la base del acantilado costero. La capa alcanza un espesor máximo de 30 cm y se adelgaza progresivamente hacia el límite de inundación, presentando una distribución mayormente discontinua. Tanto el tamaño de grano como la susceptibilidad magnética (~807 x 10^{-5} SI) también muestran una tendencia decreciente tierra adentro.

El depósito de tsunami exhibe una alta abundancia de minerales pesados, tales como magnetita (35%), anfíbol (10%) y piroxeno (10%), acompañados por pequeños fragmentos de rocas (23%) de origen metamórfico y volcánico. Minerales como cuarzo (12%), feldespatos (7%) y micas (2%) mostraron una menor abundancia relativa, seguidos por trazas de zircón, esfeno, olivino, epidota y hematita (~1%).

Las estructuras sedimentarias en el depósito de tsunami del 2010 son escasas. La capa de arena generalmente exhibió una disposición masiva, con solo ocasionales

laminaciones de minerales pesados; solo en algunos sitios fue posible distinguir una sutil gradación normal. El depósito de arena sepultó un suelo orgánico negro mediante un contacto notoriamente erosivo, el cual puede ser trazado por varias decenas de metros. Adicionalmente, pequeños *rip-up clasts* de fango orgánico fueron observados integrando la capa de arena.

Los ensambles de diatomeas en la capa de tsunami son mayormente mezclados, siendo ligeramente dominados por especies marinas. Diatomeas salobres alcanzan una abundancia relativa de 25%, destacando especies como *Navicula cryptocephala* y *Fallacia tenera*. Las diatomeas de agua dulce presentan una abundancia de 33%, incluyendo mayoritariamente la especie epifítica *Ulnaria ulna*. Especies marinas alcanzan un 42% de abundancia en los ensamblajes, predominando la especie planctónica *Paralia sulcata*.

3.4.2 El depósito de la crecida fluvial del 2023

Durante el evento hidrometeorológico del 2023, el Río Mataquito inundó completamente la marisma localizada en las inmediaciones de su desembocadura, depositando una extensa capa de arena que presentó similares características al depósito de tsunami del 2010 (Figuras 3.3 y 3.4; Tabla 3.1). El depósito fluvial es descrito como una capa de arena grisácea fina (2.9 φ) y moderadamente seleccionada, la cual se extiende hasta la base de un pequeño escarpe localizado cerca de 70 m tierra adentro. La capa presenta un espesor máximo de ~20 cm en la orilla del río (Figura 3.5a), mostrando una tendencia de adelgazamiento tierra adentro, hasta alcanzar ~1 cm en la base del escarpe del valle del río. El espesor se incrementa localmente en sitios de abundante vegetación, estando esta usualmente aplastada en la dirección del flujo (Figura 3.4a). La granulometría y la susceptibilidad magnética (~747 x 10^{-5} SI) también mostraron una tendencia a disminuir tierra adentro, alcanzando valores mínimos cerca del límite de inundación (Figura 3.5a). Árboles, restos de madera y redes de pesca fueron observados esparcidos por la superficie de la marisma, especialmente apilados en la base del escarpe (Figura 3.4d).

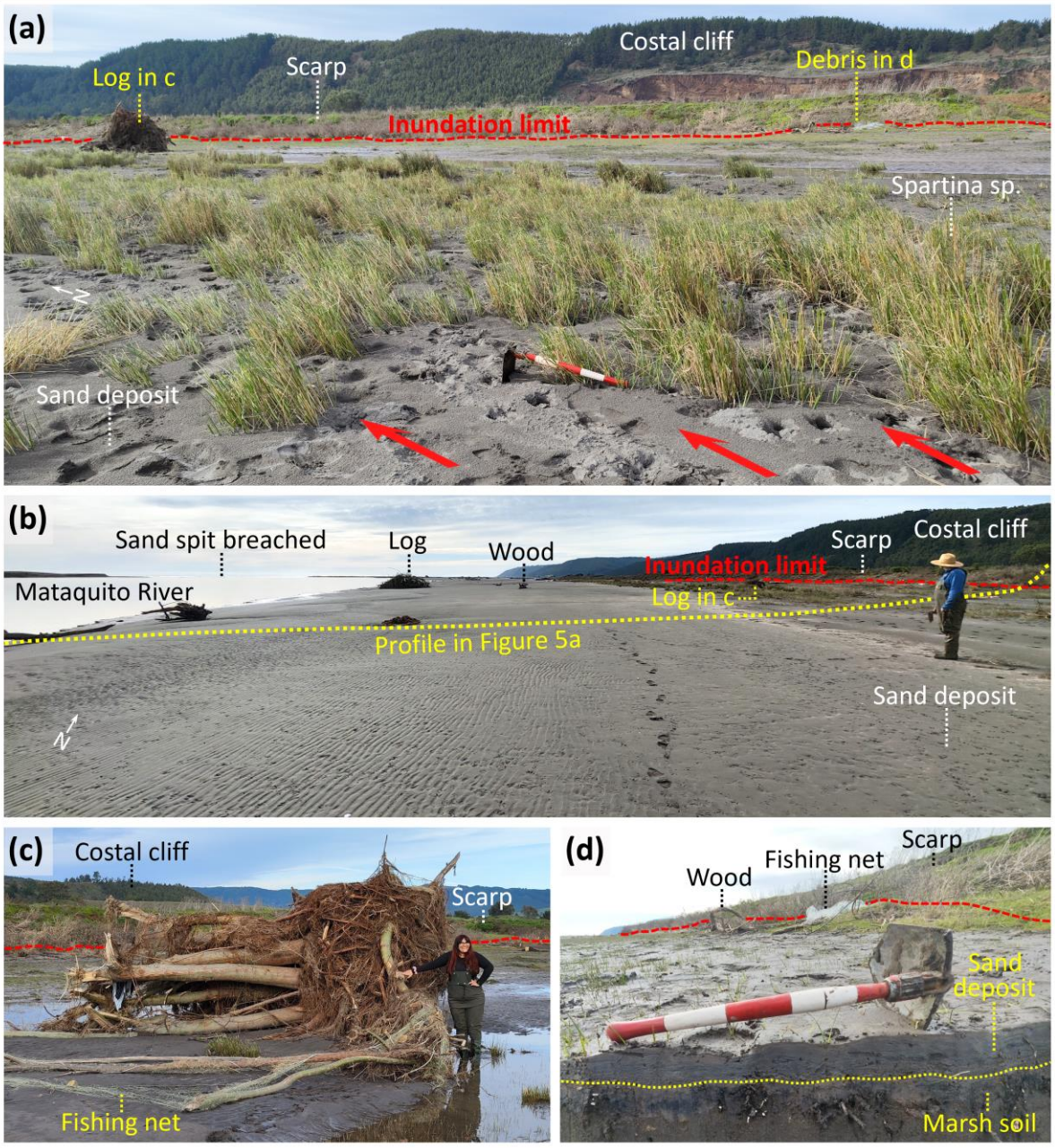

Figura 3.4. Fotografías mostrando el depósito de arena y otros restos dejados por la inundación del Río Mataquito. (a) Depósito de arena cubriendo la completa marisma adyacente a la desembocadura del río. Notar la vegetación ligeramente aplanada en la dirección preferencial del flujo (flechas rojas). El límite de inundación se encuentra justo en la base del pequeño escarpe visto en el fondo. (b) Vista hacia el norte de la extensión del depósito de arena cubriendo la planicie mareal y la marisma. Notar cómo las mareas ya han retrabajado parcialmente el depósito. (c) Tronco dejado por el río cerca del límite de inundación. (d) Detalle del depósito de arena cubriendo la superficie de la marisma. Barras de colores de la pala miden 10 cm. Notar al fondo cómo restos de madera, redes de pesca y otros escombros son apilados contra la base del escarpe.

Tabla 3.1. Criterios usados para evaluar las similitudes y diferencias entre ambos depósitos

Criterios de comparación	Depósito de tsunami del 2010	Depósito de río del 2023
Espesor promedio	20 a 30 cm	~20 cm
Tamaño de grano	Arena fina (2.5 φ)	Arena fina (2.9 φ)
Mineralogía	Alta abundancia de minerales pesados (Magnetita >30%)	Alta abundancia de minerales pesados (Magnetita >30%)
Susceptibilidad magnética	Alta susceptibilidad magnética (~807 x 10^{-5} SI)	Alta susceptibilidad magnética (~747 x 10^{-5} SI)
Ensamblajes de diatomeas	Ensamblaje mezclado: Marinas (42%), Dulces (33%), Salobres (25%)	Ensamblaje mezclado: Marinas (45%), Dulces (37%), Salobres (18%)
Estructuras sedimentarias principales	Rara gradación normal. Ocasionales laminaciones Generalmente masivo	Sin gradación o laminaciones. Generalmente masivo
Tendencias generales observadas	Disminución de susceptibilidad magnética, adelgazamiento y afinamiento tierra adentro	Disminución de susceptibilidad magnética, adelgazamiento y afinamiento tierra adentro
Rasgos de erosión	Contacto basal erosivo. Ocasionalmente *rip-up clasts*	Contacto basal abrupto, pero no erosivo. *Rip-up clasts* no fueron observados
Extensión tierra adentro	~500 m	~70 m
Run-up máximo	~10 m	<3 m

El color oscuro del depósito fluvial está determinado por su mineralogía, la cual es similar a la del depósito de tsunami del 2010. Un alto contenido de minerales pesados, tales como magnetita (34%), piroxeno (10%) y anfíbol (5%), contribuyen a su distintiva coloración grisácea oscura. Fragmentos de rocas metamórficas y volcánicas también son abundantes en el depósito (25%), mientras minerales como cuarzo (14%) feldespatos (9%) y micas (2%) muestran baja concentración. Minerales trazas como zircón, esfeno, olivino y hematita también fueron observados ocupando cerca del 1% de las muestras. Aunque el depósito fluvial del 2023 muestra similar mineralogía que el depósito de tsunami del 2010, este último muestra una coloración más rojiza debido a que ciertos minerales han sufrido continua oxidación.

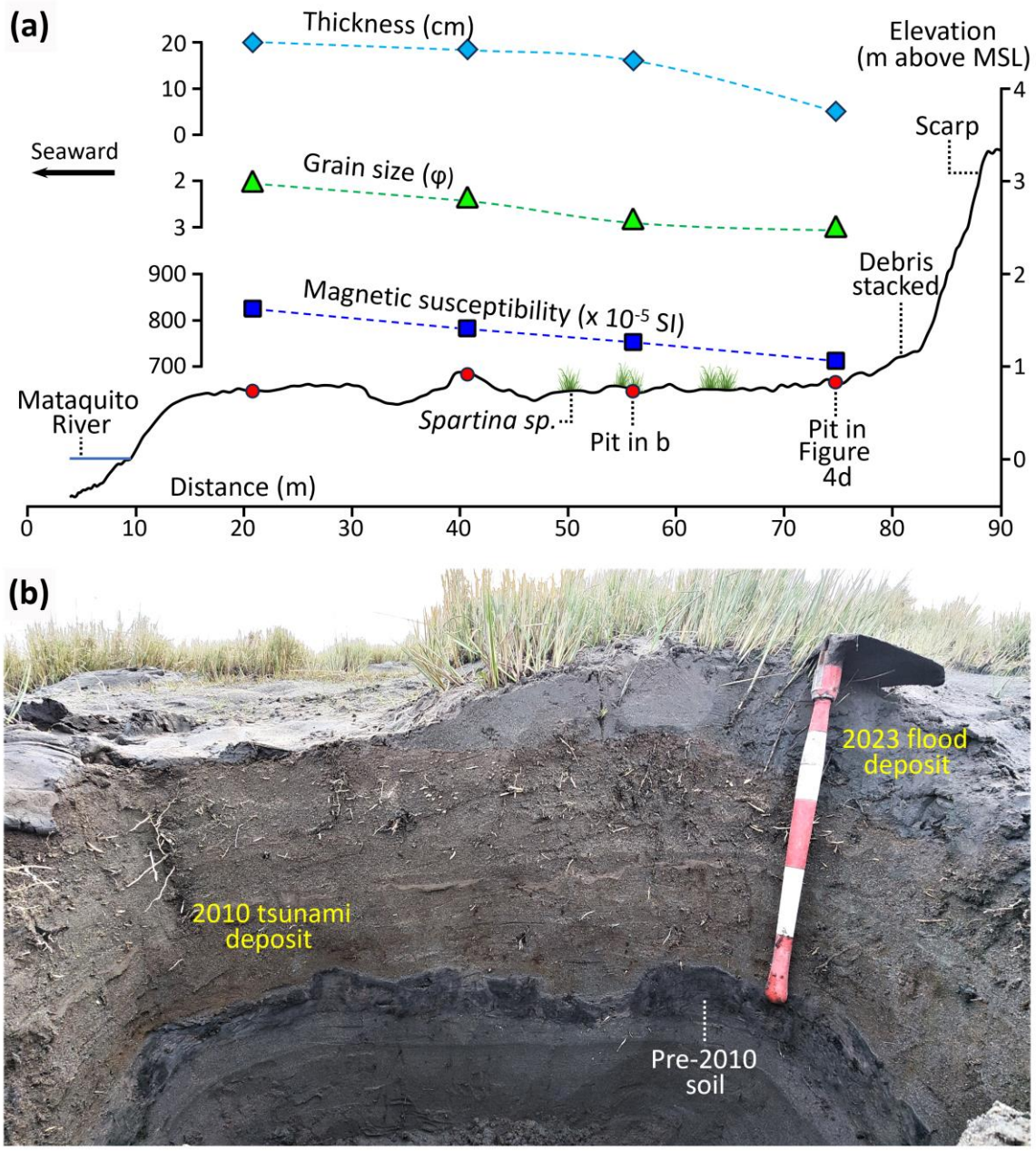

Figura 3.5. Perfil y fosa principal mostrando la estratigrafía del sector. (a) Perfil perpendicular al Río Mataquito (ver Figura 3.4b) mostrando la tendencia decreciente tierra adentro del espesor, tamaño de grano y susceptibilidad magnética del depósito de arena. (b) Fosa mostrando tanto el depósito de tsunami del 2010 como el depósito de inundación del 2023. Ambos depósitos difieren en su color debido a que el depósito de tsunami se encuentra mayormente oxidado en comparación al reciente depósito de inundación. Notar el contacto basal erosivo del depósito de tsunami, mientras que este no es evidente en la base del depósito de inundación. Parte del depósito de inundación en superficie ha sido notoriamente pisoteado, siendo su espesor original mayormente preservado en sitios de abundante vegetación. Barras de colores de la pala miden 10 cm.

Estructuras sedimentarias distintivas no fueron observadas en el depósito fluvial del 2023. La capa de arena depositada por el Río Mataquito es mayormente masiva, sin evidentes laminaciones ni gradación. El contacto basal del depósito es abrupto; sin embargo, rastros de erosión en la superficie del suelo subyacente fueron poco comunes.

Al igual que el depósito de tsunami, el depósito fluvial del 2023 se caracteriza por ensambles mezclados de diatomeas, prevaleciendo ligeramente las especies marinas. Especies salobres como *Cocconeis placentula*, *Navicula cryptocephala* y *Navicula gregaria* presentan la menor abundancia, cercana al 18%. Especies de agua dulce, las cuales son mayoritariamente epifíticas (e.g., *Ulnaria ulna*, *Nitzschia palea* y *Nitzschia amphibia*), alcanzan una abundancia de 37%. Especies marinas predominan en el depósito con un 45% de abundancia, especialmente especies planctónicas como *Paralia sulcata*.

3.5 Discusión

3.5.1 Depósitos similares, orígenes diferentes

Un problema crítico en la desembocadura del Río Mataquito, y probablemente también en otras desembocaduras de ríos andinos, es que inusuales crecidas fluviales pueden crear un engañoso registro de tsunamis (Figura 3.6a,b). Durante el trabajo paleosismológico conducido en mayo del 2023 en la costa de Chile central, se estudiaron tres capas de arena preservadas bajo la planicie de inundación del Río Mataquito, las cuales fueron interpretadas preliminarmente como antiguos depósitos de tsunami. Esta inferencia fue fuertemente apoyada por la reciente ocurrencia del tsunami del 2010 y su extenso depósito de arena que cubrió la mayoría de los terrenos bajos en el área (Garret et al., 2013; Lario et al., 2016; Saldaña et al., 2025a). Adicionalmente, los registros escritos reportan al menos tres grandes tsunamis en Chile central que probablemente fueron comparables o incluso mayores al evento del 2010: en 1730, 1751 y 1835 (Montessus de Ballore, 1912; Lomnitz, 2004; Udías et al., 2012; Stewart, 2019). Basado en esta evidencia fue razonable interpretar que las capas de arena encontradas en el Río Mataquito fueron dejadas

por los predecesores del tsunami del 2010. Sin embargo, la inundación fluvial de junio del 2023 demostró que crecidas de grandes ríos andinos también son capaces de dejar un depósito de arena similar a los dejados por tsunamis (Figura 3.4a,d).

Fue notado que tanto el depósito de tsunami como el depósito fluvial comparten similares características que los hacen virtualmente indistinguibles. Ambos depósitos no solo mostraron similar morfología, granulometría, mineralogía y susceptibilidad magnética, sino que también similares tendencias de adelgazamiento y afinamiento tierra adentro, probablemente explicadas por desaceleración del flujo en ambos casos (Spiske, 2020). Tales similitudes provenientes desde análogos modernos implican que resultaría difícil diferenciar entre un depósito de tsunami y un depósito de río desde el registro estratigráfico, conduciendo probablemente a malinterpretaciones.

El análisis de los ensambles de diatomeas tampoco asistió en la diferenciación de ambos depósitos. Intuitivamente se podría suponer que depósitos de tsunami tienen una mayor concentración de diatomeas marinas en comparación con depósitos de río, sin embargo, tanto el depósito de tsunami del 2010 como el depósito fluvial del 2023 mostraron similares ensambles. Ambos depósitos son dominados por diatomeas marinas (>40%), destacando la abundancia de la especie planctónica *Paralia sulcata*. Diatomeas marinas y salobres encontradas en el depósito fluvial del 2023 probablemente provienen desde el estuario y la superficie de la marisma, las cuales fueron también incorporadas en el depósito de tsunami del 2010 (Garret et al., 2013).

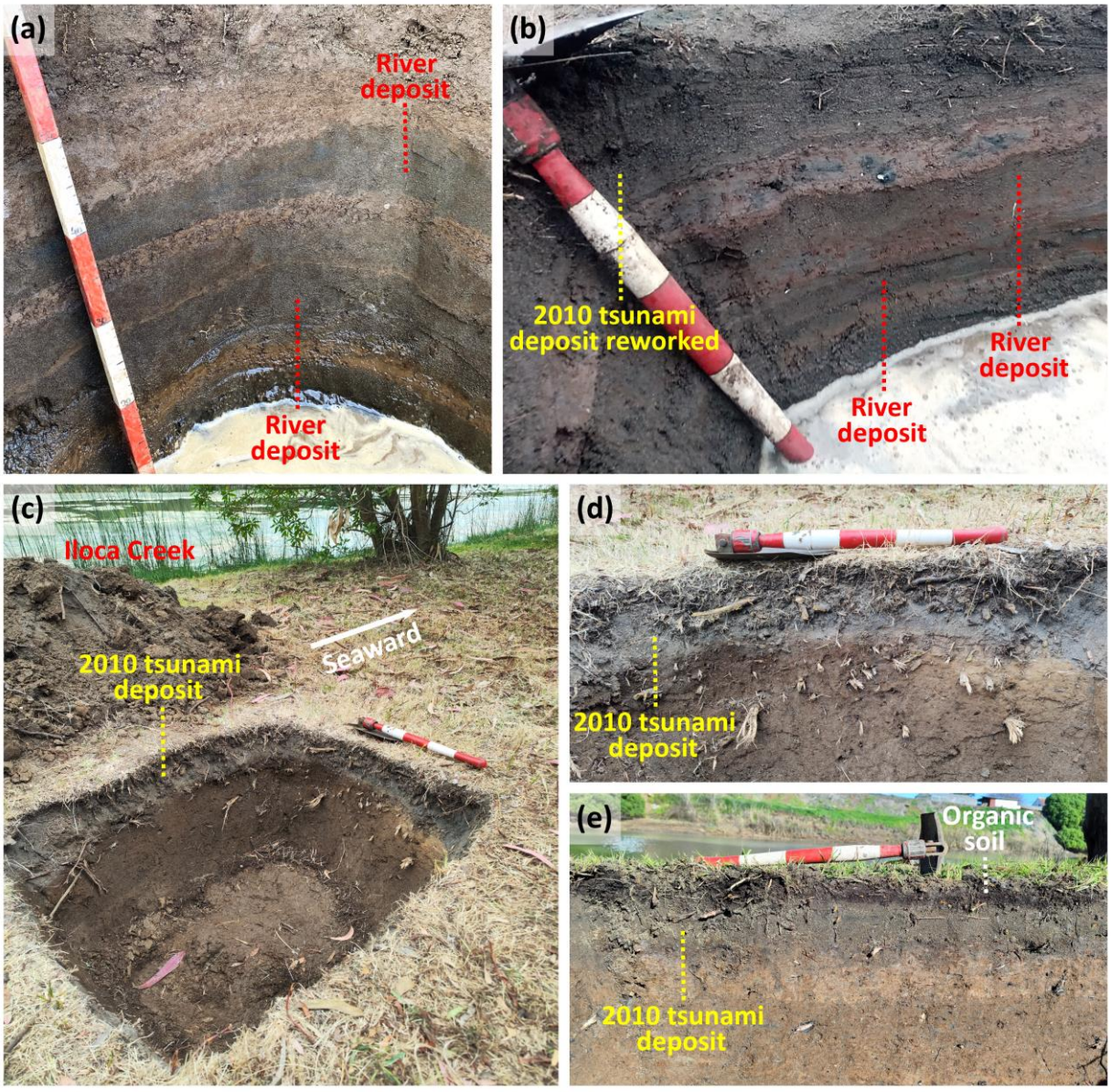

Figura 3.6. Fotografías mostrando las similitudes entre depósitos de río y depósitos de tsunami. (a) y (b) muestran depósitos de arena probablemente asociados a inusuales crecidas del Río Mataquito en las inmediaciones de su desembocadura (en rojo). Estos fueron inicialmente interpretados como depósitos de tsunami debido a sus similitudes con el depósito de tsunami del 2010 (en amarillo). (c-d) muestran el depósito de tsunami del 2010 preservado en el Estero Iloca. Barras de colores de la pala y la regla miden 10 cm.

3.5.2 Diferencias claves entre ambos depósitos

A pesar de las limitaciones mencionadas para discriminar entre un depósito de tsunami y un depósito de río, dos criterios observables, aunque no siempre presentes, podrían ser considerados para asistir en una posible diferenciación. Primero, diferencias en el contacto basal de ambos depósitos. Mientras el contacto basal del depósito de inundación del 2023 mostró limitados rasgos de erosión, el contacto basal del depósito de tsunami del 2010 fue marcadamente erosivo. Adicionalmente, pequeños *rip-up clast* fueron observados integrando exclusivamente el depósito de tsunami, sugiriendo una fuerte erosión del suelo subyacente. Esto puede deberse a la alta velocidad de flujo alcanzada por un tsunami (Spiske, 2020), la cual puede ser mucho mayor en comparación con la velocidad de inundación de un río. Sin embargo, los depósitos de tsunami no siempre mostraran un contacto basal erosivo, pudiendo a menudo estar ausentes hacia tierra y en especial cerca del límite de inundación, donde la velocidad de flujo disminuye a valores mínimos que impiden la erosión. Segundo, diferencias en la extensión hacia tierra de ambos depósitos. Mientras el depósito del Río Mataquito se extiende por solo ~70 m tierra adentro, hasta la base de un pequeño escarpe, el depósito de tsunami del 2010 se extiende por cerca de 500 m tierra adentro, hasta la base del acantilado costero (Fritz et al., 2011; Vargas et al., 2011; Garret et al., 2013). Los tsunamis tienen el potencial para alcanzar mayores distancias tierra adentro, sin embargo, esto depende fuertemente de la magnitud del evento y factores locales, tales como la topografía y la pendiente del terreno (Cheng y Weiss, 2013; Abe et al., 2020; Saldaña et al., 2025a; Yamashita et al., 2025).

Basado en estos dos criterios, el contacto basal erosivo y la extensión tierra adentro, los depósitos de arena preservados en el registro sedimentario del Río Mataquito probablemente estén asociados a crecidas del río más que a eventos de tsunami (Figura 3.6a,b). Los tres depósitos de arena que fueron atribuidos preliminarmente a tsunamis no muestran claros signos de erosión basal ni una amplia extensión. De hecho, estos no se extienden más allá del escarpe que limitó la inundación fluvial del 2023. A su vez, ninguna otra capa de arena en este sitio mostró un contacto basal

erosivo, siendo un rasgo exclusivo del depósito de tsunami del 2010. Probablemente uno de estos depósitos de arena corresponda a la inundación causada por el Río Mataquito en 2008 (Figura 3.2b), la cual produjo en Licantén similares efectos a los reportados en 2023 (CIGIDEN, 2023).

3.5.3 Implicancias para el estudio de depósitos de tsunami

Este trabajo plantea una dificultad para el estudio de depósitos de tsunami, la cual hasta ahora no había sido abordada en detalle. Previos estudios se han enfocado solamente en la identificación de criterios claves para distinguir entre depósitos de tsunami y de tormenta, concluyendo que varios criterios pueden ser considerados útiles, pero no diagnósticos (Kortekaas y Dawson, 2007; Morton et al., 2007; Engel y Brückner, 2011; Goff et al., 2012; Phantuwongraj y Choowong, 2012; Ramírez-Herrera et al., 2012; Shanmugam, 2012; Kongsen et al., 2022). Adicionalmente, se ha argumentado que solo integrando múltiples fuentes de evidencia, tales como estratigráfica, sedimentológica y paleontológica, es posible diferenciar apropiadamente el origen de los depósitos (Goff et al., 2012; Kongsen et al., 2022). Sin embargo, la ocurrencia del evento del 2023 y su depósito de arena no solo demuestra que otras variables fluviales pueden estar involucradas, sino que pone en evidencia que incluso la utilización de múltiples enfoques puede ser insuficiente. Alternativamente, *proxies* geoquímicos, los cuales no fueron utilizados en este estudio, podrían ayudar a una mejor diferenciación entre fuentes de sedimentos marinas y continentales (Chagué-Goff, 2010; Araya et al., 2022; 2024).

En Chile, sitios cercanos a desembocaduras de ríos andinos han sido utilizados con frecuencia para el estudio de depósitos de tsunami (Ely et al., 2014; Hong et al., 2016; Aedo et al., 2021; Hocking et al., 2021; Easton et al., 2022; Araya et al., 2022; 2024). Esto debido a que son lugares bajos y de fácil acceso, además de preservar, usualmente, un buen registro de eventos extremos. Adicionalmente, varios trabajos conducidos en estos sitios han aplicado distintos criterios para probar una depositación por tsunami, como por ejemplo la extensión lateral, múltiples fuentes de sedimento, adelgazamiento tierra adentro, anómalas diatomeas marinas y

coincidentes cambios del nivel del terreno acompañando a los depósitos (Hong et al., 2016; Aedo et al., 2021; Hocking et al., 2021). Sin embargo, los hallazgos proporcionados por este estudio sugieren que solo este último podría ser un criterio realmente convincente para un origen por tsunami con fuente en la zona de subducción. Aun así, debido al mezclado registro existente en desembocaduras de ríos andinos, estos sitios debieran ser preferentemente evitados como blancos de exploración o, al menos, ser tratados con especial precaución al momento de interpretar el origen de los depósitos.

Estos evidentes problemas observados en la desembocadura del Río Mataquito son inexistentes en pequeños cursos de agua como esteros y canales. A diferencia de los grandes ríos provenientes desde la Cordillera de los Andes, los cuales transportan importantes volúmenes de agua y arena, los esteros con fuente en la Cordillera de la Costa transportan poca agua y sedimentos finos y claros que contrastan con cualquier depósito de tsunami. En el Estero Iloca, ~2 kilómetros al norte de la desembocadura del Río Mataquito (Figura 3.1c), Saldaña et al. (2025a) reportaron el depósito de tsunami del 2010 como una capa de arena grisácea distintiva, la cual contrastaba notoriamente con los sedimentos subyacentes y el superior suelo orgánico (Figura 3.6c-e). Adicionalmente, estos autores no reportaron ninguna otra capa de arena en el área, implicando que el evento del 2023 no fue registrado. Esto demuestra que la configuración depositacional es crucial para la interpretación de depósitos de tsunami (Shanmugam, 2012), siendo sitios de baja energía mejores registradores de eventos extremos.

En definitiva, la ocurrencia del evento del 2023 nos condujo a reinterpretar los depósitos de arena encontrados en la desembocadura del Río Mataquito como originados por previas crecidas fluviales, las cuales son mucho más frecuentes en el área que eventos tsunamigénicos. Probablemente, futuras y precisas dataciones aplicando conocidas técnicas de luminiscencia (OSL), las cuales han sido utilizadas exitosamente en ambientes costeros (e.g., Tamura et al., 2019), proporcionaran asistencia en discernir el origen de los depósitos.

3.6 Conclusiones

El depósito de arena dejado por la reciente inundación del Río Mataquito en 2023 demostró que crecidas de ríos andinos son capaces de dejar un registro geológico similar al originado por tsunamis, complejizando aún más los estudios paleosismológicos. Tanto el depósito de inundación del 2023 como el depósito de tsunami del 2010 presentaron similar arquitectura, granulometría, mineralogía, susceptibilidad magnética y ensambles de diatomeas, resultando casi indistinguibles. Evidentes similitudes entre estos dos análogos modernos destacan los desafíos que implicaría diferenciar entre ambos desde el registro estratigráfico, conduciendo probablemente a interpretaciones erróneas. Los hallazgos proporcionados por este estudio sugieren que las desembocaduras de ríos andinos no son lugares apropiados para la búsqueda de depósitos de tsunami, ya que en estos sitios confluyen múltiples fuentes de sedimento que dan origen a un mezclado registro. En contraste, sitios menos dinámicos, tales como esteros o canales, son mejores registradores de tsunamis y, por tanto, deberían ser preferidos.

Capítulo 4. Paleoseismological evidence of a century of coastal deformation in central Chile: lasting emergence and ongoing submergence

Saldaña, B., Cisternas, M., Carvajal, M., Melnick, D., Cortés-Aranda J., Francois, J.P., Carreño, A. & Guerra, M. (2025b). Paleoseismological evidence of a century of coastal deformation in central Chile: lasting emergence and ongoing submergence. Quaternary Science Advances, 19, 100291. Available from: https://doi.org/10.1016/j.qsa.2025.100291

Abstract

Understanding vertical deformation associated with cycles of great megathrust earthquakes is crucial for assessing coastal hazards and advancing in our knowledge of tectonic processes in subduction zones. However, this requires long datasets that extend beyond the era of space geodesy. Here, we use paleoseismological evidence, including lithological and paleoecological data, from a former coastal lagoon in central Chile to reconstruct land-level changes during the 20th century, spanning two great (M ≥ 8) megathrust earthquakes in 1906 and 1985. Diatom and seed assemblages across an abrupt lithological change from mud to peat recorded a sudden relative sea level (RSL) fall in the early 20th century. This environmental shift correlates with the disappearance of the lagoon between 1904 and 1914 as documented in historical maps, revealing an emergence event most likely associated with ~0.7 m of coseismic uplift in 1906. For the following eight decades, diatoms suggest relatively stable RSL conditions, implying that the coast remained emerged. This is partially supported by the record of a nearby tide gauge showing relatively stable RSL between 1944 and the mid-1980s. Around the time of the 1985 earthquake, both diatoms and tide gauge records suggest the onset of a gradual RSL rise. The inferred long-term trend aligns with modern GPS measurements showing persistent coastal subsidence since 1997 until today. This multiproxy RSL history reveals a more complex vertical deformation

pattern than previously assumed in the central Chile subduction zone, with subsidence starting eight decades after sustained post-1906 uplift. Our findings provide key insights into the vertical deformation cycles of great subduction zone earthquakes in central Chile and elsewhere.

Keywords

Land-level changes, lasting emergence, diatoms, central Chile, megathrust earthquakes, environmental change

4.1 Introduction

Coasts adjacent to subduction zones have repeatedly experienced vertical changes during and between earthquakes, causing abrupt environmental and social impacts. Metric-scale coastal uplift and subsidence has accompanied recent earthquakes in Chile (e.g., Plafker and Savage, 1970; Farías et al., 2010), Alaska (e.g., Plafker, 1965; 1969), Sumatra (e.g., Meltzner et al., 2006; Subarya et al., 2006) Mexico (e.g., Cosenza-Muralles et al., 2022) and Japan (e.g., Ozawa et al., 2011; Nishimura, 2014). For example, both the mainland coast of southern Chile and Alaska subsided about 2 m during the great 1960 (Mw 9.5) and 1964 (Mw 9.2) earthquakes, respectively, resulting in the abrupt lowering of forests and marshes into the intertidal zone (Plafker, 1965; 1969; Plafker and Savage, 1970; Shennan et al., 1999). Such coseismic vertical deformation is traditionally thought to be followed by years to decades of gradual opposite motion, driven by afterslip, viscoelastic mantle relaxation and interseismic plate locking (Wang et al., 2012). Indeed, regions that subsided during the 1960 Chile and 1964 Alaska earthquakes were raised several decimeters in the subsequent decades as result of these processes (Brown et al., 1977; Barrientos et al., 1992; Luo and Wang, 2021). Most recently, coseismic subsidence caused by the 2011 Tohoku-oki earthquake (Mw 9.0) on the northeastern coast of Japan was followed by gradual postseismic uplift continuing for more than a decade (Nishimura, 2014; Iinuma, 2018). However, coseismic land-level changes associated with some large earthquakes, such as the 1995 Antofagasta (Mw 8.0) and 2007 Tocopilla (Mw 7.7) events in northern Chile, have not experienced an evident

recovery phase (Melnick, 2016; González-Alfaro et al., 2018), emphasizing that vertical deformation patterns are still poorly understood.

Modern geodetic instrumentation has substantially improved the monitoring of vertical deformation changes during subduction earthquake cycles (Wang et al., 2012). However, our knowledge still remains limited because such geodetic datasets, which span only a few decades, are unable to capture land-level changes throughout complete seismic cycles associated with earthquakes of different magnitudes and depths. This limitation has spurred complementary, non-instrumental approaches able to extend deformation records beyond the instrumental period (e.g., Zong and Horton, 1999; Sawai et al., 2004; Sieh et al., 2008; Garret et al., 2013; 2015; Wesson et al., 2015).

Among these approaches, stratigraphic and biostratigraphic evidence from coastal sediments allows to quantify vertical deformation (Pilarczyk et al., 2014; Dura et al., 2016a). Information recorded in coastal sediments bordering subduction zones has guided numerous paleoseismological studies, allowing to extend the earthquake record over centuries to millennia (e.g., Atwater, 1987; Nelson et al., 1996). Abrupt land-level changes are usually represented by sharp lithologic changes and associated shifts in microfossil assemblages (e.g., diatoms, foraminifera and pollen) revealing sea level fluctuations (Nelson et al., 1996; Pilarczyk et al., 2014; Shennan et al., 2014; 2016; Horton et al., 2017). Particularly, diatoms, which are sensitive to environmental factors such as salinity and tidal exposure, have proven to be valuable indicators of relative sea-level (RSL) changes resulting from seismo-tectonic land-level changes (Hemphill-Haley, 1995; Atwater and Hemphill-Haley, 1997; Dura et al., 2015; 2016a; Garret et al., 2015). For example, multiple episodes of late Holocene coseismic subsidence along the Alaska-Aleutian megathrust, including that from the 1964 earthquake, were recorded in marshes by sharp lithological and diatom changes (Shennan et al., 1999; Hamilton et al., 2005; Hamilton and Shennan, 2005a; Shennan and Hamilton, 2006). Additionally, diatoms have proven to be sensitive to more subtle, interseismic land-level changes, making them a powerful paleoseismological

tool (Shennan et al., 1999; Sawai et al., 2004; Hamilton and Shennan, 2005b; Dura et al., 2015).

Here, we use lithological and paleoecological evidence from a coastal site in central Chile to reconstruct a century of land-level changes. We complement this stratigraphic source with former maps, historical reports, and tide gauge and satellite geodesy records. Our reconstruction suggests that sudden uplift, caused by the large 1906 earthquake, was followed by little to no vertical change until the 1985 earthquake, when gradual subsidence began. It had resulted from temporal variations of interplate slip. These results will provide constraints for assessing the performance of deformation models and contribute to a better understanding of the behavior and rheological structure of subduction zones.

4.2 Regional setting

4.2.1 Great historical earthquakes in central Chile

Chile is frequently affected by megathrust earthquakes as result of the convergence between the Nazca and South American plates at a rate of ~65 mm/year (Figure 4.1a; Jarrin et al., 2023). Particularly, the central zone of Chile (~32° - 34° S; Figure 4.1b), which hosts most of the country's population and has one of the most complete earthquake records since the Spanish arrival in 1541, has been regularly struck by great (M>8) megathrust earthquakes every ~85 years (Nishenko, 1985; Comte et al., 1986). Four great megathrust earthquakes have affected central Chile in historical times, in 1730 (M>9), 1822 (M8-8.5), 1906 (M8-8.5) and 1985 (M8) (Montessus de Ballore, 1912; Lomnitz, 2004; Carvajal et al., 2017a; Ruiz and Madariaga, 2018). Additionally, several smaller, intercalated M<8 events like that of 1971 complicate the seismic sequence (Eisenberg et al., 1972; Malgrange et al., 1981; Korrat and Madariaga, 1986). The 1730 earthquake is considered the largest in the historical sequence due to the extent of the building damage and the resulting large tsunami in both the near- and far-field (Udías et al., 2012; Urbina et al., 2016; Carvajal et al., 2017a). In contrast, building damage was less extensive in 1822, 1906 and 1985, and the accompanying tsunamis were much smaller. Also, although coastal land-level

changes were rarely reported for the 1730 event, they were among the most conspicuous effects during the 1822, 1906, and 1985 earthquakes (Graham, 1824; Steffen 1907a, b; IGM, 1985; Castilla, 1988). Therefore, despite a roughly regular recurrence interval of about eight decades, differences in the extent of reported shaking, land-level changes and tsunamis suggest that these earthquakes varied sharply in size and source.

4.2.2 The 1906 earthquake

The 16 August 1906 earthquake appears to be the second largest historical event in the seismic sequence of central Chile after the 1730 earthquake in terms of rupture extent. Severe damage extended latitudinally along 500 km between Illapel (31.7°S) and Cauquenes (36°S), causing more than 3800 casualties (Figure 4.1b; Montessus de Ballore, 1915; Carvajal et al., 2017b). A rupture length of about 350 km between Los Vilos and Llico was estimated by Nishenko (1985), overlapping with the recent 2010 and 2015 earthquakes to the south and north, respectively (Figure 4.1b; Moreno et al., 2012; Tilmann et al., 2016). A small, non-destructive tsunami was locally reported (Soloviev and Go, 1984). Uplift was well reported along the coast between Los Vilos (31.9°S) and Constitución (35.3°S), with Campiche, our study area, in between (Figure 4.1b; Steffen, 1907a, b; Machado, 1909; Harnecker, 1914; Montessus de Ballore, 1915). Uplift amount varied along the coast, with estimates of about 0.6 m between Concón and Valparaíso (20 km south of Campiche), and at least 0.8 m between Zapallar and Horcón (5 km north of Campiche), the two closest sites to our study area (Figure 4.1c). Carvajal et al. (2017b; 2019) showed that all the above effects are best explained by a megathrust rupture beneath land, favoring the uplift of the coast instead of the seafloor. Additionally, they estimated a moment magnitude between 8.2 and 8.5 for this historical earthquake.

4.2.3 The 1985 earthquake

The 3 March 1985 earthquake is the most recent and perhaps smallest event in the seismic sequence of central Chile. Compared to its predecessor in 1906, the greater damage in 1985 was concentrated in a coastal strip of only 150 km (Comte et al.,

1986), between Quintero (32.7°S) and Matanzas (34°S; Figure 4.1b). The area of aftershocks extended between Quintero and Pichilemu (Comte et al., 1986), abutting to the south with the 2010 earthquake rupture (Moreno et al., 2012). Coastal uplift of 0.1 to 0.6 m was observed between Valparaíso (33°S) and south of San Antonio (33.9°S; IGM, 1985; Plafker, 1985; Comte et al., 1986; Kausel, 1986; Castilla, 1988). A minor tsunami was triggered with maximum amplitudes of less than a meter recorded at the Valparaiso tide gauge (Carvajal et al., 2019). Slip distributions from geodetic and/or seismic inversion models suggest a maximum slip of ~3 m and moment magnitude between 7.8 and 8.0 (Mendoza et al., 1994; Barrientos, 1988; 1997; Bravo et al., 2019). Most of these models propose a rupture propagating under the coast between south of Quintero Bay and San Antonio (Figure 4.1b,c).

4.2.4 The Campiche lowland

The Campiche lowland is located about 2 m above mean sea level (MSL) in the densely industrialized Quintero Bay, immediately adjacent to oil and natural gas terminals, a large copper smelter, thermoelectric plants and port infrastructure active since the 1960's (Figures 4.1d and 4.2a). The emissions of pollutants resulting from such intense industrial activity have been imprinted in the surface sediments of the area, transforming it into a zone of environmental sacrifice (Gayo et al., 2022).

A coastal cliff up to 80 m in height, exposing Plio-Pleistocene rocks covered by Late Pleistocene paleodunes (Carrillo-Briceño et al., 2013; Flores-Aqueveque et al., 2021; García et al., 2019; Rivano et al., 1993), delimits the Campiche lowland. To the west, Campiche is bounded by the active coastal dune and a large copper smelter slag pile (Figure 4.2a). The lowland is dissected by the Puchuncaví Creek, which drains a 110 km2 watershed incised in the western flank of the Coastal Range. Freshwater vegetation extensively covers the surface of the plain (Figure S1a), whereas small, scattered water bodies, such as the Campiche and Los Maitenes wetlands, are restricted to peripheral locations (Figure 4.2a). These wetlands may be remnants of a former coastal lagoon in the area (Figure 4.3).

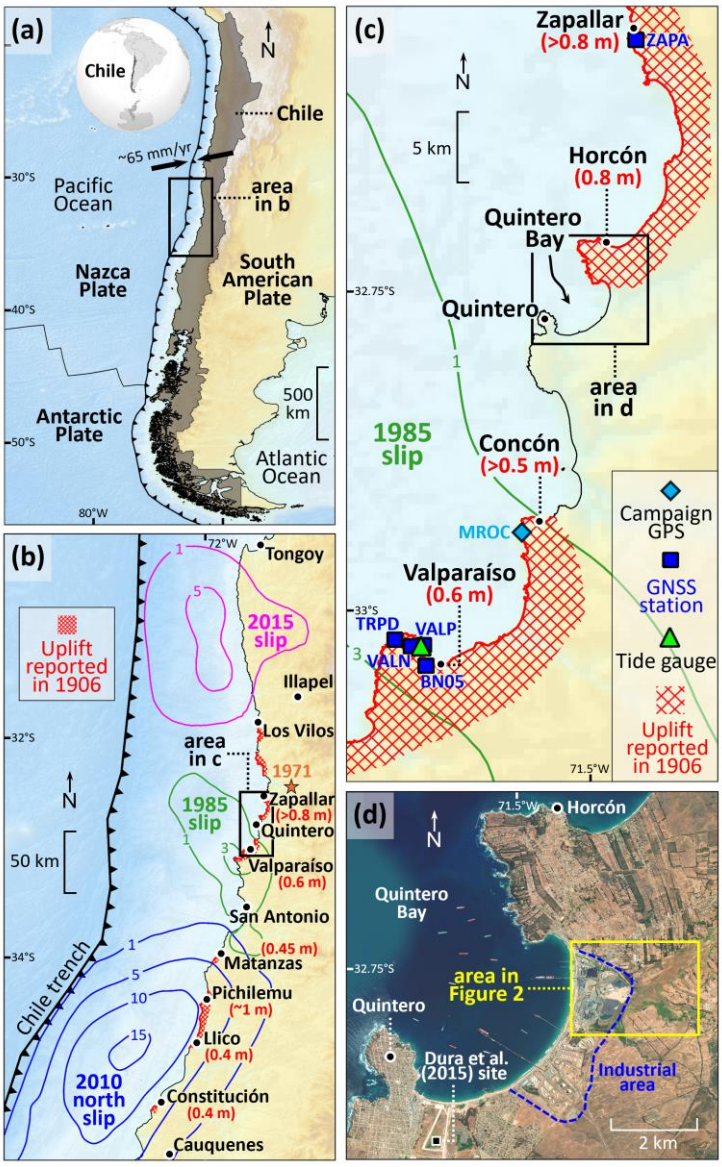

Figure 4.1. Index maps. (a) Plate-tectonic setting of Chile in southwestern South America. The black barbed line marks the seaward edge of the subduction zone between the Nazca and South American plates. Paired arrows indicate the rate of convergence between both plates (Jarrin et al., 2023). (b) Slip contours (m) of recent great earthquakes in central Chile (Moreno et al., 2012; Tilmann et al., 2016; Bravo et al., 2019). For the 1971 event only the epicenter is shown (orange star from Malgrange et al., 1981). Red hatched areas mark locations where coastal uplift was reported after the 1906 earthquake. Uplift magnitudes are given in parentheses (Steffen, 1907a, b; Machado, 1909; Harnecker, 1914; Montessus de Ballore, 1915). (c) Uplift reported 1906 near our study site. The five GNSS stations, the campaign GPS benchmark, and the Valparaiso tide gauge, whose records were used in this study, are shown. Note that the northern limit of the proposed 1985 earthquake rupture by Bravo et al. (2019) lies south and offshore of Quintero Bay. (d) Detail of Quintero Bay showing its dense industrial development and the site of Dura et al. (2015).

4.3 Material and methods

4.3.1 Fieldwork

We studied the Campiche stratigraphy through 30 hand-driven cores and 7 vibracorer slices recovered between October 2023 and December 2024 (Figures 4.2a and S1). Coring elevations were tied to local MSL using a dGPS and a tidal datum of the Hydrographic and Oceanographic Service of the Chilean Navy (SHOA) at Quintero. We focused on the surficial stratigraphy, including a sharp lithologic contact of peat over inorganic mud that lies about 32 cm depth (Figures 4.2b and 4.4). Detailed lithologic descriptions were made in the field and complemented with further laboratory analysis (Figure S1).

4.3.2 Diatom analysis

To reconstruct the history of RSL changes and paleoenvironments at Campiche we analyzed fossil diatoms preserved in the sediments. Following the procedures described by Dura and Hemphill-Haley (2020), we sampled 2 cores and 4 slices that showed minimal signs of disturbance at 2 to 3 cm vertical intervals. A minimum of 300 diatom valves were counted for each sediment sample, which were identified to the species level under a microscope with 1000x magnification. A total of 90 species in the 101 samples analyzed were identified and classified by salinity preference (freshwater, brackish, and marine) and life form (benthic, epiphytic, and planktonic). Identification and classification was made using local (Dura et al., 2015), regional (Horton et al., 2011; Chagué-Goff et al., 2015; Dura et al., 2017; Hocking et al., 2017; Sawai et al., 2017), and global (Vos and de Wolf, 1988; 1993; Denys,1991; Hemphill-Haley, 1993; Van Dam et al., 1994; Sawai et al., 2004; Hassan et al., 2009; Zong and Sawai, 2015; Spaulding et al., 2021; DePaolis et al., 2024) references.

Land-level changes at Campiche were inferred from RSL diatom reconstructions. We restricted our results to qualitative reconstructions as the absence of published modern diatom assemblages in central Chile precluded the use of transfer functions and other quantitative methods. Nevertheless, we used the ratio of brackish and marine to freshwater diatoms to infer RSL changes (Figure 4.5d), which was

successfully applied at a nearby site (Dura et al., 2015; Figure 4.1d). A decrease in this ratio indicates a RSL fall (emergence), whereas an increase indicates a RSL rise (submergence).

Using the CONISS program (Grimm, 1986), we applied a stratigraphically restricted cluster analysis to diatom samples to identify similar species associations between adjacent samples. The cluster analysis was made using the method of incremental sum of squares and considering only diatoms with abundance above 5% in at least a sample to minimize the statistical influence of insignificant taxa (Figures 4.4, S3 and S4; Table S1).

4.3.3 Organic matter and seed records

Organic matter content was obtained by the loss on ignition method for 25 samples spaced vertically every 2 cm from slice SL-3 (Figure S5). Following the methods of Dean (1974), the organic matter content was estimated by weight loss after burning each sample to 550°C.

We also determined the presence and abundance of *Schoenoplectus californicus* seeds. Because this emergent aquatic plant belonging to the Cyperaceae family is indicative of salt-tolerant environments (e.g., Ramírez and Añazco, 1982; Atwater et al., 1992), its presence and relative abundance provides support for our diatom ecological interpretations. For the analysis, a sediment volume of 10 cm^3 for each sample was wet sieved to remove large plant debris. The resulting fine fraction was observed under a binocular stereoscopic microscope, where all the *S. californicus* seeds were counted to obtain their concentration (Figure 4.5c). Other seeds with lower abundance, mainly belonging to grasses, were used for ecological interpretations but were not counted.

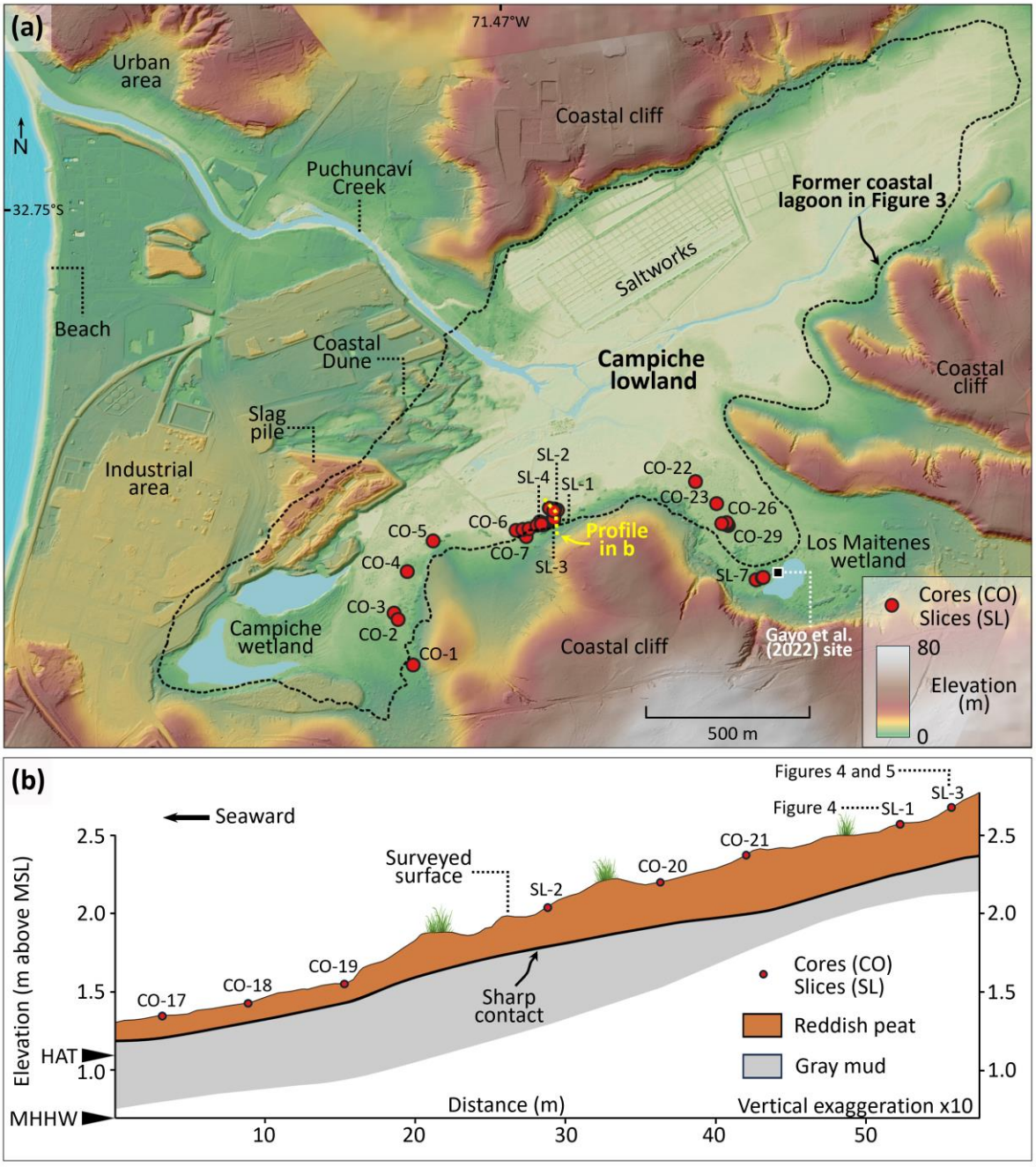

Figure 4.2. Campiche lowland fringing Quintero Bay. (a) Digital terrain model (DTM) of Campiche derived from LiDAR data. The dashed line outlines the extent of the former coastal lagoon according to old maps (see Figure 4.3). Thirty sediment cores and seven vibracorer slices were collected from the southern margin of the former lagoon (red dots). The core site of Gayo et al. (2022), from which our age model was transferred, is located southeast in the Los Maitenes wetland. (b) Stratigraphic cross-section through our site. The underlying mud layer thins inland, while the overlying peat layer thickens. Elevations are relative to mean sea level (MSL). Tidal datums shown on the vertical axis include Mean Higher High Water (MHHW: ~0.7 m) and Highest Astronomical Tide (HAT: ~1.1 m).

4.3.4 Chronology using ^{210}Pb and pine pollen

To provide a time frame for our stratigraphy, we used two approaches, including a ^{210}Pb chronology previously reported for the site and a temporal marker based on the presence of pollen of an introduced tree species.

The isotope chronology is provided by ^{210}Pb ages previously obtained from a core taken near our sampling site for a study of environmental pollutants (Gayo et al., 2022). The core was taken about 0.6 km from our slice SL-3, within the Los Maitenes wetland (Figure 4.2a). To correlate stratigraphically the core with our slice, we relocated the site with the guidance of JPF, coauthor of the previous and present study. There, we shoveled a pit (Figure S2), recovered the slice SL-7 (Figure 4.2a) and described the stratigraphy. Because both stratigraphies turned out to be almost identical (Figure 4.5a,b), we transferred the ^{210}Pb age model to our slice stratigraphy.

Pine pollen was analyzed to provide a further check of the transferred ^{210}Pb chronology and to constrain the age of the sediments as proposed by Cisternas et al. (2001; 2017) for south-central Chile and by Frugone-Álvarez et al. (2017) for central Chile. Pine trees were first introduced in Chile at the end of the 19th century, when *Pinus radiata*, native from California (USA), was planted in south-central Chile in 1885 (Aztorquiza, 1929; Donoso and Lara, 1996; Vargas et al., 2017). In the early 20th century, pine tree plantations spread throughout the country as a national government policy to control soil erosion and provide timber (Contesse, 1987). Later, from 1974 onwards there was a massive growth of planted hectares due to the enactment of the economic incentive law to encourage afforestation (Maestripieri et al., 2017). About 1.5 million hectares of pine trees were planted between 1975 and 2007, accounting for 65% of the total planted area (INFOR, 2008). Because this history makes pine pollen in central Chile no older than the 1900s, the Campiche deposits of about that age should contain the deepest *P. radiata* pollen (Figure 4.5c). Additionally, sediments from the mid-1970s onwards should contain much more pollen than before. Accordingly, we looked for pine pollen along the stratigraphy of slice SL-3, analyzing a total of 25 samples (2 cm^3 sediment volume) following Faegri and Iversen

(1989) to extract pollen grains. Lycopodium tablets were added for calculating pollen concentration (grains/cm^3; Stockmarr, 1971). Pollen grains were identified and quantified under a microscope (400x and 1000x magnification) using Heusser (1971) and a local reference pollen collection (UPLA). Pollen counts include >300 terrestrial pollen grains excluding paludal taxa. Pollen of other species was recognized, but not counted, throughout the whole slice SL-3 to check that the absence of *P. radiata* pollen at depth was not the result of post-depositional decay of pollen grains.

4.3.5 Historical maps

To support our ecological interpretations and chronology, we examined seven hydrographic maps of Quintero Bay from 1803 to 1930 and a 1954 aerial photograph (Figure 4.3). This graphic information is complemented by detailed reports from contemporary naturalists and scholars. Relevant information of the maps, such as sources and scales, is provided in the Supporting Information in Anexo 2 (Table S2).

4.3.6 Tide gauge and geodetic observations

The record of the Valparaiso tide gauge, which is located 30 km south of Campiche, was used for comparison with our RSL history reconstruction. The complete record extending from 1944 to 2025 was provided by SHOA, with only a data gap of 11 years between 1971 and 1982. Following the approach described in the Supporting Information we estimated the two linear trends of RSL shown in Figure 4.5e (see also Figures S6-S8).

Additionally, land-level trends over the last decade were obtained from five continuous GNSS stations located north (Zapallar) and south (Valparaíso) of Campiche (Figure 4.1c). We used the linear trajectory method (Bevis and Brown, 2014; Melnick et al., 2017) to model the East, North, and Up components, which are shown in the Supporting Information along with the description of the method (Figures S9-S13). The Up component was used to estimate vertical land motion. A campaign GPS benchmark (MROC; Figure 4.1c), installed by the central Andes GPS Project

(CAP; Kendrick et al., 1999) at Concón in 1997 and resurveyed in 2004, allowed extend backward the geodetic data (Figure S14).

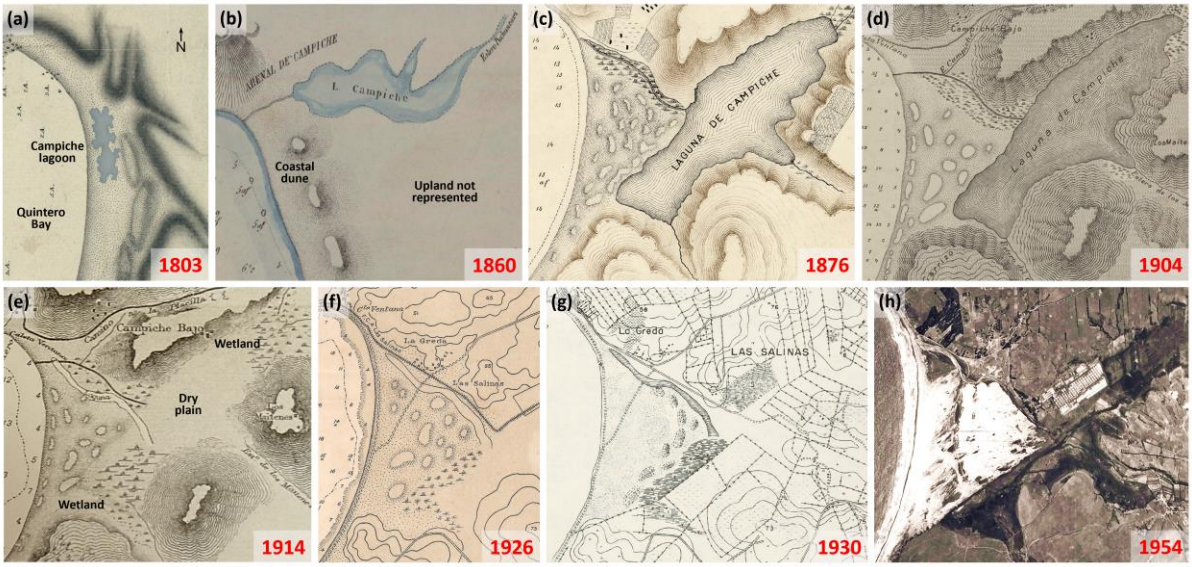

Figure 4.3. Sequence of historical maps and early aerial photography documenting changes in the Campiche lowland since the early 19th century. (a-d) Pre-1906 depictions of the Campiche coastal lagoon. (e-g) Post-1906 depictions showing the plain that replaced the lagoon. Note the presence of fences delimiting the land in 1930 (g). (h) First aerial photograph of Campiche, taken in 1954 before industrial development, showing part of the vegetated plain and inland dune migration over the former lagoon bed.

4.4 Results

4.4.1 Campiche stratigraphy

The sediments fringing the Campiche lowland, at the base of the surrounding hills where freshwater wetlands are developed, show two distinct layers down to the meter depth (Figure 4.2a,b). The lower layer is composed of gray, organic-poor, massive fine mud, which extends towards the center of the plain as a brick-colored mud. This mud layer varies in thickness between 0.2 and 1 m, occasionally exhibits darker laminations at its base and pinches out towards the hills (Figure 4.2b). The organic matter content, mainly composed by small rootlets and other plant macrofossils, varies between 22 and 32% (Figure S5). Seeds of salt-tolerant aquatic plants are often found in the mud, especially from the sedge *Schoenoplectus californicus* in

concentrations up to 60 seeds/10 cm^3 (Figure 4.5c). Although pollen of native species is present in this mud, no pollen of *P. radiata* was found (Figure 4.5c). Diatom assemblages are mostly dominated by brackish (e.g., *Navicula peregrina*, *Nitzschia sigma* and *Cocconeis placentula*) and marine (e.g., *Tabularia fasciculata*) species, reaching a combined abundance of 55% (Figures 4.4 and 4.5d). Freshwater species are also abundant in the mud, especially epiphytic species (e.g., *Gomphonema affine*, *Gomphonema parvulum* and *Nitzschia amphibia*). Planktonic diatoms (e.g., *Aulacoseira granulata*, *Paralia sulcata* and *Stephanocyclus meneghinianus*) represent up to 13% of the assemblages. The ratio of brackish and marine to freshwater species ranges from 0.6 to 0.77 (Figure 4.5d).

The mud layer is abruptly overlaid by a layer of dark reddish peat ranging from 0.2 to 0.4 m thick (Figure 4.2b). The peat contains up to 80% of organic matter (Figure S5), with abundant grass seeds and plant remains. In contrast to the lower mud, the peat layer does not contain *S. californicus* seeds, except at its basal section with concentrations of less than 15 seeds/10 cm^3 (Figure 4.5c). Pollen assemblages are constituted by both native and exotic taxa, reaching higher concentrations than in the mud layer. Pine pollen was found throughout almost the entire peat layer, increasing in concentration upwards (Figure 4.5c). Diatom assemblages in the peat layer are almost completely dominated by freshwater species (~90%; Figures 4.4 and 4.5d), either benthic (e.g., *Diploneis ovalis*, *Navicula cryptotenella* and *Pinnularia subcapitata*) or epiphytic (e.g., *Epithemia gibba*, *Epithemia gibberula* and *Planothidium lanceolatum*). Brackish species have an abundance generally less than 10%, showing a slight increase to about 20% in the upper section (e.g., *Halamphora coffeaeformis* and *Navicula cryptocephala*). Marine species are almost absent, with an abundance of less than 1%. Planktonic diatoms are also absent in the peat layer, except for the lowest section with an abundance of less than 2%. The ratio of brackish and marine to freshwater species is less than 0.13 in the lower section, increasing to 0.23 in the upper section (Figure 4.5d).

Cluster analyses of diatom assemblages using CONISS confirm an abrupt change in salinity across the lithologic contact from mud to peat (Figures 4.4, S3 and S4). Brackish and marine taxa dominating the mud layer assemblages, such as *Navicula peregrina* and *Tabularia fasciculata*, are typically found in high salinity environments, usually in coastal sites near MSL. In contrast, freshwater taxa dominating the peat layer, such as *Diploneis ovalis* and *Pinnularia subcapitata*, are typical of a vegetated environment above the mean higher high water (MHHW) in Quintero Bay. Cluster analyses also detect a more subtle shift in the diatom assemblages at the top of the peat, showing a higher occurrence of brackish taxa, such as *Halamphora coffeaeformis* and *Navicula cryptocephala* (Figures 4.4 and S3). These taxa proliferate in the Puchuncaví Creek (salinity >2%) and are usually more abundant in the underlying mud layer, so their occurrence in the peat layer suggests a slight increase in salinity.

4.4.2 Chronology of slice SL-3

The presence of pine pollen supports the transfer of the ^{210}Pb chronology from Gayo et al. (2022) to our slice SL-3 (Figure 4.5a-c), providing a time frame that spans the entire 20th century. The deepest occurrence of pine pollen at 29 cm depth in slice SL-3 (Figure 4.5c), which corresponds to 1910-1920 in the chronology of Gayo et al. (2022), probably reflects the first spread of pine plantations throughout central Chile in the early 20th century (Contesse, 1987). This constrains the occurrence of the sharp lithological change from mud to peat at 32 cm depth between 1900 and 1910 (Figure 4.5a,b). A prominent pollen peak at 13 cm depth (Figure 4.5c), corresponding to 1970-1980, probably marks the massive afforestation that followed the 1974 economic incentive law for pine plantations (Maestripieri et al., 2017). Thus, because there is no visual evidence of erosion, bioturbation, or mixing in the stratigraphy of slice SL-3, it likely recorded at least the last 120 years of sedimentation and ecological changes along the central Chilean coast.

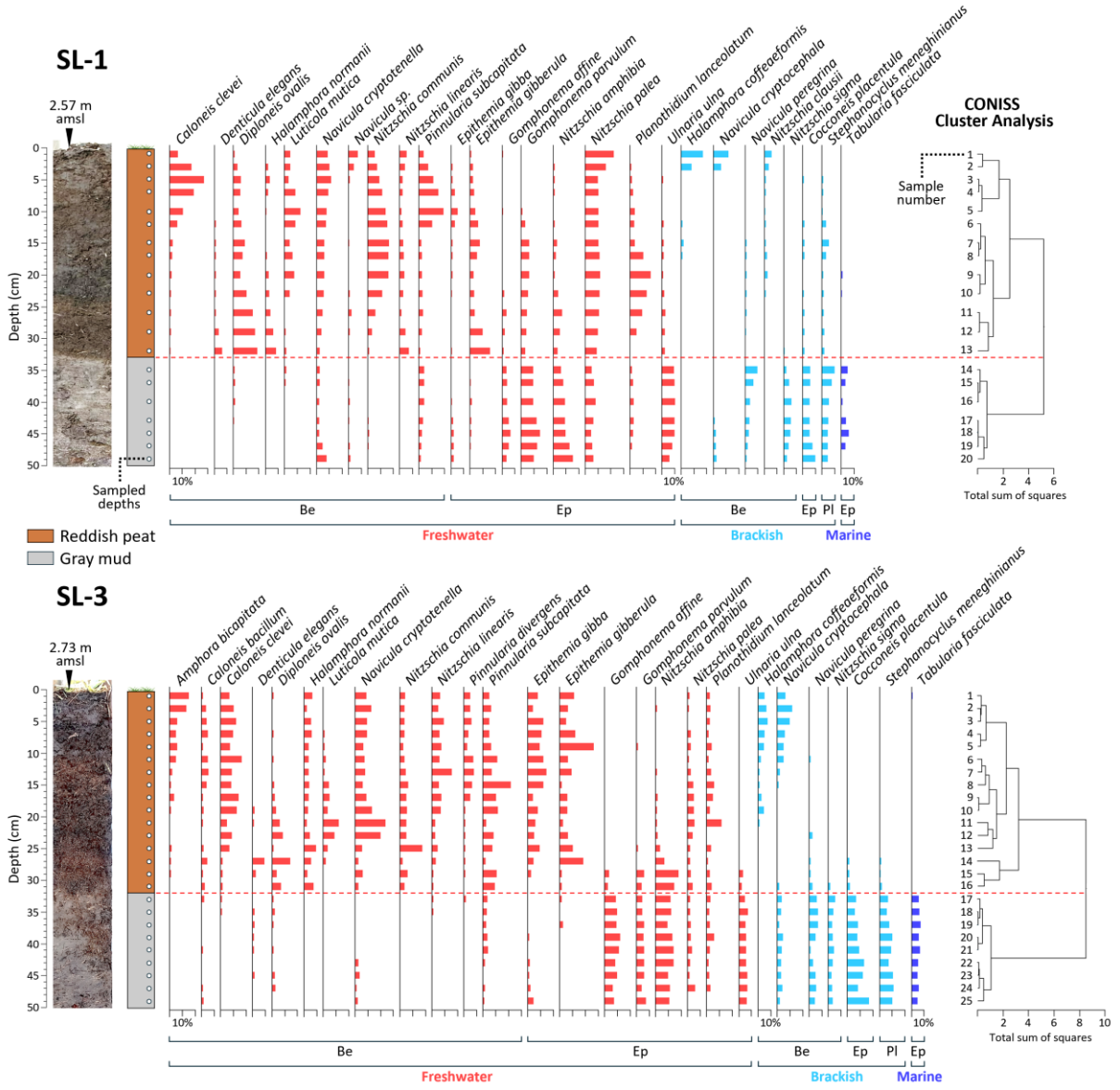

Figure 4.4. Relative abundance of diatoms in slices SL-1 and SL-3. Photographs and schematic stratigraphies of each slice are shown on the left. Only species with relative abundance >5% are included and are grouped by salinity preference (freshwater, brackish, and marine) and life form (Be: benthic, Ep: epiphytic, Pl: planktonic). Elevations above mean sea level (amsl) at which each slice was collected are indicated (see also Figure 4.2b). Results of the CONISS cluster analysis on the right show an abrupt shift in diatom assemblages coinciding with the change from mud to peat (marked by the red dashed line). Note the gradual increase of brackish species in the uppermost peat section.

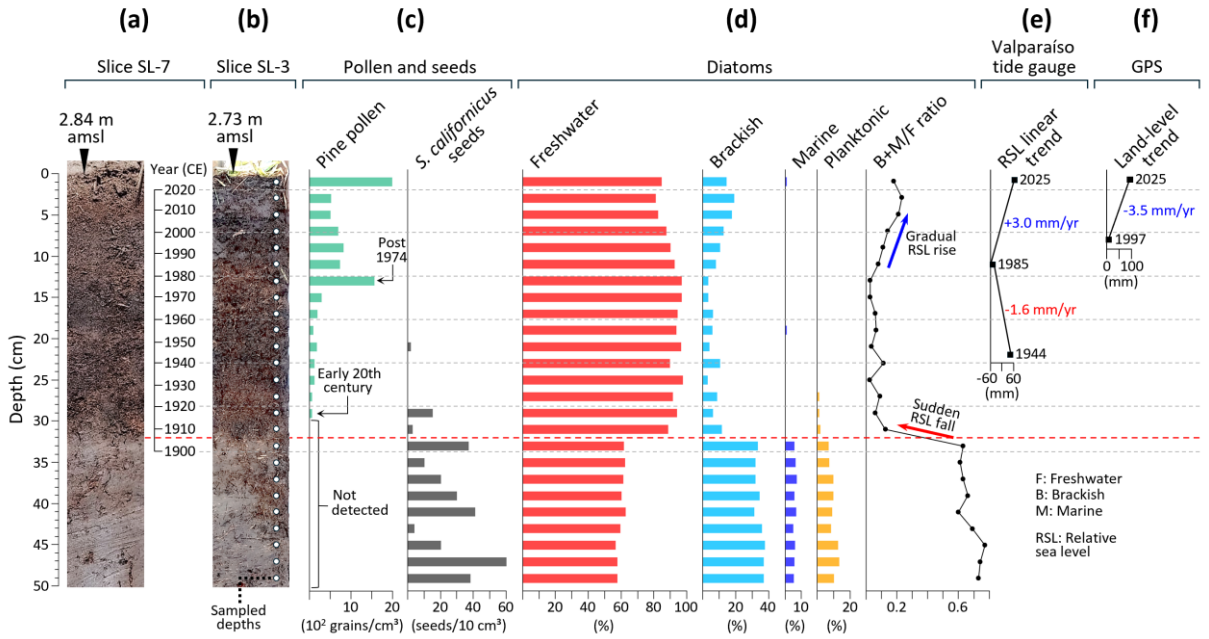

Figure 4.5. Biostratigraphic record in slice SL-3 and relative sea level (RSL) and land-level trends. (a) Photograph of slice SL-7 at the site originally studied by Gayo et al. (2022), including their published ^{210}Pb chronological model. (b) Photograph of slice SL-3 extracted from a nearby location (see Figure 4.2a). Note the strong stratigraphic similarity between both slices. (c) Concentrations of pine pollen and *Schoenoplectus californicus* seeds. (d) Summary of relative abundance of diatoms grouped by salinity preference (freshwater, brackish, and marine) and life form (planktonic). The ratio of brackish and marine to freshwater diatoms, used to infer RSL changes, is shown on the right. (e) Long-term RSL trend recorded by the Valparaíso tide gauge. (f) Land-level trend averaged from geodetic measurements between Zapallar and Valparaíso.

4.4.3 Campiche in the 19th and 20th centuries

Although the Campiche lowland is currently an extensive, partially dried and vegetated plain, 19th century maps consistently depict it as a coastal lagoon (Figure 4.3a-d). Maps since 1803 onwards show that this former lagoon extended for several kilometers and was connected to the sea through a narrow channel where the Puchuncaví Creek is currently located. This representation continues until 1904, but by 1914 the lagoon no longer appears on maps, indicating a sudden disappearance in the intervening decade (Figure 4.3e-g). Post-1914 maps show a dry plain bordered by wetlands, including the presence of fences delimiting properties on the new land (Figure 4.3g).

Contemporary scholars describe the Campiche lagoon as a shallow waterbody about 5 km long surrounded by reeds and other aquatic plants, as well as being home to a variety of fish and birds (Pissis, 1854; Vicuña Mackenna, 1874; Pomar, 1876; Vidal Gormaz, 1880). During the dry season the lagoon is reported as reaching a maximum depth of 2 m, whereas during the wet season it is described as suitable for canoeing and abundant fishing (Vicuña Mackenna, 1874; Pomar, 1876; Vidal Gormaz, 1880). According to descriptions made by Vidal Gormaz (1880), the lagoon outlet is found closed during the summer as a sand bar is established due to the slow flow of water and opened in winter due to the rains that increase the level of the lagoon.

The earliest aerial photograph of Campiche, taken in 1954 before industrial development, shows the area already resembling its current state, characterized by inland-advancing dunes and increased vegetation cover (Figure 4.3h). Peripheral water bodies, such as the Campiche and Los Maitenes wetlands, likely represent the last remnants of the former lagoon (Figure 4.2a).

4.4.4 Sea and land level changes

The Valparaiso tide gauge record reveals a significant change in the RSL trend in the early 1980s, marking distinct periods of sea level fall and rise in central Chile. For the complete tide gauge time series, the resulting trajectory model with quadratic term suggests a reversal in the polarity of RSL change between 1981 and 1982 (Figure S6). The maximum likelihood of the probability density function for the minimum of the quadratic function is the year 1981.3 ± 0.4, three years before the large 1985 earthquake. Derived from this, we estimated linear trends of RSL for two periods of about 40 years each (Figures S7 and S8). The first, between 1944 and 1985, shows RSL fall at a rate of 1.6 ± 0.03 mm/yr (Figure 4.5e). The second, between 1985 and 2025, shows RSL rise at a rate of 3.0 ± 0.02 mm/yr (Figure 4.5e).

GNSS data from stations north and south of Quintero Bay show ongoing coastal subsidence along the coast of central Chile over the past decade, with rates varying between 1 and 6 mm/yr (Figure 4.1c). The station at Zapallar (ZAPA), about 20 km

north of Campiche, shows continued subsidence from 2010 to 2025 at a rate of 2.44 ± 0.26 mm/yr (Figure S9). In Valparaíso, about 30 km south of Campiche, two stations show slightly lower subsidence rates than those recorded to the north. The VALP station shows a subsidence rate of 1.44 ± 0.56 mm/yr between 2008 and 2015, whereas the VALN station indicates a rate of 1.04 ± 0.70 mm/yr between 2013 and 2023 (Figures S10 and S11). Other two Valparaíso stations show subsidence at a higher rate. While the BN05 station shows a rate of 4.32 ± 0.28 mm/yr between 2011 and 2024, the TRPD station presents a rate of 5.9 ± 0.92 mm/yr between 2016 and 2025 (Figures S12 and S13). Additionally, the campaign GPS benchmark MROC at Concón, about 20 km south of Campiche (Figure 4.1c), indicates a subsidence rate of 3.57 ± 0.81 mm/yr between 1997 and 2004 (Figure S14). Together, for the area between Zapallar and Valparaíso, GPS measurements indicate an average subsidence rate of approximately 3.5 mm/year since at least 1997 (Figure 4.5f).

4.5 Discussion

4.5.1 Evidence for early 20th century sudden emergence

The sharp lithologic and ecological contact observed in the Campiche lowland indicates an abrupt environmental shift, most likely driven by sudden emergence in the early 20th century. Seed assemblages and planktonic diatoms suggest that the lower gray mud layer was deposited in a low-energy, shallow lagoon environment surrounded by reeds and sedges (Figure 4.6a). In contrast, the overlying reddish peat layer dominated by grass seeds and pollen along with abundant benthic and epiphytic diatoms, reflects accumulation in a terrestrial setting capable of sustaining dense vegetation (Figure 4.6c,d). This change in the depositional environment was accompanied by an abrupt decrease in salinity as indicated by the diatom assemblages shift from mostly brackish to freshwater taxa (Figures 4.4 and 4.5d), which is consistent with an emergence event resulting from a sudden RSL fall as has been suggested by other studies (Figure 4.6b; Sawai, 2001; Atwater et al., 2004; Shennan et al., 2009; 2014; DePaolis et al., 2024). According to our composite chronology, this emergence event marked by the transition from mud to peat likely

occurred in the early 20th century, between 1900 and 1910 (Figure 4.5a-c), coinciding with the 1906 megathrust earthquake and its associated coseismic uplift.

This emergence-driven ecological change also corresponds with the sequence of historical maps documenting the disappearance of the Campiche lagoon (Figure 4.3). The gray mud, containing seeds of plants and diatoms associated with brackish water, was likely deposited in the former lagoon, which was mapped until 1904 (Figure 4.3a-d), while the peat with freshwater diatoms developed on the emerged lagoon bed where plants could establish, as shown in maps from 1914 onward (Figure 4.3e-g).

Together, the stratigraphic and historical evidence points to an abrupt uplift event at Campiche, most likely linked to the 1906 earthquake. Several key criteria used elsewhere to relate coseismic land-level changes with similar evidence are present in the Campiche stratigraphy. They include the suddenness and continuity of the lithologic contact, as well as the abrupt and sustained ecological change indicated by microfossil assemblages (Nelson et al., 1996; Shennan et al., 2016). More evidence for coastal uplift in 1906 is provided by a historical report mentioning that former saltworks at Campiche were no longer reached by the tides after the earthquake (Figure 4.2a), forcing the building of a system of steam pumps and pipelines to bring the water from the sea (Martija, 2016).

Alternatively, other processes could explain the stratigraphic record at Campiche. One possibility is a previously undocumented intraplate earthquake in the early 20th century that produced localized uplift. However, this explanation seems unlikely, as no cortical faults have been identified near Quintero Bay (Rivano et al., 1993; Maldonado et al., 2021), and it is improbable that such an event would have gone unnoticed in the already densely populated Santiago–Valparaíso region at that time. Alternative explanations involving non-tectonic processes, including slight sea level fluctuations or blockage of the Puchuncaví Creek outlet, fail to explain the sharpness and persistence of the stratigraphic and landscape changes observed at Campiche. A

slow RSL fall would result in a gradual change in lithology and diatom assemblages. However, both changed abruptly in all sediment cores and slices collected (Figures 4.4, S3 and S4). A permanent blockage of the Puchuncaví Creek outlet could eventually result in a salinity change, but not in the disappearance of the lagoon. If the Puchuncaví Creek had been permanently closed, the lagoon's water level would have risen, submerging the Campiche lowland under freshwater. Although we have observed that this outlet can be seasonally blocked by beach sand, such closures are temporary, as reported by Vidal Gormaz (1880). This seasonal behavior would produce a stratigraphic record characterized by thin, rhythmic layers reflecting alternating periods of lagoon opening and closure and not a stratigraphy composed by only two units spanning more than a century.

Additionally, the fossil diatom assemblages across the lithologic contact and their typical elevational ranges within the tidal frame allow to constrain the amount of uplift at Campiche. Based on the modern tidal range in Quintero Bay (~1.6 m) and the diatom assemblages preserved in the sediments, which indicate a shift from a near MSL environment to one above MHHW, we estimate a minimum coastal uplift of ~0.7 m (Figure 4.6e). This value is consistent with those reported by eyewitnesses of the 1906 earthquake effects near Quintero Bay, which range between 0.6 and 0.8 m (see Section 2.2; Figure 4.1c).

Taken together, our evidence suggests that the 1906 earthquake uplifted the Campiche area, leading to the drainage of the lagoon and the emergence of its muddy bed, which was subsequently colonized by vegetation (Figure 4.6b-d). Comparable landscape changes have also been observed elsewhere following major earthquakes, such as in Alaska after the 1964 event (DePaolis et al., 2024).

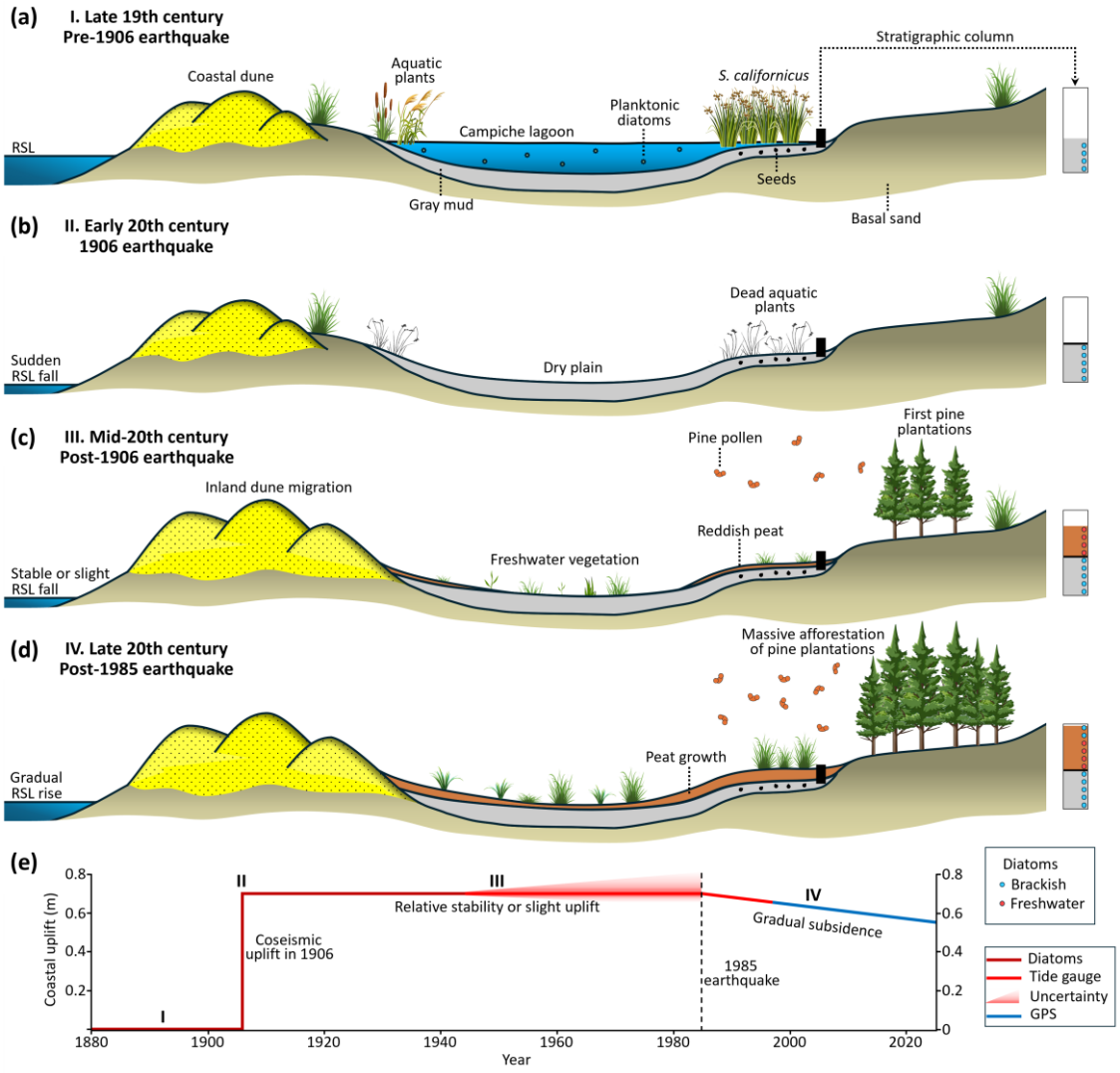

Figure 4.6. Conceptual reconstruction of relative sea-level (RSL) changes at Campiche during the 20th century, based on environmental indicators. (a) In the 19th century, the Campiche lowland was occupied by a coastal lagoon surrounded by aquatic vegetation such as reeds and sedges. Fine mud, seeds, and predominantly brackish diatoms accumulated on the lagoon bed. (b) In the early 20th century, the lagoon was abruptly drained due to a sudden RSL fall associated with the 1906 coseismic uplift, leading to the death of aquatic plants. (c) During the following eight decades, the exposed surface was colonized by freshwater vegetation and diatoms, promoting peat formation. Inland migration of the coastal dune partially covered the new plain, and pine plantations were introduced to the area. (d) By the late 20th century, vegetation and peat accumulation became more extensive. However, around the time of the 1985 earthquake, an increasing presence of brackish diatoms in the upper peat indicates a slight RSL rise towards the return of tidal influence. (e) Coastal elevation changes at Campiche during the 20th century. Roman numerals correspond to the environmental stages shown in (a-d). Different colors in this reconstruction represent land-level changes supported by different evidence sources indicated on the right.

4.5.2 Evidence for mid-20th century lasting emergence

A key finding of this study is the absence of significant vertical recovery (i.e., expected subsidence) of the Campiche lowland in the eight decades following the 1906 earthquake uplift. This is suggested by the reduced variation over several decades in the diatom assemblages of the post-1906 peat. Numerous freshwater taxa that prospered in the new environment imposed by the coseismic uplift are found vertically throughout the peat layer (Figures 4.4 and 4.5d). This implies that the tidal influence was effectively interrupted for a prolonged duration, resulting in lasting emergence throughout much of the 20th century (Figure 4.6e). Brackish and marine taxa disappeared almost completely, with a slight increase recorded in the cap of the peat layer (discussed in the next section). Post-1906 seed and pollen assemblages throughout the peat agree well with the terrestrial environment seen today, dominated by freshwater plants such as giant rhubarbs and willows (Figure S1a). It implies that the area remained raised above the tidal range during most of the 20th century (Figure 6e).

The inferred lasting emergence is partially supported by the tide gauge record of the RSL at Valparaíso, which starts in 1944 (Figure 4.1c). Between 1944 and 1985, the record shows a linear trend of slight RSL fall at a rate of ~1.6 mm/yr (Figure 4.5e). However, the tide gauge data includes a gap between 1971 and 1982, which complicates the quantification of this trend. If the data is analyzed between 1944 and 1971, when the record is continuous, a linear trend of RSL rise at 0.15 ± 0.06 mm/yr is obtained, suggesting relative stability (Figure S16). This is close to the stability inferred from diatoms at Campiche between 1944 and 1985. In any case, the tide gauge record from Valparaíso supports the notion that the coast remained raised for several decades. Additionally, since the peat diatom assemblages pre- and post-1944 are similar, we infer that the lasting emergence persisted since the 1906 uplift. This trend suggested by diatoms over a period of eight decades is shown in Figure 4.6e together with the uncertainty of the tide gauge data.

It is worth noting that two significant earthquakes occurred between 1944 and the present: the 1971 (Mw 7.8) and 1985 (Mw 8.0) events, both potentially capable of producing land-level changes in the region (Figure 4.1b). While the larger 1985 earthquake is discussed in the following section, the 1971 event is known to have uplifted Valparaíso by about 0.15 m (Barrientos, 1997) and may have caused minor uplift at Campiche. However, the absence of lithological or diatom changes in the sediments corresponding to the 1970s suggests limited vertical displacement associated with this earthquake (Shennan et al., 2016; Brader et al., 2021), making it unlikely to explain the magnitude and persistence of the emergence recorded in Campiche.

Although prolonged emergence may seem counterintuitive within the seismic cycle, where coseismic land-level changes are typically expected to recover during the postseismic and/or interseismic stage, similar patterns have occurred in central and northern Chile. The 1822 earthquake, which preceded the 1906 event, caused notable uplift in Valparaíso (~0.9 m) and Quintero Bay (~1.2 m; Graham, 1824; Miers, 1826; Vowell, 1831), leaving the coast uplifted for at least a decade. This pattern was reported by the naturalist Meyen (1834), who observed remains of shelly intertidal organisms still attached to emerged rocks in Valparaíso nine years after the earthquake. During his visit in 1834, Darwin also noted the persistent effects of that uplift and, based on this and other evidence, proposed that earthquakes contribute to long-term land elevation (Darwin, 1846). If part of the uplift caused by this historic earthquake persisted throughout the 19th century, the drainage of the Campiche lagoon may not be only due to the 1906 uplift, but to a cumulative effect since at least 1822. Similarly, in northern Chile, the ~0.3 m uplift from the 2007 Tocopilla earthquake (Mw 7.7) has shown no significant postseismic or interseismic reversal, with GPS data indicating that the coast has remained elevated for over a decade (González-Alfaro et al., 2018), pointing to a similar pattern of sustained emergence that continues until today (Figure S15). Modern GPS measurements also show that the coast of Constitución, about 300 km south of Campiche, has remained elevated after the 2012 earthquake (Mw 7.0; Ruiz et al., 2013), causing sustained uplift of

~0.15 m (Figure S15). Future geodetic measurements will clarify whether the uplift caused by these two earthquakes is transient or long-lasting, as seemingly occurred in central Chile after 1906.

We suggest that the lasting emergence inferred after the 1906 earthquake resulted from its deep interplate source. According to Carvajal et al. (2017b; 2019), the combination of strong ground shaking, minor tsunami, and coastal uplift in 1906 indicates a rupture confined to the downdip portion of the megathrust, directly beneath central Chile's coastline. Earthquakes occurring in this deeper, conditionally stable segment of the seismogenic zone, such as the 2007 Tocopilla and 2012 Constitución events, are thought to generate permanent deformation in the overlying plate, leading to sustained coastal uplift (Melnick, 2016). Supporting this idea, and echoing Darwin's (1846) early observations, Freisleben et al. (2023) proposed that deep megathrust earthquakes have driven the long-term uplift of the South American western margin, as evidenced by sequences of marine terraces dating back to the Pleistocene.

4.5.3 Evidence for late 20th century gradual submergence

Slight but measurable submergence of the 1906-uplifted central Chilean coast appears to have begun after several decades of sustained emergence, around the mid-1980s, as suggested by diatom assemblages along with tide gauge and GPS records. Such submergence is first supported by a modest increase in brackish and marine diatoms at the top of the peat layer. This trend begins in slice SL-3 around 12-13 cm depth, corresponding to the early 1980s, and continues gradually upward (Figures 4.4 and 4.5d). Brackish and marine taxa, typically found living in the Puchuncaví Creek where salinity ranges between 2 and 2.5%, reach nearly 20% in the uppermost peat samples (Figure 4.5d). This subtle but consistent ecological shift also shown by slices SL-1 and SL-2 (Figures 4.4 and S3) likely reflects the gradual return of tidal influence to Campiche driven by a RSL rise (Figure 4.6d). A comparable pattern was reported by Dura et al. (2015), who inferred a gradual RSL rise following mid-Holocene uplift events in Quintero Bay (Figure 4.1d). They also

documented increases in brackish and marine species, identifying indicator taxa that closely match those observed at the top of the Campiche peat.

A second line of evidence supporting gradual submergence since the mid-1980s comes from the Valparaíso tide gauge record and modern geodetic observations. The trend of RSL fall shown by the Valparaiso tide gauge since 1944 was reversed to RSL rise in the 1980s, continuing to the present at a rate of ~3.0 mm/yr (Figure 4.5e). This new trend of RSL rise is consistent with independent geodetic data showing ongoing coastal subsidence since the late 20th century. Five GNSS stations located in Zapallar and Valparaíso, to the north and south of Campiche respectively (see Figure 4.1c), have recorded coastal subsidence over the last decade, with rates ranging from 1 to 6 mm/yr (Figures S9-S13). Additionally, measurements from a campaign GPS benchmark at Concón (MROC), about 20 km south of Campiche, show that subsidence was already occurring at the end of the past century, between 1997 and 2004, at a rate of approximately 3.5 mm/yr (Figure S14). Thus, stratigraphic, oceanographic and geodetic observations together point to a protracted land subsidence in central Chile since the mid-1980s (Figure 4.6e).

Explaining the onset of subsidence along the central Chilean coast in the mid-1980s, after decades of sustained emergence, requires considering its temporal coincidence with the 1985 earthquake. This event is well known for having uplifted the coast between Valparaíso and San Antonio by more than 0.3 m, with maximum slip inferred beneath the coastline (IGM, 1985; Comte et al., 1986; Castilla, 1988; Bravo et al., 2019). Although this uplift occurred farther south of Valparaíso, no land-level changes were reported farther north, in Quintero Bay, making it difficult to argue that the rupture extended into that area or directly caused the observed subsidence. Bravo et al. (2019), however, proposed a rupture model that indeed includes slip offshore Quintero Bay and predicts up to 0.1 m of subsidence at Campiche (Figure 4.1b). When this potential coseismic signal is combined with postseismic deformation lasting months to years, as proposed for the 1985 event by Barrientos (1988, 1995, 1997) and Araneda and Avendaño (1993), it offers a possible mechanism for the initiation of

gradual submergence. However, this process is unlikely to explain continued subsidence over multiple decades, as medium-sized earthquakes typically generate only short-lived postseismic effects (Wang et al., 2012).

Alternatively, the onset of subsidence recorded at Campiche may reflect a late interseismic phase following much larger megathrust earthquakes, such as the 1730 event, which likely exceeded magnitude Mw 9 (Carvajal et al., 2017a). Li and Chen (2024) recently proposed that coastal uplift may be reversed to gradual subsidence during the late interseismic phase, driven by viscoelastic mantle relaxation as interplate locking strengthens. In support of this view, geodetic observations indicate that both the shallow and deep portions of the central Chile megathrust are already highly coupled, accumulating border stress since the 2010 and 2015 earthquakes ruptured adjacent segments (Métois et al., 2016; Melnick et al., 2017; Sippl et al., 2021).

4.5.4 Coastal deformation and seismic cycle interplay in central Chile

Despite the slight subsidence recorded at Campiche since the mid-1980s, the environmental conditions that prevailed prior to 1906 have not been reestablished. This is evident not only in the landscape but also in the uppermost diatom assemblages of the peat layer, which still show a dominance of freshwater taxa rather than the brackish taxa typical of the 19th century (Figures 4.4 and S3). Such freshwater dominance suggests that the coast remains above the tidal influence that prevailed before the 1906 earthquake. Consistently, the former lagoon has not reappeared and remains absent from recent maps and aerial photographs.

Although modest, the subsidence that began in the mid-1980s allows us to estimate the amount of recovered deformation since 1906 by using our inferred uplift at Campiche and the current GNSS-derived subsidence rate. Assuming a coseismic uplift of 0.7 m in 1906 and a constant subsidence rate of 3.5 mm/yr since 1985, only about 20% of the uplift has been reversed to date (Figure 4.6e). This estimate

assumes that the present-day subsidence rate has remained constant since the mid-1980s. Extending this rate into the future, it would take at least 160 years to fully recover the vertical deformation of 1906; nearly twice the average recurrence interval of moderate-sized earthquakes in central Chile (~85 years; Nishenko et al., 1985; Comte et al., 1986). From this, it can be concluded that there is insufficient time to recover all the deformation if current subsidence rates persist, at least within the seismic cycle of moderate events like those of 1822, 1906, and 1985, though recovery might be possible if longer cycles associated with great earthquakes, such as the one in 1730, are considered.

This apparent mismatch between deformation recovery time and earthquake recurrence is not unique to central Chile. Evidence from other historical earthquakes elsewhere in Chile suggests that a significant fraction of coseismic uplift may not be fully reversed within a single seismic cycle. For instance, Wesson et al. (2015), using historical bathymetric charts from Isla Santa María in south-central Chile, found that interseismic subsidence between the 1835 and 2010 uplifting earthquakes only partially compensated the uplift from 1835, resulting in up to 20% of permanent vertical deformation.

Alternatively, earthquakes involving large shallow ruptures in central Chile may generate sudden coastal subsidence, as proposed for the giant 1730 earthquake (Carvajal et al., 2017a). In this scenario, although future subsidence rates could increase due to enhanced interplate locking (Meltzner et al., 2015; Melnick et al., 2018), or if a major shallow rupture were to occur (Carvajal et al., 2017a), both possibilities still suggest that a substantial portion of the vertical deformation produced by the 1906 earthquake may remain unrecovered. This supports the hypothesis proposed by Melnick (2016), which posits that deep megathrust earthquakes play a fundamental role in the building of long-term coastal topography in the central Andes.

4.6 Conclusions

We reconstructed the history of land-level changes during the 20th century in central Chile, including the effects of the 1906 and 1985 megathrust earthquakes. Our multidisciplinary study combined sedimentological and paleoecological data from the Campiche lowland in Quintero Bay with historical maps and reports, tide gauge records, and modern geodetic measurements. A distinct shift from brackish to freshwater diatom and seed assemblages across a sharp lithological contact from inorganic mud to peat reveals a sudden RSL fall consistent with coastal emergence. Radiometric dating and pine pollen inputs constrain this environmental shift to the early 20th century, coinciding with the disappearance of the Campiche lagoon between 1904 and 1914 as documented in historical maps. This emergence is attributed to at least 0.7 m of coastal uplift caused by the 1906 earthquake. Following this uplift, diatom assemblages indicate relatively stable RSL conditions for nearly eight decades, suggesting lasting emergence. This is partially supported by a modest RSL fall of ~1.6 mm/yr recorded by the Valparaíso tide gauge since 1944. However, this trend reversed in the mid-1980s, showing a RSL rise of ~3 mm/yr, which is consistent with gradual submergence as suggested by an increase of brackish diatoms in the peat. Gradual submergence is also corroborated by modern geodetic measurements showing ongoing coastal subsidence of ~3.5 mm/yr since 1997. We suggest that the prolonged uplift after 1906 resulted from a deep megathrust rupture, while the onset of subsidence since the mid-1980s may reflect postseismic deformation following the 1985 earthquake, enhanced interplate locking, or a late interseismic phase after a much larger megathrust event in 1730. Our findings highlight the complex interplay between coseismic, postseismic, and interseismic processes governing coastal deformation in central Chile. They provide critical constraints for refining vertical deformation models and advance our understanding of subduction zone dynamics in this tectonically active margin.

Capítulo 5. Discusión

5.1 Relevancia de enfoques multidisciplinarios

Uno de los aspectos fundamentales que pretende destacar esta investigación es el uso de un enfoque multidisciplinario para comprender los procesos de deformación costera y sedimentación asociados a grandes terremotos y tsunamis en Chile central. La combinación de distintas líneas de evidencia, incluyendo sedimentológica, paleoecológica, geomorfológica y satelital, permitió superar las limitaciones propias de cada método por separado, fortaleciendo las interpretaciones sobre la magnitud, extensión y persistencia de la deformación vertical asociada a ciclos de terremotos, así como la caracterización detallada de los depósitos de tsunami y su distribución espacial.

En el Capítulo 2 se demostró el potencial del análisis de imágenes satelitales para detectar y mapear depósitos de tsunami, aplicando un modelo de clasificación supervisada sobre imágenes multiespectrales de alta resolución (QuickBird y WorldView-2). Este enfoque permitió delimitar con precisión las áreas afectadas por la inundación y estimar su extensión a lo largo de la costa estudiada. Los resultados mostraron una correspondencia notable entre las zonas clasificadas como afectadas y los límites de inundación obtenidos en terreno, validando la eficacia de la percepción remota como herramienta de apoyo en estudios de depósitos de tsunami. Sin embargo, es importante destacar que el trabajo de campo sigue siendo una pieza fundamental e insustituible dentro de este enfoque satelital. Ya sea para calibrar o validar los modelos de clasificación, contar con al menos un limitado set de puntos de control siempre será recomendable.

A pesar de la eficacia de la percepción remota en el estudio de depósitos de tsunami, las limitaciones aquí detectadas, tales como la dependencia de imágenes adquiridas temporalmente cercanas al evento, la dificultad para identificar depósitos delgados o parcialmente enmascarados por vegetación, y la pérdida progresiva de la señal espectral en el tiempo, abren oportunidades claras de mejora en futuras

investigaciones. Entre ellas, se destaca el uso de sensores hiperespectrales y de radar de apertura sintética (SAR) en la detección de los depósitos, los cuales han ya sido usados satisfactoriamente en otros campos de investigación asociados a tsunamis (Koshimura et al., 2020; Sublime and Kalinicheva, 2019). En paralelo, la incorporación de modelos de aprendizaje profundo (*deep learning*) podría optimizar la detección automática de patrones sedimentarios en imágenes multitemporales, reduciendo la dependencia de entrenamiento manual y aumentando la robustez de las clasificaciones.

En el Capítulo 3 se abordó las dificultades para distinguir entre depósitos fluviales y depósitos de tsunami en las inmediaciones de desembocaduras de ríos andinos, donde ambos tipos de eventos pueden dejar registros sedimentarios de apariencia similar. A través del análisis de campo y laboratorio se evidenció que, en ambientes dominados por la influencia de ríos andinos, los aportes fluviales pueden enmascarar o sobreimponer señales marinas. Criterios de comparación utilizados como la granulometría, mineralogía, susceptibilidad magnética y análisis de diatomeas fueron insuficientes para distinguir inequívocamente el origen de los depósitos. Por tanto, es sugerido que sitios altamente dinámicos, como las desembocaduras de ríos andinos, deben ser evitados como blancos de exploración para la búsqueda de depósitos de tsunami ya que podrían conducir a interpretaciones erróneas. Futuras investigaciones podrían evaluar la aplicación de técnicas complementarias, como dataciones usando técnicas de luminiscencia (OSL), sensores hiperespectrales y simulaciones hidráulicas, para mejorar la interpretación del registro sedimentario.

En el Capítulo 4, múltiples fuentes de datos fueron integrados para reconstruir la deformación vertical costera durante el último siglo, con el objetivo de identificar patrones de alzamiento y subsidencia asociados al ciclo de terremotos en Chile central. La aplicación de información paleoecológica apoyada por mapas históricos y datos mareográficos permitieron extender el limitado registro instrumental proporcionado por modernas mediciones geodésicas. A partir de los cambios en comunidades de diatomeas preservadas en los sedimentos se infiere alzamiento

cosismico asociado al terremoto de 1906, sostenido levantamiento de la costa durante las siguientes ocho décadas, y posterior subsidencia gradual prevaleciendo hasta hoy. Estos resultados sugieren que la costa de Chile central ha estado sujeta a una evolución compleja durante ciclos de terremotos con fuente profunda en la zona de subducción, cuyos efectos acumulativos podrían tener implicancias en la construcción de la topografía a largo plazo.

5.2 Factores que limitan la formación y preservación del registro paleosismológico en Chile central

Los resultados de esta investigación permitieron identificar tres factores claves que condicionan el escaso registro paleosismológico en Chile central, limitando tanto su formación como su posterior preservación a lo largo del tiempo. En primer lugar, la tectónica es un factor de primer orden y por lo tanto juega un rol fundamental. El predominio del alzamiento costero en la zona centro de Chile reduce el espacio de acomodación necesario para la acumulación de sedimentos, favoreciendo la erosión por sobre la depositación. En segundo lugar, el clima mediterráneo semiárido, con prolongadas sequías estivales y lluvias concentradas en invierno, intensifica los procesos erosivos e impide el desarrollo de suelo orgánico para ofrecer protección a los depósitos. Por último, actividades antrópicas, como la urbanización costera y la expansión agrícola, han perturbado numerosos sitios con potencial paleosismológico. Estos tres factores, los cuales conjuntamente han generado un registro geológico fragmentario y discontinuo en Chile central, son discutidos por separado en los siguientes apartados (Figura 5.1).

5.2.1 Factor tectónico

El sostenido alzamiento costero en Chile central ha limitado la formación y preservación del registro geológico de terremotos y tsunamis, ya que reduce el espacio de acomodación para los sedimentos y contribuye a la degradación de ambientes deposicionales de baja energía (Figura 5.1b). De acuerdo con la reconstrucción de los cambios de nivel durante el último siglo en Campiche (Capítulo 4), el terremoto histórico de 1906 alzó la costa cerca de 0.7 m, provocando que la

antigua laguna de Campiche se secara. Este cambio ambiental ha sido persistente, como lo indica la evidencia paleoecológica, histórica e instrumental, implicando que la costa aún permanece alzada. Este es un hallazgo clave para Chile central, ya que sugiere que terremotos con una particular fuente profunda en la zona de subducción, como el terremoto de 1906 (Carvajal et al. 2017b; 2019), generan un alzamiento sostenido de la costa. Esto a su vez es sustentado por las previas conclusiones de Melnick (2016) y Freisleben et al. (2023), quienes argumentaron que terremotos profundos juegan un rol fundamental en la construcción de topografía costera a largo plazo en los Andes centrales.

Aparentemente, los terremotos profundos han generado un sostenido alzamiento costero que caracteriza al margen de Chile central. El terremoto de 1822, predecesor del evento de 1906, causó también notable alzamiento en Valparaíso y Quintero (Graham, 1824; Miers, 1826; Vowell, 1831), dejando la costa alzada por al menos una década (Meyen, 1834). Similarmente, modernas mediciones de GPS muestran que la costa de Constitución ha permanecido alzada por más de una década después del terremoto profundo del 2012 (Mw 7.0; Ruíz et al., 2013), así como también la costa del norte de Chile luego del terremoto de Tocopilla del 2007 (Mw 7.7; González-Alfaro et al., 2018). Tales ejemplos parecen apuntar a que los terremotos profundos alzan la costa permanentemente, o al menos por un prolongado periodo. Adicionalmente, los terremotos con fuente profunda ocurren con mayor frecuencia que los eventos someros en Chile central, aproximadamente cada 85 años (Comte et al., 1986; Nishenko, 1985), contribuyendo a un alzamiento neto del margen costero.

Este patrón de sostenido y frecuente alzamiento costero es especialmente relevante para la formación del registro geológico de terremotos y tsunamis en Chile central. En primer lugar, rupturas de terremotos profundos poseen un bajo potencial para generar un tsunami. Por ejemplo, los terremotos históricos de 1822 y 1906 causaron pequeños tsunamis que fueron reportados solo localmente (Carvajal et al., 2017a,b). Únicamente el tsunami causado por el terremoto de 1730, para el cual se atribuye

una fuente somera, provocó un masivo tsunami que dañó tanto la costa chilena como japonesa (Carvajal et al., 2017a). Ya que tales terremotos someros son inusuales en Chile central, es esperable que el registro geológico de tsunamis sea limitado. En segundo lugar, el continuo alzamiento de la costa limita el espacio de acomodación disponible para los sedimentos (Figura 5.1b). Completas secuencias de sedimentos costeros son impedidas de formarse en costas que experimentan progresivo alzamiento (e.g., Dura et al., 2016b). Esto contrasta ampliamente, por ejemplo, con la costa de Cascadia y el sur de Chile (Figura 5.1b), donde subsidencia causada por terremotos someros crea el espacio suficiente para hospedar depósitos de tsunami, propiciando la formación de completos registros (e.g., Atwater, 1987; Nelson et al., 1996; Garret et al., 2015).

Debe ser notado que el sostenido alzamiento de la costa de Chile central podría en cambio propiciar la formación de otros tipos de depósitos no asociados directamente al ciclo sísmico. Por ejemplo, el crecimiento de dunas y la formación de depósitos eólicos pueden verse beneficiados por el continuo alzamiento tectónico (e.g., Aedo et al., 2023; Araya-Cornejo et al., 2025), ya que episodios de emergencia podrían promover que una mayor cantidad de sedimentos costeros permanecieran disponibles para ser redistribuidos por deflación. En el norte de Chile, cerca de 70 km al suroeste de Copiapó, la formación de eolianitas en la base de la Cordillera de la Costa ha sido atribuido al continuo y rápido alzamiento tectónico durante el Cuaternario Tardío (Nash et al., 2018).

Por último, el alzamiento costero contribuye a la desecación de humedales y lagunas costeras (Figura 5.1b), transformando estos ambientes deposicionales de baja energía en superficies emergidas, las cuales son expuestas a la erosión, al retrabajo sedimentario y a la oxidación de sus compuestos orgánicos. Así como el terremoto de 1906 drenó la laguna de Campiche en la Bahía de Quintero, este evento podría haber también contribuido a la desaparición de otras lagunas a lo largo de Chile central. Por ejemplo, de acuerdo con Harnecker (1914), una pequeña laguna ubicada en Papudo, cerca de 30 km al norte de Campiche, desapareció en respuesta al

alzamiento costero del terremoto de 1906. Esta pérdida de ambientes protegidos, de baja energía y orgánicos, reduce significativamente el potencial de preservación de depósitos de tsunami y limita la formación de secuencias estratigráficas continuas (Figura 5.1b), dificultando así la reconstrucción de la historia sísmica y tsunamigénica en Chile central.

5.2.2 Factor climático

El régimen climático de Chile central constituye otro elemento limitante para la preservación del registro geológico de terremotos y tsunamis. El clima mediterráneo imperante en la zona centro de Chile, caracterizado por escasas precipitaciones y prolongados periodos secos, limita el desarrollo de suelos orgánicos que permiten la rápida protección de los sedimentos una vez que son depositados (Figura 5.1c). Esto a menudo resulta en significativa erosión, causando un registro estratigráfico fragmentario. Agentes erosivos, tales como el viento (Figura 5.1c), pueden retrabajar los sedimentos expuestos en superficie, redistribuyendo el material fino y borrando las estructuras sedimentarias originales (Goto et al., 2011; Higman y Bourgeois, 2008; Morton et al., 2011; Spiske et al., 2013). Similarmente, lagunas, humedales y otros ambientes costeros presentan bajas tasas de sedimentación que impiden el rápido enterramiento de los sedimentos antes de que puedan ser retrabajados. En consecuencia, el registro de terremotos y tsunamis en Chile central es incompleto y usualmente enmascarado por procesos post-depositacionales.

Estas características en Chile central contrastan ampliamente con aquellas observadas en el sur de Chile, donde un clima templado con altas precipitaciones favorece el desarrollo de densa vegetación y la buena preservación del registro geológico (e.g., León et al., 2023). La mayor disponibilidad de humedad hacia el sur permite la formación de suelos orgánicos bien desarrollados que ofrecen rápida protección a los sedimentos (Figura 5.1c). A su vez, hay mayor desarrollo de ambientes de baja energía, como lagunas o marismas, que actúan como reservorios naturales para el registro de eventos extremos. En tales ambientes costeros, tasas de sedimentación incrementadas favorecen el rápido enterramiento y, por tanto, la

preservación de los depósitos. Como resultado, el registro paleosismológico en el sur de Chile es más continuo y robusto (Figura 5.1c), proporcionando secuencias estratigráficas completas que han permitido reconstruir con mayor precisión la recurrencia y magnitud de grandes terremotos y tsunamis (e.g., Cisternas et al., 2005; 2017; Garret et al., 2015).

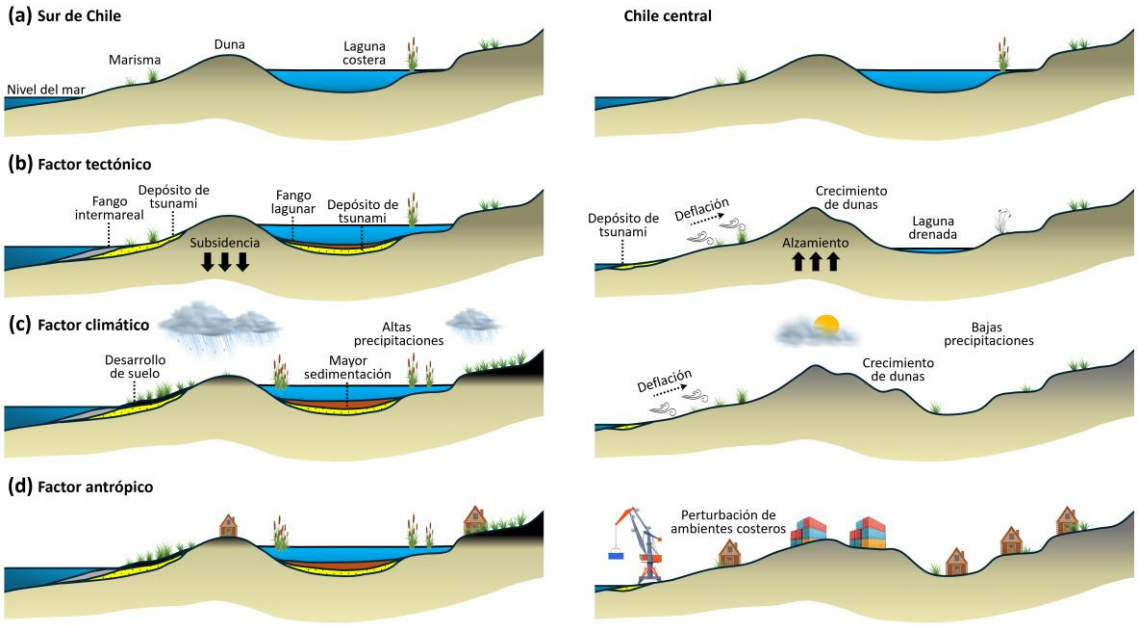

Figura 5.1. Reconstrucción conceptual mostrando como los factores tectónicos, climáticos y antrópicos condicionan las notables diferencias entre el registro paleosismológico del sur y centro de Chile. (a) Sur y centro de Chile vistos a partir de una misma configuración costera. (b) El factor tectónico genera las primeras diferencias entre ambos sitios. Episodios de subsidencia cosísmica son más comunes en el sur de Chile, lo cual favorece el aumento del espacio de acomodación para los sedimentos. En contraste, Chile central es caracterizado por más frecuentes episodios de alzamiento, los cuales limitan el espacio de acomodación y generan la desaparición de lagunas costeras y otros ambientes de sedimentación de baja energía. Adicionalmente, el alzamiento costero promueve una mayor disponibilidad de sedimentos costeros que pueden ser redistribuidos por deflación, favoreciendo el crecimiento de dunas. (c) El factor climático condiciona el desarrollo de suelo orgánico en ambos sitios. Mayores precipitaciones en el sur de Chile promueven el rápido desarrollo de suelos orgánicos y las altas tasas de sedimentación en ambientes costeros, permitiendo la protección del registro geológico de terremotos y tsunamis. En contraste, bajas precipitaciones en Chile central dificultan el desarrollo de suelos, conduciendo a la pronta erosión de los depósitos. (d) El pobre registro paleosismológico de Chile central se ve adicionalmente perjudicado por la mayor densidad poblacional en comparación al sur de Chile, que continuamente degrada e interviene los ecosistemas.

No obstante, la preservación del registro en el sur de Chile también enfrenta limitaciones particulares asociadas a procesos biogénicos, especialmente la bioturbación. En ambientes templados y húmedos, la alta productividad biológica favorece la actividad de organismos bentónicos, raíces de vegetación y fauna intermareal que remueven o mezclan los sedimentos depositados (Cisternas et al., 2005; Spiske et al., 2020; Szczuciński, 2012; 2020). Este proceso puede alterar las estructuras sedimentarias originales, difuminar los límites entre capas de tsunami y suelos enterrados, e incluso redistribuir microfósiles como diatomeas o foraminíferos, dificultando la interpretación paleoambiental (Szczuciński, 2020). En consecuencia, aunque la alta tasa de sedimentación y el desarrollo de suelos orgánicos favorecen la preservación general de los eventos, la bioturbación actúa como un agente erosivo, reduciendo la resolución temporal del registro estratigráfico. Estos efectos post-depositacionales deben ser considerados al estudiar las secuencias de sedimentos costeros del sur de Chile.

Diferencias significativas en las tasas de sedimentación entre la zona centro y sur de Chile fueron observadas por Garret et al. (2013). En la desembocadura del Río Mataquito, estos autores notaron la ausencia de sedimentación en los meses posteriores al evento del 2010, impidiendo el muestreo de diatomeas para la cuantificación del cambio vertical cosísmico. En contraste, más hacia el sur, hasta 20 mm de sedimento fueron depositados sobre la antigua marisma. La pobre sedimentación o desarrollo de suelo en Chile central plantea una complicación para el registro geológico de cambios del nivel del terreno, ya que cuando la sedimentación es reanudada los materiales preservan una señal mezclada de tanto el desplazamiento cosísmico como postsísmico.

Otra limitante asociada a las condiciones climáticas de Chile central son las inusuales crecidas de ríos andinos, las cuales ocurren principalmente durante episodios de lluvias extremas asociados a ríos atmosféricos y eventos de El Niño (Rutlant y Fuenzalida, 1991; Aceituno, 1992). Estas crecidas pueden movilizar grandes volúmenes de sedimento, generando extensos depósitos de arena sobre las

planicies de inundación (Capítulo 3). Esto representa una complicación en el estudio de depósitos de tsunami, ya que enmascaran la señal sedimentaria de eventos marinos de alta energía, generando interpretaciones erradas desde el registro geológico. Por ejemplo, la interpretación errónea de depósitos de río atribuyéndolos a tsunamis resultaría en determinar intervalos de recurrencia de tsunamis más cortos, conduciendo a una sobreestimación de la amenaza. Investigaciones orientadas a los estudios de paleotsunamis deberían tener especial precaución con sitios adyacentes a grandes ríos andinos y, en lo posible, ser evitados como blancos de exploración. En tales contextos, información histórica acoplada con precisas dataciones derivadas de técnicas de luminiscencia (OSL; Tamura et al., 2019), podría contribuir significativamente a distinguir entre depósitos de origen fluvial y marino, proporcionando una refinada cronología para la reconstrucción de eventos extremos.

5.2.3 Factor antrópico

A los factores naturales se suman los efectos antrópicos, los cuales en Chile central son especialmente relevantes debido a la alta densidad poblacional y el intenso desarrollo industrial y agrícola de la franja costera (Figura 5.1d). La urbanización de áreas litorales, la canalización de cursos de agua, el relleno de humedales y de la franja costera, la construcción de infraestructura portuaria y la expansión de cultivos han modificado profundamente el paisaje costero, degradando o alterando sitios potenciales para el estudio paleosismológico (Figura 5.1d).

Especialmente en la costa norte de la Región del Maule, entre Lipimávida y la desembocadura del Río Mataquito, las modificaciones antrópicas asociadas a actividades agrícolas han perturbado el registro estratigráfico (Capítulo 2). Actividades como el arado de los suelos para cultivo remueven y mezclan los sedimentos superficiales, destruyendo la estratificación original y dificultando la identificación de antiguos depósitos de tsunami. Además, la nivelación de suelos y rellenos usados en la construcción de edificaciones han alterado la topografía natural, borrando evidencias sedimentarias de terremotos y tsunamis pasados, y

reduciendo progresivamente el potencial de preservación del registro paleosismológico en la zona.

5.3 Implicancias para futuras investigaciones en Chile central

Esta investigación destaca la urgencia de avanzar hacia estudios multidisciplinarios que integren enfoques complementarios para superar las limitaciones presentes en Chile central. La compleja interacción entre factores tectónicos, climáticos y antrópicos requiere que los futuros trabajos no se limiten a una sola línea de análisis, sino que combinen diversas herramientas y perspectivas para obtener interpretaciones más robustas del registro de terremotos y tsunamis.

Además, esta integración metodológica es fundamental no solo para mejorar la comprensión del registro geológico, sino también para fortalecer la evaluación de la amenaza sísmica y tsunamigénica en la región. Una visión multidisciplinaria que vincule análisis sedimentológicos, paleoecológicos, datos geodésicos, y percepción remota permitirá reducir la incertidumbre respecto a la recurrencia de grandes eventos y su impacto potencial en zonas densamente pobladas.

Asimismo, resulta prioritario extender este tipo de estudios hacia otros sectores de la costa chilena que presentan condiciones geomorfológicas y antecedentes históricos comparables, pero que aún carecen de investigaciones detalladas. Entre ellos destacan la Península de Arauco en el centro-sur y las planicies litorales de Quintero en la zona central, donde existen evidencias fragmentarias de antiguos alzamientos y subsidencias cosísmicas (Dura et al., 2015; Araya-Cornejo et al., 2025). De igual modo, sectores del norte de Chile, como la desembocadura del Río Loa y las planicies de Mejillones, ofrecen un contexto valioso para contrastar los patrones de deformación vertical observados en Chile central bajo diferentes regímenes sísmicos. Explorar estos sitios permitiría establecer comparaciones latitudinales, evaluar la persistencia temporal de los levantamientos costeros y generar un marco espacial más completo para comprender la dinámica del margen de subducción chileno.

Capítulo 6. Conclusiones

Los resultados de esta investigación permiten comprender con mayor profundidad los factores que explican la limitada preservación del registro geológico de terremotos y tsunamis en la costa de Chile central, así como los procesos que controlan la deformación vertical costera a largo plazo. A partir de la integración de datos satelitales, estratigráficos, paleoecológicos, históricos e instrumentales, se desarrolló un enfoque metodológico capaz de abordar los vacíos existentes en el registro paleosismológico de esta región altamente compleja y vulnerable.

En primer lugar, se identificaron tres factores principales que condicionan la formación y preservación del registro paleosismológico en Chile central: (i) el alzamiento tectónico sostenido, que reduce el espacio de acomodación y promueve la erosión; (ii) el clima mediterráneo semiárido, que restringe la preservación de ambientes de baja energía y limita el desarrollo de suelos orgánicos protectores; y (iii) la intervención antrópica, que ha alterado o destruido numerosos sitios potenciales debido a la urbanización costera, la actividad agrícola y el relleno de humedales. En conjunto, estos factores explican el carácter fragmentario y discontinuo del registro geológico regional, y justifican la necesidad de enfoques integradores que combinen distintas líneas de evidencia.

En segundo lugar, se demostró que la percepción remota de alta resolución constituye una herramienta efectiva para la identificación y delimitación de depósitos de tsunami recientes, complementando el trabajo de campo y extendiendo su alcance espacial. El mapeo satelital permitió reconocer con precisión el depósito del tsunami de 2010 en la costa del Maule, evidenciando su correspondencia con el área inundada. Este resultado valida el uso de la teledetección en la evaluación de la amenaza costera.

Asimismo, el análisis micropaleontológico de diatomeas permitió reconstruir la deformación vertical costera durante el último siglo, revelando la persistencia del alzamiento generado por el terremoto de 1906 en Campiche. La sustitución de

especies marinas por dulces, corroborada por observaciones geomorfológicas e históricas, sugiere que parte de la deformación cosísmica ha sido permanente. Este hallazgo apoya la hipótesis de que los terremotos con fuentes profundas en la zona de subducción de Chile central contribuyen al levantamiento sostenido del margen costero, desempeñando un papel fundamental en la construcción de la topografía litoral a largo plazo.

Finalmente, se concluye que la integración de enfoques metodológicos multidisciplinarios, que combinan evidencia satelital, sedimentológica, paleoecológica e instrumental, constituye una herramienta esencial para reconstruir los patrones de deformación vertical costera y los depósitos de tsunami en márgenes donde el registro geológico es escaso o erosionado. Esta aproximación no solo permite mejorar la comprensión del ciclo sísmico en Chile central, sino que también ofrece un marco conceptual y metodológico aplicable a otras zonas de subducción con registros incompletos. Los hallazgos de esta tesis contribuyen así a fortalecer la base científica necesaria para la evaluación de la amenaza sísmica y tsunamigénica, aportando información clave para la gestión y mitigación del riesgo en el litoral chileno.

Referencias

Abe, T., Goto, K. & Sugawara, D. (2012). Relationship between the maximum extent of tsunami sand and the inundation limit of the 2011 Tohoku-oki tsunami on the Sendai Plain, Japan. Sedimentary Geology, 282, 142–150. https://doi.org/10.1016/j.sedgeo.2012.05.004

Abe, T., Goto, K. & Sugawara, D. (2020). Spatial distribution and sources of tsunami deposits in a narrow valley setting - insight from 2011 Tohoku-oki tsunami deposits in northeastern Japan. Progress in Earth and Planetary Science, 7(1). https://doi.org/10.1186/s40645-019-0318-6

Aceituno, P. (1992). El Niño, the southern oscillation, and ENSO: Confusing names for a complex ocean–atmosphere interaction. Bulletin of the American Meteorological Society, 73(4), 483–485. https://doi.org/10.1175/1520-0477-73.4.483

Acuña, D. A. (2012). Evolución paleogeográfica de la terraza marina de La Trinchera, región del Maule. https://repositorio.uchile.cl/handle/2250/100469

Aedo, D., Melnick, D., Garrett, E. & Pino, M. (2021). Source and distribution of tsunami deposits at Chaihuín marsh (40° S/73.5° W), Chile. Andean Geology 48 (1): 125-152. http://dx.doi.org/10.5027/andgeoV48n1-3258

Aedo, D., Cisternas, M., Melnick, D., Esparza, C., Winckler, P. & Saldaña, B. (2023). Decadal coastal evolution spanning the 2010 Maule earthquake at Isla Santa Maria, Chile: Framing Darwin's accounts of uplift over a seismic cycle. Earth Surface Processes and Landforms, 48(12), 2319–2333. https://doi.org/10.1002/esp.5615

Araneda, M. & Avendaño, M.S. (1993). Gravity Variations in Central Chile. In: Torge, W., Fletcher, A.G., Tanner, J.G. (eds) Recent Geodetic and Gravimetric Research in Latin America. International Association of Geodesy Symposia, vol 111. Springer, Berlin, Heidelberg. https://doi.org/10.1007/978-3-642-88055-1_14

Araya-Cornejo, C. & Carvajal, M. (2016). Efectos geomorfológicos del tsunami de Chile de 2010 frente a la zona de máximo slip, revelados por imágenes satelitales y observaciones de campo: El caso del litoral arenoso La Trinchera,

Región del Maule. Investigaciones geográficas, 52, 5. https://doi.org/10.5354/0719-5370.2016.43260

Araya-Cornejo, C., Aedo, D., Martínez, C., & Melnick, D. (2025). LiDAR and GPR data reveal the Holocene evolution of a strandplain in a tectonically active coast. Remote Sensing, 17(16), 2798. https://doi.org/10.3390/rs17162798

Araya, K., Muñoz, P., Dezileau, L., Maldonado, A., Campos-Caba, R., Rebolledo, L., Cardenas, P. & Salamanca, M. (2022). Extreme Sea Surges, Tsunamis and Pluvial Flooding Events during the Last ~1000 Years in the Semi-Arid Wetland, Coquimbo Chile. Geosciences, 12, 135. https://doi.org/10.3390/geosciences12030135

Araya, K., Dezileau, L., Muñoz, P., Maldonado, A., Condomines, M., Khalfaoui, O., Oyanadel-Urbina, P. & Araya, B. A. (2024). Reconstruction of extreme floods and tsunamis from coastal sedimentary archives in Los Choros, Coquimbo region, 28°S, Chile. Natural Hazards (Dordrecht, Netherlands). https://doi.org/10.1007/s11069-024-06644-8

Asokan, A. & Anitha, J. (2019). Change detection techniques for remote sensing applications: a survey. Earth Science Informatics, 12(2), 143–160. https://doi.org/10.1007/s12145-019-00380-5

Atwater, B. F. (1987). Evidence for great Holocene earthquakes along the outer coast of Washington state. Science (New York, N.Y.), 236, 942–944. https://doi.org/10.1126/science.236.4804.942

Atwater, B.F. & Hemphill-Haley, E. (1997). Recurrence Intervals for Great Earthquakes of the Past 3,500 Years at Northeastern Willapa Bay, vol. 1576. U.S. Geological Survey Professional Paper, Washington, pp. 1-108.

Atwater, B. F., Núñez, H. J. & Vita-Finzi, C. (1992). Net Late Holocene emergence despite earthquake-induced submergence, south-central Chile. Quaternary International: The Journal of the International Union for Quaternary Research, 15–16, 77–85. https://doi.org/10.1016/1040-6182(92)90037-3

Atwater, B. F., Furukawa, R., Hemphill-Haley, E., Ikeda, Y., Kashima, K., Kawase, K., Kelsey, H. M., Moore, A. L., Nanayama, F., Nishimura, Y., Odagiri, S., Ota, Y., Park, S.-C., Satake, K., Sawai, Y. & Shimokawa, K. (2004). Seventeenth-

century uplift in eastern Hokkaido, Japan. The Holocene, 14(4), 487–501. https://doi.org/10.1191/0959683604hl726rp

Atwater, B.F., Musumi-Rokkaku, S., Satake, K., Tsuji, Y., Ueda, K. & Yamaguchi, D.K. (2015). The orphan tsunami of 1700—Japanese clues to a parent earthquake in North America, 2nd ed.: Seattle, University of Washington Press, U.S. Geological Survey Professional Paper 1707, 135 p.

Aztorquiza, O. (1929). Lota, antecedentes históricos con una monografía de la Compañía Minera e Industrial de Chile, Sociedad Imprenta y Litografía Concepción, Concepción.

Barrientos, S. E. (1988). Slip distribution of the 1985 Central Chile earthquake. Tectonophysics, 145, 225–241. https://doi.org/10.1016/0040-1951(88)90197-7

Barrientos, S.E. (1995). Dual seismogenic behavior: The 1985 Central Chile earthquake. Geophysical Research Letters, 22 (24), 3541-3544.

Barrientos, S. E. (1997). Central Chile: An example of quasi-static crustal behavior. Island Arc, 6(3), 281–287. https://doi.org/10.1111/j.1440-1738.1997.tb00178.x

Barrientos, S. E., Plafker, G. & Lorca, E. (1992). Postseismic coastal uplift in southern Chile. Geophysical Research Letters, 19(7), 701–704. https://doi.org/10.1029/92gl00210

Bahlburg, H. & Spiske, M. (2012). Sedimentology of tsunami inflow and backflow deposits: key differences revealed in a modern example: Tsunami deposits at Isla Mocha. Sedimentology, 59(3), 1063–1086. https://doi.org/10.1111/j.1365-3091.2011.01295.x

Bahlburg, H. & Spiske, M. (2015). Styles of early diagenesis and the preservation potential of onshore tsunami deposits—A re-survey of Isla Mocha, Central Chile, 2 years after the February 27, 2010, Maule tsunami. Sedimentary Geology, 326, 33–44. https://doi.org/10.1016/j.sedgeo.2015.06.009

Belgiu, M. & Drăguţ, L. (2016). Random forest in remote sensing: A review of applications and future directions. ISPRS Journal of Photogrammetry and Remote Sensing: Official Publication of the International Society for Photogrammetry and Remote Sensing (ISPRS), 114, 24–31. https://doi.org/10.1016/j.isprsjprs.2016.01.011

Bernard, E. N., Mofjeld, H. O., Titov, V., Synolakis, C. E. & González, F. I. (2006). Tsunami: scientific frontiers, mitigation, forecasting and policy implications. Philosophical Transactions. Series A, Mathematical, Physical, and Engineering Sciences, 364(1845), 1989–2007. https://doi.org/10.1098/rsta.2006.1809

Bevis, M. & Brown, A. (2014). Trajectory models and reference frames for crustal motion geodesy. Journal of Geodesy, 88(3), 283–311. https://doi.org/10.1007/s00190-013-0685-5

Blott, S. J. & Pye, K. (2001). GRADISTAT: a grain size distribution and statistics package for the analysis of unconsolidated sediments. Earth Surface Processes and Landforms, 26(11), 1237–1248. https://doi.org/10.1002/esp.261

Borrero, J. C. (2005). Field data and satellite imagery of tsunami effects in Banda Aceh. Science (New York, N.Y.), 308(5728), 1596. https://doi.org/10.1126/science.1110957

Brader, M., Garrett, E., Melnick, D. & Shennan, I. (2021). Sensitivity of tidal marshes as recorders of major megathrust earthquakes: constraints from the 25 December 2016 Mw7.6 Chiloé earthquake, Chile. Journal of Quaternary Science, 36(6), 991–1002. https://doi.org/10.1002/jqs.3323

Bravo, F., Koch, P., Riquelme, S., Fuentes, M. & Campos, J. (2019). Slip distribution of the 1985 Valparaíso earthquake constrained with seismic and deformation data. Seismological Research Letters. https://doi.org/10.1785/0220180396

Breiman, L. (2001). Random Forests. Machine learning, 45(1), 5–32. https://doi.org/10.1023/a:1010933404324

Brown, L. D., Reilinger, R. E., Holdahl, S. R. & Balazs, E. I. (1977). Postseismic crustal uplift near Anchorage, Alaska. Journal of Geophysical Research, 82(23), 3369–3378. https://doi.org/10.1029/jb082i023p03369

Campos, J., Hatzfeld, D., Madariaga, R., Lopez, G., Kausel, E., Zollo, A., Iannacone, G., Fromm, R., Barrientos, S. & Lyon-Caen, H. (2002). A seismological study of the 1835 seismic gap in south-central Chile. Physics of the Earth and Planetary Interiors, 132(1–3), 177–195. https://doi.org/10.1016/s0031-9201(02)00051-1

Carrillo-Briceño, J.D., González-Barba, G., Landaeta, M.F. & Nielsen, S.N. (2013). Condrictios fósiles del Plioceno superior de la Formación Horcón, Región de Valparaíso, Chile central. Revista Chilena de Historia Natural, 86 (2), 191–206. http://dx.doi.org/10.4067/S0716-078X2013000200008

Carvajal, M., Cisternas, M. & Catalán, P. A. (2017a). Source of the 1730 Chilean earthquake from historical records: Implications for the future tsunami hazard on the coast of Metropolitan Chile. Journal of Geophysical Research. Solid Earth, 122(5), 3648–3660. https://doi.org/10.1002/2017jb014063

Carvajal, M., Cisternas, M., Gubler, A., Catalán, P. A., Winckler, P. & Wesson, R. L. (2017b). Reexamination of the magnitudes for the 1906 and 1922 Chilean earthquakes using Japanese tsunami amplitudes: Implications for source depth constraints. Journal of Geophysical Research. Solid Earth, 122(1), 4–17. https://doi.org/10.1002/2016jb013269

Carvajal, M., Cisternas, M., Gubler, A. & Muñoz, D. (2019). Tsunamis pasados y futuros en Chile Central. In La zona costera en Chile: Adaptación y planificación para la resiliencia. Santiago. Serie GeoLibros N°31, 395 p.

Castilla, J. C. (1988). Earthquake-caused coastal uplift and its effects on rocky intertidal kelp communities. Science (New York, N.Y.), 242(4877), 440–443. https://doi.org/10.1126/science.242.4877.440

Catalán, P. A., Cienfuegos, R. & Villagrán, M. (2014). Perspectives on the long-term equilibrium of a wave dominated coastal zone affected by tsunamis: The case of central Chile. Journal of Coastal Research, 71, 55–61. https://doi.org/10.2112/si71-007.1

CIGIDEN. (2023). Informe Post-Desastre. Evento: Inundaciones 21-26 junio 2023, cuencas del Rio Mataquito y Río Maule (Región del Maule). Addendum Informe Post Desastre. Evento: Comparación de Eventos Hidrometeorológicos de junio y agosto 2023, Cuenca Río Mataquito. Centro de Investigación para la Gestión Integrada del Riesgo de Desastres.

Chagué-Goff, C. (2010). Chemical signatures of palaeotsunamis: A forgotten proxy? Marine Geology, 271(1–2), 67–71. https://doi.org/10.1016/j.margeo.2010.01.010

Chagué-Goff, C., Goff, J., Wong, H. K. Y. & Cisternas, M. (2015). Insights from geochemistry and diatoms to characterise a tsunami's deposit and maximum inundation limit. Marine Geology, 359, 22–34. https://doi.org/10.1016/j.margeo.2014.11.009

Cheng, W. & Weiss, R. (2013). On sediment extent and runup of tsunami waves. Earth and Planetary Science Letters, 362, 305–309. https://doi.org/10.1016/j.epsl.2012.12.004

Cienfuegos, R., Villagran, M., Aguilera, J. C., Catalán, P., Castelle, B. & Almar, R. (2014). Video monitoring and field measurements of a rapidly evolving coastal system: the river mouth and sand spit of the Mataquito River in Chile. Journal of coastal research, 70, 639–644. https://doi.org/10.2112/si70-108.1

Cienfuegos, R., Catalán, P. A., Urrutia, A., Benavente, R., Aránguiz, R. & González, G. (2018). What can we do to forecast tsunami hazards in the near field given large epistemic uncertainty in rapid seismic source inversions? Geophysical Research Letters, 45(10), 4944–4955. https://doi.org/10.1029/2018gl076998

Cisternas, M., Araneda, A., Martínez, P. & Pérez, S. (2001). Effects of historical land use on sediment yield from a lacustrine watershed in central Chile. Earth Surface Processes and Landforms, 26(1), 63–76. https://doi.org/10.1002/1096-9837(200101)26:1<63::aid-esp157>3.0.co;2-j

Cisternas, M., Atwater, B. F., Torrejón, F., Sawai, Y., Machuca, G., Lagos, M., Eipert, A., Youlton, C., Salgado, I., Kamataki, T., Shishikura, M., Rajendran, C. P., Malik, J. K., Rizal, Y. & Husni, M. (2005). Predecessors of the giant 1960 Chile earthquake. Nature, 437, 404–407. https://doi.org/10.1038/nature03943

Cisternas, M., Garrett, E., Wesson, R., Dura, T. & Ely, L. L. (2017). Unusual geologic evidence of coeval seismic shaking and tsunamis shows variability in earthquake size and recurrence in the area of the giant 1960 Chile earthquake. Marine Geology, 385, 101–113. https://doi.org/10.1016/j.margeo.2016.12.007

Comte, D., Eisenberg, A., Lorca, E., Pardo, M., Ponce, L., Saragoni, R., Singh, S. K. & Suárez, G. (1986). The 1985 central Chile earthquake: a repeat of previous great earthquakes in the region? Science (New York, N.Y.), 233(4762), 449–453. https://doi.org/10.1126/science.233.4762.449

Contesse, D. (1987). Apuntes y consideraciones para la historia del Pino radiata en Chile. Boletín de la Academia Chilena de la Historia, 97, 351–373.

Contreras, M. & Winckler, P. (2013). Pérdidas de vidas, viviendas, infraestructura y embarcaciones por el tsunami del 27 de Febrero de 2010 en la costa central de Chile. Obras y Proyectos, 14, 6–19. https://doi.org/10.4067/s0718-28132013000200001

Cosenza-Muralles, B., DeMets, C., Márquez-Azúa, B., Sánchez, O., Stock, J., Cabral-Cano, E. & McCaffrey, R. (2022). Co-seismic and post-seismic deformation for the 1995 Colima–Jalisco and 2003 Tecomán thrust earthquakes, Mexico subduction zone, from modelling of GPS data. Geophysical Journal International, 228 (3), 2137–2173. https://doi.org/10.1093/gji/ggab435

Costa, P. J. M. & Andrade, C. (2020). Tsunami deposits: Present knowledge and future challenges. Sedimentology, 67(3), 1189–1206. https://doi.org/10.1111/sed.12724

Cowan, H., Beattie, G., Hill, K., Evans, N., McGhie, C., Gibson, G., Lawrance, G., Hamilton, J., Allan, P., Bryant, M., Davis, M., Hyland, C., Oyarzo-Vera, C., Quintana-Gallo, P. & Smith, P. (2011). The M8.8 Chile earthquake, 27 February 2010. Bulletin of the New Zealand Society for Earthquake Engineering, 44(3), 123–166. https://doi.org/10.5459/bnzsee.44.3.123-166

Dare, P. M. (2005). Shadow analysis in high-resolution satellite imagery of urban areas. Photogrammetric Engineering and Remote Sensing, 71(2), 169–177. https://doi.org/10.14358/pers.71.2.169

Darwin, C. R. (1846). Geological observations on South America. Being the third part of the geology of the voyage of the Beagle, under the command of Capt. Fitzroy, R.N. during the years 1832 to 1836. Smith Elder and Co.

Dean, W. E. (1974). Determination of carbonate and organic matter in calcareous sediments and sedimentary rocks by loss on ignition; comparison with other methods. Journal of Sedimentary Research, 44 (1), 242–248. https://doi.org/10.1306/74D729D2-2B21-11D7-8648000102C1865D

Dearing, J. A. (1994). Environmental Magnetic Susceptibility Using the Bartington MS2 system, Chi Publ., Kenilworth, U. K.

Delile, H. & Salomon, F. (2020). Palaeotsunami deposits at the Tiber River mouth (Ostia Antica, Italy): Do they really exist? Earth-Science Reviews, 208(103268), 103268. https://doi.org/10.1016/j.earscirev.2020.103268

Denys, L. (1991). A check-list of the diatoms in the Holocene deposits of the western Belgian coastal plain with a survey of their apparent ecological requirements.

DePaolis, J. M., Dura, T., Witter, R. C., Haeussler, P. J., Bender, A., Curran, J. H. & Corbett, D. R. (2024). Repeated coseismic uplift of coastal lagoons above the Patton Bay splay fault system, Montague Island, Alaska, USA. Journal of Geophysical Research. Solid Earth, 129, e2023JB028552. https://doi.org/10.1029/2023jb028552

Donoso, C. & Lara, A. (1996). Utilización de los bosques nativos en Chile: pasado, presente y futuro. In Ecología de los bosques nativos de Chile. Editorial Universitaria, Santiago, pp. 234–255.

Dura, T. & Hemphill-Haley, E. (2020). Diatoms in tsunami deposits. In Geological records of tsunamis and other extreme waves (pp. 291–322). Elsevier.

Dura, T., Cisternas, M., Horton, B. P., Ely, L. L., Nelson, A. R., Wesson, R. L. & Pilarczyk, J. E. (2015). Coastal evidence for Holocene subduction-zone earthquakes and tsunamis in central Chile. Quaternary science reviews, 113, 93–111. https://doi.org/10.1016/j.quascirev.2014.10.015

Dura, T., Hemphill-Haley, E., Sawai, Y. & Horton, B. P. (2016a). The application of diatoms to reconstruct the history of subduction zone earthquakes and tsunamis. Earth-Science Reviews, 152, 181–197. https://doi.org/10.1016/j.earscirev.2015.11.017

Dura, T., Engelhart, S. E., Vacchi, M., Horton, B. P., Kopp, R. E., Peltier, W. R. & Bradley, S. (2016b). The role of Holocene relative sea-level change in preserving records of subduction zone earthquakes. Current Climate Change Reports, 2(3), 86–100. https://doi.org/10.1007/s40641-016-0041-y

Dura, T., Horton, B. P., Cisternas, M., Ely, L. L., Hong, I., Nelson, A. R., Wesson, R. L., Pilarczyk, J. E., Parnell, A. C. & Nikitina, D. (2017). Subduction zone slip variability during the last millennium, south-central Chile. Quaternary Science Reviews, 175, 112–137. https://doi.org/10.1016/j.quascirev.2017.08.023

Easton, G., J. González-Alfaro, A. Villalobos, G. Álvarez, D. Melgar, S. Ruiz, B. Sepúlveda, M. Escobar, T. León, J. Carlos Báez, et al. (2022). Complex rupture of the 2015 Mw 8.3 Illapel earthquake and prehistoric events in the Central Chile tsunami gap. Seismological Research Letter, XX, 1–18. https://doi.org/10.1785/0220210283

EERI. (2010). The MW 8.8 Chile Earthquake of February 27, 2010. Earthquake Engineering Research Institute (EERI) newsletter, Special Earthquake Report: 20 p.

Egbert, G. D. & Erofeeva, S. Y. (2002). Efficient inverse modeling of barotropic ocean tides. Journal of Atmospheric and Oceanic Technology, 19(2), 183–204. https://doi.org/10.1175/1520-0426(2002)019<0183:eimobo>2.0.co;2

Eisenberg, A., Husid, R. & Luco, J. E. (1972). A preliminary report on the July 8, 1971 Chilean earthquake. Bulletin of the Seismological Society of America, 62(1), 423-430. https://doi.org/10.1785/BSSA0620010423

Ely, L. L., Cisternas, M., Wesson, R. L. & Dura, T. (2014). Five centuries of tsunamis and land-level changes in the overlapping rupture area of the 1960 and 2010 Chilean earthquakes. Geology, 42(11), 995–998. https://doi.org/10.1130/g35830.1

Engel M. & Brückner, H. (2011). The identification of palaeo-tsunami deposits— a major challenge in coastal sedimentary research. Coastline Reports 17:65–80

Faegri, K. & Iversen, J. (1989). Textbook of Pollen Analysis. London, United Kingdom.

Farías, M., Vargas, G., Tassara, A., Carretier, S., Baize, S., Melnick, D. & Bataille, K. (2010). Land-level changes produced by the Mw 8.8 2010 Chilean earthquake. Science (New York, N.Y.), 329(5994), 916. https://doi.org/10.1126/science.1192094

Fernández, J. & Venegas, C. (2010). Evaluación preliminar de peligros geológicos: Área de Duao-Iloca, Región del Maule. Mapa 15-2: Peligro de inundación por tsunami e inundación por desborde de cauces. Geología para la reconstrucción y la gestión del riesgo. Servicio Nacional de Geología y

Minería, Informe Registrado IR-10-43: 12 p., 21 mapas diferentes escalas. Santiago.

Fernández, J., Venegas, C., Contreras, J. P., Naranjo, J. A. & Marín, M. (2010). Área de inundación por tsunami del 27 febrero 2010, Duao-Iloca, Región del Maule. Atlas: Mapas de inundación por el tsunami del 27 de febrero de 2010. Servicio Nacional de Geología y Minería, Santiago.

Flores-Aqueveque, V., Ortega, C., Fernandez, R., Carabias, D., Simonetti, R., Cartajena, I., Díaz, L. & Gonzalez, C. (2021). A multi-proxy reconstruction of depositional environment of a Late Pleistocene submerged site from the Central Coast of Chile (32°): Implications for drowned sites. Quaternary International, 601, 15–27. https://doi.org/10.1016/j.quaint.2021.06.005

Folk, R. L. & Ward, W. C. (1957). Brazos River bar: a study in the significance of grain size parameters. Journal of Sedimentary Petrology, 27, 3–26.

Freisleben, R., Jara-Muñoz, J., Melnick, D., Molina, D., Tassara, A., Van der Beek, P. & Strecker, M. R. (2023). Deciphering permanent uplift along the pacific coast of South America through signal analysis of various tectonic processes. Tectonics, 42(10). https://doi.org/10.1029/2023tc007815

Fritz, H. M., Petroff, C. M., Catalán, P. A., Cienfuegos, R., Winckler, P., Kalligeris, N., Weiss, R., Barrientos, S. E., Meneses, G., Valderas-Bermejo, C., Ebeling, C., Papadopoulos, A., Contreras, M., Almar, R., Dominguez, J. C. & Synolakis, C. E. (2011). Field survey of the 27 February 2010 Chile tsunami. Pure and Applied Geophysics, 168(11), 1989–2010. https://doi.org/10.1007/s00024-011-0283-5

Frugone-Álvarez, M., Latorre, C., Giralt, S., Polanco-Martínez, J., Bernárdez, P., Oliva-Urcia, B., Maldonado, A., Carrevedo, M. L., Moreno, A., Delgado Huertas, A., Prego, R., Barreiro-Lostres, F. & Valero-Garcés, B. (2017). A 7000-year high-resolution lake sediment record from coastal central Chile (Lago Vichuquén, 34°S): implications for past sea level and environmental variability. Journal of Quaternary Science, 32(6), 830–844. https://doi.org/10.1002/jqs.2936

García, J., Andrade, B., Calderón, M. & Lüthgens, C. (2019). Multi-millennial scale climate variability during MIS 3 and MIS 2 inferred from luminescence dating of coastal sand dunes and buried paleosol sequences in central Chile, 32°S. Journal of Quaternary Science, 34(3), 203-214. https://doi.org/10.1002/jqs.3092

Garrett, E., Shennan, I., Watcham, E. P. & Woodroffe, S. A. (2013). Reconstructing paleoseismic deformation, 1: modern analogues from the 1960 and 2010 Chilean great earthquakes. Quaternary Science Reviews, 75, 11–21. https://doi.org/10.1016/j.quascirev.2013.04.007

Garrett, E., Shennan, I., Woodroffe, S.A., Cisternas, M., Hocking, E.P. & Gulliver, P. (2015). Reconstructing paleoseismic deformation, 2: 1000 years of great earthquakes at Chucalén, south central Chile. Quaternary Science Reviews, 113, 112-122. http://dx.doi.org/10.1016/j.quascirev.2014.10.010

Gayo, E. M., Muñoz, A. A., Maldonado, A., Lavergne, C., Francois, J. P., Rodríguez, D., Klock-Barría, K., Sheppard, P. R., Aguilera-Betti, I., Alonso-Hernández, C., Mena-Carrasco, M., Urquiza, A. & Gallardo, L. (2022). A cross-cutting approach for relating anthropocene, environmental injustice and sacrifice zones. Earth's Future, 10(4). https://doi.org/10.1029/2021ef002217

Gelfenbaum, G. & Jaffe, B. (2003). Erosion and sedimentation from the 17 July, 1998 Papua New Guinea tsunami. Pure and applied geophysics, 160(10–11), 1969–1999. https://doi.org/10.1007/s00024-003-2416-y

Goff, J., Chagué-Goff, C., Nichol, S., Jaffe, B. & Dominey-Howes, D. (2012). Progress in palaeotsunami research. Sedimentary Geology, 243–244, 70–88. https://doi.org/10.1016/j.sedgeo.2011.11.002

González-Alfaro, J., Vargas, G., Ortlieb, L., González, G., Ruiz, S., Báez, J. C., Mandeng-Yogo, M., Caquineau, S., Álvarez, G., del Campo, F. & del Río, I. (2018). Abrupt increase in the coastal uplift and earthquake rate since ~40 ka at the northern Chile seismic gap in the Central Andes. Earth and Planetary Science Letters, 502, 32-45. https://doi.org/10.1016/j.epsl.2018.08.043

Goto, K., Chagué-Goff, C., Fujino, S., Goff, J., Jaffe, B., Nishimura, Y., Richmond, B., Sugawara, D., Szczuciński, W., Tappin, D. R., Witter, R. C. & Yulianto, E.

(2011). New insights of tsunami hazard from the 2011 Tohoku-oki event. Marine Geology, 290(1–4), 46–50. https://doi.org/10.1016/j.margeo.2011.10.004

Goto, K., Fujima, K., Sugawara, D., Fujino, S., Imai, K., Tsudaka, R., Abe, T. & Haraguchi, T. (2012). Field measurements and numerical modeling for the run-up heights and inundation distances of the 2011 Tohoku-oki tsunami at Sendai Plain, Japan. Earth, Planets, and Space: EPS, 64(12), 1247–1257. https://doi.org/10.5047/eps.2012.02.007

Graham, M. (1824). Journal of a residence in Chile during the year 1822 and a Voyage from Chile to Brazil in 1823. Longman, Hurst, Rees, Orme, Brown, and Green (Eds.), London. 534 p.

Grimm, E.C. (1987). CONISS: A Fortran 77 program for stratigraphically constrained cluster analysis by the method of the incremental sum of squares. Computers & Geosciences, 13, 13-35. https://doi.org/10.1016/0098-3004(87)90022-7

Hamilton, S. & Shennan, I. (2005a). Late Holocene great earthquakes and relative sea-level change at Kenai, southern Alaska. Journal of Quaternary Science, 20(2), 95–111. https://doi.org/10.1002/jqs.903

Hamilton, S. & Shennan, I. (2005b). Late Holocene relative sea-level changes and the earthquake deformation cycle around upper Cook Inlet, Alaska. Quaternary Science Reviews, 24(12–13), 1479–1498. https://doi.org/10.1016/j.quascirev.2004.11.003

Hamilton, S., Shennan, I., Combellick, R., Mulholland, J. & Noble, C. (2005). Evidence for two great earthquakes at Anchorage, Alaska and implications for multiple great earthquakes through the Holocene. Quaternary Science Reviews, 24(18–19), 2050–2068. https://doi.org/10.1016/j.quascirev.2004.07.027

Harnecker, O. (1914). Estudios Seísmicos. Solevantamiento de la costa en el terremoto del 16 de agosto de 1906. Diario El Progreso de Cabildo.

Hassan, G. S., Tietze, E. & De Francesco, C. G. (2009). Modern diatom assemblages in surface sediments from shallow lakes and streams in southern Pampas

(Argentina). Aquatic Sciences, 71(4), 487–499. https://doi.org/10.1007/s00027-009-0104-4

Hemphill-Haley, E. (1993). Taxonomy of recent and fossil (Holocene) diatoms (Bacillariophyta) from northern Willapa Bay, Washington: U.S. Geological Survey Open-File Report 93-289, 151 p. https://doi.org/10.3133/ofr93289

Hemphill-Haley, E. (1995). Diatom evidence for earthquake-induced subsidence and tsunami 300 years ago in southern coastal Washington. Geol. Soc. Am. Bull. 107, 367–378. https://doi.org/10.1130/0016-7606(1995)107<0367:DEFEIS>2.3.CO;2

Heusser, C. J. (1971). Pollen and spores of Chile: modern types of the Pteridophyta, Gymnospermae, and Angiospermae. Tucson: University of Arizona Press, 167 p.

Hidalgo-Corrotea, C., Alaniz, A. J., Vergara, P. M., Moreira-Arce, D., Carvajal, M. A., Pacheco-Cancino, P. & Espinosa, A. (2023). High vulnerability of coastal wetlands in Chile at multiple scales derived from climate change, urbanization, and exotic forest plantations. The Science of the Total Environment, 903, 166130. https://doi.org/10.1016/j.scitotenv.2023.166130

Higman, B. & Bourgeois, J. (2008). Deposits of the 1992 Nicaragua tsunami. In Tsunamiites (pp. 81–103). Elsevier.

Hocking, E. P., Garrett, E. & Cisternas, M. (2017). Modern diatom assemblages from Chilean tidal marshes and their application for quantifying deformation during past great earthquakes. Journal of Quaternary Science, 32(3), 396–415. https://doi.org/10.1002/jqs.2933

Hocking, E. P., Garrett, E., Aedo, D., Carvajal, M., & Melnick, D. (2021). Geological evidence of an unreported historical Chilean tsunami reveals more frequent inundation. Communications Earth & Environment, 2(1). https://doi.org/10.1038/s43247-021-00319-z

Hong, I., Dura, T., Ely, L. L., Horton, B. P., Nelson, A. R., Cisternas, M., Nikitina, D. & Wesson, R. L. (2017). A 600-year-long stratigraphic record of tsunamis in south-central Chile. The Holocene, 27(1), 39–51. https://doi.org/10.1177/0959683616646191

Horton, B. P., Sawai, Y., Hawkes, A. D. & Witter, R. C. (2011). Sedimentology and paleontology of a tsunami deposit accompanying the great Chilean earthquake of February 2010. Marine Micropaleontology, 79(3–4), 132–138. https://doi.org/10.1016/j.marmicro.2011.02.001

Horton, B. P., Milker, Y., Dura, T., Wang, K., Bridgeland, W. T., Brophy, L., Ewald, M., Khan, N. S., Engelhart, S. E., Nelson, A. R. & Witter, R. C. (2017). Microfossil measures of rapid sea-level rise: Timing of response of two microfossil groups to a sudden tidal-flooding experiment in Cascadia. Geology, 45(6), 535–538. https://doi.org/10.1130/g38832.1

Iinuma, T. (2018). Postseismic uplift along the Pacific coast of Tohoku and Kanto districts associated with the 2011 off the Pacific coast of Tohoku earthquake. Journal of disaster research, 13(3), 496–502. https://doi.org/10.20965/jdr.2018.p0496

INFOR (2008). Anuario Forestal 2008, Centro de Información Forestal (CIF), 169 pp.

Instituto Geográfico Militar, IGM (1985). El terremoto del 3 de Marzo de 1985 y los desplazamientos de la corteza terrestre. Terra Australis, 28: 7-12.

Ishihara, M. & Tadono, T. (2017). Land cover changes induced by the great east Japan earthquake in 2011. Scientific Reports, 7(1). https://doi.org/10.1038/srep45769

Izawa, M. R. M., Cloutis, E. A., Rhind, T., Mertzman, S. A., Applin, D. M., Stromberg, J. M. & Sherman, D. M. (2019). Spectral reflectance properties of magnetites: Implications for remote sensing. Icarus, 319, 525–539. https://doi.org/10.1016/j.icarus.2018.10.002

Jaffe, B. E., Borrero, J. C., Prasetya, G. S., Peters, R., McAdoo, B., Gelfenbaum, G., Morton, R., Ruggiero, P., Higman, B., Dengler, L., Hidayat, R., Kingsley, E., Kongko, W., Lukijanto, Moore, A., Titov, V. & Yulianto, E. (2006). Northwest Sumatra and offshore islands field survey after the December 2004 Indian ocean tsunami. Earthquake Spectra : The Professional Journal of the Earthquake Engineering Research Institute, 22(3_suppl), 105–135. https://doi.org/10.1193/1.2207724

Jaffe, B. E. & Gelfenbaum, G. (2002). Using tsunami deposits to improve assessment of tsunami risk. Solutions to Coastal Disasters '02. https://doi.org/10.1061/40605(258)72

Jaffe, B. E., Gelfenbaum, G., Rubin, D., Peters, R., Anima, R., Swensson, M., Olcese, D., Anticona, L. B., Gomez, J. C. & Riega, P. C. (2003). Identification and interpretation of tsunami deposits from the June 23, 2001 Peru tsunami. Proceedings of the international conference on coastal sediments , (p.13).

Jagodziński, R., Sternal, B., Szczuciński, W., Chagué-Goff, C. & Sugawara, D. (2012). Heavy minerals in the 2011 Tohoku-oki tsunami deposits—insights into sediment sources and hydrodynamics. Sedimentary Geology, 282, 57–64. https://doi.org/10.1016/j.sedgeo.2012.07.015

Jankaew, K., Atwater, B. F., Sawai, Y., Choowong, M., Charoentitirat, T., Martin, M. E. & Prendergast, A. (2008). Medieval forewarning of the 2004 Indian Ocean tsunami in Thailand. Nature, 455(7217), 1228–1231. https://doi.org/10.1038/nature07373

Jarrin, P., Nocquet, J.-M., Rolandone, F., Mora-Páez, H., Mothes, P. & Cisneros, D. (2023). Current motion and deformation of the Nazca Plate: new constraints from GPS measurements. Geophysical Journal International, 232(2), 842–863. https://doi.org/10.1093/gji/ggac353

Kânoğlu, U., Titov, V., Bernard, E. & Synolakis, C. (2015). Tsunamis: bridging science, engineering and society. Philosophical Transactions of the Royal Society A: Mathematical, Physical, and Engineering Sciences, 373(2053), 20140369. https://doi.org/10.1098/rsta.2014.0369

Kausel, E. (1986). Proceso sísmico, parámetros focales y réplicas del sismo del 3 de Marzo, 1985. In: El sismo del 3 de Marzo 1985, Chile. J. Monge (Ed.). Facultad de Ciencias Físicas y Matemáticas, Universidad de Chile. Santiago. 264 pp.

Kelson, K., Witter, R. C., Tassara, A., Ryder, I., Ledezma, C., Montalva, G., Frost, D., Sitar, N., Moss, R. & Johnson, L. (2012). Coseismic tectonic surface deformation during the 2010 Maule, Chile, Mw8.8 earthquake. Earthquake Spectra : The Professional Journal of the Earthquake Engineering Research Institute, 28(1_suppl1), 39–54. https://doi.org/10.1193/1.4000042

Kendrick, E. C., Bevis, M., Smalley, R. F., Cifuentes, O. & Galban, F. (1999). Current rates of convergence across the central Andes: estimates from continuous GPS observations. Geophysical Research Letters 26, 541–544. https://doi.org/10.1029/1999GL900040

Kongsen, S., Phantuwongraj, S., Choowong, M., Chawchai, S., Udomsak, S., Chansom, C., Ketthong, C., Surakiatchai, P., Miocic, J. M. & Preusser, F. (2022). Multi-proxy approach to identify the origin of high energy coastal deposits from Laem Son National Park, Andaman Sea of Thailand. Quaternary International, 625, 82–95. https://doi.org/10.1016/j.quaint.2022.04.017

Korrat, I. & Madariaga, R. (1986), Rupture of the Valparaiso (Chile) gap from 1971 to 1985. In Earthquake Source Mechanics, edited by S. Das, J. Boatwright, and C. H. Scholz, pp. 247–258, AGU, Washington, D. C. https://doi.org/10.1029/GM037p0247

Kortekaas, S. & Dawson, A. G. (2007). Distinguishing tsunami and storm deposits: An example from Martinhal, SW Portugal. Sedimentary Geology, 200(3–4), 208–221. https://doi.org/10.1016/j.sedgeo.2007.01.004

Koshimura, S., Moya, L., Mas, E. & Bai, Y. (2020). Tsunami damage detection with remote sensing: A review. Geosciences, 10(5), 177. https://doi.org/10.3390/geosciences10050177

Lario, J., Zazo, C. & Goy, J. L. (2016). Tectonic and morphosedimentary features of the 2010 Chile earthquake and tsunami in the Arauco Gulf and Mataquito River (Central Chile). Geomorphology (Amsterdam, Netherlands), 267, 16–24. https://doi.org/10.1016/j.geomorph.2016.05.019

Lay, T., Kanamori, H., Ammon, C. J., Nettles, M., Ward, S. N., Aster, R. C., Beck, S. L., Bilek, S. L., Brudzinski, M. R., Butler, R., DeShon, H. R., Ekström, G., Satake, K. & Sipkin, S. (2005). The great Sumatra-Andaman earthquake of 26 December 2004. Science (New York, N.Y.), 308(5725), 1127–1133. https://doi.org/10.1126/science.1112250

León, T., Lau, A. Y. A., Easton, G., & Goff, J. (2023). A comprehensive review of tsunami and palaeotsunami research in Chile. Earth-Science Reviews, 236(104273), 104273. https://doi.org/10.1016/j.earscirev.2022.104273

Li, S. & Chen, L. (2024). Vertical crustal deformation due to viscoelastic earthquake cycles at subduction zones: Implications for Nankai and Cascadia. Journal of Geophysical Research. Solid Earth, 129(8). https://doi.org/10.1029/2024jb028817

Lomnitz, C. (2004). Major earthquakes of Chile: A historical survey, 1535-1960. Seismological research letters, 75(3), 368–378. https://doi.org/10.1785/gssrl.75.3.368

Lu, D., Mausel, P., Brondízio, E. & Moran, E. (2004). Change detection techniques. International Journal of Remote Sensing, 25(12), 2365–2401. https://doi.org/10.1080/0143116031000139863

Luo, H. & Wang, K. (2021). Postseismic geodetic signature of cold forearc mantle in subduction zones. Nature Geoscience, 14(2), 104–109. https://doi.org/10.1038/s41561-020-00679-9

Machado, M. (1909). Los temblores en Chile; su causa inmediata y el porqué de sus efectos. Boletín del Museo Nacional de Chile, 1(6): 75-86.

MacInnes, B., Bourgeois, J., Pinegina, T. K. & Kravchunovskaya, E. A. (2009a). Tsunami geomorphology: Erosion and deposition from the 15 November 2006 Kuril Island tsunami. Geology, 37(11), 995–998. https://doi.org/10.1130/g30172a.1

MacInnes, B. T., Pinegina, T. K., Bourgeois, J., Razhigaeva, N. G., Kaistrenko, V. M. & Kravchunovskaya, E. A. (2009b). Field survey and geological effects of the 15 November 2006 kuril tsunami in the middle kuril islands. Pure and Applied Geophysics, 166(1–2), 9–36. https://doi.org/10.1007/s00024-008-0428-3

MacInnes, B., Weiss, R., Bourgeois, J. & Pinegina, T. K. (2010). Slip distribution of the 1952 Kamchatka great earthquake based on near-field tsunami deposits and historical records. Bulletin of the Seismological Society of America, 100(4), 1695–1709. https://doi.org/10.1785/0120090376

Madariaga, R., Métois, M., Vigny, C. & Campos, J. (2010). Geophysics. Central Chile finally breaks. Science (New York, N.Y.), 328(5975), 181–182. https://doi.org/10.1126/science.1189197

Maestripieri, N., Selleron, G. & Paegelow, M. (2017). Monitoring of chronological stages of deforestation - afforestation: the case of Southern Chile. Photo-Interprétation. European Journal of Applied Remote Sensing (PIEJARS), 51(3), pp.2-9. https://hal.science/hal-01621831v1

Maldonado, V., Contreras, M. & Melnick, D. (2021). A comprehensive database of active and potentially-active continental faults in Chile at 1:25,000 scale. Scientific Data, 8(1), 20. https://doi.org/10.1038/s41597-021-00802-4

Malgrange, M., Deschamps, A. & Madariaga, R. (1981). Thrust and extensional faulting under the Chilean coast: 1965, 1971 Aconcagua earthquakes. Geophysical Journal International, 66(2), 313–331. https://doi.org/10.1111/j.1365-246x.1981.tb05958.x

Martija, M. (2016). Puchuncaví desde la ventana. Puerto Ventanas S.A. 145 p.

Martin, M. E., Weiss, R., Bourgeois, J., Pinegina, T. K., Houston, H. & Titov, V. V. (2008). Combining constraints from tsunami modeling and sedimentology to untangle the 1969 Ozernoi and 1971 Kamchatskii tsunamis. Geophysical Research Letters, 35(1). https://doi.org/10.1029/2007gl032349

Martínez, C. & Rangel-Buitrago, N. (2023). The Kandinsky building in Chile: A case study demonstrating extreme urbanization pressure on coastal ecosystems. Ocean & Coastal Management, 246(106905), 106905. https://doi.org/10.1016/j.ocecoaman.2023.106905

Masotti, I., Aparicio-Rizzo, P., Yevenes, M. A., Garreaud, R., Belmar, L. & Farías, L. (2018). The influence of river discharge on nutrient export and phytoplankton biomass off the central Chile coast (33°–37°S): Seasonal cycle and interannual variability. Frontiers in Marine Science, 5:423. https://doi.org/10.3389/fmars.2018.00423

Matos-Llavona, P. I., Ely, L. L., MacInnes, B., Dura, T., Cisternas, M. A., Bourgeois, J., Bruce, D., DePaolis, J., Dolcimascolo, A., Horton, B. P., Melnick, D., Nelson, A. R., Szeliga, W. & Wesson, R. L. (2022). The giant 1960 tsunami in the context of a 6000-year record of paleotsunamis and coastal evolution in south-central Chile. Earth Surface Processes and Landforms, 47(8), 2062–2078. https://doi.org/10.1002/esp.5363

McAdoo, B. G., Richardson, N. & Borrero, J. (2007). Inundation distances and run-up measurements from ASTER, QuickBird and SRTM data, Aceh coast, Indonesia. International Journal of Remote Sensing, 28(13–14), 2961–2975. https://doi.org/10.1080/01431160601091795

Melnick, D., Cisternas, M., Moreno, M. & Norambuena, R. (2012a). Estimating coseismic coastal uplift with an intertidal mussel: calibration for the 2010 Maule Chile earthquake (Mw = 8.8). Quaternary Science Reviews, 42, 29–42. https://doi.org/10.1016/j.quascirev.2012.03.012

Melnick, D., Moreno, M., Cisternas, M. & Tassara, A. (2012b). Darwin' seismic gap closed by the 2010 Maule earthquake. Andean geology, 39(3). https://doi.org/10.5027/andgeov39n3-a11

Melnick, D. (2016). Rise of the central Andean coast by earthquakes straddling the Moho. Nature Geoscience, 9(5), 401–407. https://doi.org/10.1038/ngeo2683

Melnick, D., Moreno, M., Quinteros, J., Baez, J. C., Deng, Z., Li, S. & Oncken, O. (2017). The super-interseismic phase of the megathrust earthquake cycle in Chile. Geophysical Research Letters, 44(2), 784–791. https://doi.org/10.1002/2016gl071845

Melnick, D., Li, S., Moreno, M., Cisternas, M., Jara-Muñoz, J., Wesson, R., Nelson, A., Báez, J. C. & Deng, Z. (2018). Back to full interseismic plate locking decades after the giant 1960 Chile earthquake. Nature Communications, 9(1), 3527. https://doi.org/10.1038/s41467-018-05989-6

Meltzner, A. J., Sieh, K., Abrams, M., Agnew, D. C., Hudnut, K. W., Avouac, J.-P. & Natawidjaja, D. H. (2006). Uplift and subsidence associated with the great Aceh-Andaman earthquake of 2004. Journal of Geophysical Research, 111(B2). https://doi.org/10.1029/2005jb003891

Meltzner, A.J., Sieh, K., Chiang, H.-W., Wu, C.-C., Tsang, L.L.H., Shen, C.-C., Hill, E.M., Suwargadi, B.W., Natawidjaja, D.H., Philibosian, B. & Briggs, R.W. (2015). Time-varying interseismic strain rates and similar seismic ruptures on the Nias-Simeulue patch of the Sunda megathrust. Quaternary Science Reviews 122, 258-281. https://doi.org/10.1016/j.quascirev.2015.06.003

Mendoza, C., Hartzell, S. & Monfret, T. (1994). Wide-band analysis of the 3 March 1985 central Chile earthquake: Overall source process and rupture history. Bulletin of the Seismological Society of America, 84, 269-283.

Métois, M., Vigny, C. & Socquet, A. (2016). Interseismic coupling, megathrust earthquakes and seismic swarms along the Chilean subduction zone (38°–18°S). Pure and Applied Geophysics, 173(5), 1431–1449. https://doi.org/10.1007/s00024-016-1280-5

Meyen, F. (1834). Reise um die Erde. Sander'schen Buchhandlung (Ed.), Berlin. Vol. 1. p. 221.

Miers, J. (1826). Travels in Chile and La Plata, including accounts respecting the Geography, Geology, Statistics, Government, Finances, Agriculture, Manners and Customs and the Mining Operations in Chile. Baldwin, Cradock, and Joy (Eds.), London. Vol. 1. p. 388-394.

Minghelli, A., Spagnoli, J., Lei, M., Chami, M. & Charmasson, S. (2020). Shoreline extraction from WorldView2 satellite data in the presence of foam pixels using multispectral classification method. Remote Sensing, 12(16), 2664. https://doi.org/10.3390/rs12162664

Moernaut, J., Van Daele, M., Heirman, K., Fontijn, K., Strasser, M., Pino, M., Urrutia, R., & De Batist, M. (2014). Lacustrine turbidites as a tool for quantitative earthquake reconstruction: New evidence for a variable rupture mode in south central Chile: Earthquake-triggered turbidites in lakes. Journal of Geophysical Research. Solid Earth, 119(3), 1607–1633. https://doi.org/10.1002/2013jb010738

Monecke, K., Finger, W., Klarer, D., Kongko, W., McAdoo, B. G., Moore, A. L., & Sudrajat, S. U. (2008). A 1,000-year sediment record of tsunami recurrence in northern Sumatra. Nature, 455(7217), 1232–1234. https://doi.org/10.1038/nature07374

Monecke, K., Templeton, C. K., Finger, W., Houston, B., Luthi, S., McAdoo, B. G., Meilianda, E., Storms, J. E. A., Walstra, D.-J., Amna, R., Hood, N., Karmanocky, F. J., III, Nurjanah, Rusydy, I. & Sudrajat, S. U. (2015). Beach ridge patterns in West Aceh, Indonesia, and their response to large

earthquakes along the northern Sunda trench. Quaternary science reviews, 113, 159–170. https://doi.org/10.1016/j.quascirev.2014.10.014

Montessus de Ballore, F. (1912). Historia sísmica de los Andes Meridionales al sur del paralelo XVI. Cuarta parte. Chile central. Imprenta Cervantes, Santiago, Chile, 213 pp. https://doi.org/10.5354/0717-8883.1912.25477

Montessus de Ballore, F. (1915). Historia Sísmica de los Andes Meridionales al Sur del paralelo XVI. Quinta Parte. El Terremoto del 16 de Agosto de 1906. Sociedad Imprenta-Litografía “Barcelona”, Santiago-Valparaíso, Chile, 407 pp.

Moore, A., Goff, J., McAdoo, B. G., Fritz, H. M., Gusman, A., Kalligeris, N., Kalsum, K., Susanto, A., Suteja, D. & Synolakis, C. E. (2011). Sedimentary deposits from the 17 July 2006 western java tsunami, Indonesia: Use of grain size analyses to assess tsunami flow depth, speed, and traction carpet characteristics. Pure and Applied Geophysics, 168(11), 1951–1961. https://doi.org/10.1007/s00024-011-0280-8

Moore, A., Nishimura, Y., Gelfenbaum, G., Kamataki, T. & Triyono, R. (2006). Sedimentary deposits of the 26 December 2004 tsunami on the northwest coast of Aceh, Indonesia. Earth, Planets, and Space: EPS, 58(2), 253–258. https://doi.org/10.1186/bf03353385

Moreno, M., Melnick, D., Rosenau, M., Baez, J., Klotz, J., Oncken, O., Tassara, A., Chen, J., Bataille, K., Bevis, M., Socquet, A., Bolte, J., Vigny, C., Brooks, B., Ryder, I., Grund, V., Smalley, B., Carrizo, D., Bartsch, M. & Hase, H. (2012). Toward understanding tectonic control on the Mw 8.8 2010 Maule Chile earthquake. Earth and Planetary Science Letters, 321–322, 152–165. https://doi.org/10.1016/j.epsl.2012.01.006

Mori, N., Takahashi, T., Yasuda, T., & Yanagisawa, H. (2011). Survey of 2011 Tohoku earthquake tsunami inundation and run-up. Geophysical Research Letters, 38(7). https://doi.org/10.1029/2011gl049210

Moris, R., Bergamini, K., Gilabert, H., Culagovski, R., Zaviezo, D., Medina, J. I., Alarcón, A. & Ángel, P. (2021). Impact of population growth in the central coastal zone of Chile: Factors for estimating tourism carrying capacity based

on the case study of one Latin American seaside resort. Sustainability, 13(6), 3527. https://doi.org/10.3390/su13063527

Morton, R. A., Gelfenbaum, G. & Jaffe, B. E. (2007). Physical criteria for distinguishing sandy tsunami and storm deposits using modern examples. Sedimentary Geology, 200(3–4), 184–207. https://doi.org/10.1016/j.sedgeo.2007.01.003

Morton, R. A., Gelfenbaum, G., Buckley, M. L. & Richmond, B. M. (2011). Geological effects and implications of the 2010 tsunami along the central coast of Chile. Sedimentary Geology, 242(1–4), 34–51. https://doi.org/10.1016/j.sedgeo.2011.09.004

Nanayama, F., Satake, K., Furukawa, R., Shimokawa, K., Atwater, B. F., Shigeno, K., & Yamaki, S. (2003). Unusually large earthquakes inferred from tsunami deposits along the Kuril trench. Nature, 424(6949), 660–663. https://doi.org/10.1038/nature01864

Nash, D. J., Bateman, M. D., Bullard, J. E., & Latorre, C. (2018). Late Quaternary coastal evolution and aeolian sedimentation in the tectonically-active southern Atacama Desert, Chile. Palaeogeography, Palaeoclimatology, Palaeoecology, 490, 546–562. https://doi.org/10.1016/j.palaeo.2017.11.040

Nelson, A. R., Shennan, I. & Long, A. J. (1996). Identifying coseismic subsidence in tidal-wetland stratigraphic sequences at the Cascadia subduction zone of western North America. Journal of Geophysical Research, 101(B3), 6115–6135. https://doi.org/10.1029/95jb01051

Nichol, S. L. & Kench, P. S. (2008). Sedimentology and preservation potential of carbonate sand sheets deposited by the December 2004 Indian Ocean tsunami: South Baa Atoll, Maldives: Tsunami sand sheets. Sedimentology, 55(5), 1173–1187. https://doi.org/10.1111/j.1365-3091.2007.00941.x

Nishenko, S. P. (1985). Seismic potential for large and great interplate earthquakes along the Chilean and Southern Peruvian Margins of South America: A quantitative reappraisal. Journal of Geophysical Research, 90(B5), 3589. https://doi.org/10.1029/jb090ib05p03589

Nishimura, T. (2014). Pre-, co-, and post-Seismic deformation of the 2011 Tohoku-Oki earthquake and its implication to a paradox in short-term and long-term. Journal of disaster research, 9(3), 294–302. https://doi.org10.20965/jdr.2014.p0294

Norabuena, E. O., Dixon, T. H., Stein, S., & Harrison, C. G. A. (1999). Decelerating Nazca-South America and Nazca-Pacific Plate motions. Geophysical Research Letters, 26(22), 3405–3408. https://doi.org/10.1029/1999gl005394

Norio, O., Ye, T., Kajitani, Y., Shi, P. & Tatano, H. (2011). The 2011 eastern Japan great earthquake disaster: Overview and comments. International journal of disaster risk science, 2(1), 34–42. https://doi.org/10.1007/s13753-011-0004-9

Ozawa, S., Nishimura, T., Suito, H., Kobayashi, T., Tobita, M. & Imakiire, T. (2011). Coseismic and postseismic slip of the 2011 magnitude-9 Tohoku-Oki earthquake. Nature, 475(7356), 373–376. https://doi.org/10.1038/nature10227

Paris, R., Wassmer, P., Sartohadi, J., Lavigne, F., Barthomeuf, B., Desgages, E., Grancher, D., Baumert, P., Vautier, F., Brunstein, D. & Gomez, C. (2009). Tsunamis as geomorphic crises: Lessons from the December 26, 2004 tsunami in Lhok Nga, West Banda Aceh (Sumatra, Indonesia). Geomorphology (Amsterdam, Netherlands), 104(1–2), 59–72. https://doi.org/10.1016/j.geomorph.2008.05.040

Parker, J., Kenyon, R. V. & Troxel, D. E. (1983). Comparison of interpolating methods for image resampling. IEEE Transactions on Medical Imaging, 2(1), 31–39. https://doi.org/10.1109/TMI.1983.4307610

Peel, M. C., Finlayson, B. L. & McMahon, T. A. (2007). Updated world map of the Köppen-Geiger climate classification. Hydrology and Earth System Sciences, 11(5), 1633–1644. https://doi.org/10.5194/hess-11-1633-2007

Phantuwongraj, S. & Choowong, M. (2012). Tsunamis versus storm deposits from Thailand. Natural Hazards (Dordrecht, Netherlands), 63(1), 31–50. https://doi.org/10.1007/s11069-011-9717-8

Pilarczyk, J. E., Dura, T., Horton, B. P., Engelhart, S. E., Kemp, A. C. & Sawai, Y. (2014). Microfossils from coastal environments as indicators of paleo-

earthquakes, tsunamis and storms. Palaeogeography, Palaeoclimatology, Palaeoecology, 413, 144–157. https://doi.org/10.1016/j.palaeo.2014.06.033

Pinegina, T. K., Bazanova, L. I., Zelenin, E. A., Bourgeois, J., Kozhurin, A. I., Medvedev, I. P. & Vydrin, D. S. (2018). Holocene tsunamis in avachinsky bay, Kamchatka, Russia. Pure and Applied Geophysics, 175(4), 1485–1506. https://doi.org/10.1007/s00024-018-1830-0

Pissis, A. (1854). Descripción de la Provincia de Valparaíso. Anales De La Universidad De Chile.

Plafker, G. & Savage, J. C. (1970). Mechanism of the Chilean earthquakes of may 21 and 22, 1960. Geological Society of America bulletin, 81(4), 1001. https://doi.org/10.1130/0016-7606(1970)81[1001:motceo]2.0.co;2

Plafker, G. (1965). Tectonic Deformation Associated with the 1964 Alaska Earthquake. Science (New York, N.Y.), 148(3678), 1675–1687. https://doi.org/10.1126/science.148.3678.1675

Plafker, G. (1969). Tectonics of the March 27, 1964, Alaska earthquake. In US geological survey professional paper. https://doi.org/10.3133/pp543I

Plafker, G. (1985). Geologic reconnaissance of the March 3, 1985, Chile earthquake. In: Preliminary report of investigations of the central Chile Earthquake of March 3, 1985. S.T. Algermissen (Ed.) U.S. Geological Survey, Open file Report 85-542. Denver, Colorado. 180 pp.

Pomar, L. (1876). Hidrografía. Reconocimiento de la parte del litoral de Chile, comprendida entre la Viña del Mar i la Caleta Maitencillo, por el vapor trasporte nacional Ancud, al mando del capitan de corbeta don Luis Pomar. Anales De La Universidad De Chile, Pág. 583–629.

Ramakrishnan, D., Ghosh, S. K., Raja, V. K. M., Chandran, R. V. & Jeyram, A. (2005). Trails of the killer tsunami: A preliminary assessment using satellite remote sensing technique. Current Science, 88, 709–711.

Ramírez, C. & Añazco, N. (1982). Variaciones estacionales en el desarrollo de Scirpus californicus, Typha angustifolia y Phragmites communis en pantanos valdivianos, Chile. Agro Sur 10(2): 111-123.

Ramírez-Herrera, M. T., Lagos, M., Hutchinson, I., Kostoglodov, V., Machain, M. L., Caballero, M., Goguitchaichvili, A., Aguilar, B., Chagué-Goff, C., Goff, J., Ruiz-Fernández, A.-C., Ortiz, M., Nava, H., Bautista, F., Lopez, G. I. & Quintana, P. (2012). Extreme wave deposits on the Pacific coast of Mexico: Tsunamis or storms? — A multi-proxy approach. Geomorphology (Amsterdam, Netherlands), 139–140, 360–371. https://doi.org/10.1016/j.geomorph.2011.11.002

Ramírez-Herrera, M. T. & Navarrete-Pacheco, J. A. (2013). Satellite data for a rapid assessment of tsunami inundation areas after the 2011 Tohoku tsunami. Pure and Applied Geophysics, 170(6–8), 1067–1080. https://doi.org/10.1007/s00024-012-0537-x

Reid, H.F. (1910). The mechanics of the earthquake. The California Earthquake of April 18, 1906. Report of the State Earthquake Investigation Commission, Carnegie Institution of Washington, Washington DC.

Richmond, B., Szczuciński, W., Chagué-Goff, C., Goto, K., Sugawara, D., Witter, R., Tappin, D. R., Jaffe, B., Fujino, S., Nishimura, Y. & Goff, J. (2012). Erosion, deposition and landscape change on the Sendai coastal plain, Japan, resulting from the March 11, 2011 Tohoku-oki tsunami. Sedimentary Geology, 282, 27–39. https://doi.org/10.1016/j.sedgeo.2012.08.005

Rivano, S., Sepúlveda, P., Boric, R. & Espiñeira, D. (1993). Hojas Quillota y Portillo, V Región. Servicio Nacional de Geología y Minería, Carta Geológica de Chile, No. 73.

Ruegg, J. C., Rudloff, A., Vigny, C., Madariaga, R., de Chabalier, J. B., Campos, J., Kausel, E., Barrientos, S. & Dimitrov, D. (2009). Interseismic strain accumulation measured by GPS in the seismic gap between Constitución and Concepción in Chile. Physics of the Earth and Planetary Interiors, 175(1–2), 78–85. https://doi.org/10.1016/j.pepi.2008.02.015

Ruiz, S., Grandin, R., Dionicio, V., Satriano, C., Fuenzalida, A., Vigny, C., Kiraly, E., Meyer, C., Baez, J. C., Riquelme, S., Madariaga, R. & Campos, J. (2013). The Constitución earthquake of 25 March 2012: A large aftershock of the Maule

earthquake near the bottom of the seismogenic zone. Earth and Planetary Science Letters, 377, 347–357. https://doi.org/10.1016/j.epsl.2013.07.017

Ruiz, S. & Madariaga, R. (2018). Historical and recent large megathrust earthquakes in Chile. Tectonophysics, 733, 37–56. https://doi.org/10.1016/j.tecto.2018.01.015

Rutllant, J. & Fuenzalida, H. (1991). Synoptic aspects of the central chile rainfall variability associated with the southern oscillation. International Journal of Climatology: A Journal of the Royal Meteorological Society, 11(1), 63–76. https://doi.org/10.1002/joc.3370110105

Saldaña, B., Cisternas, M., Chávez, R.O., Aedo, D., Guerra, M. & Carreño, A. (2025a) Mapping tsunami deposits through a classification model based on satellite images. Earth Surface Processes and Landforms, 50(1), e6055. https://doi.org/10.1002/esp.6055

Saldaña, B., Cisternas, M., Carvajal, M., Melnick, D., Cortés-Aranda J., Francois, J.P., Carreño, A. & Guerra, M. (2025b). Paleoseismological evidence of a century of coastal deformation in central Chile: lasting emergence and ongoing submergence. Quaternary Science Advances, 19, 100291. https://doi.org/10.1016/j.qsa.2025.100291

Saldías, G. (2011). Variabilidad espacio-temporal de plumas fluviales en Chile central a partir de mediciones satelitales de alta resolución. Thesis for: Master of Science in Oceanography. Universidad de Concepción.

Saldías, G. S., Sobarzo, M., Largier, J., Moffat, C. & Letelier, R. (2012). Seasonal variability of turbid river plumes off central Chile based on high-resolution MODIS imagery. Remote Sensing of Environment, 123, 220–233. https://doi.org/10.1016/j.rse.2012.03.010

Satake, K. (2014). Advances in earthquake and tsunami sciences and disaster risk reduction since the 2004 Indian ocean tsunami. Geoscience Letters, 1(1). https://doi.org/10.1186/s40562-014-0015-7

Sawai, Y. (2001). Episodic emergence in the past 3000 years at the Akkeshi estuary, Hokkaido, northern Japan. Quaternary Research, 56(2), 231–241. https://doi.org/10.1006/qres.2001.2258

Sawai, Y., Satake, K., Kamataki, T., Nasu, H., Shishikura, M., Atwater, B. F., Horton, B. P., Kelsey, H. M., Nagumo, T. & Yamaguchi, M. (2004). Transient uplift after a 17th-century earthquake along the Kuril subduction zone. Science (New York, N.Y.), 306(5703), 1918–1920. https://doi.org/10.1126/science.1104895

Sawai, Y., Namegaya, Y., Okamura, Y., Satake, K., & Shishikura, M. (2012). Challenges of anticipating the 2011 Tohoku earthquake and tsunami using coastal geology. Geophysical Research Letters, 39(21). https://doi.org/10.1029/2012gl053692

Sawai, Y., Nagumo, T., Namegaya, Y., Cisternas, M. V., Lagos, M. & Shishikura, M. (2017). Diatom (Bacillariophyceae) assemblages in salt marshes of south-Central Chile: relations with tidal inundation time and salinity. Phycological Research, 65, 29–37. https://doi.org/10.1111/pre.12156

Schlegel, A., Alvarado, S. F. & Wachter, P. (1979). Optical properties of magnetite (Fe3O4). Journal of physics, 12(6), 1157–1164. https://doi.org/10.1088/0022-3719/12/6/027

Shanmugam, G. (2012). Process-sedimentological challenges in distinguishing paleo-tsunami deposits. Natural Hazards (Dordrecht, Netherlands), 63(1), 5–30. https://doi.org/10.1007/s11069-011-9766-z

Shennan, I. & Hamilton, S. (2006). Coseismic and pre-seismic subsidence associated with great earthquakes in Alaska. Quaternary Science Reviews, 25(1–2), 1–8. https://doi.org/10.1016/j.quascirev.2005.09.002

Shennan, I., Bruhn, R., Barlow, N., Good, K. & Hocking, E. (2014). Late Holocene great earthquakes in the eastern part of the Aleutian megathrust. Quaternary science reviews, 84, 86–97. https://doi.org/10.1016/j.quascirev.2013.11.010

Shennan, I., Garrett, E. & Barlow, N. (2016). Detection limits of tidal-wetland sequences to identify variable rupture modes of megathrust earthquakes. Quaternary Science Reviews, 150, 1–30. https://doi.org/10.1016/j.quascirev.2016.08.003

Shennan, I., Scott, D. B., Rutherford, M. & Zong, Y. (1999). Microfossil analysis of sediments representing the 1964 earthquake, exposed at Girdwood Flats, Alaska, USA. Quaternary International: The Journal of the International Union

for Quaternary Research, 60(1), 55–73. https://doi.org/10.1016/s1040-6182(99)00007-5

Shennan, I., Bruhn, R. & Plafker, G. (2009). Multi-segment earthquakes and tsunami potential of the Aleutian megathrust. Quaternary Science Reviews, 28, 7–13. https://doi.org/10.1016/j.quascirev.2008.09.016

Sieh, K., Natawidjaja, D. H., Meltzner, A. J., Shen, C.-C., Cheng, H., Li, K.-S., Suwargadi, B. W., Galetzka, J., Philibosian, B. & Edwards, R. L. (2008). Earthquake supercycles inferred from sea-level changes recorded in the corals of West Sumatra. Science (New York, N.Y.), 322(5908), 1674–1678. https://doi.org/10.1126/science.1163589

Sippl, C., Moreno, M. & Benavente, R. (2021). Microseismicity appears to outline highly coupled regions on the Central Chile megathrust. Journal of Geophysical Research: Solid Earth, 126(11), e2021JB022252. https://doi.org/10.1029/2021JB022252

Soloviev, S. L. & Go, Ch. N. (1984). Catalogue of tsunamis on the eastern shore of the Pacific Ocean. Canadian Translation of Fisheries and Aquatic Sciences No. 5078, Canada Institute for Scientific and Technical Information, National Research Council, Ottawa, 293 pp.

Spaulding, S. A., Potapova, M. G., Bishop, I. W., Lee, S. S., Gasperak, T. S., Jovanoska, E., Furey, P. C. & Edlund, M. B. (2021). Diatoms.org: Supporting taxonomists, connecting communities. Diatom Research, 36(4), 291–304. https://doi.org/10.1080/0269249x.2021.2006790

Spiske, M. (2020). The sedimentology and geometry of fine-grained tsunami deposits from onshore environments. In Geological Records of Tsunamis and Other Extreme Waves (pp. 213–238). Elsevier.

Spiske, M., Piepenbreier, J., Benavente, C. & Bahlburg, H. (2013). Preservation potential of tsunami deposits on arid siliciclastic coasts. Earth-Science Reviews, 126, 58–73. https://doi.org/10.1016/j.earscirev.2013.07.009

Spiske, M., Tang, H. & Bahlburg, H. (2020). Post-depositional alteration of onshore tsunami deposits – Implications for the reconstruction of past events. Earth-

Science Reviews, 202(103068), 103068. https://doi.org/10.1016/j.earscirev.2019.103068

Srinivasalu, S., Thangadurai, N., Switzer, A. D., Ram Mohan, V. & Ayyamperumal, T. (2007). Erosion and sedimentation in Kalpakkam (N Tamil Nadu, India) from the 26th December 2004 tsunami. Marine Geology, 240(1–4), 65–75. https://doi.org/10.1016/j.margeo.2007.02.003

Steffen, H. (1907a). Contribuciones para un estudio científico del Terremoto del 16 de Agosto de 1906. Imprenta Cervantes, Santiago de Chile, 83 pp.

Steffen, H. (1907b). Einige Ergebnisse der Untersuchungen über das mittelchilenische Erdbeben vom 16. August 1906. Petermanns Geographische Mitteilungen, 6: 1-7.

Stewart, D. M. (2019). Historical tsunamis in the Concepcion bay, as seen in the reconstructed flood levels from the colonial city of Concepcion (Penco), Chile (1570-1835). Revista de Historia (Concepción), 26(2), 97–127. https://doi.org/10.4067/s0717-88322019000200097

Stockmarr, J. (1971). Tables with spores used in absolute pollen analysis. Pollen et spores, 13, 615-621.

Subarya, C., Chlieh, M., Prawirodirdjo, L., Avouac, J.-P., Bock, Y., Sieh, K., Meltzner, A. J., Natawidjaja, D. H. & McCaffrey, R. (2006). Plate-boundary deformation associated with the great Sumatra-Andaman earthquake. Nature, 440(7080), 46–51. https://doi.org/10.1038/nature04522

Sublime, J. & Kalinicheva, E. (2019). Automatic post-disaster damage mapping using deep-learning techniques for change detection: Case study of the Tohoku tsunami. Remote Sensing, 11(9), 1123. https://doi.org/10.3390/rs11091123

Sugawara, D., Takahashi, T. & Imamura, F. (2014). Sediment transport due to the 2011 Tohoku-oki tsunami at Sendai: Results from numerical modeling. Marine Geology, 358, 18–37. https://doi.org/10.1016/j.margeo.2014.05.005

Szczuciński, W. (2012). The post-depositional changes of the onshore 2004 tsunami deposits on the Andaman Sea coast of Thailand. Natural Hazards (Dordrecht, Netherlands), 60(1), 115–133. https://doi.org/10.1007/s11069-011-9956-8

Szczuciński, W. (2020). Post-depositional changes to tsunami deposits and their preservation potential. In Geological Records of Tsunamis and Other Extreme Waves (pp. 443–469). Elsevier.

Szczuciński, W., Chaimanee, N., Niedzielski, P., Rachlewicz, G., Saisuttichai, D., Tepsuwan, T., Lorenc, S. & Siepak, J. (2006). Environmental and Geological Impacts of the 26 December 2004 Tsunami in Coastal Zone of Thailand - Overview of Short and Long-Term Effects. Polish Journal of Environmental Studies, 15(5).

Szczuciński, W., Rachlewicz, G., Chaimanee, N., Saisuttichai, D., Tepsuwan, T. & Lorenc, S. (2012). 26 December 2004 tsunami deposits left in areas of various tsunami run up in coastal zone of Thailand. Earth, Planets, and Space: EPS, 64(10), 843–858. https://doi.org/10.5047/eps.2012.07.007

Tamura, T., Cunningham, A. C., & Oliver, T. S. N. (2019). Two-dimensional chronostratigraphic modelling of OSL ages from recent beach-ridge deposits, SE Australia. Quaternary Geochronology, 49, 39–44. https://doi.org/10.1016/j.quageo.2018.03.003

Tappin, D. R., Evans, H. M., Jordan, C. J., Richmond, B., Sugawara, D. & Goto, K. (2012). Coastal changes in the Sendai area from the impact of the 2011 Tōhoku-oki tsunami: Interpretations of time series satellite images, helicopter-borne video footage and field observations. Sedimentary Geology, 282, 151–174. https://doi.org/10.1016/j.sedgeo.2012.09.011

Tilmann, F., Zhang, Y., Moreno, M., Saul, J., Eckelmann, F., Palo, M., Deng, Z., Babeyko, A., Chen, K., Baez, J. C., Schurr, B., Wang, R. & Dahm, T. (2016). The 2015 Illapel earthquake, central Chile: A type case for a characteristic earthquake? Geophysical Research Letters, 43(2), 574–583. https://doi.org/10.1002/2015gl066963

Titov, V., Rabinovich, A. B., Mofjeld, H. O., Thomson, R. E. & González, F. I. (2005). The global reach of the 26 December 2004 Sumatra tsunami. Science (New York, N.Y.), 309(5743), 2045–2048. https://doi.org/10.1126/science.1114576

Toledo, X. & Zapater E. (1989). Geografía general y regional de Chile. Santiago, Chile: Editorial Universitaria.

Udías, A., Madariaga, R., Buforn, E., Munoz, D. & Ros, M. (2012). The large Chilean historical earthquakes of 1647, 1657, 1730, and 1751 from contemporary documents. Bulletin of the Seismological Society of America, 102(4), 1639–1653. https://doi.org/10.1785/0120110289

Urbina, M. X., Gorigoitía, N. & Cisternas, M. (2016). Aportes a la historia sísmica de Chile: el caso del gran terremoto de 1730. Anuario de estudios americanos, 73(2), 657–687. https://doi.org/10.3989/aeamer.2016.2.11

Van Dam, H., Mertens, A. & Sinkeldam, J. (1994). A coded checklist and ecological indicator values of freshwater diatoms from The Netherlands. Netherlands Journal of Aquatic Ecology, 28(1), 117–133. https://doi.org/10.1007/bf02334251

Vargas, G., Farías, M., Carretier, S., Tassara, A., Baize, S. & Melnick, D. (2011). Coastal uplift and tsunami effects associated to the 2010 Mw8.8 Maule earthquake in Central Chile. Andean Geology, 38(1), 219–238.

Vargas, P., Torrejón, F., Pauchard, A. & Urrutia, R. (2017). Rápido movimiento de plantas exóticas en la zona central de Chile. Una reconstrucción a través de evidencia histórica y palinológica. Boletín de la Sociedad Argentina de Botánica. Sociedad Argentina de Botánica, 52(1), 121–140. https://doi.org/10.31055/1851.2372.v52.n1.16914

Vicuña Mackenna, B. (1874). Quintero: su estado actual y su porvenir. Valparaíso: Imprenta del Mercurio, de Tornero y Letelier. 173 p.

Vidal Gormaz, F. (1880). Jeografía náutica de la República de Chile (3ª entrega). Santiago: Imprenta nacional, 168 p.

Vigny, C., Socquet, A., Peyrat, S., Ruegg, J.-C., Métois, M., Madariaga, R., Morvan, S., Lancieri, M., Lacassin, R., Campos, J., Carrizo, D., Bejar-Pizarro, M., Barrientos, S., Armijo, R., Aranda, C., Valderas-Bermejo, M.-C., Ortega, I., Bondoux, F., Baize, S., …& Kendrick, E. (2011). The 2010 Mw 8.8 Maule megathrust earthquake of Central Chile, monitored by GPS. Science (New York, N.Y.), 332(6036), 1417–1421. https://doi.org/10.1126/science.1204132

Villagran, M., Cienfuegos, R., Catalán, P. & Almar, R. (2013). Morphological response of central Chile sandy beaches to the 8.8 Mw 2010 earthquake and tsunami. Proceeding of Coastal Dynamics, 13, 1823–1834.

Vos, P.C. & de Wolf, H. (1988). Methodological aspects of paleo-ecological diatom research in coastal areas of the Netherlands. Geologie en Mijnbouw 67, 31–40.

Vos, P. C. & de Wolf, H. (1993). Diatoms as a tool for reconstructing sedimentary environments in coastal wetlands; methodological aspects. Hydrobiologia, 269–270(1), 285–296. https://doi.org/10.1007/bf00028027

Vowel, R. L. (1831). Campaigns and Cruises, in Venezuela and New Grenada, and in the Pacific Ocean; from 1817 to 1830. Longman and Co. (Ed.), London. Vol. 1. p. 290-295.

Wang, K., Hu, Y. & He, J. (2012). Deformation cycles of subduction earthquakes in a viscoelastic Earth. Nature, 484(7394), 327–332. https://doi.org/10.1038/nature11032

Wesson, R. L., Melnick, D., Cisternas, M., Moreno, M. & Ely, L. L. (2015). Vertical deformation through a complete seismic cycle at Isla Santa María, Chile. Nature Geoscience, 8(7), 547–551. https://doi.org/10.1038/ngeo2468

Wirth, E. A., Sahakian, V. J., Wallace, L. M. & Melnick, D. (2022). The occurrence and hazards of great subduction zone earthquakes. Nature Reviews. Earth & Environment, 3(2), 125–140. https://doi.org/10.1038/s43017-021-00245-w

Yamashita, K., Sugawara, D., Goto, K., Ishizawa, T. & Takahashi, T. (2025). A similarity law for sandy tsunami deposits. Journal of Geophysical Research: Earth Surface, 130(7). https://doi.org/10.1029/2024jf008244

Zong, Y. & Horton, B. P. (1999). Diatom-based tidal-level transfer functions as an aid in reconstructing Quaternary history of sea-level movements in the UK. Journal of Quaternary Science, 14(2), 153–167. https://doi.org/10.1002/(sici)1099-1417(199903)14:2<153::aid-jqs425>3.0.co;2-6

Zong, Y. & Sawai, Y. (2015). Diatoms. In Handbook of Sea-Level Research (eds I. Shennan, A.J. Long and B.P. Horton). John Wiley & Sons, Ltd, Chichester, UK. https://doi.org/10.1002/9781118452547.ch15

Anexo 1. Supporting Information for Capítulo 2

Mapping tsunami deposits through a classification model based on satellite images

Bladimir Saldaña [a,b] *, Marco Cisternas [b,c], Roberto O. Chávez [c], Diego Aedo [a,b], Mario Guerra [b,c], Alexandra Carreño [c]

[a] Departamento de Ciencias de la Tierra, Facultad de Ciencias Químicas, Universidad de Concepción, Concepción, Chile

[b] Millennium Nucleus The Seismic Cycle Along Subduction Zones CYCLO, Valdivia, Chile

[c] Instituto de Geografía, Pontificia Universidad Católica de Valparaíso, Valparaíso, Chile

* Corresponding author

E-mail address: bsaldana@udec.cl

Contents of this file

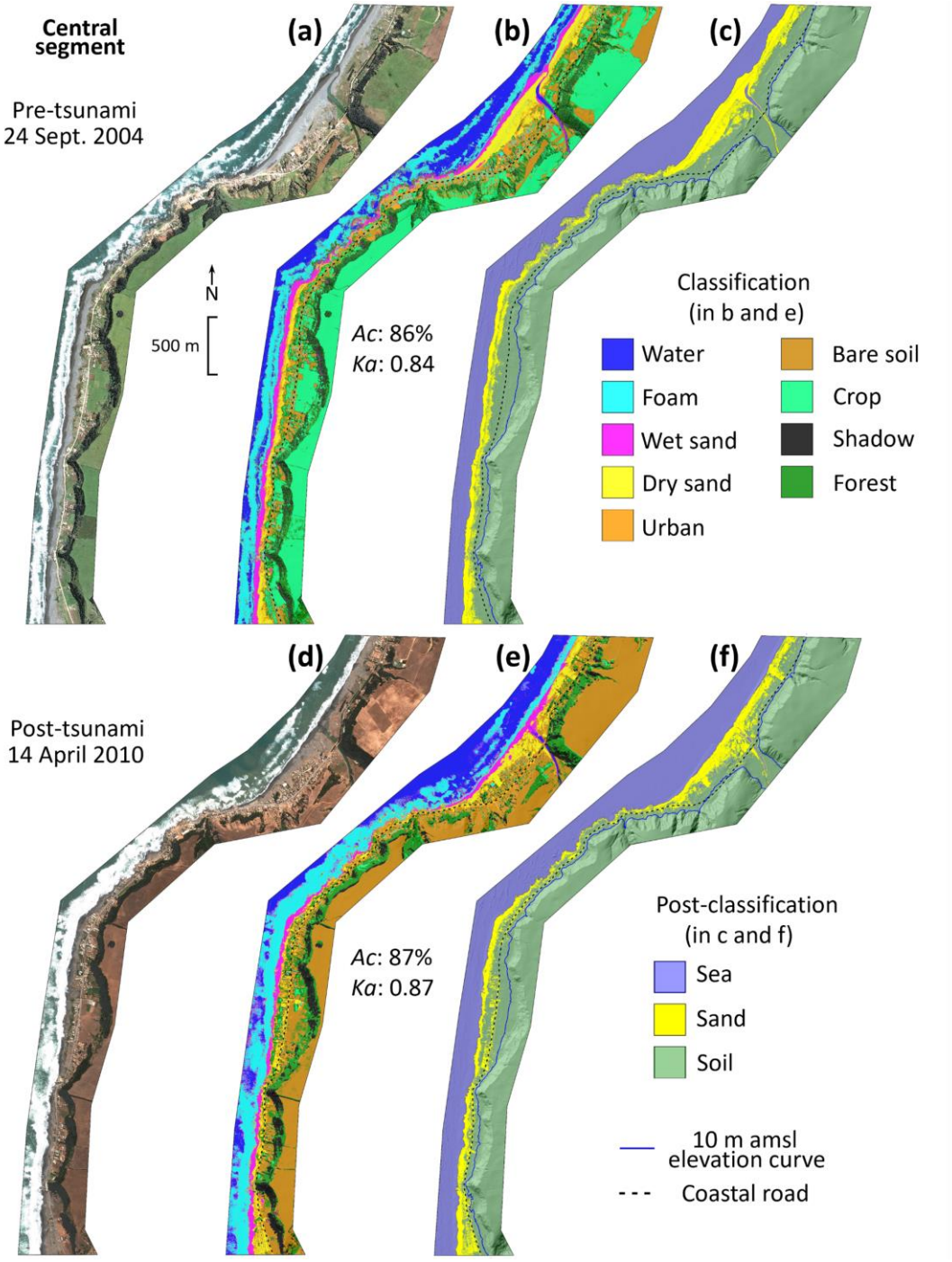

Figure S1. Pre- and post-tsunami satellite images and resulting land use and land cover (LULC) maps from the classification model for the Central segment (see Figure 1). (a) A true-color composition of the pre-tsunami satellite image. (b) LULC map obtained from the supervised classification model applied to (a). Ac and Ka indicate the overall accuracy and Kappa coefficient resulting from the classification model, respectively. Confusion matrices and specific accuracies for sand classes are shown in Figure S12. (c) LULC map with classes shown in (b) combined and outlier pixels removed. (d-f) As in (a-c) for the post-tsunami image.

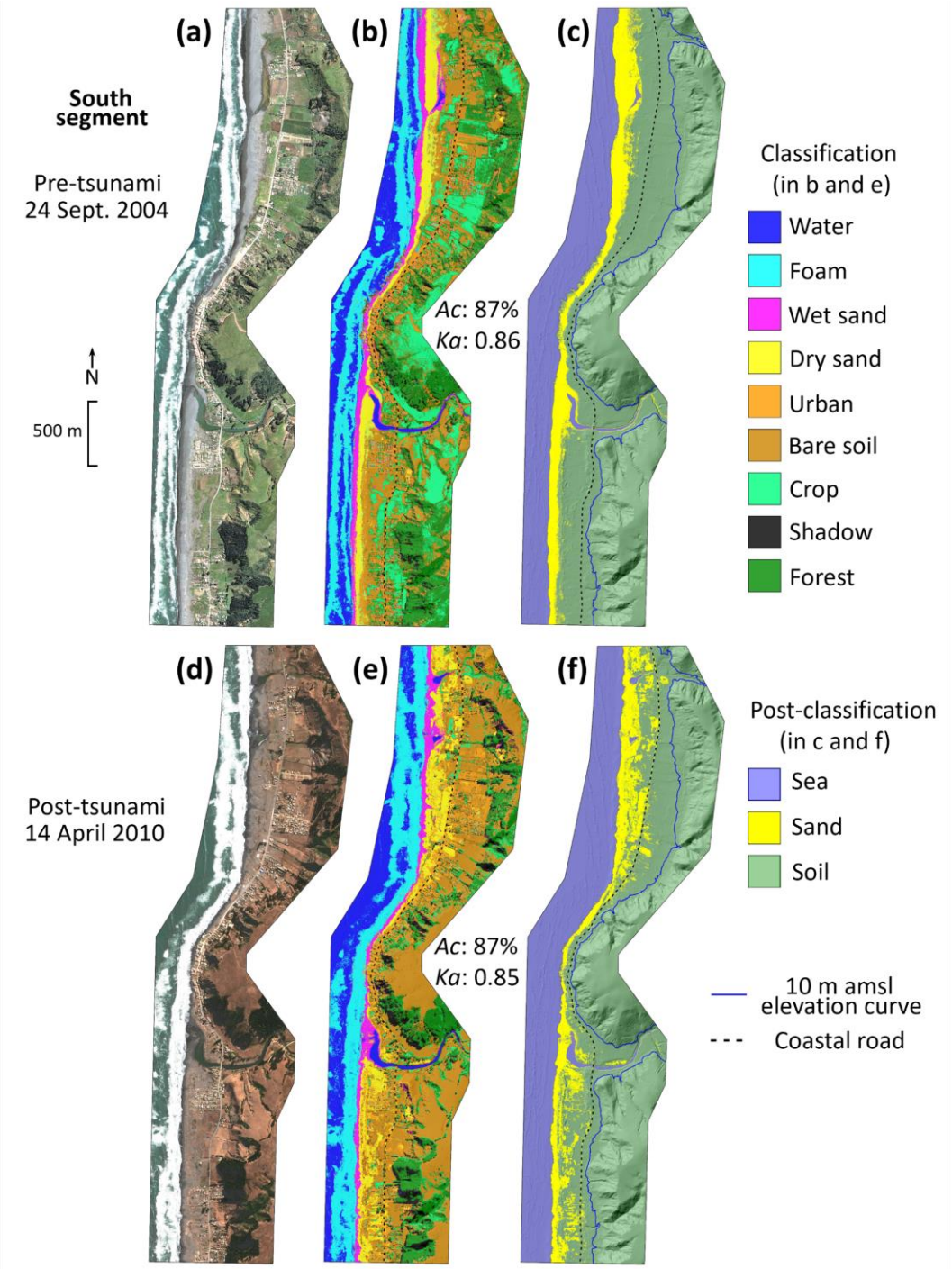

Figure S2. Pre- and post-tsunami satellite images and resulting land use and land cover (LULC) maps from the classification model for the South segment (see Figure 1). (a) A true-color composition of the pre-tsunami satellite image. (b) LULC map obtained from the supervised classification model applied to (a). Ac and Ka indicate the overall accuracy and Kappa coefficient resulting from the classification model, respectively. Confusion matrices and specific accuracies for sand classes are shown in Figure S14. (c) LULC map with classes shown in (b) combined and outlier pixels removed. (d-f) As in (a-c) for the post-tsunami image.

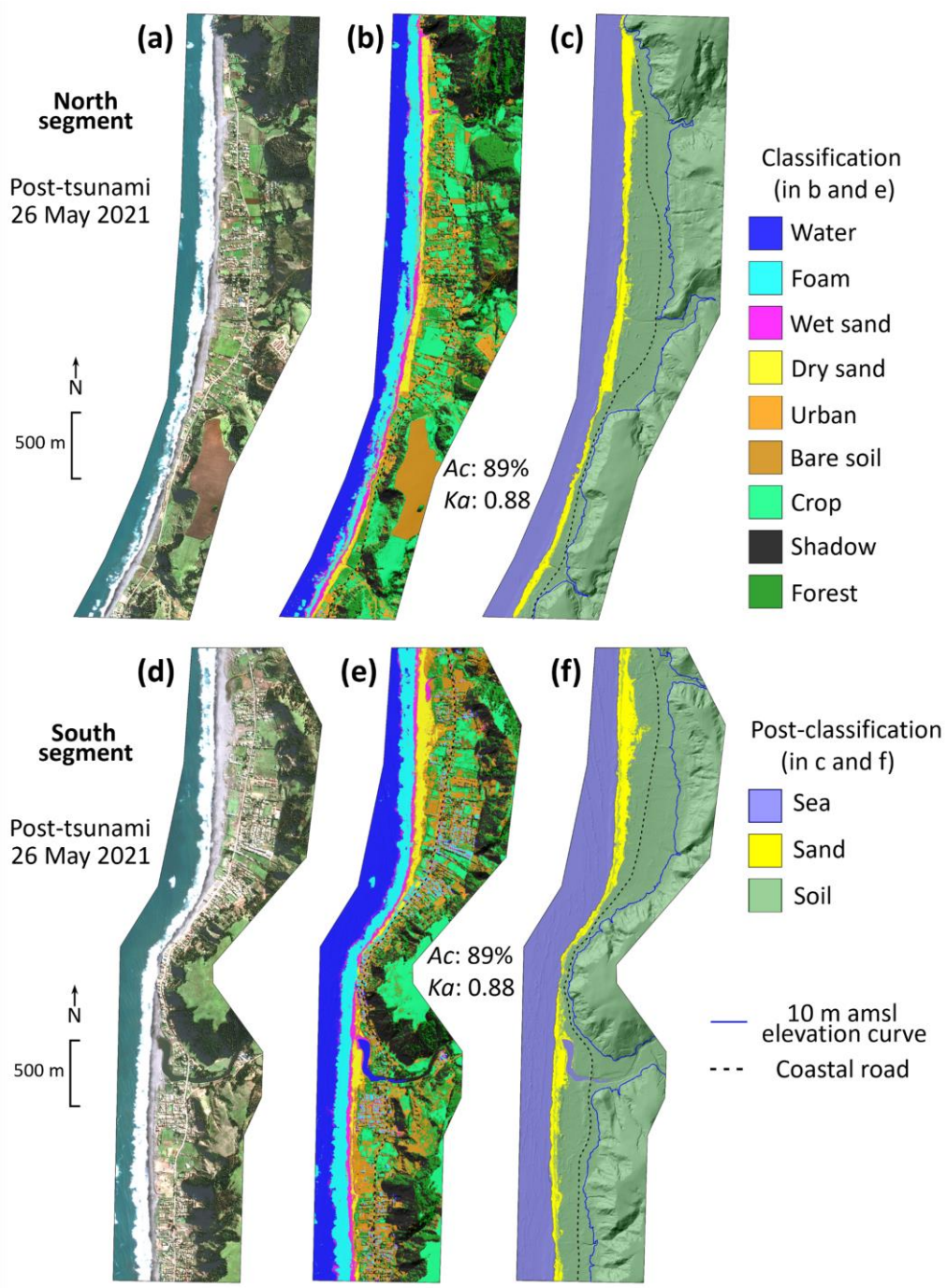

Figure S3. Post-tsunami satellite images and resulting land use and land cover (LULC) maps from the classification model for the North and South segments (see Figure 1). (a) A true-color composition of the post-tsunami satellite image for the North segment. (b) LULC map obtained from the supervised classification model applied to (a). Ac and Ka indicate the overall accuracy and Kappa coefficient resulting from the classification model, respectively. Confusion matrices and specific accuracies for sand classes are shown in Figure S16. (c) LULC map with classes shown in (b) combined and outlier pixels removed. (d-f) As in (a-c) for the South segment.

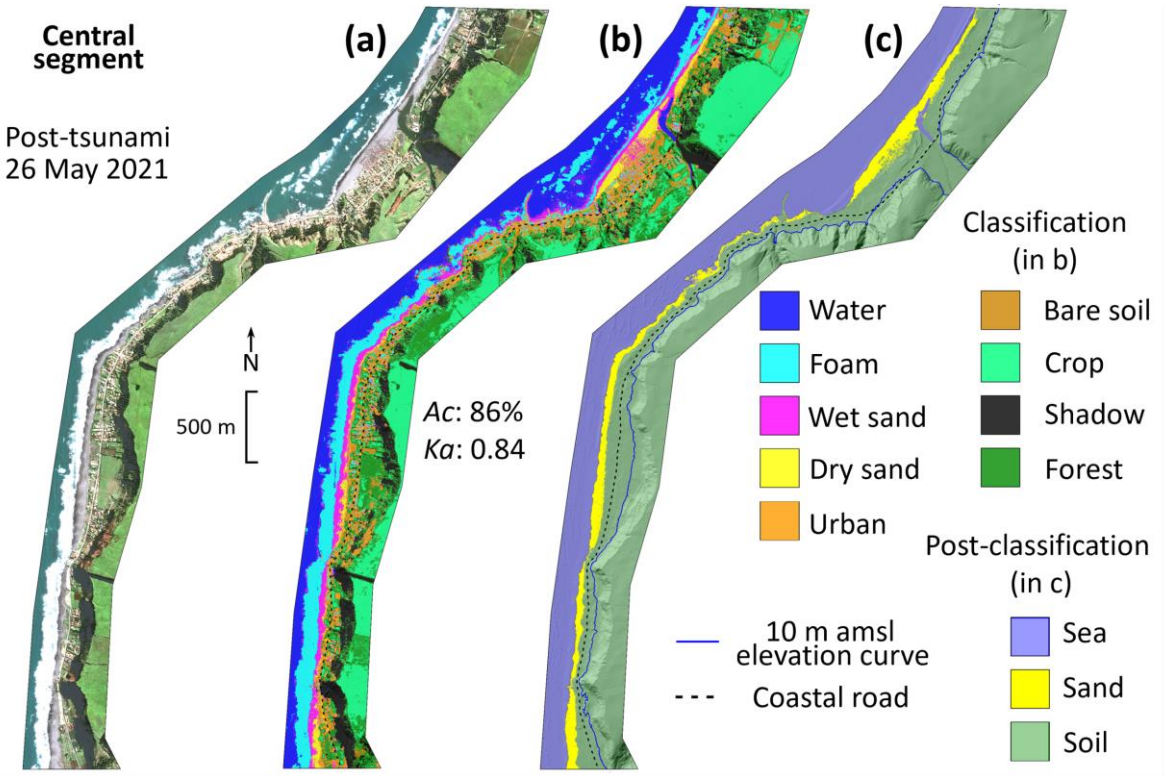

Figure S4. Post-tsunami satellite image and resulting land use and land cover (LULC) map from the classification model for the Central segment (see Figure 1). (a) A true-color composition of the post-tsunami satellite image. (b) LULC map obtained from the supervised classification model applied to (a). Ac and Ka indicate the overall accuracy and Kappa coefficient resulting from the classification model, respectively. Confusion matrices and specific accuracies for sand classes are shown in Figure S17. (c) LULC map with classes shown in (b) combined and outlier pixels removed.

Table S1. Eyewitness interviews conducted along the North (1-31), Central (32-64) and South (65-97) segments. Each number (N°) corresponds to one person interviewed. All these interviews describing the tsunami sand deposit were predicted by our classification model (97 in total).

N°	Name (age)	Latitude Longitude Elevation	Interview date	Summary of reported observations	Occupation or reference
1	José Luis Díaz (58)	34.83177°S 72.14378°W 4.490 m	March 2023	The tsunami reached the edge of the hill and left a sand layer. Sand covered his house and yard. The sand was removed days later with shovels and wheelbarrows. Sand patches are still observable.	Goose breeder
2	Jorge Jofré (~70)	34.83246°S 72.14343°W 4.698 m	March 2023	His potato plantations were completely covered by a ~20 cm thick layer of sand. He lost his house and crop. Months later he plowed his field.	Potato field owner
3	Manuel Jofré (52)	34.83279°S 72.14314°W 6.717 m	March 2023	The tsunami reached a light pole up the street, leaving a layer of sand about 40 cm thick.	Farmer
4	Bernardita Beltrán (~50)	34.83326°S 72.14328°W 5.318 m	March 2023	The tsunami crossed the coastal road, leaving sand inside the restaurant where she works and her neighbors' houses.	Waitress
5	Gustavo Pavez (45)	34.83365°S 72.14319°W 5.832 m	April 2022	Sand from the tsunami covered almost half of his yard. The thickness of the sand layer reached 50 cm and at its most landward limit it reached a thickness of 2 cm.	Bus and truck maintainer
6	Gustavo Pavez Jr. (~20)	34.83496°S 72.14291°W 6.246 m	April 2022	The water reached his front yard but with a flow depth of only a couple of centimeters. Only patches of beach sand were deposited.	Student (Gustavo Pavez's son)
7	Claudio Melendez	34.83596°S 72.14266°W 3.839 m	February 2022	The flow depth reached 60 cm in the wall of his house. The tsunami deposit thickness was ~15 cm. The tsunami deposit was mainly sand and garbage.	Builder
8	René Borquez	34.83646°S 72.14192°W 4.870 m	February 2022	His house is located high up and was not hit by the tsunami. The lower plain was covered with tsunami sand. The tsunami was channeled upstream at Cardonal Creek.	Builder

9	José Luis Farías (69)	34.83699°S 72.14205°W 4.305 m	March 2009 August 2010	Sand from the tsunami covered the field where he planted potatoes. The thickness of the layer ranged from 15 to 30 cm. He had to plow the land to resume planting (Figure S19). The tsunami reached about 200 m inland where he saw a line of debris. This potato field was visited in 2009 (pre-tsunami) and no trace of a surface sand layer was found.	Caretaker and Farmer (Figure 4e)
10	Alfonsina Correa Jofré	34.83894°S 72.14275°W 4.066 m	May 2022	The tsunami crossed the coastal road and left a sand deposit of up to 80 cm thick.	Saleswoman
11	Damari Silva	34.83916°S 72.14246°W 4.261 m	May 2022	The second tsunami wave flooded her house and was as high as a light pole (~8 m). The walls of her house are still corroded by seawater. The thickness of the sand deposit was at least 1 m. Local landslides from the coastal cliff were observed due to the shaking.	Flower shop owner
12	Juan Carlos Salinas	34.83914°S 72.14202°W 4.787 m	May 2022	Sand from the tsunami spread further inland than the coastal road. His house was not damaged.	-
13	Jorge Olivo	34.84010°S 72.14247°W 5.094 m	May 2022	He remembered only patches of sand on the coastal road. He stated that the damage in Lipimávida was less than that observed in Iloca.	-
14	Feliciano Díaz	34.84057°S 72.14247°W 5.032 m	October 2021	There was no damage to their cabins. The tsunami left only patches of sand in his yard. The depth of flow was less than a few centimeters.	Owner of tourist cabins
15	Nibaldo Díaz	34.84074°S 72.14252°W 4.775 m	October 2021	He confirmed Nibaldo Díaz's account (uncle and nephew were interviewed separately). He provided details on the less than 5 cm thickness of the tsunami deposit.	Farmer (Feliciano Díaz's uncle)
16	Rodrigo Beltrán	34.84183°S 72.14259°W 4.341 m	October 2021	His workplace was severely damaged and a deposit of sand covered the field. Days later he removed the sand to try to save the crops.	Papaya farmer

17	Abelina Correa	34.84245°S 72.14261°W 4.863 m	May 2022	The tsunami sand piled up inside its storage up to 1 m thick. Fish and crabs were also washed inland. A ~80 cm high cooler was covered by beach sand. Neighbors and friends helped her to remove the sand. The tsunami deposit reached at least the coastal road.	Bakery owner
18	Ramón Jofré (78)	34.84342°S 72.14294°W 5.013 m	May 2022	His yard was completely covered with sand. He remembered that the deposit was at least knee-deep (~30 cm thick). His children and neighbors helped him clean up his property.	Retired
19	Fernando Bravo (~80)	34.84478°S 72.14319°W 4.531 m	May 2022	When he heard the tsunami warning, moments after the shock, he fled with his family to the hill. The tsunami warning tower was covered with sand at its base.	Jam seller
20	Tatiana González	34.84511°S 72.14359°W 4.938 m	May 2022	Her house and those of her neighbors in the front line were swept away. Tsunami sand covered much of the low land and the area around the tsunami warning tower.	Fernando Bravo's neighbor
21	Julia Jiles	34.84786°S 72.14345°W 3.521 m	May 2022	The tsunami damaged all the houses between the shoreline and the coastal road. Sand and garbage were scattered all over the plain.	Milk saleswoman
22	Patricia Flores (68)	34.84933°S 72.14271°W 2.794 m	May 2022	The first wave was very light. Before the second wave came, she escaped to high ground with her dogs. She spent the whole night on the hill. The next morning, she found patches of beach sand and plant debris outside her house.	Teacher
23	Palmenia Rojas	34.84963°S 72.14228°W 3.347 m	May 2022	The tsunami left only patches of sand and debris. The water did not reach the community health center and church located near the coastal road.	Nurse
24	Oscar Jofré	34.85008°S 72.14239°W 3.486 m	April 2022	The tsunami penetrated at least 200 m from the shoreline, covering the entire plain with a thick layer of sand.	-

25	Marcela Beltrán	34.85176°S 72.14280°W 3.600 m	May 2022	All the land between the shoreline and the coastal road was covered with sand brought from the beach.	Store Assistant
26	Miguel "Caleuche"	34.85405°S 72.14386°W 3.120 m	April 2022	Tsunami sand covered his campsite up to 35 cm thick. Weeks after the tsunami, he plowed the land and removed the sand to harvest potatoes.	Farmer and campsite owner
27	Marcela Díaz (~25)	34.85509°S 72.14416°W 3.328 m	May 2022	The tsunami severely damaged the restaurant where she works and deposited an extensive sheet of sand in the surrounding area. The shoreline was noticeably changed. At least 50 m of beach was lost. The restaurant is now almost reached by the high tides.	Restaurant assistant
28	Juan Orellana	34.85588°S 72.14442°W 3.324 m	May 2022	The tsunami flooded his house and left sand accumulations everywhere.	Cook
29	María Correa	34.85630°S 72.14462°W 3.435 m	May 2022	The tsunami left extensive layers of sand on her property. Her son had to remove the sand with great effort to reopen the hotel to tourists.	Hotel owner
30	Arturo Flores	34.85674°S 72.14540°W 3.650 m	March 2023	The tsunami overtopped the coastal road and then the water moved laterally towards Maria Correa's property, which was on slightly lower land. The tsunami also left thick layers of sand inside his house and in his yard.	Gardener
31	Raúl Pradenas	34.85832°S 72.14613°W 4.882 m	March 2023	The tsunami almost reached the base of the coastal cliff. The water swept away his cabins and deposited sand in the surrounding area.	Owner of tourist cabins
32	Genaro Correa	34.88020°S 72.15646°W 1.941 m	March 2023	His land located at the mouth of Pichibudi Creek was completely covered with sand. Remnants of the tsunami deposit are still observable, but mostly trampled by cows. The dune was eroded by the tsunami and the underlying soil was exposed (Figure S5).	Cow breeder

33	Rafael Acevedo	34.88079°S 72.15574°W 2.357 m	March 2023	Sand completely covered his campsite located next to Pichibudi Creek, which is still visible in some places. The tsunami destroyed the bridge and a temporary crossing needed to be constructed. A bus parked next to this bridge was swept away by the tsunami at least 100 m inland (Figure S5).	Campsite owner
34	Carlos Acevedo	(House) 34.88138°S 72.15534°W 2.595 m (Nursery) 34.88110°S 72.15617°W 3.362 m	March 2023	a) The flow depth in his house located next to Pichibudi Creek was about 2 m. Sand and debris surrounded his property. b) The family's nursery was destroyed. No plants were left in the nursery, only sand from beach.	Plant nursery worker (Rafael Acevedo's relative)
35	Rosa Bravo	34.88121°S 72.15638°W 3.922 m	March 2023	Her restaurant was destroyed by the tsunami. Nothing was left standing. Trees in her yard were uprooted. The tsunami deposited sand even on the second floor of the house.	Restaurant owner
36	Pedro Medina	34.88179°S 72.15810°W 7.580 m	March 2023	Landslides were caused by the earthquake. From high ground he saw the arrival of three waves, the second being the largest and most destructive. Fishing boats were swept away. The sand on the beach was completely scattered inland. The high tide line was permanently shifted landward.	Fisherman
37	Luis Correa Peña	34.88275°S 72.15976°W 5.033 m	March 2023	Tsunami marks on the walls of his house indicated a flow depth of ~1 m. The sand left inside the house was up to 20 cm thick. The shoreline receded significantly, at least 50 m.	Fisherman
38	Margarita Santelices	34.88328°S 72.15980°W 5.618 m	March 2023	She observed thick layers of sand in low relief and unobstructed locations. Buildings blocked the passage of sand inland.	Seaweed saleswoman
39	Miguel Angel Pardo	34.88494°S 72.16141°W 4.938 m	March 2023	Sand redistributed from the beach covered his campsite and all the land extending from the shoreline to the coastal road.	Campsite owner

40	Edward Barroso	34.88494°S 72.16278°W 3.353 m	February 2023	He remembered the floor of the restaurant and all the surrounding area covered with sand brought from the beach.	Restaurant owner
41	Dorila Ahumada	34.88582°S 72.16566°W 4.857 m	March 2023	Her clothing store was located on the front line, so the tsunami destroyed it. The next day she found only sand and debris.	Clothes store saleswoman
42	Claudia Concha Bravo	34.88588°S 72.16604°W 4.930 m	March 2023	The water entered the liquor store and threw all the bottles out. The sand deposit reached 1 m thick.	Liquor store saleswoman
43	Luis Díaz	34.88584°S 72.16804°W 4.698 m	March 2023	Tsunami sand covered the floor of his house and piled up at the door of his neighbor's house.	Fast food salesman
44	Mario Silva	34.88736°S 72.17055°W 6.897 m	March 2023	The gas station and its surroundings were covered with tsunami sand. Trucks were needed to remove the sand and restore service.	Gas station attendant
45	Belarmino Pizarro	34.88761°S 72.17145°W 5.187 m	March 2023	His house and his neighbor's restaurant were damaged by the tsunami. Sand from the beach covered everything in its path.	-
46	José del Carmen Héctor Díaz Díaz	34.89031°S 72.17418°W 4.947 m	March 2023	His workplace was inundated, but the tsunami left no trace of sand. Frontline houses acted as a barrier and protected his store from further damage.	Seaweed seller
47	Ivan Nuñez	34.89058°S 72.17437°W 4.569 m	March 2023	The yard of his house was covered with beach sand. A few days later, the site was cleaned.	-
48	Juan Baros	34.89092°S 72.17405°W 3.009 m	March 2023	The place where he was working was not damaged, as it was located on a second floor. However, the lower parking lot was completely covered with sand.	Waiter
49	Gilberto Véliz	34.89111°S 72.17440°W 7.101 m	March 2023	The tsunami left seaweed debris hanging from the electric lighting (~7 m high). The door of his house was locked due to the pile of sand.	-

50	Margarita Díaz	34.89295°S 72.17672°W 6.517 m	March 2023	The tsunami arrived approximately 25 minutes after the earthquake. The second wave was the largest with a height of ~8 m. Beach sand entered through the door and windows of her house.	Dressmaker
51	Flavio Ramírez Suazo (82)	34.89634°S 72.17932°W 4.114 m	March 2023	The tsunami did not cross the coastal road and therefore did not reach his house further inland. A layer of sand extensively covered those places between the shoreline and about 200 m landward. He estimated a height of 8 m for the second wave.	Parapsychologist and writer
52	Paola Soto	34.89779°S 72.17955°W 5.643 m	March 2023	The tsunami debris was scattered all along the coastal road. The dark sand-laden water entered her house from all sides.	Jam store owner
53	Jonathan Bravo	34.90040°S 72.17939°W 4.801 m	March 2023	He recalled that the tsunami was not devastating at this location, leaving only small patches of sand.	-
54	José Gamboa	34.90289°S 72.17986°W 4.283 m	March 2023	Like his neighbor Jonathan Bravo, he recalled only minor flooding with localized sand patches from the shoreline to the coastal road.	Jonathan Bravo's neighbor
55	Verónica Bobadilla	34.90455°S 72.17992°W 4.818 m	March 2023	The tsunami hit her restaurant and deposited an extensive sheet of sand that reached the coastal road and the house of her neighbors across the street.	Restaurant owner
56	María Rebeca Jara	34.90520°S 72.17999°W 4.741 m	March 2023	A layer of sand about 50 cm thick was left inside the liquor store, covering boxes and bottles. Her house, which was ~150 m inland, was also reached by the water.	Liquor store saleswoman
57	Clorindo Correa	34.90613°S 72.18007°W 5.312 m	March 2023	The tsunami did not reach his mechanic shop because it was on high ground, however the lower part was flooded, and a thick layer of sand was left behind. The beach receded at least 50 m. Rocks on the coast that were previously exposed are now submerged after the earthquake.	Mechanic shop owner

58	Kevin Oyarce (27)	34.90672°S 72.18049°W 5.759 m	March 2023	He was very young when the tsunami struck, but he remembered the water crossing the coastal road inland and depositing a thick layer of beach sand piled up against a concrete wall.	Lumberjack
59	Teresa Jofré (~40)	34.90839°S 72.18152°S 4.611 m	March 2023	The water and sand brought by the tsunami stopped right in front of the restaurant where she works. There was no damage to the interior.	Assistant cook
60	Alicia Díaz	34.91089°S 72.18129°W 5.408 m	March 2023	The tsunami left patches of sand on the front of her house, which she swept up days later.	-
61	Fabián Santelices (~40)	34.91314°S 72.18162°W 4.666 m	February 2023	The dune was completely flattened by the tsunami. Sand from the dune was redistributed by the tsunami and carried inland to the base of some palm trees.	Worker in resort
62	Dennis Santelices (~25)	34.91332°S 72.18165°W 4.822 m	February 2023	Landslides were triggered by the earthquake. The tsunami deposited sand in her neighbor's front yard. Tidal surges are now stronger in winter and even reach the coastal road due to the strip of beach that was lost.	Worker in resort
63	Iván Díaz	34.91854°S 72.18150°W 4.776 m	March 2023	His house and the campsite next to his property were completely covered by sand and debris brought by the tsunami.	Builder
64	María Peredo	34.91944°S 72.18125°W 4.590 m	March 2023	That night she was camping with friends. After the earthquake she and other tourists ran to high ground for fear that the sea would come out. The next morning there were no tents left at the campsite, only beach sand brought by the water.	-
65	Hector Rivera	34.92459°S 72.18079°W 3.162 m	February 2023	His property was covered by a thick layer of dark, wet sand. This sand was brought from the beach by the tsunami and even extended to the coastal road. The sand prevented vehicular traffic for several weeks.	-

66	Waldo Muñoz	34.92474°S 72.18098°W 3.058 m	February 2023	Remnants of seaweed and fishermen's nets were left hanging 7 m high on the light poles. The earthquake raised a cloud of dust, and the tsunami left sand on the fields. He removed the sand and filled with debris to rebuild his house.	Owner of tourist cabins
67	Fernanda Cespedes	34.92500°S 72.17916°W 4.344 m	February 2023	She reported that the dune was eroded by the tsunami and that the sand was piled up inside her house up to 40 cm thick.	-
68	Lalo Correa	34.92848°S 72.17966°W 4.892 m	April 2022	His house located further inland than the coastal road was not damaged. The water and sand only reached the lower areas.	-
69	Luis Orostiga	34.93102°S 72.17977°W 4.143 m	February 2023	A flow depth of ~80 cm was recorded at his home. He observed tsunami sand in the surroundings of the coastal road. His neighbors bemoaned the ruined crops caused by the salty sand on their fields. Soon after, they plowed the land again to reactivate the crops.	Builder
70	Eufrasio Verdugo (~80)	34.93257°S 72.18013°W 3.700 m	February 2023	Tsunami sand covered everything from the shoreline to the coastal road. He and his neighbors worked together to remove it.	-
71	SERVIU	34.93527°S 72.17980°W 5.602 m	February 2022	The land was completely covered with sand and debris brought by the tsunami. The sand was promptly removed with trucks and government resources.	Land belonging to the Ministry of Housing and Urban Development (SERVIU). Caretaker did not give his name.
72	Nicolás Márquez (37)	34.93671°S 72.18165°W 4.490 m	October 2021	Sand from the tsunami surrounded the entire site, along with the remains of destroyed houses. The sand spread as far as the coastal road.	Restaurant owner
73	Alfonso Farías	34.93688°S 72.18092°W 5.354 m	February 2023	Sand from the beach was washed inland by the tsunami, blocking several streets and houses.	-
74	Miguel Canales	34.93693°S 72.18086°W 5.696 m	February 2023	The tsunami brought sand and debris from houses, scattering them all over the sector.	-

75	María Lopez	34.93712°S 72.18114°W 5.266 m	February 2023	The sand accumulated forming a mound of about 1 m on the coastal road, which blocked the circulation of vehicles and people. Neighbors improvised a bridge with wood that the tsunami brought. Days later they cleared the road, carrying the sand back to the beach.	-
76	Doris Ahumada	34.93750°S 72.18200°W 4.672 m	October 2021	She was able to escape to the hill before the tsunami hit even though she was pregnant. Her home and grocery store were devastated. Extensive sand sheets covered all her groceries. Her nephew's school located near the coast was destroyed and is now relocated to a safe place inland. The sand and debris were removed days later. She also noticed changes in the coast. At least 100 m of beach were lost after the event.	Grocery store owner
77	Guillermo Palacios	34.93776°S 72.18274°W 4.217 m	February 2023	The fair where his chocolate store was located was washed away by the tsunami. The next day all the stores were full of beach sand. His valuables that had been scattered inland by the waves were found some time later near the coastal road and covered by wet sand.	Chocolate store owner
78	María Lisette González Correa (55)	34.93871°S 72.18306°W 5.072 m	February 2023	The dark sand brought by the tsunami was even on the roof of her house at 5 m high. She stated that the inside of her house was a real beach as there was sand in every hallway and piece of furniture.	-
79	Claudio Ramírez	34.94227°S 72.18624°W 5.779 m	February 2023	He gave a description of the low damage to an emblematic hotel in Iloca. Although the hotel is located a few meters from the shoreline, it was surprisingly undamaged and remained intact. Probably due to its reinforced structure and its elevation with respect to the beach. He only observed patches of sand on the floor and in the pool. The major damage was at the town fair (see Guillermo Palacios).	Land owner south of the Mataquito River. He visited and photographed with his sons several areas affected by the tsunami (Figure 4f).

80	Nelsy González Castro	34.94365°S 72.18667°W 5.786 m	February 2023	Hotel walls still show traces of corrosion from seawater. Water marks over 7 m high. The beach sand formed deposits up to 70 cm thick, exceeding the coastal road in several sectors.	Hotelier
81	Heriberto Poblete Correa	34.94380°S 72.18644°W 6.275 m	February 2023	Houses between the shoreline and the coastal road were washed away. Sand from the tsunami almost completely covered the coastal road with thicknesses of up to 1m. A backhoe had to be brought in to remove it. The parking lot of his hotel was covered with sand as well. Buses parked at the fair (see Guillermo Palacios) were swept almost 200 m inland.	Hotelier (husband of Nelsy González Castro)
82	Patricia Piñones	34.94695°S 72.18597°W 4.631 m	February 2023	No house in her neighborhood was spared from being covered by sand and debris from the tsunami.	-
83	Angel Custodio (~60)	34.94717°S 72.18571°W 5.055 m	February 2023	The rooms in his house were completely covered with sand. Cleanup required shovels and wheelbarrows.	-
84	José Miguel Ibarra	34.95007°S 72.18244°W 2.502 m	October 2021	Tourists who were spending the night at the campsite were able to flee before the tsunami hit. The entire campsite was flooded and covered by sand. Scraps of wood, fishermen's nets and clothing were scattered all over the site. For the next three years the campsite was permanently closed, which favored the preservation of the sand deposit under the overgrown grass. It was not until mid-2012 that a cleanup process began to reopen the campsite to tourists.	Owner of campsite next to Iloca Creek. At this campsite the 2010 tsunami deposit was well preserved and most of the pits were excavated (Figure S7).
85	Homero Perez "El Tata"	34.95064°S 72.18458°W 6.819 m	October 2021	His neighborhood was covered by sand and everything else the sea brought. The second wave was the biggest. He still remembers the thunderous sound the wave made when it hit the bridge of Iloca Creek. The water overtopped the bridge and went directly towards José Miguel Ibarra's campsite.	-

86	Patricia Meléndez	34.95057°S 72.18352°W 2.862 m	October 2021	She confirmed Homero Perez's account. Her house on the south bank of Iloca Creek was left intact. However, José Miguel Ibarra's campsite on the north bank was destroyed. A sheet of black sand covered almost all the green grass.	-
87	Luis Meléndez	34.95034°S 72.18163°W 3.769 m	October 2021	That night he saw numerous tourists at the Iloca campsite fleeing in panic after the earthquake. Minutes later, a small wave approached upstream, like a rising tide. The noise of the second wave frightened him and he decided to run. The next morning, he returned and found patches of sand on his property. His neighbor José Miguel Ibarra's once green campsite had turned black from all the tsunami sand.	Caretaker of land in Iloca Creek (Patricia Meléndez's father)
88	Hector Correa	34.94885°S 72.17893°W 5.268 m	February 2023	The tsunami spread upstream along the Iloca Creek and reached the water treatment plant located about 1 km inland. The already slowed flow at this site only deposited isolated patches of sand.	Water treatment plant worker
89	Sergio Bastidas	34.95176°S 72.18530°W 3.618 m	January 2023	Garbage accompanied by sand was scattered all over his neighborhood. However, neither water nor sand crossed the coastal road inland.	Supermarket worker
90	Irma Dualde	34.95191°S 72.18583°W 2.803 m	February 2023	Because she lived just meters from the beach, she was severely affected by the tsunami. Puddles of water, beach sand and tree debris washed up near the coastal road.	-
91	María Figueroa	34.95268°S 72.18492°W 4.150 m	February 2023	Destruction of all the houses, which were washed away. Beach sand piled up in every corner, extending several meters inland.	-
92	Paola Peña	34.95320°S 72.18569°W 3.583 m	February 2023	The beach sand reached a greater distance inland than it had prior to the tsunami. Patches of sand were seen even in the area around the coastal road.	-

93	Manuel Rodelindo	34.95638°S 72.18561°W 6.343 m	August 2022	The plain located between the shoreline and the coastal road was extensively covered by beach and dune sand.	Caretaker
94	Georgina Yáñez	34.95916°S 72.18489°W 5.780 m	February 2023	Her house was not damaged by the tsunami. Only thin layers of sand were left by the flow in her front yard. She provided shelter for her sister-in-law Irma Dualde.	Irma Dualde's sister-in-law
95	Eugenia Vidal	34.96146°S 72.18474°W 4.759 m	February 2023	Water and sand from the tsunami entered her house. The children's room was completely covered with a sand layer up to 2 m thick. The whole family shoveled the sand out of the house.	Baker
96	Juan Segundo Valderrama	34.96189°S 72.18450°W 5.368 m	February 2023	He described the tsunami at his home, located far from the shoreline, as a small runoff of water with a flow depth of only a few centimeters. Sand from the beach blocked the coastal road with thicknesses exceeding 20 cm.	-
97	Olivia Salinas	34.96187°S 72.18403°W 7.525 m	February 2023	She reported a similar situation to her neighbor Juan Segundo Valderrama. The coastal road remained blocked for several days due to sand deposition. In addition, while the sand only reached the coastal road, the water penetrated at least 50 m further inland.	Juan Segundo Valderrama's neighbor

Questions used for eyewitness interviews and brief answers obtained

At the beginning of each interview, people provided their name and occupation. In some cases, they were also asked their age.

1- How long have you lived in the area?

- Most of the interviewees were locals. They were born and grew up in the area.

2- Do you remember any important natural phenomenon that has occurred in the area recently?
   - Most answers pointed to the 2010 earthquake and tsunami as the last major event in the area.
3- Where were you when the 2010 earthquake occurred? Do you remember the exact day and time?
   - Because the earthquake occurred on a Saturday at 03:34 local time, most people were resting at home. These questions allowed us to assess whether the memories of the interviewees were still clear. Interviews with doubtful or vague answers were discarded.
4- What did you do immediately after the earthquake?
   - As a result of the strong shaking caused by the earthquake, most people decided to flee to higher ground in case of a tsunami. Most interviewees did not return home until the next morning, when it was safer.
5- Regarding the tsunami, how much time elapsed between the earthquake and the first wave? What was the direction of that wave? How many waves in all? Which was the largest?
   - We collected variable and, in some cases, contradictory answers. Probably the panic and darkness of that night generated confusion. We included the most consistent answers in Table S1.
6- Did the tsunami flood your land?
   - Interviewees recalled in considerable detail the damage the tsunami caused to their homes. Most of them described a sheet of sand and garbage over their yards and crops (see Table S1).

Finally, each person interviewed was asked to indicate the maximum landward extent of tsunami sand. In a few cases the interviewees also gave an estimate of the thickness of the sand layer. Where possible, we made measurements on walls that still exhibited water marks.

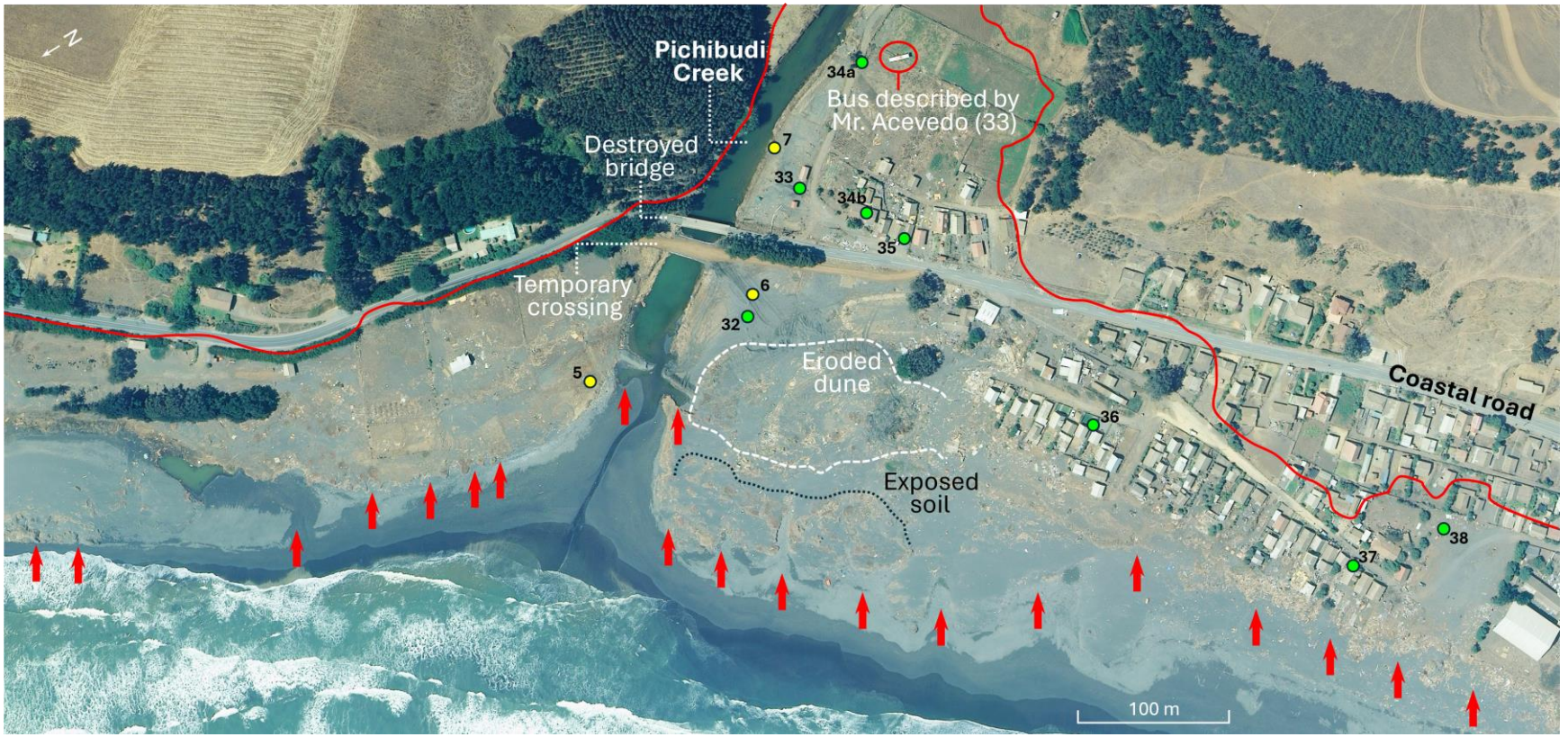

Figure S5. Post-tsunami aerial photograph (10 March 2010) showing sand deposit and erosion features in Pichibudi Creek. Red line denotes the landward limit of the 2010 tsunami by Fernández et al. (2010) and Fernández & Venegas (2010). Red arrows indicate scours and conspicuous erosion marks from the tsunami. Green and yellow dots show sites where interviews and pits were conducted, respectively. Numbers beside these points are associated with tables S1 and S2. Note the tsunami deposit as a discontinuous gray sand sheet extending inland, which has a greater intrusion near the creek.

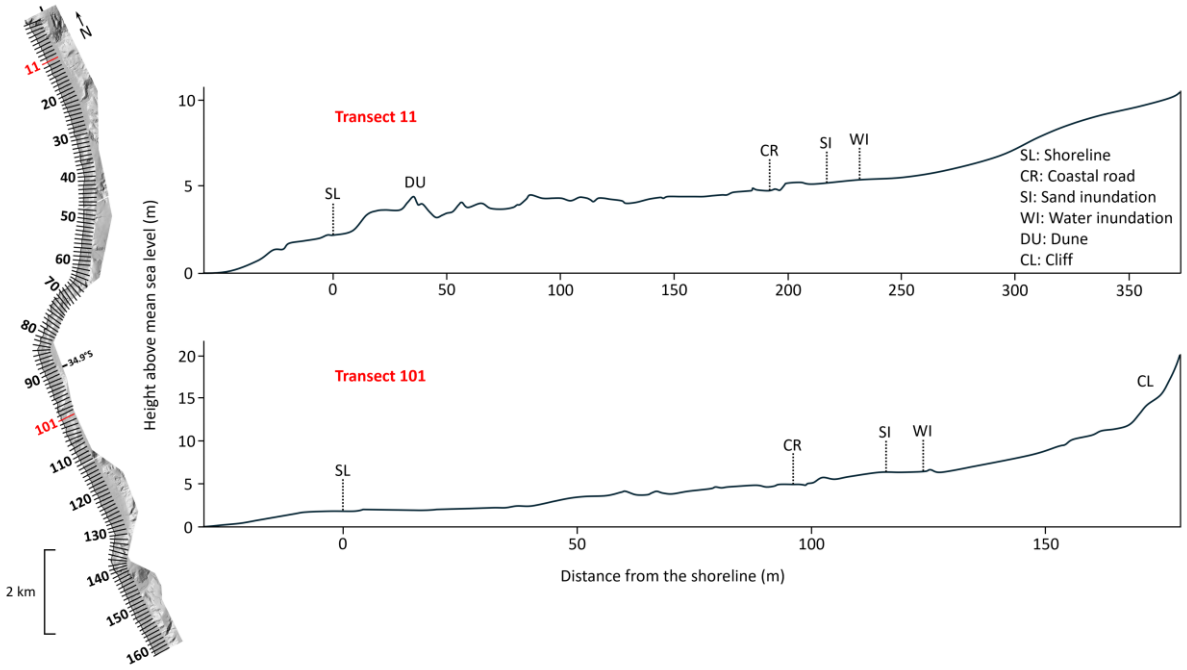

Figure S6. Typical profiles along the Lipimávida-Iloca coast. Low slope profiles (transect 11) are usually characterized by a dune located a few meters from the shoreline and about 5 m high. Steeper slope profiles (transect 101) are characterized by a reduced or absent dune and the cliff positioned closer to the shoreline. Note the different horizontal and vertical scale in both profiles. Map on the left shows the location of both transects and the remaining 160 transects used for inundation measurements.

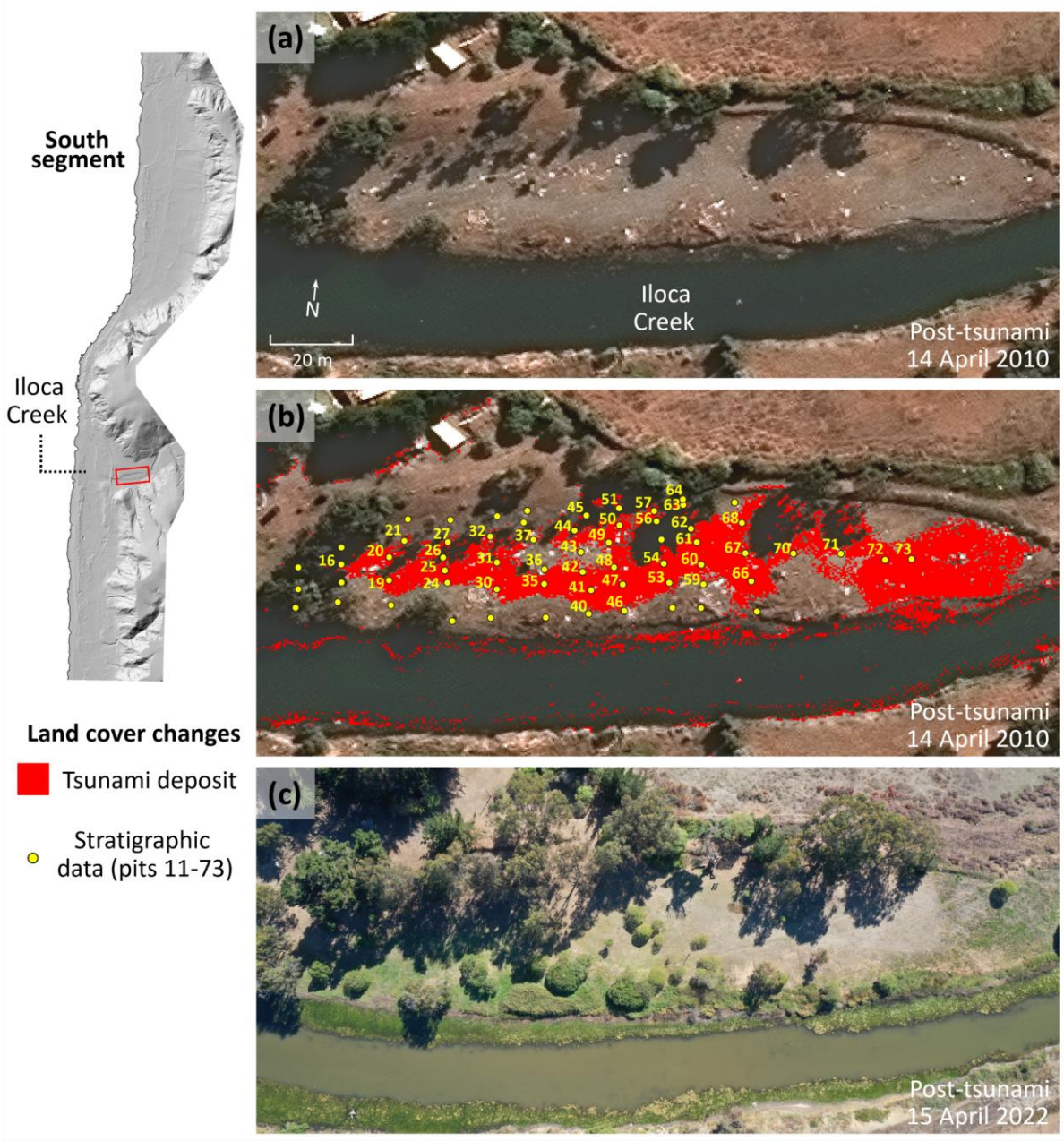

Figure S7. Match between pits exhibiting the 2010 tsunami sand layer and the sand deposit inferred from our classification model. (a) Post-tsunami satellite image showing the sand sheet and debris that was deposited by the 2010 tsunami on the floodplain of Iloca Creek. (b) Red shading is the sand deposit that was mapped by our classification model. The 63 pits that were excavated in Iloca Creek are shown by yellow dots. Pits exhibiting the preserved sand layer that matched the predictions of the classification model are labeled (see table S2). Note how tree canopies and shadows obscure the tsunami deposit and prevent its detection through the classification model. (c) Aerial photograph of Iloca Creek, taken 12 years after the tsunami, showing the sand deposit covered by vegetation. Red box on the map to the left indicates the location of (a), (b) and (c) in Iloca Creek.

Supplemental methods for sedimentary analysis

Sampling was completed in 26 pits, collecting 200 g of the tsunami sand layer (Table S2). Additionally, the beach (3 samples), dune (1), soil underlying the tsunami deposit (2) and creek bank (1) were also sampled as possible sources of sediment (Table S3). Samples were washed to remove the fine fraction (>4 φ) and treated with hydrogen peroxide (30% concentration) to remove organic material. Subsequently, the samples were dried inside an oven at medium temperature for 24 hours. The sediments were separated by grain size in a mechanical sieve, ranging from -1 to 4 φ at intervals of 0.25 φ. Statistical parameters were obtained with GRADISTAT v. 9.1 software following Blott and Pye (2001) and presented according to Folk and Ward (1957). Mineralogical analyzes were based on descriptions in a binocular stereoscopic microscope. Using a Bartington Susceptibility Meter MS2E, magnetic susceptibility tests (SI x 10-5) were performed on identical sediment volumes, drawing an average after measuring each sample three times. Structures and thicknesses of the tsunami deposit were made by field observations. Results obtained from the thickness, grain size, sorting, magnetic susceptibility, erosive basal contact and normal grading of the tsunami sand layer found in the 63 pits that were excavated in Iloca Creek are shown as distribution maps in Figure S9. Missing data from unsampled pits were interpolated using the algorithm Multilevel B-Spline in QGIS software.

Results of sedimentary analysis

The tsunami deposit is described as a tabular layer composed of well-sorted medium to fine grayish sand (Table S2), in a few cases displaying upward fining on an erosive basal contact and entrained rip-up clasts. Although the thickness of the sand deposit was variable, it had an inland thinning trend (Figure S9). Trends in mean grain size, sorting and magnetic susceptibility can also be traced landward and are likely related with flow slowing (Figure S9). See inferred tsunami direction for more details.

The dark color of the tsunami sand is contributed by the high content of heavy minerals (Figure S8), such as magnetite (33%), amphibole (12%), pyroxene (8%),

and in smaller quantity zircon, sphene, rutile, olivine, epidote, biotite, and hematite (2%). Concentrations of heavy minerals were in some cases seen as laminations. Lithics derived from metamorphic rocks were also abundant (20%). The light minerals are less in abundance such as quartz (15%), glass (5%) and feldspars (5%). No shell fragments observed.

Among the sedimentary environments sampled, the dune and beach share features with the tsunami sand deposit (Tables S2 and S3). Similarities in granulometry, mineralogy and high magnetic susceptibility values point to the beach and dune as presumed sources of the tsunami sand layer (Figure S8). Finer sediment may have been incorporated from the underlying eroded soil and the Iloca Creek bed.

Inferred tsunami direction

Landward trends of thickness, granulometric parameters, magnetic susceptibility and some structures observed in the sand layer were used to infer the direction of the tsunami in Iloca Creek (Figure S9). A general landward thinning trend, which is visible both upstream and away from Iloca Creek channel, may be attributable to a progressive deceleration of the inland flow and loss of transport capacity (Spiske et al., 2020). In addition, superimposed on this trend, local variability in topography is also a factor controlling the thickness of the deposit. Thicker deposits of up to 14 cm are observed in low-lying areas and topographic depressions of the floodplain of Iloca Creek (Figure S9).

Landward fining and sorting trends can also be explained by the decreasing flow velocity (Spiske et al. 2020). The mean grain size reached a maximum value near Iloca Creek and tended to decrease away from the main channel, roughly in a NE direction (Figure S9). Likewise, sorting increased landward, exhibiting a similar direction to that of grain size. Landward trends in grain size and sorting imply selective sedimentation of coarser grains close to the creek and an increased fines load as the flow velocity decreases inland.

A visible trend in the magnetic susceptibility of the sand layer can also be interpreted as a response to changes in flow energy (e.g., Kempf et al., 2015). Higher magnetic susceptibility values, about 943 x 10-5 SI, may reflect a more energetic flow capable of transporting coarser and denser grains, which is attenuated in a direction normal to the main channel of the creek, reaching minimum values of 457 x 10-5 SI (Figure S9).

Sedimentary structures such as erosive basal contact and normal grading are restricted to pits located near the Iloca Creek channel (Figure S9). Rip-up-clast entered in the sand layer also shows approximately the same distribution. These structures probably reflect an initial erosive behavior of the tsunami flow near Iloca Creek and then an attenuation or stagnation phase that allowed the deposition of finer suspended sediments.

Our results from sedimentary analysis suggest that the sand layer preserved in the Iloca Creek floodplain was deposited by a single wave with a preferential direction both upstream and normal to the creek channel. This is consistent with information provided by eyewitnesses (Table S1). Locals around Iloca Creek who witnessed the tsunami, reported three main waves following the 2010 earthquake. However, only the second was large enough to inundate the entire floodplain. Based on these accounts, the first tsunami wave entered smoothly through the creek channel and was similar to a sudden rise in sea level. The second wave had a height of at least 7 m, which lowered the dune, overtopped the bridge located ~300 m from the shoreline and inundated the floodplain depositing sand and other debris (mainly wood, clothing and fishing nets). The third wave, which arrived several hours later, was smaller and did not reach the site where the pits were excavated.

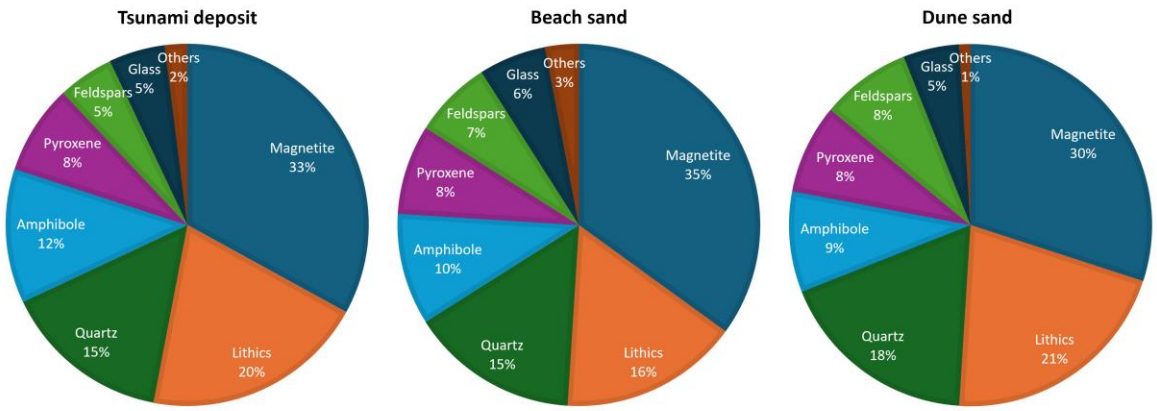

Figure S8. Pie charts showing the mineralogical composition of tsunami, beach and dune sand. The mineralogical similarity suggests a source from the beach and/or dune for the tsunami deposit.

Table S2. Pits excavated along the North (1-4), Central (5-8) and South (9-73) segments. In each pit the thickness of the tsunami deposit was recorded. Mean grain size, sorting and magnetic susceptibility (Mag. susc.) is indicated for those pits in Iloca Creek where the deposit was sampled. Pits exhibiting tsunami sand deposit and that were predicted by our classification model are indicated by an asterisk (53 in total).

N°	Latitude Longitude Elevation	Thickness (cm)	Mean grain size (φ)	Sorting (φ)	Mag. susc. (x 10^{-5} SI)	Sedimentary structures	Pit date
1*	34.83667°S 72.14230°W 3.435 m	28	-	-	-	Erosive cont.	August 2010
2*	34.86344°S 72.14751°W 4.420 m	10	-	-	-	-	December 2021
3*	34.86361°S 72.14753°W 4.634 m	8	-	-	-	-	December 2021
4*	34.86389°S 72.14763°W 6.179 m	11	-	-	-	-	December 2021
5*	34.87915°S 72.15651°W 0.675 m	15	-	-	-	-	December 2021
6*	34.88026°S 72.15634°W 1.946 m	25	-	-	-	Erosive cont.	December 2021
7*	34.88069°S 72.15555°W 2.219 m	12	-	-	-	Erosive cont.	December 2021
8*	34.88233°S 72.15433°W 1.305 m	5	-	-	-	Erosive cont.	April 2022
9*	34.92247°S 72.18031°W 4.320 m	7	-	-	-	-	February 2022
10*	34.922768°S 72.180006°W 3.339 m	14	-	-	-	-	February 2022

11	34.95021°S 72.18318°W 1.980 m	14	-	-	-	Erosive cont. Normal grading	October 2021
12	34.95016°S 72.18318°W 2.450 m	10	1.904	1.159	943	Erosive cont.	October 2021 July 2023
13	34.95010°S 72.18319°W 2.687 m	<1	-	-	-	-	October 2021
14	34.95018°S 72.18307°W 2.115 m	<1	-	-	-	Erosive cont. Normal grading	October 2021
15	34.95013°S 72.18307°W 2.202 m	10	2.061	0.909	774	Erosive cont.	October 2021
16*	34.95008°S 72.18307°W 2.374 m	9	2.229	0.475	794	-	October 2021
17	34.95004°S 72.18308°W 2.683 m	7	-	-	-	-	October 2021
18	34.95018°S 72.18293°W 2.390 m	8	-	-	-	Erosive cont. Normal grading	October 2021
19*	34.95011°S 72.18294°W 2.329 m	9	2.177	0.721	532	Erosive cont.	October 2021
20*	34.95005°S 72.18295°W 2.428 m	14	2.165	0.439	609	-	October 2021
21*	34.95000°S 72.18291°W 2.841 m	8	-	-	-	-	October 2021
22	34.94994°S 72.18291°W 4.006 m	<1	-	-	-	-	October 2021
23	34.95020°S 72.18276°W 2.230 m	10	2.284	0.552	718	Erosive cont. Normal grading	October 2021

24*	34.95010°S 72.18278°W 2.379 m	6	2.074	0.727	593	Erosive cont. Normal grading	October 2021
25*	34.95007°S 72.18279°W 2.371 m	9	-	-	-	-	October 2021
26*	34.95004°S 72.18280°W 2.395 m	14	2.232	0.496	548	-	October 2021
27*	34.94999°S 72.18279°W 2.597 m	14	2.267	0.469	536	-	October 2021
28	34.94993°S 72.18279°W 3.850 m	<1	-	-	-	-	October 2021
29	34.95018°S 72.18266°W 2.302 m	10	-	-	-	Erosive cont. Normal grading	October 2021
30*	34.95011°S 72.18265°W 2.467 m	12	2.222	0.521	694	Erosive cont. Normal grading	October 2021
31*	34.95003°S 72.18266°W 2.443 m	12	2.258	0.476	544	-	October 2021
32*	34.94997°S 72.18268°W 2.528 m	10	-	-	-	-	October 2021
33	34.94991°S 72.18267°W 3.572 m	<1	-	-	-	-	October 2021
34	34.95017°S 72.18251°W 2.555 m	10	2.279	0.601	697	Erosive cont. Normal grading	October 2021
35*	34.95008°S 72.18253°W 2.428 m	8	-	-	-	Erosive cont. Normal grading	October 2021
36*	34.95004°S 72.18253°W 2.406 m	12	2.294	0.541	593	Erosive cont.	October 2021

37*	34.94996°S 72.18257°W 2.530 m	8	-	-	-	-	October 2021
38	34.94992°S 72.18260°W 3.116 m	<1	-	-	-	-	October 2021
39	34.94989°S 72.18259°W 3.756 m	<1	-	-	-	-	October 2021
40*	34.95015°S 72.18240°W 2.492 m	7	-	-	-	Erosive cont. Normal grading	October 2021
41*	34.95008°S 72.18240°W 2.518 m	7	-	-	-	Erosive cont. Normal grading	October 2021
42*	34.95004°S 72.18243°W 2.519 m	7	2.314	0.547	585	-	October 2021
43*	34.94998°S 72.18244°W 2.467 m	7	-	-	-	-	October 2021
44*	34.94993°S 72.18246°W 2.655 m	5	2.355	0.569	569	-	October 2021
45*	34.94988°S 72.18243°W 3.089 m	<1	-	-	-	-	October 2021
46*	34.95013°S 72.18231°W 2.667 m	6	-	-	-	Erosive cont.	October 2021
47*	34.95006°S 72.18232°W 2.549 m	7	-	-	-	-	October 2021
48*	34.95001°S 72.18234°W 2.576 m	7	2.288	0.487	627	-	October 2021
49*	34.94995°S 72.18237°W 2.560 m	7	2.337	0.537	498	-	October 2021

50*	34.94990°S 72.18234°W 2.783 m	5	-	-	-	-	October 2021
51*	34.94986°S 72.18235°W 3.121 m	<1	-	-	-	-	October 2021
52	34.95011°S 72.18218°W 2.969 m	7	2.289	0.696	785	Erosive cont.	October 2021
53*	34.95004°S 72.18219°W 2.648 m	7	-	-	-	-	October 2021
54*	34.94999°S 72.18221°W 2.662 m	7	2.329	0.555	660	-	October 2021
55	34.94993°S 72.18223°W 2.640 m	7	2.295	0.608	672	-	October 2021
56*	34.94988°S 72.18224°W 2.779 m	5	-	-	-	-	October 2021
57*	34.94985°S 72.18225°W 2.841 m	<1	-	-	-	-	October 2021
58	34.95010°S 72.18210°W 2.784 m	<1	-	-	-	-	October 2021
59*	34.95003°S 72.18210°W 2.722 m	8	2.158	0.876	719	Normal grading	October 2021
60*	34.94998°S 72.18211°W 2.719 m	8	2.343	0.708	743	-	October 2021
61*	34.94992°S 72.18213°W 2.707	6	-	-	-	-	October 2021
62*	34.94989°S 72.18215°W 2.692 m	5	-	-	-	-	October 2021

63*	34.94983°S 72.18218°W 2.730 m	3	-	-	-	Normal grading	October 2021
64*	34.94981°S 72.18218°W 3.098 m	3	-	-	-	Normal grading	October 2021
65	34.95009°S 72.18195°W 2.803 m	5	2.297	0.654	943	Normal grading	October 2021
66*	34.95001°S 72.18198°W 2.728 m	8	2.127	0.922	724	Normal grading	October 2021
67*	34.94994°S 72.18200°W 2.743 m	8	-	-	-	-	October 2021
68*	34.94986°S 72.18202°W 2.721 m	10	2.266	0.620	553	-	October 2021
69	34.94981°S 72.18204°W 2.791 m	<1	-	-	-	-	October 2021
70*	34.94993°S 72.18187°W 2.733 m	6	2.342	0.779	457	-	October 2021
71*	34.94991°S 72.18174°W 2.771 m	5	-	-	-	-	October 2021
72*	34.94992°S 72.18162°W 2.711 m	5	-	-	-	-	October 2021
73*	34.94991°S 72.18155°W 2.656 m	<1	-	-	-	-	October 2021

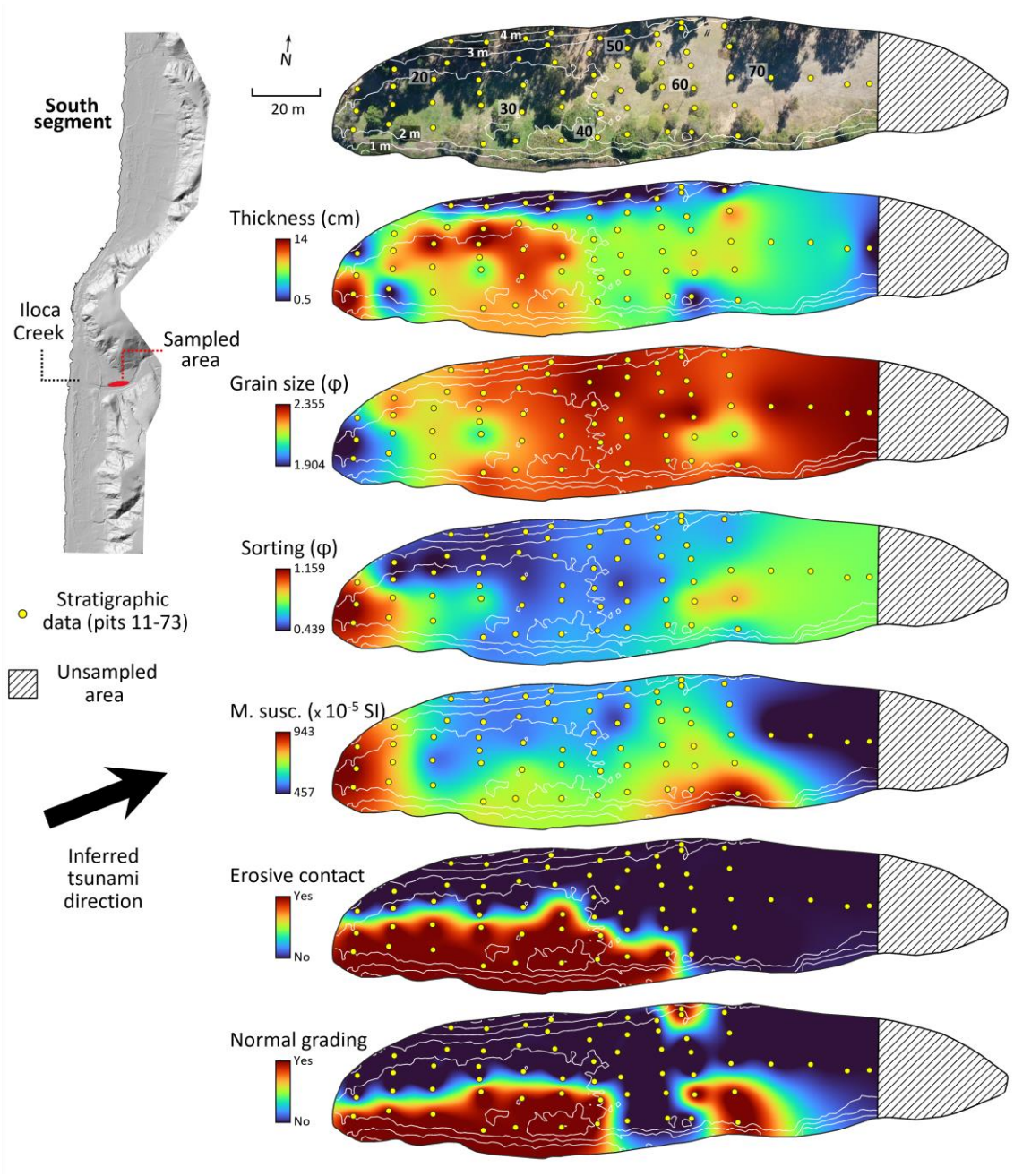

Figure S9. Distribution maps of thickness, grain size, sorting, magnetic susceptibility (M. susc.), erosive basal contact and normal grading of the tsunami sand deposit found in Iloca Creek (see Figure S7). A landward trend of these features in the sand layer allows inferring an approximate NE direction for the tsunami. The 63 pits that were surveyed in Iloca Creek are shown by yellow dots and labeled every 10 of them (see Table S2). Contour lines are shown in white and labeled every 1 m.

Table S3. Sediment sources that were sampled in the study area.

N°	Sediment source	Latitude Longitude Elevation	Mean grain size (φ)	Sorting (φ)	Magnetic suscep. (x 10^{-5} SI)
1	Wet beach (South segment)	34.94998°S 72.18715°W 1.427 m	2.189	0.428	509
2	Dry beach (South segment)	34.95009°S 72.18663°W 2.967 m	2.153	0.474	606
3	Dry beach (North segment)	34.83691°S 72.14357°W 2.549 m	1.965	0.477	1122
4	Dune (South segment)	34.95085°S 72.18664°W 5.250 m	2.156	0.319	390
5	Iloca Creek bed	34.95024°S 72.18306°W 1.423 m	3.175	1.366	577
6	Pre-tsunami soil (Iloca Creek)	34.95002°S 72.18248°W 2.474 m	3.925	1.893	634
7	Pre-tsunami soil (Iloca Creek)	34.94996°S 72.18214°W 2.702 m	4.118	1.934	532

Table S4. Measurements along each transect for water inundation, sand inundation, runup and land slope. The difference between water and sand inundation is indicated as a gap. Average for each segment and total average are indicated in bold.

Segment	Transect	Water inundation (m)	Sand inundation (m)	Gap (m)	% Sand inundation	Runup (m)	Land slope (°)
	1	87.88	84.25	3.62	95.88	4.67	5.40
	2	99.14	98.99	0.15	99.84	4.23	4.40
	3	149.04	122.81	26.23	82.40	6.43	2.60
	4	155.85	142.38	13.47	91.36	6.60	2.54
	5	165.64	116.18	49.47	70.14	7.97	2.34
	6	199.16	190.83	8.33	95.82	4.72	1.82

	7	296.62	281.40	15.23	94.87	6.63	1.48
	8	228.06	219.26	8.80	96.14	4.42	1.17
	9	233.62	220.42	13.20	94.35	3.99	1.39
	10	256.24	229.28	26.97	89.48	5.13	1.27
	11	232.37	217.81	14.56	93.74	5.24	1.33
	12	206.57	204.75	1.81	99.12	4.67	1.26
	13	225.53	224.54	1.00	99.56	5.13	1.25
	14	252.96	234.14	18.82	92.56	5.82	1.22
	15	220.72	185.62	35.10	84.10	5.96	1.25
	16	197.35	163.55	33.80	82.87	5.07	1.16
	17	239.60	188.80	50.80	78.80	5.82	1.19
	18	229.62	142.16	87.46	61.91	4.45	1.13
	19	245.53	125.24	120.29	51.01	3.64	1.08
	20	234.06	175.15	58.91	74.83	3.73	1.07
	21	321.48	314.86	6.62	97.94	3.56	1.04
	22	361.90	361.47	0.43	99.88	5.79	1.15
	23	365.85	277.50	88.34	75.85	4.16	0.95
North	24	366.57	334.59	31.98	91.28	4.95	1.03
	25	271.50	144.73	126.77	53.31	3.91	1.08
	26	276.53	206.27	70.25	74.59	3.73	1.06
	27	245.95	236.07	9.88	95.98	3.89	1.07
	28	221.59	204.11	17.48	92.11	3.70	1.16
	29	192.73	189.64	3.09	98.40	3.50	1.38
	30	162.59	146.53	16.07	90.12	5.58	2.55
	31	105.71	102.89	2.82	97.33	7.74	3.72
	32	109.56	109.56	0.00	100.00	10.35	3.72
	33	92.57	90.62	1.95	97.90	7.88	4.10
	34	107.60	106.60	1.00	99.07	10.00	4.07
	35	76.00	72.48	3.53	95.36	7.09	4.04
	36	82.96	81.95	1.01	98.79	9.47	4.28
	37	117.50	94.39	23.11	80.33	6.04	2.93
	38	124.35	107.20	17.16	86.20	6.74	2.65
	39	123.34	115.34	7.99	93.52	6.69	2.61
	40	132.90	124.37	8.53	93.58	8.50	2.53
	41	129.37	127.87	1.50	98.84	8.52	2.84
	42	162.50	79.39	83.11	48.86	6.23	2.35
	43	300.60	285.37	15.24	94.93	9.61	1.73
	44	154.22	142.14	12.08	92.17	5.51	2.40
	45	137.98	105.21	32.77	76.25	7.02	2.91
	46	140.39	119.67	20.71	85.24	7.73	3.14
	47	164.08	155.25	8.83	94.62	8.95	2.75
	Average	**195.83**	**170.29**	**25.54**	**87.90**	**5.98**	**2.16**
	48	166.59	130.93	35.66	78.59	8.28	2.60

	49	181.26	166.00	15.25	91.59	9.00	2.35
	50	179.98	111.27	68.71	61.82	5.90	2.30
	51	163.87	162.64	1.22	99.25	6.32	2.54
	52	156.82	156.82	0.00	100.00	8.49	2.77
	53	141.07	114.47	26.60	81.14	6.76	2.88
	54	147.17	147.12	0.05	99.97	6.47	2.67
	55	177.44	177.44	0.00	100.00	6.58	2.57
	56	218.32	218.19	0.13	99.94	6.55	2.11
	57	268.02	262.97	5.04	98.12	5.17	1.50
	58	470.37	444.89	25.48	94.58	2.96	0.76
	59	397.80	288.24	109.56	72.46	3.42	0.52
	60	239.16	220.86	18.31	92.35	7.42	1.73
	61	168.33	156.85	11.47	93.18	7.64	2.08
	62	178.70	178.70	0.00	100.00	6.29	2.22
	63	159.15	158.17	0.98	99.38	6.84	2.25
	64	172.27	172.27	0.00	100.00	6.37	2.07
	65	146.30	141.65	4.65	96.82	6.34	3.04
	66	96.48	62.17	34.31	64.44	7.31	4.52
	67	105.74	98.03	7.71	92.71	7.15	5.00
	68	82.39	69.70	12.69	84.60	9.99	6.49
	69	94.07	60.07	34.01	63.85	9.85	6.78
	70	108.82	108.82	0.00	100.00	6.61	5.90
	71	57.96	51.55	6.41	88.94	9.43	6.91
	72	97.22	71.29	25.94	73.32	7.52	4.54
	73	76.78	69.10	7.68	90.00	8.20	7.34
	74	97.60	97.60	0.00	100.00	7.10	3.94
	75	86.14	85.63	0.50	99.42	6.90	6.13
	76	91.33	81.47	9.86	89.20	6.73	4.51
	77	62.12	62.12	0.00	100.00	6.79	7.33
	78	109.44	105.35	4.10	96.26	8.50	4.27
Central	79	83.67	82.44	1.23	98.53	7.39	5.70
	80	88.44	83.76	4.68	94.71	7.89	4.91
	81	108.50	99.15	9.35	91.38	9.99	5.93
	82	150.64	143.23	7.41	95.08	7.04	3.70
	83	147.53	132.83	14.69	90.04	10.24	4.14
	84	176.14	158.59	17.55	90.04	9.97	2.95
	85	178.82	154.03	24.79	86.14	7.79	2.51
	86	106.27	103.14	3.13	97.05	5.70	2.62
	87	96.39	74.42	21.97	77.20	4.42	2.94
	88	131.06	100.43	30.62	76.63	4.86	2.50
	89	160.27	152.96	7.31	95.44	5.73	2.11
	90	153.81	153.81	0.00	100.00	5.97	1.93
	91	166.41	165.68	0.73	99.56	6.06	1.95

	92	144.21	139.87	4.34	96.99	4.94	1.96
	93	153.09	150.52	2.57	98.32	5.96	2.03
	94	155.56	154.63	0.94	99.40	6.21	2.23
	95	168.89	164.75	4.15	97.55	6.69	2.42
	96	182.51	168.70	13.81	92.43	8.32	2.28
	97	144.20	114.20	30.00	79.20	6.92	3.11
	98	64.48	60.88	3.60	94.42	4.59	4.15
	99	67.78	67.78	0.00	100.00	5.28	4.57
	100	107.23	93.66	13.57	87.35	9.15	3.63
	101	124.20	116.40	7.80	93.72	6.57	2.95
	102	109.49	109.49	0.00	100.00	6.33	3.13
	103	99.38	79.19	20.19	79.68	5.14	3.08
	104	103.14	100.06	3.08	97.02	5.31	3.44
	105	100.51	91.91	8.60	91.44	5.01	3.50
	106	91.02	76.73	14.28	84.31	5.58	4.26
	107	73.66	73.66	0.00	100.00	5.35	4.20
	108	113.08	113.08	0.00	100.00	10.43	3.32
	109	149.81	138.12	11.69	92.20	7.20	2.96
	110	154.07	139.93	14.14	90.82	7.01	2.44
	111	192.72	184.52	8.20	95.74	8.19	2.12
	112	216.28	216.28	0.00	100.00	6.02	1.89
	Average	**144.03**	**132.17**	**11.86**	**91.76**	**6.89**	**3.39**
	113	243.20	218.49	24.71	89.84	6.09	1.34
	114	333.62	264.45	69.17	79.27	4.11	1.17
	115	371.66	363.26	8.40	97.74	8.77	1.14
	116	292.61	258.03	34.58	88.18	5.67	1.34
	117	284.21	284.21	0.00	100.00	4.51	1.31
	118	373.17	340.05	33.12	91.12	6.60	1.17
	119	357.57	305.67	51.90	85.49	5.36	1.18
	120	288.45	273.16	15.29	94.70	4.95	1.12
	121	270.27	233.66	36.62	86.45	5.29	1.09
	122	275.16	189.09	86.06	68.72	4.69	1.04
	123	298.69	234.43	64.26	78.49	4.03	0.97
	124	311.90	307.97	3.93	98.74	3.48	0.99
	125	302.00	291.66	10.34	96.58	3.66	1.00
	126	313.86	299.08	14.78	95.29	4.11	0.99
	127	345.92	277.73	68.19	80.29	4.89	1.03
	128	305.83	305.83	0.00	100.00	6.34	1.12
	129	292.68	285.84	6.83	97.66	7.03	1.28
	130	264.47	249.92	14.54	94.50	7.08	1.40
	131	142.27	142.27	0.00	100.00	6.30	1.91
	132	139.26	111.94	27.32	80.38	9.42	3.22
	133	148.36	148.36	0.00	100.00	8.56	3.80

South	134	88.82	54.47	34.35	61.32	7.78	5.75
	135	97.23	92.62	4.61	95.26	9.56	6.79
	136	78.71	49.51	29.20	62.90	5.52	5.88
	137	83.35	66.55	16.80	79.84	6.77	5.65
	138	86.38	86.38	0.00	100.00	6.25	5.86
	139	69.35	69.35	0.00	100.00	6.80	5.41
	140	67.75	55.67	12.08	82.17	5.39	7.68
	141	97.59	91.60	5.99	93.86	6.80	4.97
	142	115.96	108.36	7.60	93.45	7.74	5.01
	143	129.53	129.53	0.00	100.00	5.33	3.13
	144	235.25	209.69	25.56	89.14	6.47	2.08
	145	316.65	263.82	52.84	83.31	6.11	1.07
	146	626.88	582.13	44.75	92.86	3.50	0.74
	147	454.05	265.07	188.98	58.38	6.33	0.95
	148	254.29	254.29	0.00	100.00	4.56	1.57
	149	298.23	271.60	26.63	91.07	8.48	1.53
	150	315.35	299.80	15.55	95.07	7.90	1.31
	151	306.00	293.77	12.23	96.00	7.69	1.35
	152	287.87	256.83	31.04	89.22	8.26	1.57
	153	254.15	185.00	69.15	72.79	7.27	1.85
	154	232.68	170.98	61.70	73.48	6.51	1.87
	155	240.50	183.93	56.57	76.48	6.60	2.22
	156	236.92	138.36	98.56	58.40	6.83	2.10
	157	245.33	245.33	0.00	100.00	6.36	1.83
	158	270.16	266.87	3.28	98.79	6.29	1.58
	159	313.01	268.53	44.48	85.79	8.84	1.46
	160	286.58	258.38	28.20	90.16	6.82	1.39
	161	277.09	277.09	0.00	100.00	6.83	1.46
	162	308.76	284.82	23.95	92.24	7.97	1.42
	Average	**252.59**	**223.31**	**29.28**	**88.31**	**6.37**	**2.30**
Total average		**192.56**	**171.36**	**21.21**	**89.57**	**6.47**	**2.70**

Figure S10. Confusion matrix with 180 validation points for the pre-tsunami (2005) LULC map of the North segment (Figure 2b). Classes are abbreviated as follows: (W) Water, (F) Foam; (Ws) Wet sand; (Ds) Dry sand; (U) Urban; (Bs) Bare soil; (C) Crop; (S) Shadow; (Fr) Forest.

		Reference								
		W	**F**	**W_s**	**D_s**	**U**	**B_s**	**C**	**S**	**F_r**
Prediction	**W**	18	0	1	0	0	0	0	0	0
	F	1	19	0	1	1	0	0	0	0
	W_s	1	1	17	0	1	0	0	1	0
	D_s	0	0	1	19	0	0	0	0	0
	U	0	0	0	0	14	7	0	0	0
	B	0	0	0	0	4	13	4	0	0
	C	0	0	0	0	0	0	13	0	0
	S	0	0	1	0	0	0	0	14	4
	F_r	0	0	0	0	0	0	3	5	16

Overall accuracy: 0.79
Kappa coefficient: 0.77
Producer's accuracy for Ws: 0.85
Producer's accuracy for Ds: 0.95
User’s accuracy for Ws: 0.81
User’s accuracy for Ds: 0.95

Figure S11. Confusion matrix with 180 validation points for the post-tsunami (2010) LULC map of the North segment (Figure 2e). Classes are abbreviated as follows: (W) Water, (F) Foam; (Ws) Wet sand; (Ds) Dry sand; (U) Urban; (Bs) Bare soil; (C) Crop; (S) Shadow; (Fr) Forest.

		Reference								
		W	**F**	**W_s**	**D_s**	**U**	**B_s**	**C**	**S**	**F_r**
Prediction	**W**	20	0	0	0	0	0	0	0	0
	F	0	20	0	0	1	0	0	0	0
	W_s	0	0	20	0	0	0	0	0	0
	D_s	0	0	0	17	2	1	0	0	0
	U	0	0	0	3	12	3	1	0	0
	B	0	0	0	0	5	16	1	0	0
	C	0	0	0	0	0	0	17	0	1
	S	0	0	0	0	0	0	0	19	0
	F_r	0	0	0	0	0	0	1	1	19

Overall accuracy: 0.89
Kappa coefficient: 0.88
Producer's accuracy for Ws: 1.00
Producer's accuracy for Ds: 1.00
User’s accuracy for Ws: 1.00
User’s accuracy for Ds: 0.85

Figure S12. Confusion matrix with 180 validation points for the pre-tsunami (2004) LULC map of the Central segment (Figure S1b). Classes are abbreviated as follows: (W) Water, (F) Foam; (Ws) Wet sand; (Ds) Dry sand; (U) Urban; (Bs) Bare soil; (C) Crop; (S) Shadow; (Fr) Forest.

		Reference								
		W	**F**	**W_s**	**D_s**	**U**	**B_s**	**C**	**S**	**F_r**
Prediction	**W**	19	0	0	0	0	0	0	1	0
	F	0	20	0	0	1	0	0	0	0
	W_s	0	0	19	0	0	1	0	0	0
	D_s	0	0	0	19	1	0	0	0	0
	U	1	0	0	1	15	8	0	1	0
	B	0	0	0	0	3	11	0	0	0
	C	0	0	0	0	0	0	20	0	4
	S	0	0	0	0	0	0	0	18	0
	F_r	0	0	1	0	0	0	0	0	16

Overall accuracy: 0.87
Kappa coefficient: 0.86
Producer's accuracy for Ws: 0.95
Producer's accuracy for Ds: 0.95
User's accuracy for Ws: 0.95
User's accuracy for Ds: 0.95

Figure S13. Confusion matrix with 180 validation points for the post-tsunami (2010) LULC map of the Central segment (Figure S1e). Classes are abbreviated as follows: (W) Water, (F) Foam; (W_s) Wet sand; (D_s) Dry sand; (U) Urban; (B_s) Bare soil; (C) Crop; (S) Shadow; (F_r) Forest.

		Reference								
		W	**F**	**W_s**	**D_s**	**U**	**B_s**	**C**	**S**	**F_r**
Prediction	**W**	19	0	0	0	0	0	0	0	0
	F	0	20	0	0	1	0	0	0	0
	W_s	1	0	20	0	0	0	0	0	0
	D_s	0	0	0	17	3	1	0	0	0
	U	0	0	0	3	10	4	0	0	0
	B	0	0	0	0	6	15	0	0	0
	C	0	0	0	0	0	0	16	0	0
	S	0	0	0	0	0	0	0	20	1
	F_r	0	0	0	0	0	0	4	0	19

Overall accuracy: 0.87
Kappa coefficient: 0.85
Producer's accuracy for W_s: 1.00
Producer's accuracy for D_s: 0.85
User's accuracy for W_s: 0.95
User's accuracy for D_s: 0.81

Figure S14. Confusion matrix with 180 validation points for the pre-tsunami (2004) LULC map of the South segment (Figure S2b). Classes are abbreviated as follows: (W) Water, (F) Foam; (Ws) Wet sand; (Ds) Dry sand; (U) Urban; (Bs) Bare soil; (C) Crop; (S) Shadow; (Fr) Forest.

		Reference								
		W	**F**	**W_s**	**D_s**	**U**	**B_s**	**C**	**S**	**F_r**
Prediction	**W**	20	0	0	0	0	0	0	0	0
	F	0	19	0	0	5	0	0	0	0
	W_s	0	0	18	0	1	0	0	0	0
	D_s	0	0	1	18	0	1	0	0	0
	U	0	1	0	1	10	1	0	0	0
	B	0	0	0	1	3	17	0	0	0
	C	0	0	0	0	0	1	16	0	1
	S	0	0	1	0	1	0	0	17	0
	F_r	0	0	0	0	0	0	4	3	19

Overall accuracy: 0.86
Kappa coefficient: 0.84
Producer's accuracy for W_s: 0.90
Producer's accuracy for D_s: 0.90
User's accuracy for W_s: 0.95
User's accuracy for D_s: 0.90

Figure S15. Confusion matrix with 180 validation points for the post-tsunami (2010) LULC map of the South segment (Figure S2e). Classes are abbreviated as follows: (W) Water, (F) Foam; (Ws) Wet sand; (Ds) Dry sand; (U) Urban; (Bs) Bare soil; (C) Crop; (S) Shadow; (Fr) Forest.

		Reference								
		W	**F**	**W_s**	**D_s**	**U**	**B_s**	**C**	**S**	**F_r**
Prediction	**W**	20	0	3	0	0	0	0	0	3
	F	0	20	0	0	0	0	0	0	0
	W_s	0	0	17	0	0	0	0	0	0
	D_s	0	0	0	20	2	0	0	0	0
	U	0	0	0	0	14	6	0	0	0
	B	0	0	0	0	3	14	0	0	0
	C	0	0	0	0	0	0	19	0	4
	S	0	0	0	0	1	0	0	20	0
	F_r	0	0	0	0	0	0	1	0	13

Overall accuracy: 0.87
Kappa coefficient: 0.87
Producer's accuracy for W_s: 0.85
Producer's accuracy for D_s: 1.00
User's accuracy for W_s: 1.00
User's accuracy for D_s: 0.91

Figure S16. Confusion matrix with 180 validation points for the post-tsunami (2021) LULC map of the North segment (Figure S3b). Classes are abbreviated as follows: (W) Water, (F) Foam; (Ws) Wet sand; (Ds) Dry sand; (U) Urban; (Bs) Bare soil; (C) Crop; (S) Shadow; (Fr) Forest.

		Reference								
		W	**F**	**W_s**	**D_s**	**U**	**B_s**	**C**	**S**	**F_r**
Prediction	**W**	20	0	0	0	0	0	0	0	0
	F	0	20	0	0	2	0	0	0	0
	W_s	0	0	19	0	1	0	0	0	0
	D_s	0	0	0	19	1	0	0	0	0
	U	0	0	1	1	12	3	0	0	0
	B	0	0	0	0	4	16	0	0	1
	C	0	0	0	0	0	0	16	0	0
	S	0	0	0	0	0	0	0	20	1
	F_r	0	0	0	0	0	1	4	0	18

Overall accuracy: 0.89
Kappa coefficient: 0.88
Producer's accuracy for Ws: 0.95
Producer's accuracy for Ds: 0.95
User's accuracy for Ws: 0.95
User's accuracy for Ds: 0.95

Figure S17. Confusion matrix with 180 validation points for the post-tsunami (2021) LULC map of the Central segment (Figure S4b). Classes are abbreviated as follows: (W) Water, (F) Foam; (Ws) Wet sand; (Ds) Dry sand; (U) Urban; (Bs) Bare soil; (C) Crop; (S) Shadow; (Fr) Forest.

		Reference								
		W	**F**	**W_s**	**D_s**	**U**	**B_s**	**C**	**S**	**F_r**
Prediction	**W**	20	0	0	0	0	0	0	0	0
	F	0	17	0	0	0	0	0	0	0
	W_s	0	0	20	0	0	0	0	0	0
	D_s	0	2	0	20	2	0	0	0	0
	U	0	1	0	0	10	4	0	0	0
	B	0	0	0	0	6	16	0	0	0
	C	0	0	0	0	0	0	17	0	3
	S	0	0	0	0	0	0	0	18	0
	F_r	0	0	0	0	2	0	3	2	17

Overall accuracy: 0.86
Kappa coefficient: 0.84
Producer's accuracy for Ws: 1.00
Producer's accuracy for Ds: 1.00
User's accuracy for Ws: 1.00
User's accuracy for Ds: 0.83

Figure S18. Confusion matrix with 180 validation points for the post-tsunami (2021) LULC map of the South segment (Figure S3e). Classes are abbreviated as follows: (W) Water, (F) Foam; (Ws) Wet sand; (Ds) Dry sand; (U) Urban; (Bs) Bare soil; (C) Crop; (S) Shadow; (Fr) Forest.

		Reference								
Prediction		**W**	**F**	**W_s**	**D_s**	**U**	**B_s**	**C**	**S**	**F_r**
	W	20	0	1	0	0	0	0	2	0
	F	0	19	0	0	2	0	0	0	0
	W_s	0	0	19	0	0	0	0	0	0
	D_s	0	1	0	20	0	0	0	0	0
	U	0	0	0	0	12	2	0	0	0
	B	0	0	0	0	6	17	0	0	1
	C	0	0	0	0	0	0	18	0	1
	S	0	0	0	0	0	1	0	18	0
	F_r	0	0	0	0	0	0	2	0	18

Overall accuracy: 0.89
Kappa coefficient: 0.88
Producer's accuracy for Ws: 0.95
Producer's accuracy for Ds: 1.00
User’s accuracy for Ws: 1.00
User’s accuracy for Ds: 0.95

Figure S19. Photos taken in August 2010 on Mr. Farías' land next to Cardonal Creek (Figure 4e; Table S1). (a) Potato crop covered by the extensive tsunami sand sheet. Orange dashed line partially outlines pieces of asphalt ripped out by the tsunami from the coastal road. (b) Weeks later the land was plowed to resume planting and the tsunami deposit was lost. Red arrow indicates in both photos the same house for reference.

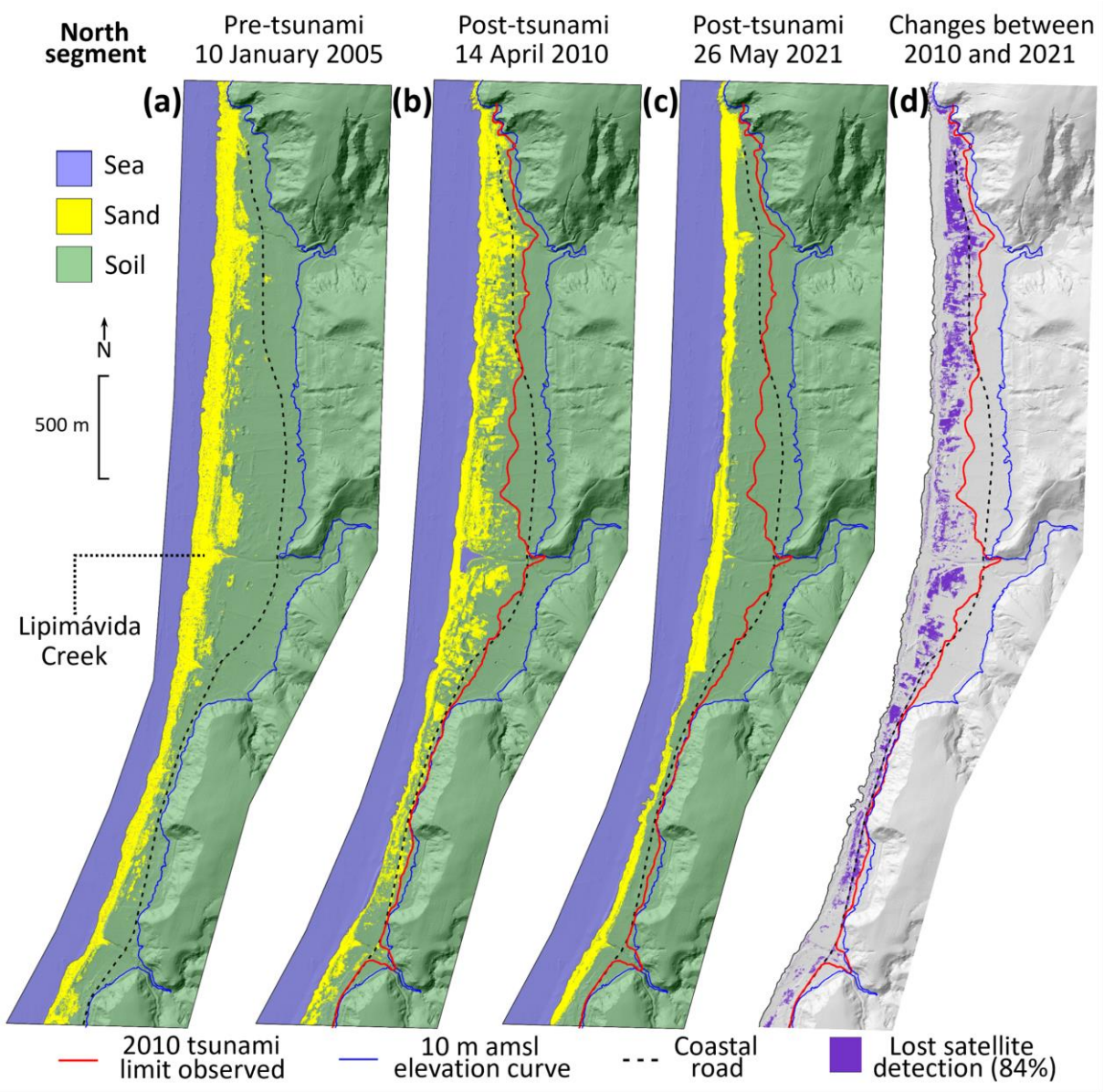

Figure S20. Satellite detection of the tsunami deposit that was lost by the classification model a decade after the 27 February 2010 event along the North segment (see Figure 1). (a) Sand detected before the 2010 tsunami, mainly restricted to beach and dune. (b) Sand detected weeks after the tsunami, including that from beach and dune but also that transported inland by the tsunami. (c) Sand detected a decade after the tsunami, resembling pre-tsunami condition. (d) Changes detected between the immediate post-tsunami condition and that of a decade later. The purple shading shows the area where the satellite detection of the tsunami deposit was lost (84%), either by masking due to new soil development or by destruction related to human activity.

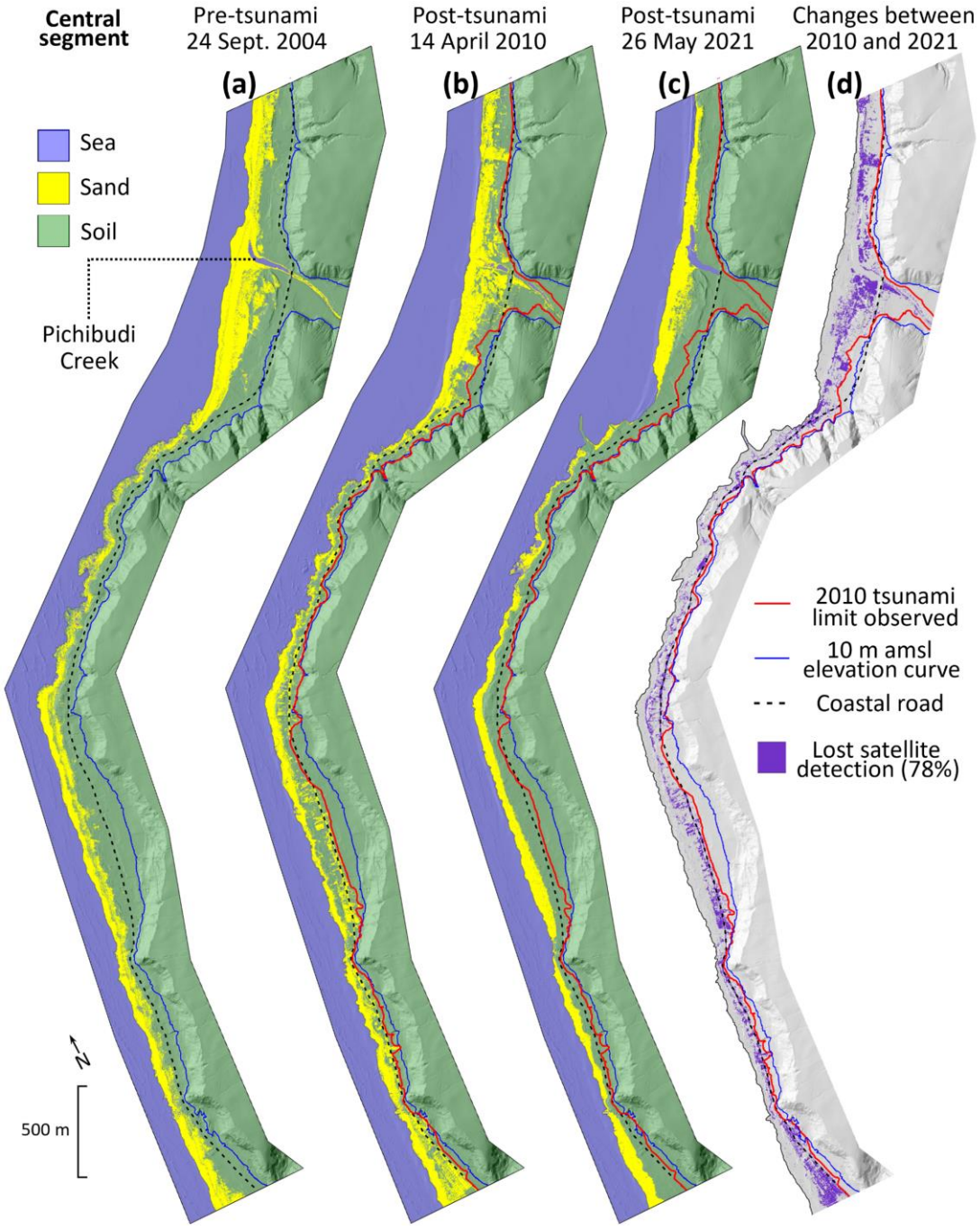

Figure S21. Satellite detection of the tsunami deposit that was lost by the classification model a decade after the 27 February 2010 event along the Central segment (see Figure 1). (a) Sand detected before the 2010 tsunami, mainly restricted to beach and dune. (b) Sand detected weeks after the tsunami, including that from beach and dune but also that transported inland by the tsunami. (c) Sand detected a decade after the tsunami, resembling pre-tsunami condition. (d) Changes detected between the immediate post-tsunami condition and that of a decade later. The purple shading shows the area where the satellite detection of the tsunami deposit was lost (78%), either by masking due to new soil development or by destruction related to human activity.

References for Anexo 1

Blott, S. J. & Pye, K. (2001). GRADISTAT: a grain size distribution and statistics package for the analysis of unconsolidated sediments. Earth Surface Processes and Landforms, 26(11), 1237–1248. https://doi.org/10.1002/esp.261

Folk, R. L. & Ward, W. C. (1957). Brazos River bar: a study in the significance of grain size parameters. Journal of Sedimentary Petrology, 27, 3–26.

Kempf, P., Moernaut, J., Van Daele, M., Vermassen, F., Vandoorne, W., Pino, M., Urrutía, R., Schmidt, S., Garrett, E. & De Batist, M. (2015). The sedimentary record of the 1960 tsunami in two coastal lakes on Isla de Chiloé, south central Chile. Sedimentary Geology, 328, 73–86. https://doi.org/10.1016/j.sedgeo.2015.08.004

Spiske, M. (2020). The sedimentology and geometry of fine-grained tsunami deposits from onshore environments. In Geological Records of Tsunamis and Other Extreme Waves (pp. 213–238). Elsevier.

Anexo 2. Supporting Information for Capítulo 4

Paleoseismological evidence of a century of coastal deformation in central Chile: lasting emergence and ongoing submergence

Bladimir Saldaña [a,b] *, Marco Cisternas [b], Matías Carvajal [b], Daniel Melnick [c], Joaquín Cortés-Aranda [a], Jean Pierre Francois [d], Alexandra Carreño [b], Mario Guerra [b]

[a] Departamento de Ciencias de la Tierra, Facultad de Ciencias Químicas, Universidad de Concepción, Concepción, Chile

[b] Instituto de Geografía, Pontificia Universidad Católica de Valparaíso, Valparaíso, Chile

[c] Instituto de Ciencias de la Tierra, Universidad Austral de Chile, Valdivia, Chile

[d] Departamento de Ciencias y Geografía, Universidad de Playa Ancha, Valparaíso, Chile

* Corresponding author

E-mail address: bsaldana@udec.cl

Contents of this file

Figures S1 to S16

Tables S1 and S2

Methods of tide gauge and geodetic data

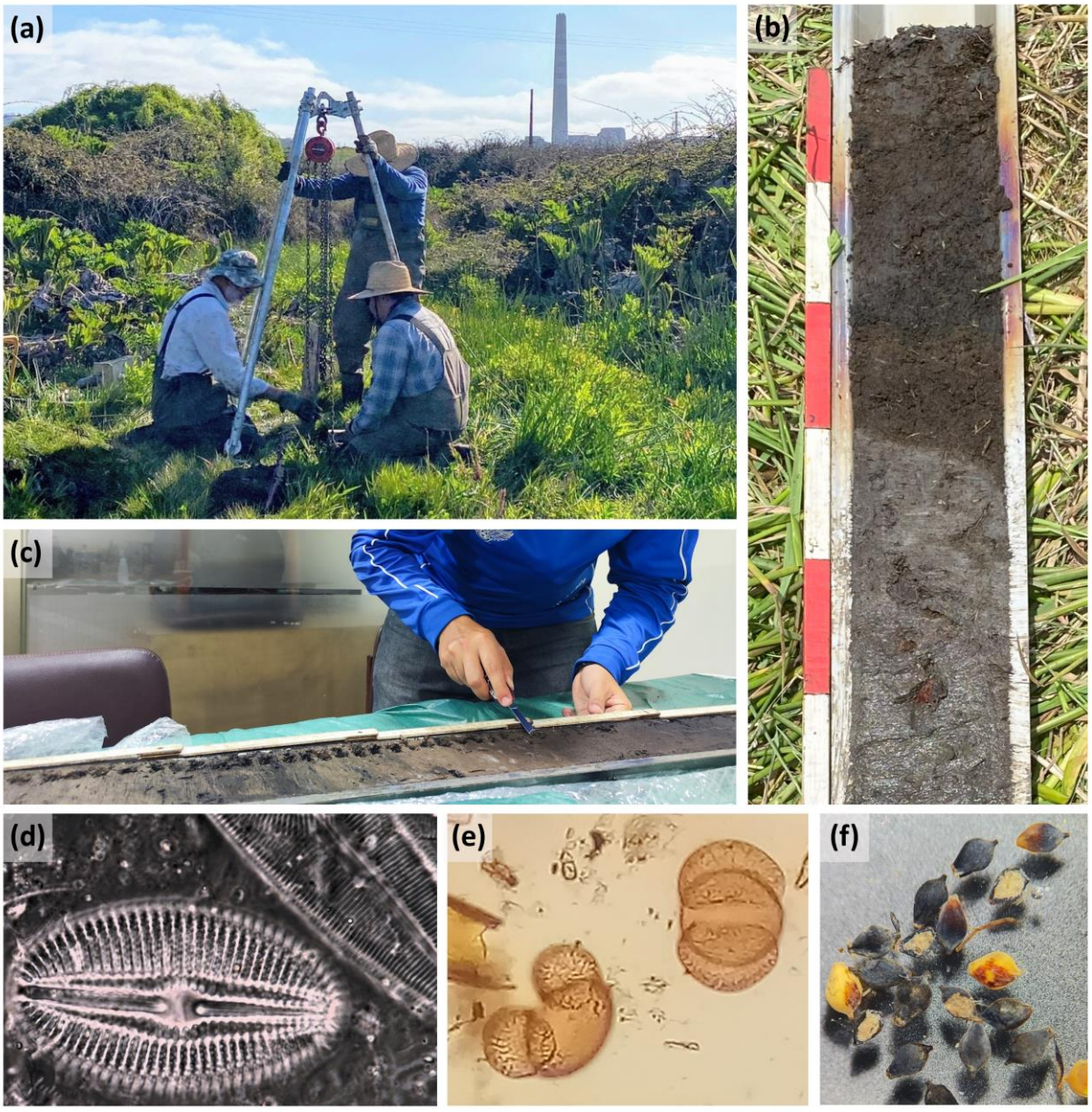

Figure S1. Fieldwork and laboratory analysis. (a) Recovery of a vibracorer slice at Campiche. Note the abundant freshwater vegetation. Industrial area in Quintero Bay can be seen in the background. (b) Sediment slice showing the sharp lithologic contact between the lower mud layer and the overlying peat layer. (c) Sampling for diatom and pollen analysis. (d) Marine diatom (*Diploneis smithii*) found in the mud layer. (e) Pine pollen found in the peat layer. (f) Seeds of *Schoenoplectus californicus* found in the mud layer.

Figure S2. Pit excavated near the site of Gayo et al. (2022) at Los Maitenes wetland (see Fig. 2a). Peat layer overlying the mud layer is indicated on the pit wall. Next to this wall slice SL-7 shown in Fig. 5 was recovered.

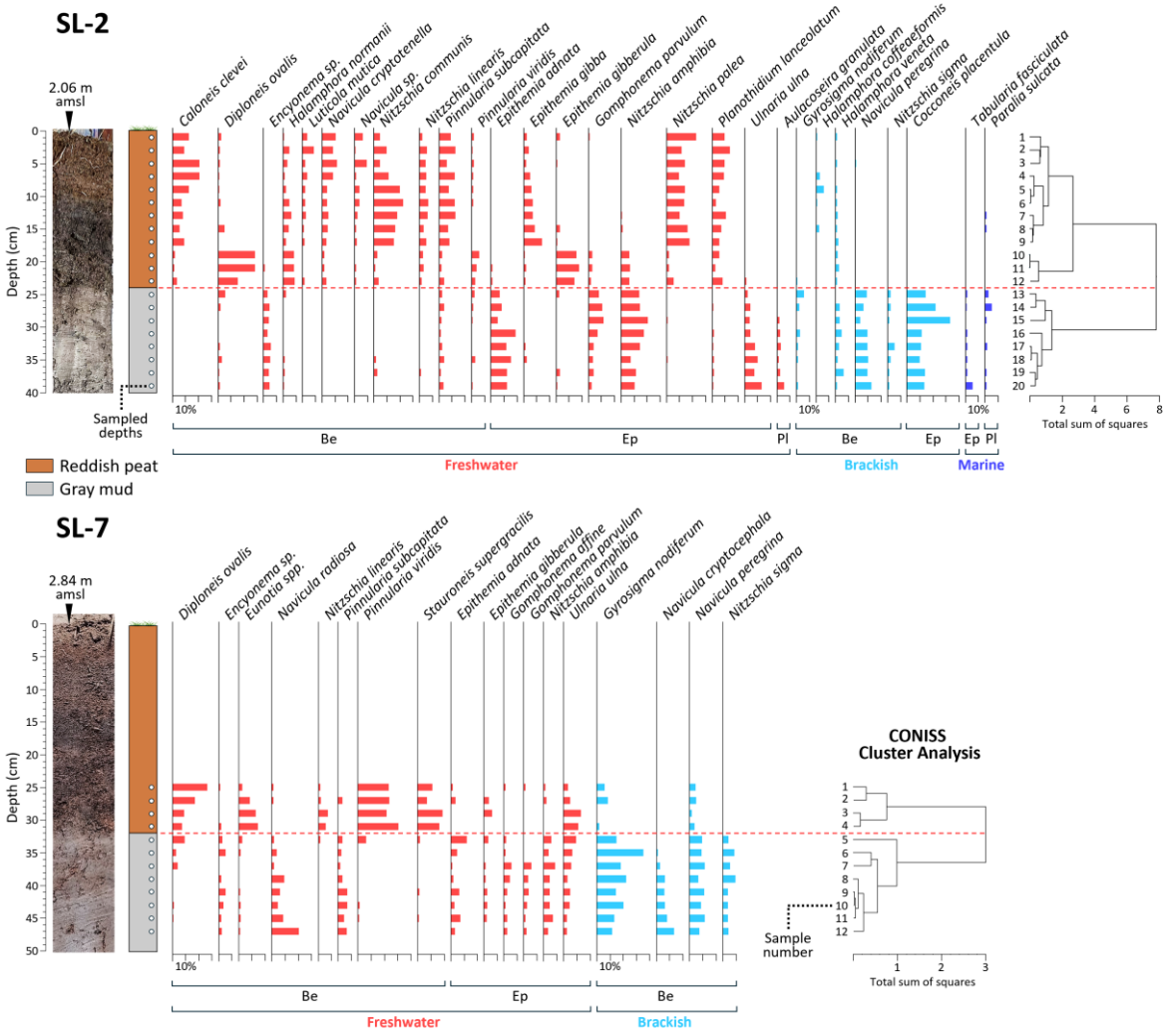

Figure S3. Relative abundance of diatoms in slices SL-2 and SL-7. Photographs and schematic stratigraphies of each slice are shown on the left. Only species with relative abundance >5% are included and are grouped by salinity preference (freshwater, brackish, and marine) and life form (Be: benthic, Ep: epiphytic, Pl: planktonic). Elevations above mean sea level (amsl) at which each slice was collected are indicated. Results of the CONISS cluster analysis on the right show an abrupt shift in diatom assemblages coinciding with the change from mud to peat (marked by the red dashed line). Note the gradual increase of brackish species in the uppermost peat section of slice SL-2.

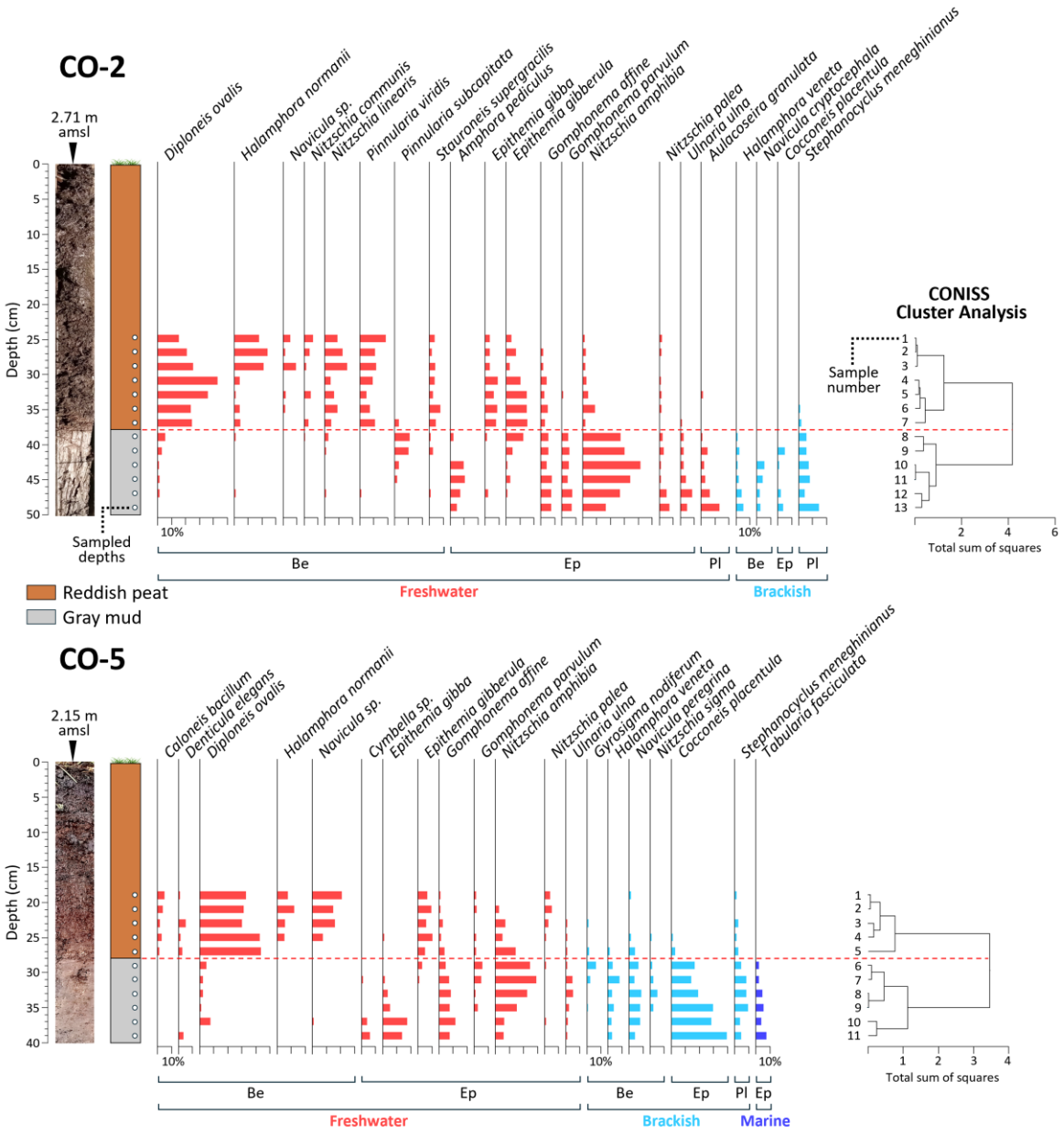

Figure S4. Relative abundance of diatoms in cores CO-2 and CO-5. Photographs and schematic stratigraphies of each core are shown on the left. Only species with relative abundance >5% are included and are grouped by salinity preference (freshwater, brackish, and marine) and life form (Be: benthic, Ep: epiphytic, Pl: planktonic). Elevations above mean sea level (amsl) at which each core was collected are indicated. Results of the CONISS cluster analysis on the right show an abrupt shift in diatom assemblages coinciding with the change from mud to peat (marked by the red dashed line).

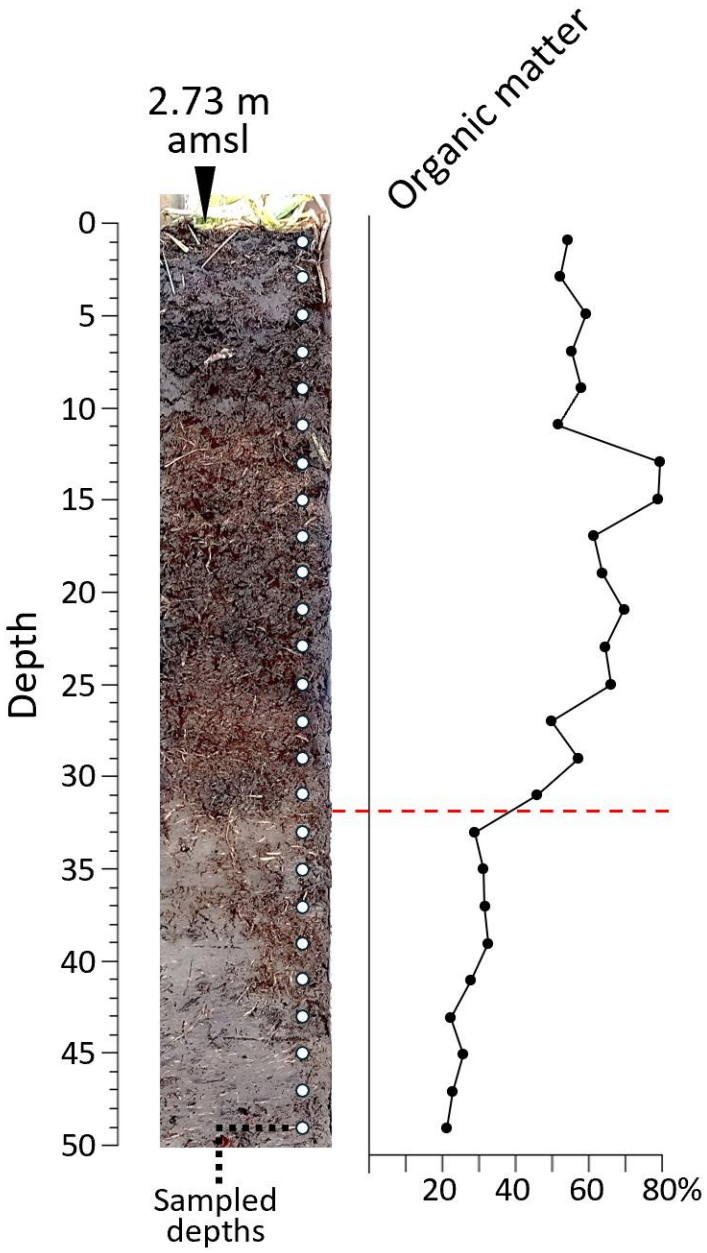

Figure S5. Organic matter content in slice SL-3. See material and methods in the main text. The ^{210}Pb chronological model for the slice is shown in Fig. 5.

Table S1. Key diatom species with their salinity preferences and life forms. Taxa listed exceed 5% of total diatom valves counted in at least one sample. Ecological information from Vos and de Wolf (1988; 1993), Denys (1991), Hemphill-Halley (1993), Van Dam et al. (1994), Hassan et al. (2009), Dura et al. (2015) and Zong and Sawai (2015).

Diatom species (>5%)	Salinity	Life form
Amphora bicapitata	Freshwater	Benthic
Amphora pediculus	Freshwater	Epiphytic
Aulacoseira granulata	Freshwater	Planktonic
Caloneis bacillum	Freshwater	Benthic
Caloneis clevei	Freshwater	Benthic
Cocconeis placentula	Brackish	Epiphytic
Cymbella sp.	Freshwater	Epiphytic
Denticula elegans	Freshwater	Benthic
Diploneis ovalis	Freshwater	Benthic
Encyonema sp.	Freshwater	Benthic
Epithemia adnata	Freshwater	Epiphytic
Epithemia gibba	Freshwater	Epiphytic
Epithemia gibberula	Freshwater	Epiphytic
Eunotia spp.	Freshwater	Benthic
Gomphonema affine	Freshwater	Epiphytic
Gomphonema parvulum	Freshwater	Epiphytic
Gyrosigma nodiferum	Brackish	Benthic
Halamphora coffeaeformis	Brackish	Benthic
Halamphora normanii	Freshwater	Benthic
Halamphora veneta	Brackish	Benthic
Luticola mutica	Freshwater	Benthic
Navicula cryptocephala	Brackish	Benthic
Navicula cryptotenella	Freshwater	Benthic
Navicula sp.	Freshwater	Benthic
Navicula peregrina	Brackish	Benthic
Navicula radiosa	Freshwater	Benthic
Nitzschia amphibia	Freshwater	Epiphytic
Nitzschia clausii	Brackish	Benthic
Nitzschia communis	Freshwater	Benthic
Nitzschia linearis	Freshwater	Benthic
Nitzschia sigma	Brackish	Benthic
Nitzschia palea	Freshwater	Epiphytic
Paralia sulcata	Marine	Planktonic
Pinnularia divergens	Freshwater	Benthic
Pinnularia subcapitata	Freshwater	Benthic
Pinnularia viridis	Freshwater	Benthic
Planothidium lanceolatum	Freshwater	Epiphytic
Stauroneis supergracilis	Freshwater	Benthic
Stephanocyclus meneghinianus	Brackish	Planktonic
Tabularia fasciculata	Marine	Epiphytic
Ulnaria ulna	Freshwater	Epiphytic

Table S2. Relevant information of historical maps and aerial photography used in this study.

Year	Type	Name	Author	Scale	Source	Information
1803	Hydrographic map	Plano geométrico del Puerto de la Herradura de Quintero	Officers aboard the Bergantín Peruano and Goleta Extremeña	1:20000	Hydrographic and Oceanographic Service of the Chilean Navy	The position of the lagoons is approximate
1860	Hydrographic map	Plano del puerto de Quintero	Francisco Vidal Gormaz	1:25000	Chilean National Library	The position of the lagoons is approximate
1876	Hydrographic map	Bahía de Quintero i Caleta Horcón	Luis Pomar	1:40000	Chilean National Library	-
1904	Hydrographic map	Bahía de Quintero	Luis Pomar	1:30000	Chilean National Library	-
1914	Hydrographic map	Bahía de Quintero in America del Sur Costa Oeste, Chile	Hydrographic and Oceanographic Service of the Chilean Navy	1:60000	Chilean National Library	-
1926	Hydrographic map	Bahía y Puerto Quintero	Hydrographic and Oceanographic Service of the Chilean Navy	1:30000	Hydrographic and Oceanographic Service of the Chilean Navy	-
1930	Topographic map	Quintero	Chilean Military Geographic Institute	1:25000	Chilean National Library	-
1954	Aerial photograph	Quintero Bay, 16 December 1954.	Chilean Aerial Photogrammetric Service	-	Chilean Aerial Photogrammetric Service	First aerial photograph of Quintero Bay

Relative sea-level estimated from tide gauge data

To estimate the history of RSL change and the associated rates, we used data from the Valparaiso tide gauge station obtained from the Hydrographic and Oceanographic Service of the Chilean Navy (SHOA) available at https://www.shoa.cl extending between 1944 and 2025 with an hourly temporal resolution (Fig. S6). We first removed astronomic tides using the MATLAB *Tidal fitting toolbox* (Grinstead, 2024), downloaded from https://www.mathworks.com/matlabcentral/fileexchange/19099-tidal-fitting-toolbox. We first detrended the data and stored the linear coefficients, then removed the modeled tidal signal using the inverted constituents from the tide gauge data and then added back the stored coefficients of the first detrend stage. To remove outliers that may result from storms, we applied a 1-day running mean filter. Then, we modeled the trajectory of *rsl(t)*, the daily residual tide as:

$$rsl(t) = A\,(t - t_R) \;\; + \sum_{j=1}^{nj} B_j\, H\left(t - t_j\right) + C\,(t - t_R) + D\,\log(1 + \Delta t - t_{eq}/T)$$

where A is the coefficient of a linear function, t_R is a reference time defined as t_0, B is the coefficient of a Heaviside jump function included to simulate a static offset during earthquakes at time t_j, C is the coefficient of the contribution from the anomalous El Niño-Southern Oscillation (ENSO) atmosphere-ocean conditions, and D is the coefficient of the transient post-seismic logarithmic component where t_{eq} is the time of the earthquake (We added a term to the 2010 Maule earthquake Mw=8.8), and T is a constant determining the timescale of the logarithmic transient set to 0.1 based on a previous study (Melnick et al., 2017). The ENSO contribution was modeled using the SOI-Index time series file *soi_3dp.dat* downloaded from https://crudata.uea.ac.uk/cru/data/soi/, linearly interpolated to the tide gauge time vector, and added to the design matrix to perform a least square inversion of the coefficients. Because neither the tide gauge data nor the SOI index is associated with formal uncertainties, we solved the inverse problem using the MATLAB function *mldivide*, and estimated the uncertainties by bootstrapping the function 1,000 times and estimating a probability function of the results.

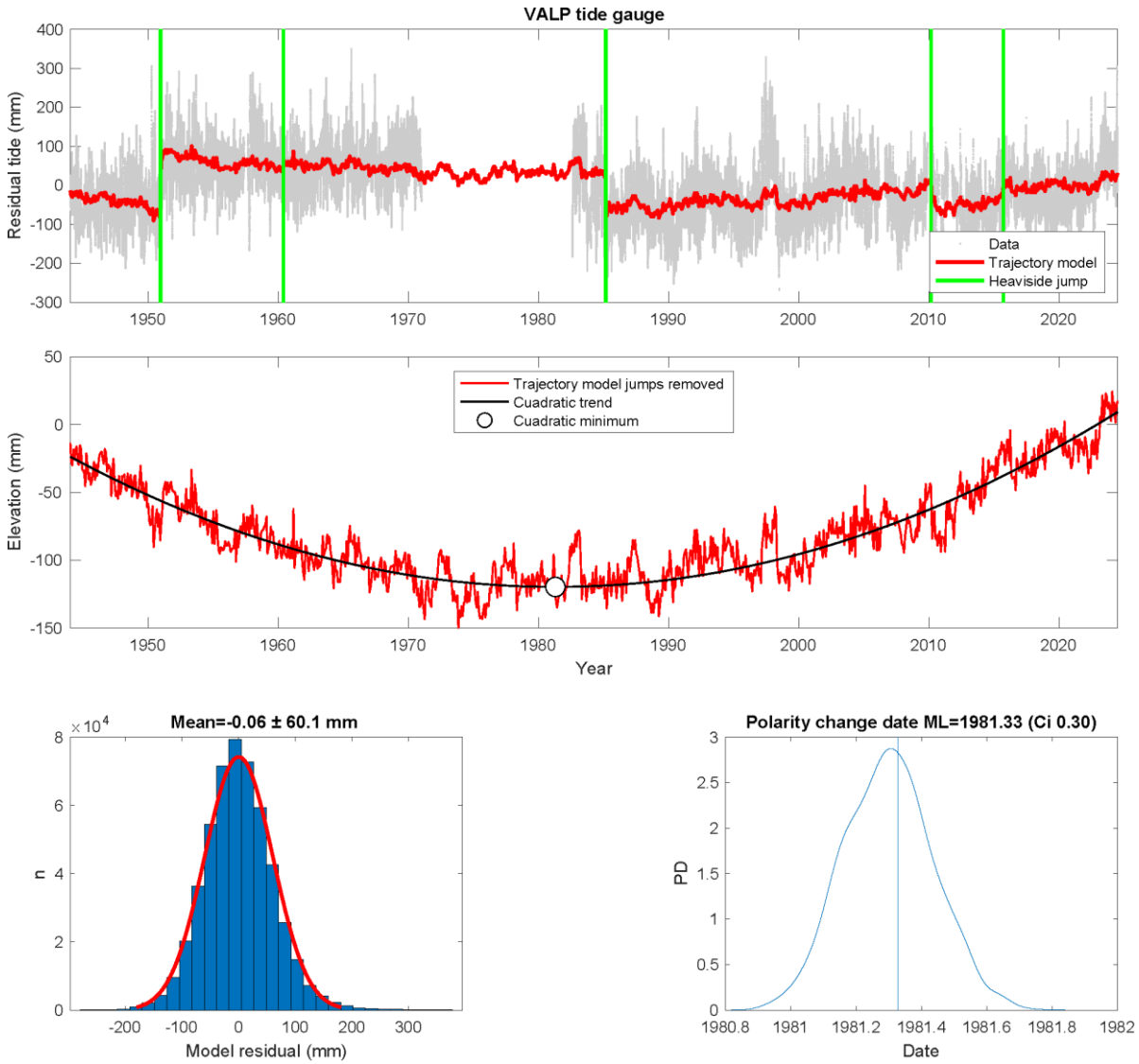

Figure S6. Time series analysis of the Valparaíso tide gauge. Complete tide gauge record from 1944 to 2025 (upper panel). Note the data gap between 1971 and 1982. Red line shows the trajectory model and green lines represent heaviside jumps. Trajectory model with quadratic term is shown in the center panel. White circle shows the minimum of the quadratic function, indicating a reversal in the relative sea level (RSL) trend. Residuals and date of RSL change are shown in the lower panel.

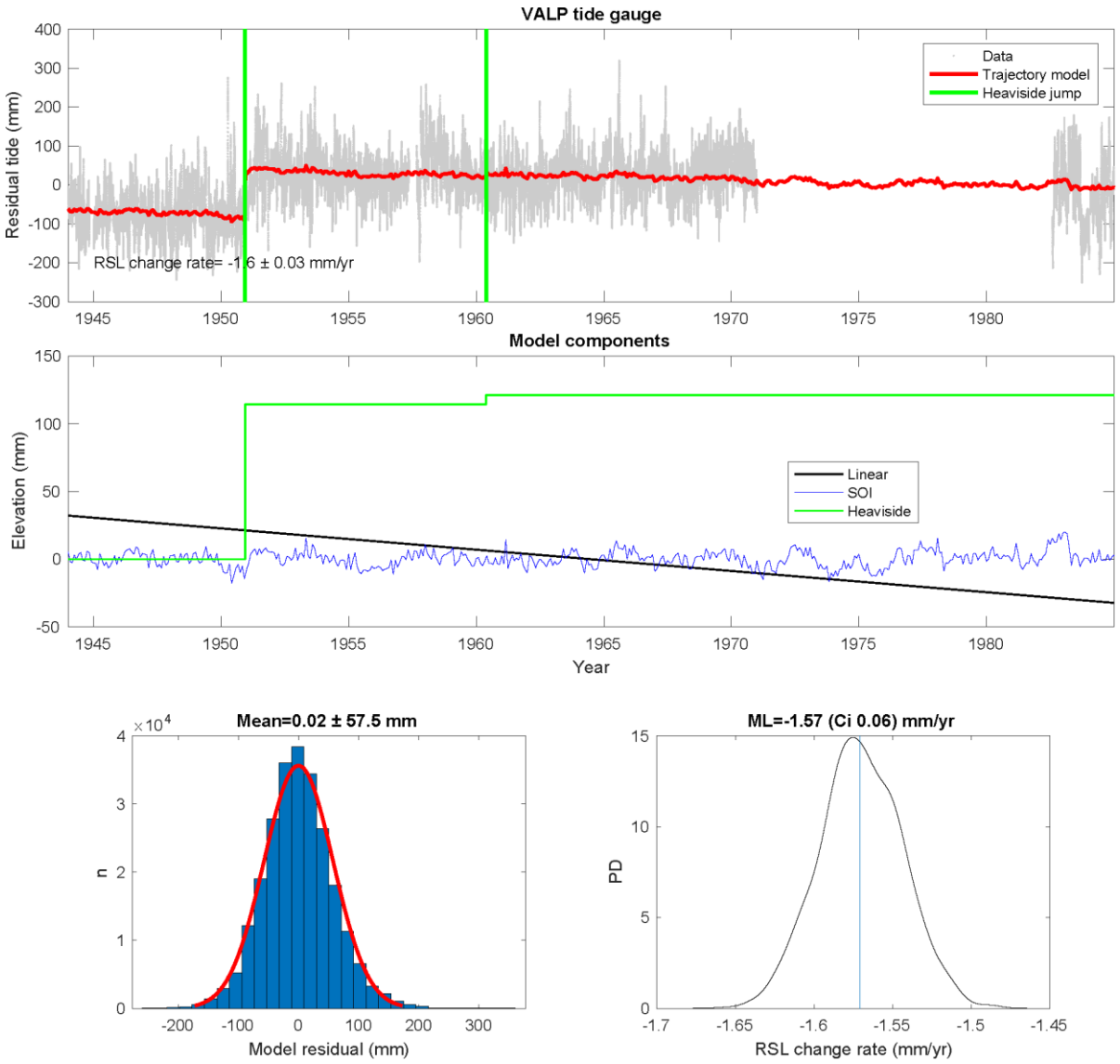

Figure S7. Time series analysis of the Valparaíso tide gauge. Tide gauge record from 1944 to 1985 (upper panel). Note the data gap between 1971 and 1982. Red line shows the trajectory model and green lines represent heaviside jumps. Relative sea level (RSL) linear trend is shown in the center panel (black line). Residuals and change rate are shown in the lower panel.

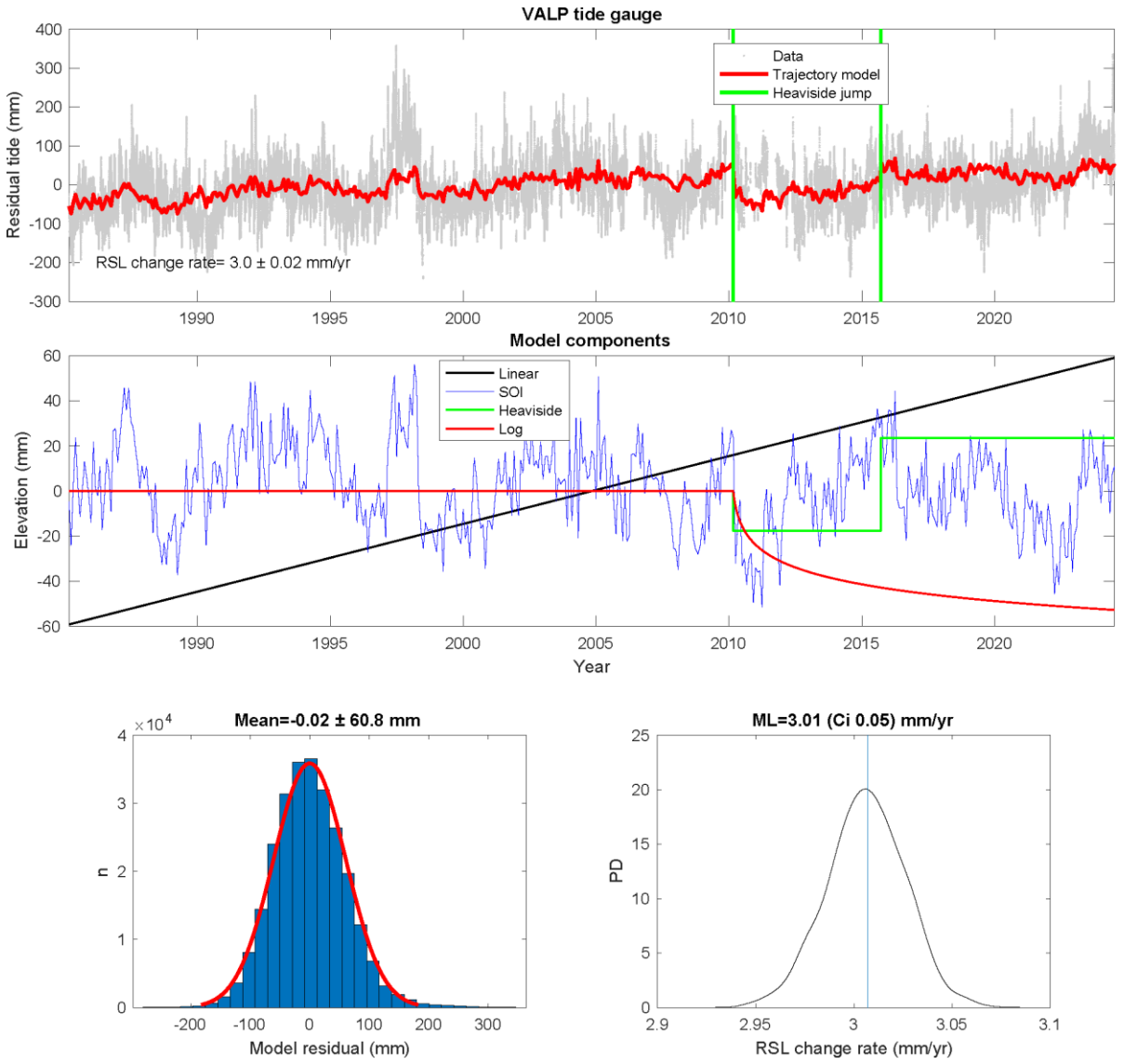

Figure S8. Time series analysis of the Valparaíso tide gauge. Tide gauge record from 1985 to 2025 (upper panel). Red line shows the trajectory model and green lines represent heaviside jumps. Relative sea level (RSL) linear trend is shown in the center panel (black line). Residuals and change rate are shown in the lower panel.

Vertical land motion estimates from GNSS data

The daily positions of 5 continuous GNSS stations with at least 2.5 years of data were downloaded from the Nevada Geodetic Laboratory site http://geodesy.unr.edu/, which have been processed as detailed by (Blewitt et al., 2018) in the IGS14 reference frame (Figs. S9-13). We used the linear trajectory method (Bevis and Brown, 2014; Melnick et al., 2017) to model *vlm*(*t*), the GNSS daily position time series in the East, North, and Up components as:

$$vlm(t) = A\,(t - t_R) \quad + \sum_{j=1}^{nj} B_j\, H\left(t - t_j\right) + \sum_{k=1}^{2} [C \sin(\frac{2\pi}{\tau_k}\, t) + D \cos(\frac{2\pi}{\tau_k}\, t)] + E \log(1 + \Delta t - t_{eq}/T)$$

where A is the coefficient of a linear function of n_p=1 power, t_R is a reference time defined as t_0, B are the coefficients of H heaviside jumps to simulate earthquakes and non-tectonic effects such as instrumental changes, C and D are the coefficients of a truncated Fourier Series to account for seasonal variations mostly induced by the hydrological cycle (we used τ=1 year for annual and τ=0.5 year for semi-annual periods), and E is the coefficient of the transient post-seismic logarithmic component where t_{eq} is the time of the Maule earthquake (27 February 2010), and T is a constant determining the timescale of the logarithmic transient set to 0.1 based on a previous study (Melnick et al., 2017). Heaviside jumps were included for earthquakes from the National Earthquake Information Catalogue (NEIC) of the US Geological Survey found at $d \leq 10^{(0.5 * mag - 0.8)}$, where d is the distance between the epicenter and the GPS station and *mag* is the earthquake moment magnitude. We used the MATLAB function *lscov* to perform the least-squares inversion in the presence of covariance accounting for the positioning error in the daily station coordinates. The inversion was performed for the East, North, and Up components simultaneously; the Up component is used to estimate vertical land motion.

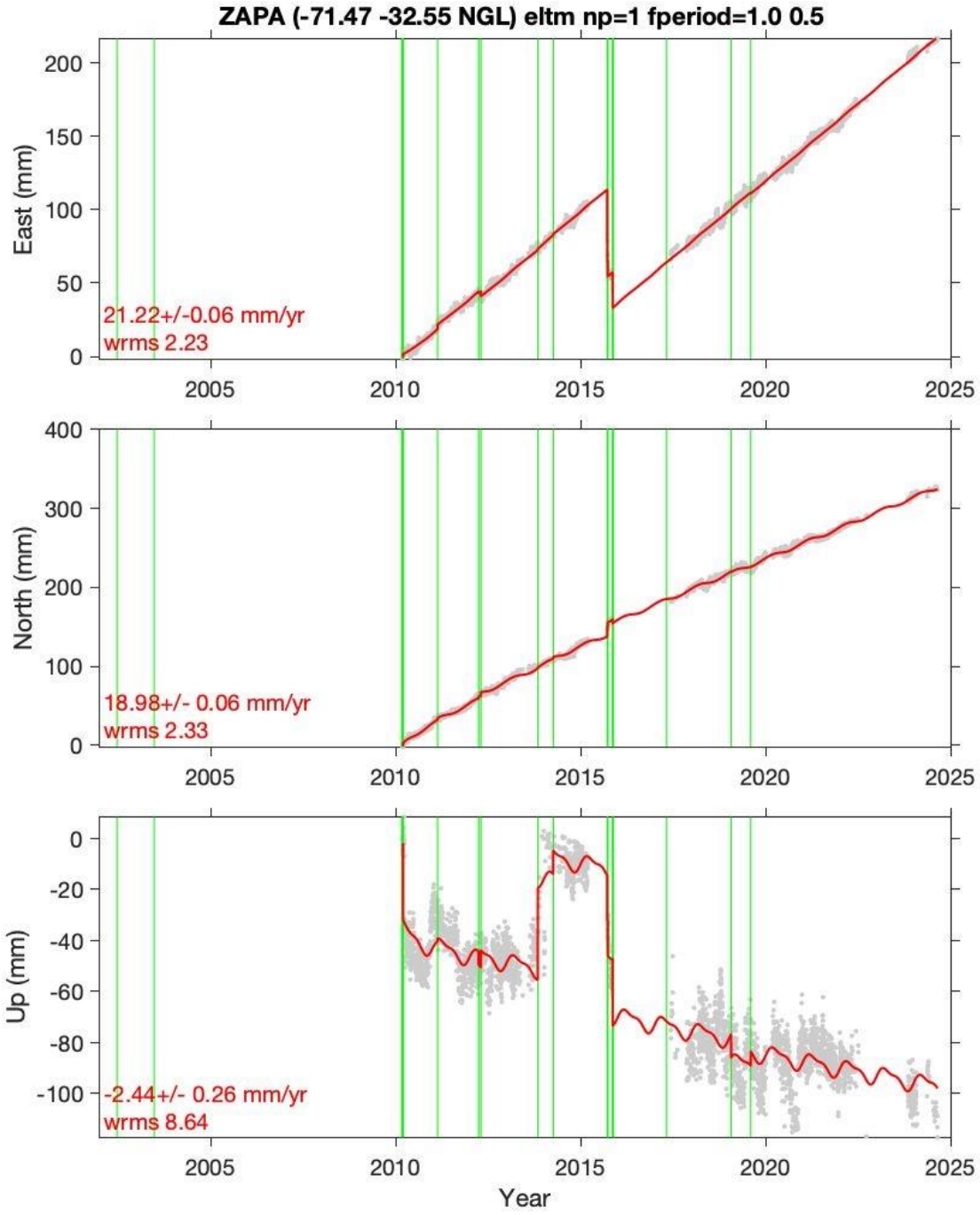

Figure S9. Daily position time series of continuous GNSS station ZAPA located at Zapallar (see Fig. 1c). East, North and Up components are shown with their respective rates. Red line shows trajectory model computed using the linear trajectory method from Bevis and Brown (2014). Green lines are heaviside jumps. wrms: weighted root mean square error.

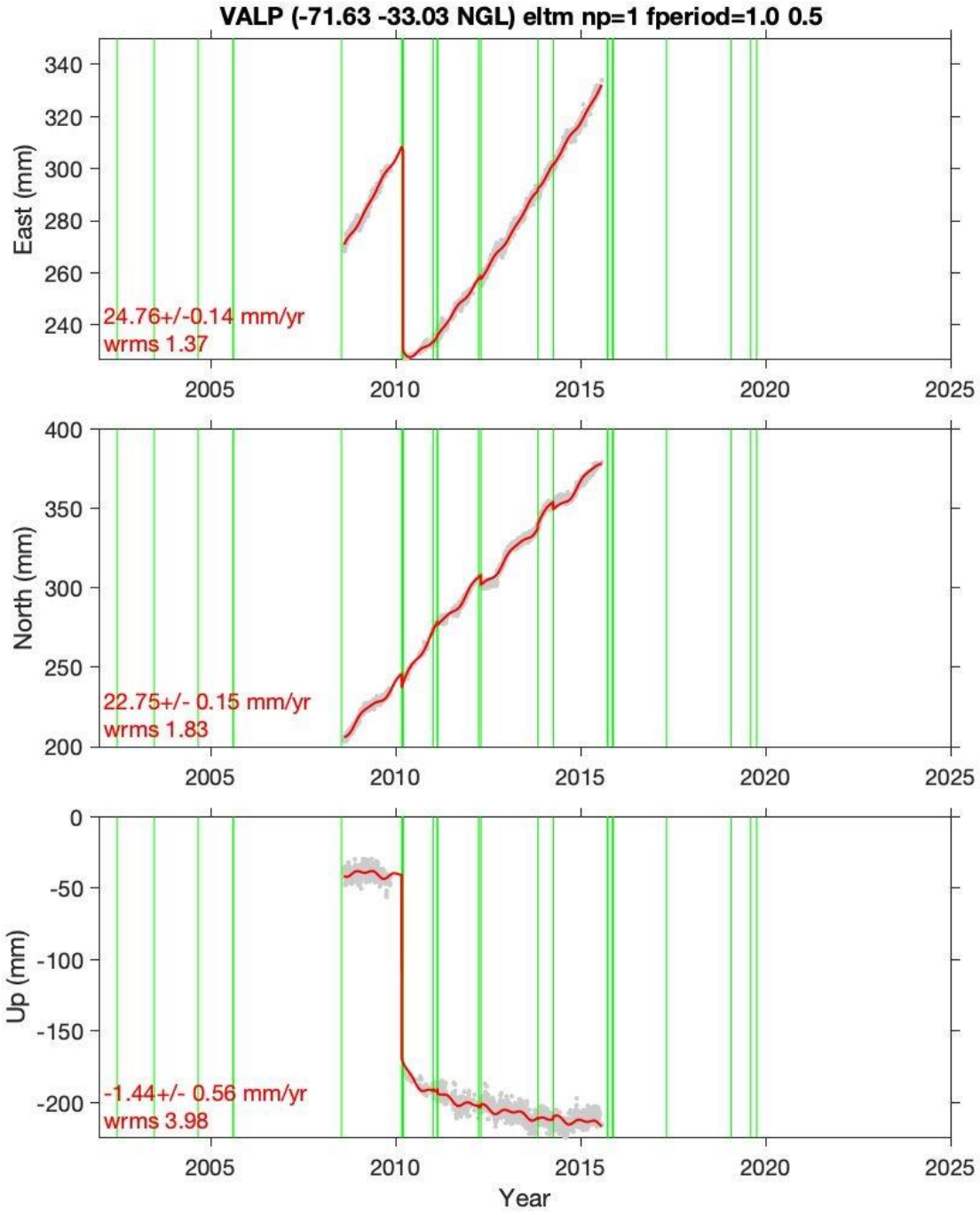

Figure S10. Daily position time series of continuous GNSS station VALP located at Valparaíso (see Fig. 1c). East, North and Up components are shown with their respective rates. Red line shows trajectory model computed using the linear trajectory method from Bevis and Brown (2014). Green lines are heaviside jumps. wrms: weighted root mean square error.

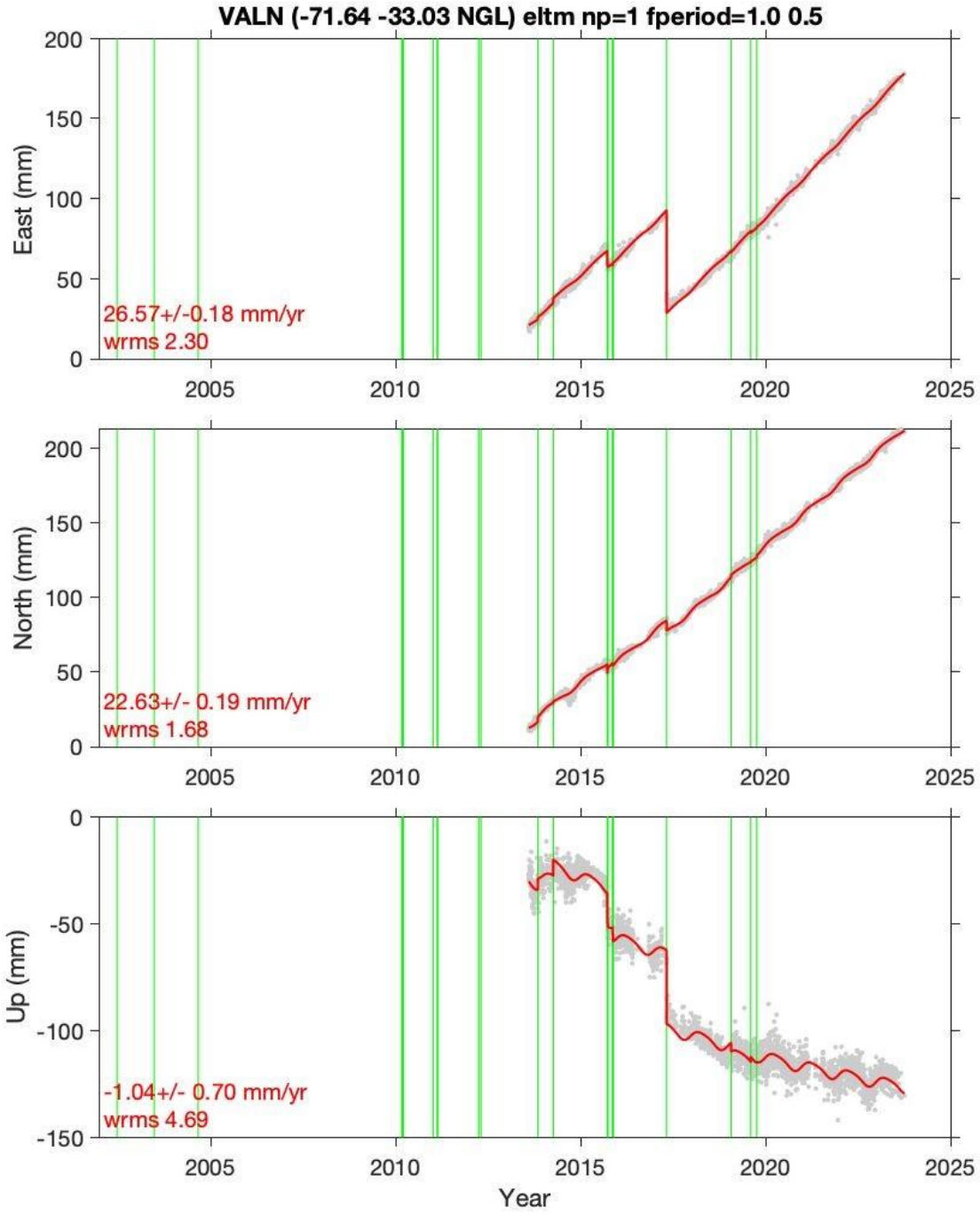

Figure S11. Daily position time series of continuous GNSS station VALN located at Valparaíso (see Fig. 1c). East, North and Up components are shown with their respective rates. Red line shows trajectory model computed using the linear trajectory method from Bevis and Brown (2014). Green lines are heaviside jumps. wrms: weighted root mean square error.

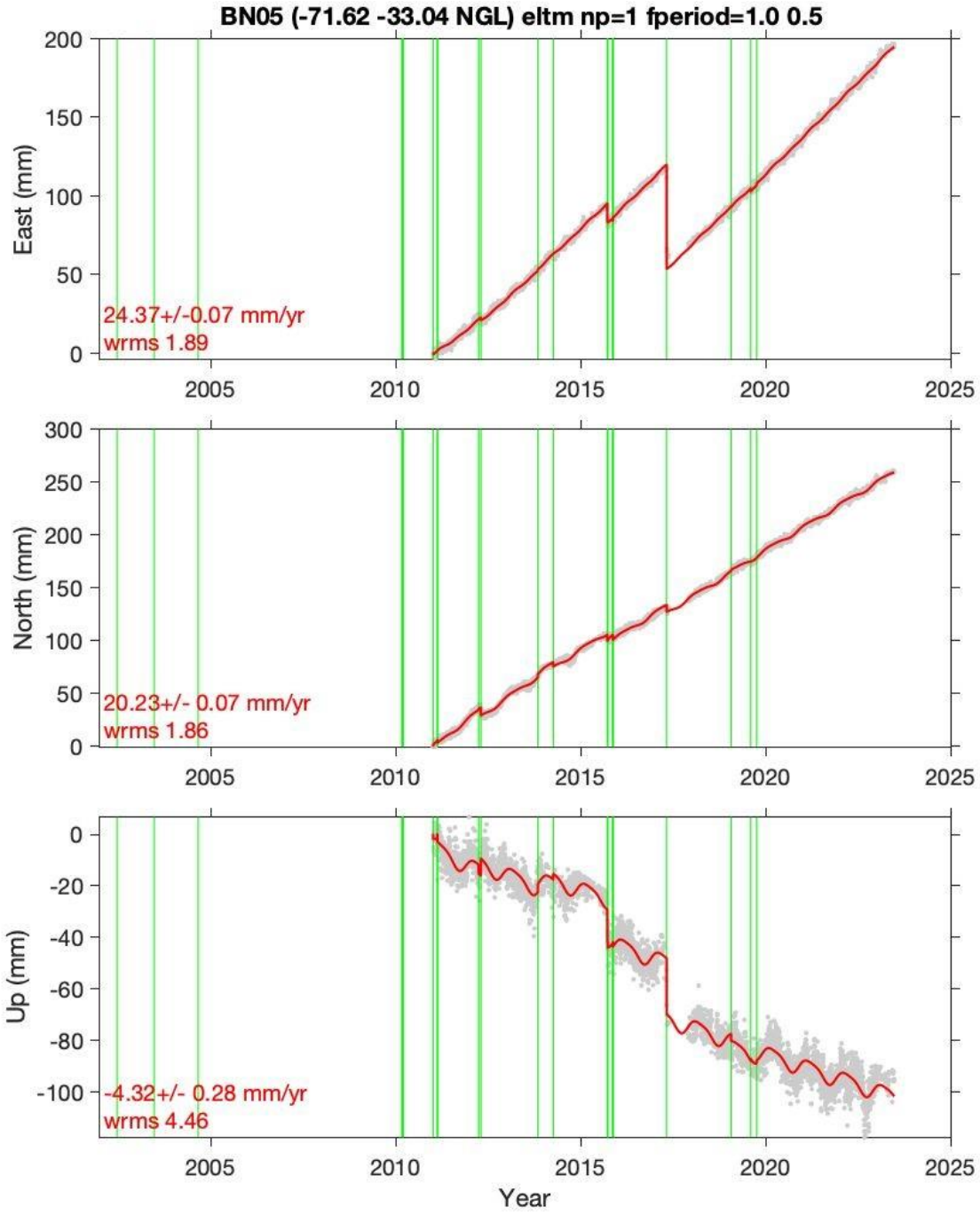

Figure S12. Daily position time series of continuous GNSS station BN05 located at Valparaíso (see Fig. 1c). East, North and Up components are shown with their respective rates. Red line shows trajectory model computed using the linear trajectory method from Bevis and Brown (2014). Green lines are heaviside jumps. wrms: weighted root mean square error.

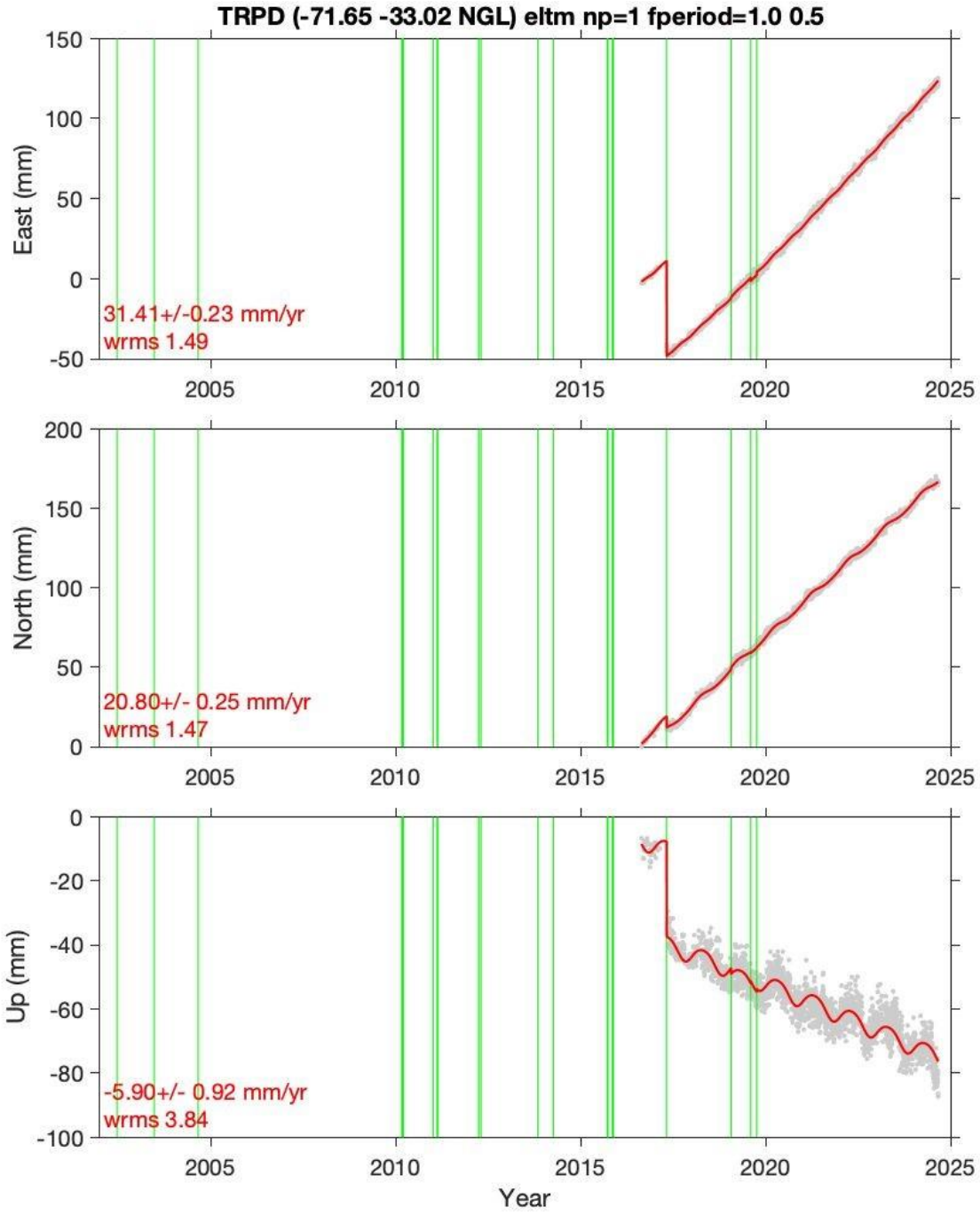

Figure S13. Daily position time series of continuous GNSS station TRPD located at Valparaíso (see Fig. 1c). East, North and Up components are shown with their respective rates. Red line shows trajectory model computed using the linear trajectory method from Bevis and Brown (2014). Green lines are heaviside jumps. wrms: weighted root mean square error.

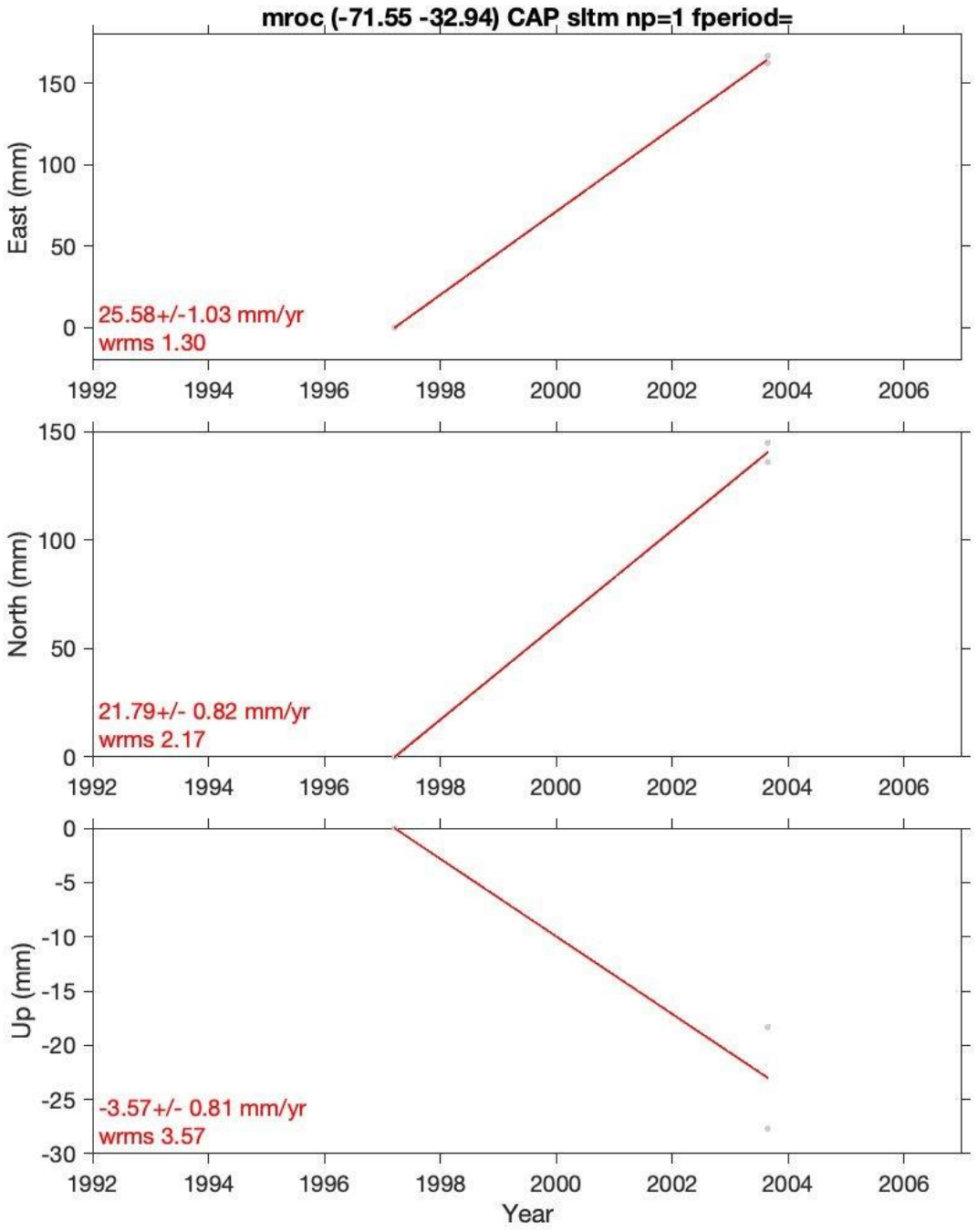

Figure S14. Data from campaign GPS benchmark MROC located at Concón (see Fig. 1c). East, North and Up components are shown with their respective rates. Red line shows trajectory model computed using the linear trajectory method from Bevis and Brown (2014). wrms: weighted root mean square error.

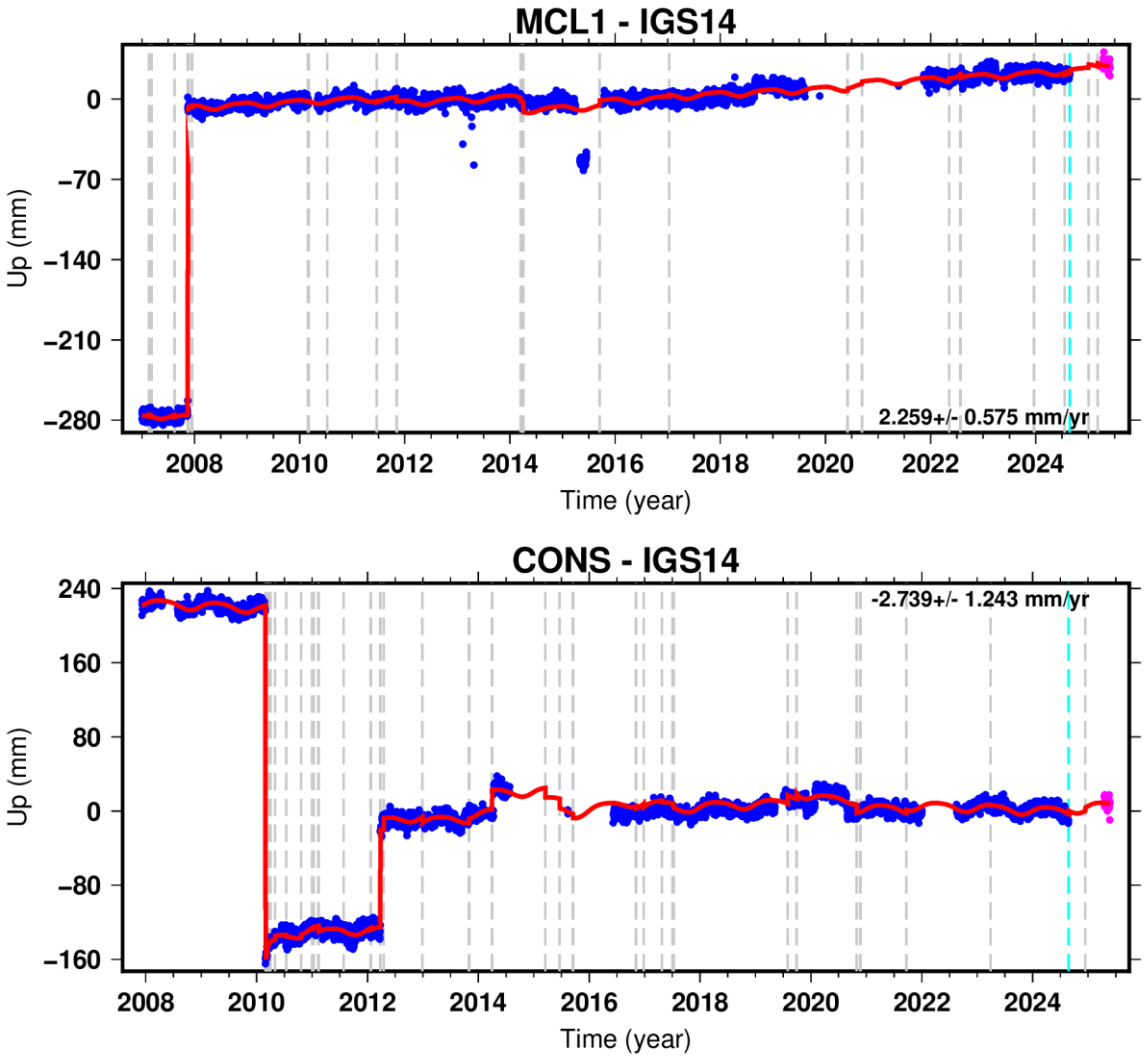

Figure S15. Continuous GNSS stations showing sustained coastal uplift after modern earthquakes in northern and central Chile. Station MCL1 (above) at Michilla, northern Chile, shows sustained uplift after the 2007 Tocopilla earthquake (Mw 7.7). Station CONS (below) at Constitución, central Chile, shows subsidence caused by the 2010 Maule earthquake (Mw 8.8) and sustained uplift following the 2012 Constitución earthquake (Mw 7.0). Daily position time series were obtained from the Nevada Geodetic Laboratory site http://geodesy.unr.edu/.

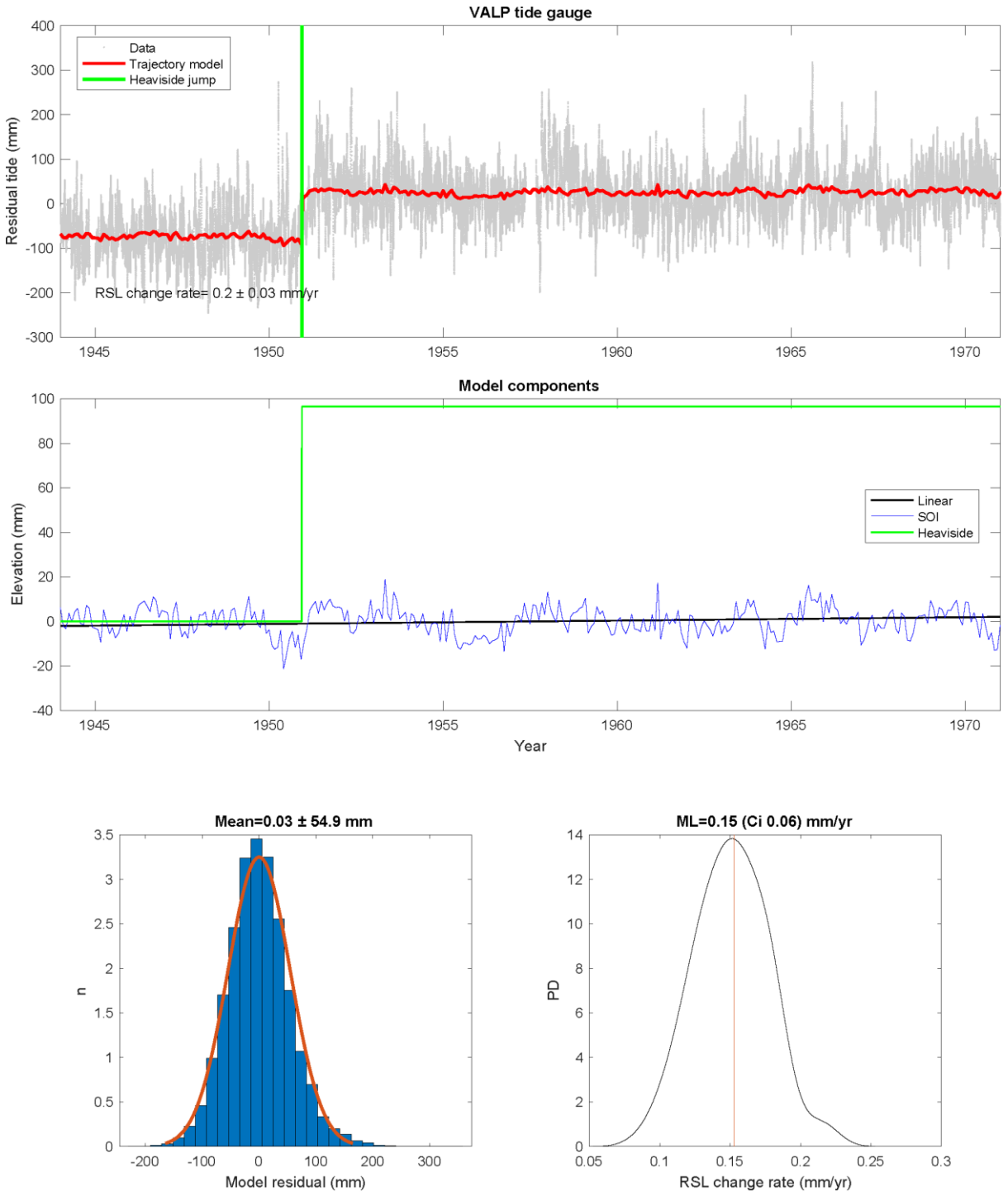

Figure S16. Time series analysis of the Valparaíso tide gauge. Tide gauge record from 1944 to 1971 (upper panel). Red line shows the trajectory model and green lines represent heaviside jumps. Relative sea level (RSL) linear trend is shown in the center panel (black line). Residuals and change rate are shown in the lower panel.

References for Anexo 2

Bevis, M. & Brown, A. (2014). Trajectory models and reference frames for crustal motion geodesy. Journal of Geodesy, 88(3), 283–311. https://doi.org/10.1007/s00190-013-0685-5

Blewitt, G., Hammond, W. C. & Kreemer, C. (2018). Harnessing the GPS data explosion for interdisciplinary science, Eos, 99, https://doi.org/10.1029/2018EO104623.

Denys, L. (1991). A check-list of the diatoms in the Holocene deposits of the western Belgian coastal plain with a survey of their apparent ecological requirements.

Dura, T., Cisternas, M., Horton, B. P., Ely, L. L., Nelson, A. R., Wesson, R. L. & Pilarczyk, J. E. (2015). Coastal evidence for Holocene subduction-zone earthquakes and tsunamis in central Chile. Quaternary science reviews, 113, 93–111. https://doi.org/10.1016/j.quascirev.2014.10.015

Grinsted, A. (2024). Tidal fitting toolbox, MATLAB Central File Exchange.

Hassan, G. S., Tietze, E. & De Francesco, C. G. (2009). Modern diatom assemblages in surface sediments from shallow lakes and streams in southern Pampas (Argentina). Aquatic Sciences, 71(4), 487–499. https://doi.org/10.1007/s00027-009-0104-4

Hemphill-Haley, E. (1993). Taxonomy of recent and fossil (Holocene) diatoms (Bacillariophyta) from northern Willapa Bay, Washington: U.S. Geological Survey Open-File Report 93-289, 151 p. https://doi.org/10.3133/ofr93289

Melnick, D., Moreno, M., Quinteros, J., Baez, J. C., Deng, Z., Li, S. & Oncken, O. (2017). The super-interseismic phase of the megathrust earthquake cycle in Chile. Geophysical Research Letters, 44(2), 784–791. https://doi.org/10.1002/2016gl071845

Van Dam, H., Mertens, A. & Sinkeldam, J. (1994). A coded checklist and ecological indicator values of freshwater diatoms from The Netherlands. Netherlands Journal of Aquatic Ecology, 28(1), 117–133. https://doi.org/10.1007/bf02334251

Vos, P.C. & de Wolf, H. (1988). Methodological aspects of paleo-ecological diatom research in coastal areas of the Netherlands. Geologie en Mijnbouw 67, 31–40.

Vos, P. C. & de Wolf, H. (1993). Diatoms as a tool for reconstructing sedimentary environments in coastal wetlands; methodological aspects. Hydrobiologia, 269–270(1), 285–296. https://doi.org/10.1007/bf00028027

Zong, Y. & Sawai, Y. (2015). Diatoms. In Handbook of Sea-Level Research (eds I. Shennan, A.J. Long and B.P. Horton). John Wiley & Sons, Ltd, Chichester, UK. https://doi.org/10.1002/9781118452547.ch15